POLYPUBLIE
Polytechnique Montréal

POLYTECHNIQUE MONTRÉAL
UNIVERSITÉ D'INGÉNIERIE

Titre: Title:	Investigation of the Natural Mixing Behavior of Dumped Waste Rock and Paste Backfill
Auteur: Author:	Yuyu Zhang
Date:	2024
Type:	Mémoire ou thèse / Dissertation or Thesis
Référence: Citation:	Zhang, Y. (2024). Investigation of the Natural Mixing Behavior of Dumped Waste Rock and Paste Backfill [Thèse de doctorat, Polytechnique Montréal]. PolyPublie. https://publications.polymtl.ca/59207/

Document en libre accès dans PolyPublie
Open Access document in PolyPublie

URL de PolyPublie: PolyPublie URL:	https://publications.polymtl.ca/59207/
Directeurs de recherche: Advisors:	Li Li
Programme: Program:	Génie minéral

Ce fichier a été téléchargé à partir de PolyPublie, le dépôt institutionnel de Polytechnique Montréal
This file has been downloaded from PolyPublie, the institutional repository of Polytechnique Montréal

https://publications.polymtl.ca

POLYTECHNIQUE MONTRÉAL

affiliée à l’Université de Montréal

Investigation of the natural mixing behavior of dumped waste rock and paste backfill

YUYU ZHANG

Département des génies civil, géologique et des mines

Thèse présentée en vue de l’obtention du diplôme de *Philosophiæ Doctor*

Génie minéral

Août 2024

© Yuyu Zhang, 2024.

POLYTECHNIQUE MONTRÉAL

affiliée à l'Université de Montréal

Cette thèse intitulée :

Investigation of the natural mixing behavior of dumped waste rock and paste backfill

présentée par **Yuyu ZHANG**

en vue de l'obtention du diplôme de *Philosophiæ Doctor*

a été dûment acceptée par le jury d'examen constitué de:

Carlos OVALLE, président
Li LI, membre et directeur de recherche
Serge OUELLET, membre et codirecteur de recherche
Pedro CACCIARI, membre
Tikou BELEM, membre
Liang CUI, membre externe

DEDICATION

To my family

To my friends

ACKNOWLEDGEMENTS

First, I am extremely grateful for the support and supervision of my supervisor, Prof. Li Li. This work would not have been possible without his tremendous help and support. Throughout my Ph.D. journey, I have been deeply influenced by Prof. Li's attitude and dedication to the research. I have learned invaluable lessons from him. These experiences will undoubtedly benefit my future career and life. I will be forever grateful for the knowledge and experiences he has shared with me.

I would like to thank Dr. Serge Ouellet, who agreed to be my co-supervisor and provide support for my Ph.D. thesis. I am very grateful for his time and guidance.

Many thanks go to Prof. Carlos Ovalle, Prof. Pedro Cacciari, Prof. Tikou Belem, and Prof. Liang Cui for their time and willingness to serve as jury members for my Ph.D. thesis. Prof. Ahmad Shakibaeinia is acknowledged for being the representative of the Directrice d'études supérieures. I also appreciate Prof. Carlos Ovalle and Dr. Feitao Zeng for their evaluation of my pre-doctoral proposal during my comprehensive examination.

Many thanks go to Patrick Berneche and Noura El-Harrak, who provided tremendous help in preparing my experimental materials and molds. Monica Monzon is acknowledged for her kindness and support in my study. I am also grateful to my dear colleagues for their tremendous help in my laboratory tests, academic presentations and studies, etc. My Ph.D. journey has been so interesting because of the support from all of you.

I acknowledge the financial support from the Natural Sciences and Engineering Research Council of Canada (NSERC), Natural Sciences and Engineering Research Council of Canada (NSERC), Fonds de recherche du Québec – Nature et technologies (FRQNT), and industrial partners of the Research Institute on Mines and the Environment (RIME UQAT – Polytechnique; http://rime-irme.ca).

Finally, I want to express my deepest appreciation to my family members, my sisters and brothers, and especially my beloved parents and my grandma, who have always supported me with so much love. There are no words can be used to express my gratitude for them! I love them so much.

RÉSUMÉ

Les mines souterraines produisent de grandes quantités de roches stériles pour accéder aux gisements de minerai. Traditionnellement, en raison des espaces de stockage limités sous terre, la plupart des roches stériles doivent être transportées et remontées à la surface. Ce processus de transport nécessite une consommation d'énergie substantielle et des coûts opérationnels élevés. Une pratique alternative courante dans des mines au Canada consiste à déverser directement les roches stériles dans les chantiers de mine en cours de remplissage avec un remblai en pâte cimentée. Cette approche peut réduire de manière significative le volume de roches stériles à transporter et à entreposer en surface, diminuant ainsi la consommation d'énergie et les coûts opérationnels. De plus, si les roches stériles peuvent être complètement mélangées avec le remblai en pâte cimenté, le mélange naturel des deux matériaux devrait présenter des propriétés mécaniques même meilleures par rapport au remblai en pâte seul ou aux roches stériles individuelles.

Malgré ces avantages, cette pratique présente également certains risques. Si les roches stériles déversées ne sont pas bien mélangées avec le remblai en pâte cimentée, les matériaux sans cohésion peuvent s'effondrer lors de l'exploitation adjacente, ce qui pourrait entraîner une dilution du minerai ou même une perte de minerai. Par conséquent, comprendre le comportement de mélange naturel des roches stériles et du remblai en pâte est crucial pour atténuer ces risques.

À cette fin, une série d’essais en laboratoire ont été réalisés. Une nouvelle définition du degré de mélange a également été proposée pour évaluer quantitativement le degré de mélange naturel des roches stériles et du remblai en pâte. Les résultats montrent que la pénétration des roches stériles dans le remblai en pâte et le degré de mélange peuvent être améliorés en utilisant un remblai en pâte moins épais, des roches stériles de tailles plus grandes, et une hauteur de chute des roches stériles plus élevée.

Tandis que les travaux de laboratoire sont utiles et nécessaires pour permettre de bien comprendre et quantifier le mélange naturel entre les deux types de matériau, il est impossible de compter uniquement sur les essais en laboratoire pour comprendre et quantifier le mélange naturel des roches stériles et des remblais en pâte en conditions de terrain. Cette limitation n’est pas due uniquement aux dimensions très grandes des chantiers, mais aussi due aux tailles très grandes des roches stériles produites et utilisées sur le terrain. La modélisation numérique est nécessaire pour

prendre en compte des effets d'échelle liés aux dimensions des chantiers et aux tailles des particules des roches stériles.

Dans ce sens, un composant a été développé et incorporé dans un code numérique basant sur la méthode des éléments discrets, appelé EDEM, pour permettre la simulation de la sédimentation des particules dans un fluide. Le nouveau modèle numérique, appelé f-EDEM, a été validé contre une solution analytique. L'applicabilité et la capacité du modèle numérique ont été examinées en reproduisant et en prédisant des résultats expérimentaux. Le modèle numérique calibré et validé peut normalement être appliqué pour prédire le comportement de mélange naturel des roches stériles et du remblai en pâte sous diverses conditions. Or, nous avons constaté que le public et beaucoup de chercheurs et de professionnels ont peu de confiance sur la modélisation numérique, un phénomène assez particulier en géotechnique. Les raisons peuvent être nombreuses. La première raison principale est que des chercheurs ont mis souvent trop d'emphase sur la réduction du temps et du coût de calculs et moins sur la stabilité et la fiabilité des résultats numériques. Une autre raison principale est que les chercheurs ont souvent mis trop d'emphase sur la « validation » des modèles numériques contre des résultats expérimentaux. Les valeurs des paramètres avec ou sans sens physique ont été ajustées pour trouver de bonnes corrélations entre les résultats numériques et expérimentaux et ce, sans questionner ni la stabilité et la fiabilité des résultats numériques, ni celles des résultats expérimentaux. En plus, ce processus de calibration est souvent confondu avec le processus de prédiction. Des efforts sont donc nécessaires pour corriger la situation et dresser la confiance du public à la modélisation numérique en géotechnique.

Pour cette raison, nous avons montré comment construire un modèle numérique optimal afin d'obtenir des résultats numériques stables et fiables avec un temps de calculs minimal sur le comportement mécanique des roches stériles. La validation du modèle numérique contre des solutions analytiques et les analyses de sensibilité des paramètres sont nécessaires et essentielles. Ainsi, nous sommes les premiers à montrer que la granulométrie d'un matériau granulaires ne peut pas être coupée pour exclure des particules fines sans l'analyse de sensibilité de la coupure de la granulométrie. De plus, nous avons montré aussi que la réduction de la valeur du module de Young des particules de roche stérile change le problème physique même si cette approche permet de diminuer le temps de calculs tant que la valeur du module de Young est supérieure à un seuil à partir de l'analyse de sensibilité. D'ailleurs, nous avons montré qu'il est important de réduire le nombre de paramètres déterminés par le processus de calibration (c.-à-d. ajustement). La calibration des paramètres doit être faite uniquement sur ceux qui n’ont pas de sens physique ou qui ne peuvent pas être mesurés. Tout cela a été démontré par la reproduction numérique des angles de repose des roches stériles obtenus par des essais en laboratoire.

Une fois validés par des solutions analytiques et des résultats expérimentaux, les modèles EDEM et f-EDEM sont prêts à utiliser pour simuler le mélange naturel des roches stériles et des remblais en pâte sous différentes conditions, du laboratoire au terrain, en considérant les effets d’échelle liés aux dimensions des chantiers et aux tailles maximales ($d_{\max}$) des particules des roches stériles. Pour ce faire, une première séries d’essais a été réalisée sur des échantillons de roches stériles préparés à l’aide de la technique d’échelle réduite tronquée. La reproduction numérique de ces résultats expérimentaux nécessite la calibration du coefficient de résistance au roulement puisque tous les autres paramètres du modèle ont été mesurées. Vu clairement l’augmentation de l’angle de repos des échantillons de roches stériles avec l’augmentation de la valeur de $d_{\max}$, on a attendu aussi une variation de la valeur du coefficient de résistance au roulement calibré en fonction de $d_{\max}$. Or les modélisations numériques ont montré que le coefficient de résistance au roulement calibré est constant et indépendant de la variation de $d_{\max}$. Cela est contradictoire à l’augmentation des angles de repos mesurés avec l’augmentation de $d_{\max}$ puisque le coefficient de résistance au roulement et l’angle de repos sont tous des propriétés intrinsèques des matériaux granulaires. Plus d’analyses sur cette contradiction ont finalement permis de révéler que l’angle de repos mesuré dépend de la quantité de matériau granulaire utilisé et l’ouverture à la base d’entonnoir. Des résultats expérimentaux stables, fiables et représentatifs peuvent être obtenus seulement quand la quantité de matériau utilisé est suffisante et l’ouverture à la base d’entonnoir est suffisamment grande. Des analyses de sensibilité sont nécessaires pour déterminer la quantité minimale nécessaire de matériau et l’ouverture minimale requise d’entonnoir. Une autre séries d’essais réalisés en utilisant des quantités de matériau suffisantes et un entonnoir ayant une ouverture à la base suffisamment grande a montré finalement que l’angle de repos des échantillons de roches stériles préparés à l’aide de la méthode tronquée ne varie pas avec la variation de $d_{\max}$. Ces résultats confirment de nouveau que la technique tronquée est une méthode appropriée pour préparer des échantillons d’échelle réduite, du moins pour la mesure d’angle de repos. Le modèle numérique EDEM calibré peut être utilisé pour analyser le comportement géotechnique des infrastructures faites des matériaux granulaires comme des roches stériles.

Pour tester l’applicabilité et la prédictibilité des modèles numériques validés et calibrés f-EDEM dans l’analyse du mélange naturel entre des roches stériles déversées et des remblais en pâte, plusieurs essais additionnels ont été effectués avec deux boîtes de dimensions différentes et des roches stériles ayant des tailles maximales différentes. Les résultats expérimentaux obtenus ont été comparés avec les prédictions numériques obtenues par le modèle numérique validé et calibré (c.-à-d., le modèle numérique avec les paramètres de modèle obtenus dans les études précédentes). En général, les corrélations qualitatives et quantitatives entre les résultats numériques et expérimentaux sont assez bonnes, indiquant que le modèle numérique peut être appliqué pour évaluer ou prédire le mélange naturel des remblais en pâte et des roches stériles déversées en conditions de laboratoire et de terrain. Plus d’analyses sur les moins bonnes corrélations ont permis de révéler que certains détails négligés lors des essais de laboratoire pourraient avoir des impacts sur les résultats. Cela montre de nouveau que les modélisations numériques sont utiles si elles se font correctement, au lieu de chercher de bonnes corrélations entre les résultats numériques et expérimentaux à tout prix.

ABSTRACT

Underground mines produce large amounts of waste rock in order to access orebodies. Traditionally, due to limited underground storage spaces, most of the waste rock needs to be transported and hoisted to the ground surface. This transportation process requires substantial energy consumption and operational costs. A common alternative practice in Canada is to directly pour the waste rock into mine stopes that are being filled with cemented paste backfill. This approach can significantly reduce the volume of waste rock to be transported and disposed of on ground surface, thus lowering the energy consumption and operation costs. Moreover, if the waste rock can be fully mixed with the cemented paste backfill, the natural mixture of the two materials can exhibit better mechanical properties compared to individual paste backfill or waste rock. Despite these advantages, this practice also presents certain risks. If the poured waste rock is not well mixed with the cemented paste backfill, the cohesionless waste rock may fail and collapse upon neighboring stope excavation, leading to ore dilution or even ore loss. Therefore, understanding the natural mixing behavior of dumped waste rock and paste backfill is crucial to mitigate these risks.

To this end, a series of laboratory tests were conducted. A new definition of mixing degree was also proposed to quantitatively evaluate the natural mixture of waste rock and paste backfill. The results demonstrate that the penetration of waste rock into paste backfill and the mixing degree can be improved through using lower solids content paste backfill, larger particle size of waste rock, and higher waste rock falling height.

While laboratory tests are useful and necessary to well understand and quantify the natural mixture between the two types of material, it is impossible to rely solely on laboratory tests to understand and quantify the natural mixture of waste rock and paste backfill in field conditions. This limitation is not only due to the very large dimensions of stopes, but also due to the very large sizes of field produced and used waste rock. Numerical modeling is necessary to take into account scale effects related to stope dimensions and waste rock particle sizes.

For this end, a component was developed and incorporated in a numerical code based on discrete element method, named EDEM, to simulate the settlement of particles in a fluid. The new numerical model, called f-EDEM, was validated against an analytical solution. The applicability and ability of the numerical model were verified by reproducing and predicting some experimental

results. This validated and calibrated numerical model can normally be applied to predict the natural mixing behavior of dumped waste rock and paste backfill under diverse conditions. However, we noted that the public and many researchers and professionals do not have high confidence in numerical modeling, a particular phenomenon in geotechnical engineering. The reasons can be numerous. The first main reason is probably due to the fact that many researchers usually put too much emphasis on reducing the time and cost of calculations and less on the stability and reliability of numerical results. Another main reason is due to the fact that researchers usually put too much emphasis on the "validation" of numerical models against experimental results. The values of parameters with or without physical meaning have been adjusted to find good agreements between numerical and experimental results without questioning either the stability and reliability of numerical results or those of experimental results. In addition, this calibration process is often confused with the prediction process. Efforts are therefore necessary to correct the situation and gain the public’s confidence in numerical modeling in geotechnical engineering.

For this reason, we have demonstrated how to construct an optimal numerical model in order to achieve stable and reliable numerical results with the minimum time of calculation for the mechanical behaviors of waste rock. The numerical model validation against analytical solution and parameter sensitivity analyses are necessary and essential. We are the first ones having shown that the particle size distribution (PSD) curve of a granular material cannot be cut by excluding a portion of fine particles without PSD cut sensitivity analysis. In addition, we have demonstrated that the reduction of Young’s modulus of waste rock particles changes the physical problem, even though the time of calculation can be reduced as long as the Young’s modulus is higher than a threshold based on sensitivity analysis. We have also demonstrated the importance of reducing the number of parameters determined through the process of calibration (i.e. adjustment). Normally, calibration should be performed only on model parameters that do not have any physical meaning or cannot be measured. All these have been demonstrated through numerical reproduction of waste rock repose angles obtained by laboratory tests.

Once validated against analytical solutions and experimental results, EDEM and f-EDEM are ready to be used for simulating the natural mixture of dumped waste rock and paste backfill under diverse conditions, from laboratory to field, by taking into account scale effects related to stope sizes and the largest particle sizes of waste rock, $d_{\max}$. A first series of laboratory tests was realized on waste rock samples prepared by applying the scalping down technique. Numerical reproduction of these test results needs the calibration of rolling resistance coefficient because all the other model parameters have been obtained by measurement. As one clearly sees an increase in the repose angle with increasing $d_{\max}$, a change in the calibrated rolling resistance coefficient was expected when the value of $d_{\max}$ changes. However, the numerical results showed that the calibrated rolling resistance coefficient is constant and independent on the variation of $d_{\max}$. This is contradictory to the increase of repose angle with increasing $d_{\max}$ because the rolling resistance coefficient and repose angle are two intrinsic properties of granular material. More analyses on this contradiction reveal that the measured repose angle of granular material depends on the used quantity of granular material and on the opening diameter at the base of funnel. Stable, reliable, and representative test results can be obtained only when the used quantity of material is sufficient and the opening diameter at the base of funnel is large enough. Sensitivity analyses are necessary to determine the minimum required quantity of used material and the minimum required base opening of funnel. Another series of laboratory tests realized by using large enough quantity of waste rock and a funnel having a large enough base opening finally shows that the repose angle of waste rock samples prepared by applying the scalping down technique does not change significantly with the variation of $d_{\max}$. These results confirm once again that the scalping down technique is suitable for preparing scaled down waste rock samples, at least for repose angle tests. The calibrated numerical model EDEM can be used to analyze the geotechnical behavior of infrastructures made of granular materials like waste rock.

To test the applicability and predictability of the validated and calibrated f-EDEM numerical models in analyzing the natural mixing behavior of dumped waste rock and paste backfill, several additional laboratory tests were performed with two different size boxes and waste rock having different values of $d_{\max}$. The obtained test results were compared with the numerical predictions obtained with the validated and calibrated numerical model (i.e, the numerical model with the model parameters obtained in previous studies). In general, the qualitative and quantitative agreements between the numerical and experimental results are quite good, indicating that the numerical model can be applied to evaluate or predict the natural mixing behavior of paste backfill and dumped waste rock under laboratory and field conditions. More analyses on the poor agreement allowed revealing that some neglected details during the laboratory tests could have non negligible impact on the results. This shows once again that the numerical modeling can be useful as long as it is well conducted, instead of always looking for good agreements between numerical and experimental results at all price.

TABLE OF CONTENTS

LIST OF TABLES

LIST OF FIGURES

LISTE OF SYMBOLS AND ABBREVIATIONS

Symbol

A	Cross-section area of a spherical particle (mm^2)
C	Solids content by mass of paste backfill in a mixture (%)
C_d	Drag coefficient
C_u	Coefficient of uniformity
d	Diameter of particle (mm)
d_max	Maximum particle size of waste rock (mm or m)
$d_{\_steel}$	Diameter of steel ball (mm)
$d_{\_sphere}$	Diameter of sphere (mm)
d_{wr}	Particle size of waste rock (mm)
D	Diameter of waste rock pile (cm or m)
e_f	Final void ratio of dried paste backfill
E	Young’s modulus of particle (Pa or GPa)
E_1	Young’s modulus of sphere 1 (Pa or GPa)
E_2	Young’s modulus of sphere 2 (Pa or GPa)
$f(d)$	Probability distribution of particle (%)
F_b	Buoyance force acting on the particles (N)
F_c	Contact force between particles (N)
F_f	Fluid force acting on the particles (N)
F_g	Gravitational force (N)
F_n	Normal contact force between two spheres (N)
F_t	Tangential force at the contact (N)
g	Acceleration of gravity (m/s^2)

G	Shear modulus of particle (Pa or GPa)
G_1	Shear modulus of sphere 1 (Pa or GPa)
G_2	Shear modulus of sphere 2 (Pa or GPa)
H	Height of waste rock pile (cm)
H_f	Falling height of waste rock (cm)
H_l	Lift height of a steel plate (cm)
H_{paste}	Height of paste backfill (cm)
H_r	Re-bounce height of steel ball (mm)
I	Moment of inertia (kg·m^2)
L	Distance between the vertex at the angle and the vertex at the vertical angle (cm)
m	Mass of a particle (g)
M	Contact torque acting on a particle (N·m)
M_{paste}	Mass of paste backfill (g)
$M_{paste.dried}$	Dried mass of paste backfill (g)
M_{wr}	Mass of waste rock (g or kg)
N	Number of steel ball
n_{wr}	Porosity of waste rock
$n_{paste.dried}$	Porosity of dried paste backfill
P	Solids content by mass of paste backfill (%)
r_p	Particle radius (mm)
R	Radius of the sphere (mm)
R_1	Radius of sphere 1 (mm)
R_2	Radius of sphere 2 (mm)
R_e	Particle Reynolds number

R'_e	Particle Reynolds number in a non-Newtonian fluid
R_{opt}	Optimum mixture ratio
S	Mixing degree of a mixture (%)
S'	Dimensionless slump height
S_t	Tangential stiffness (N/m)
t	Time (s)
T_R	Rayleigh time (s)
v	Velocity of a particle (m/s)
v_{ter}	Terminal velocity of a particle settling in a fluid (m/s)
$V_{paste.dried}$	Volume of dried paste backfill in a mixture (cm^3)
V_v	Voids volume of waste rock (cm^3)
V_{wr}	Volume of waste rock (cm^3)
W	Base diameter of funnel (mm)
$\dot{\gamma}$	Shear rate (1/s)
ΔT	Time step (s)
δ_t	Tangential overlap (mm)
δ_n	Normal overlap (mm)
η	Viscosity of a Newtonian fluid (Pa·s)
η_a	Apparent viscosity of a non-Newtonian fluid (Pa·s)
η_B	Plastic viscosity of a Bingham fluid (Pa·s)
θ	Repose angle (°)
μ	Mean diameter of particles (mm)
μ_e	Restitution coefficient
μ_r	Rolling resistance coefficient

μ_s	Static friction coefficient
μ_w	Viscosity of water (Pa·s)
ν	Poisson's ratio of particle
ν_1	Poisson's ratio of sphere 1
ν_2	Poisson's ratio of sphere 2
$\rho_{\_clay}$	Density of clay (kg/m^3)
ρ_f	Density of fluid (kg/m^3)
ρ_p	Density of particle (kg/m^3)
$\rho_{paste.dried}$	Density of dried paste backfill in a mixture (kg/m^3)
ρ_s	Density of tailings particles (kg/m^3)
$\rho_{\_sphere}$	Density of sphere (kg/m^3)
$\rho_{\_steel}$	Density of steel ball (kg/m^3)
ρ_w	Density of water (kg/m^3)
ρ_{wr}	Density of waste rock (kg/m^3)
σ	Standard deviation
τ	Shear stress (Pa)
τ_y	Yield stress (Pa)
τ_y'	Dimensionless yield stress
w	Angular velocity (rad/s)

Abbreviations

API	Application programming interface
CFD	Computational fluid dynamics
CHF	Cemented hydraulic fill

DEM	Discrete element method
DLL	Dynamic loading library
H-M	Hertz-Mindin contact model
ITH	In-the-hole technology
PAF	Paste aggregate fill
PSD	Particle size distribution
RPF	Rocky paste fill
SPH	Smoothed particle hydrodynamics
UCS	Uniaxial compressive strength
VCR	Vertical crater retreat
WR	Waste rock
W&T	Waste rock and tailings

LIST OF APPENDICES

CHAPTER 1 INTRODUCTION

1.1 Background and problematics

During the development work to access ore bodies, underground mines generate a significant amount of waste rock. Traditionally, most of these waste rocks need to be transported and hoisted to the ground surface due to limited underground storage space. This transportation process requires considerable energy consumption and operational costs. A common alternative practice in Canada is to directly dump the waste rock into underground mine stopes being filled with cemented paste backfill. The practice can significantly reduce the quantity of waste rock needs to be transported, thus reducing the energy consumption and operational costs. Additionally, the mixture between waste rock and cemented paste backfill can be expected to have better mechanical properties than either the paste backfills or waste rock alone as long as the two materials can be well mixed (Hane et al. 2017; Qiu et al. 2020, 2022).

However, this practice also involves some risks. If the dumped waste rock does not properly mix with the cemented paste backfill, the poor mixture may fail and collapse during the excavation of the secondary stope. This failure and collapse could lead to ore dilution or even ore loss. To avoid these risks, it is crucial to have a good understanding of the natural mixing behavior of the dumped waste rock and paste backfill.

Until now, almost all existing studies related to backfills have been focused on one single type of backfill, such as hydraulic fill, cemented paste fill, or rockfill. Only a few publications have explored the mixtures of graded waste rocks and cemented hydraulic fill or tailings slurry for underground backfilling (e.g., Baldwin and Grice 2000; Kugan & Ian 2001; Lee and Gillot 2014; Hane et al. 2016; Sun et al. 2018). These mixtures typically need crushed and well-graded waste rock with mechanical mixing process. Energy consumption and operation costs are necessary. This approach differs from the natural mixture between dumped waste rock and paste backfill. To date, no studies have been devoted to investigating the natural mixture of dumped waste rock and paste backfill. The natural mixing behavior of the dumped waste rock and paste backfill thus remains unknown.

1.2 Thesis objectives and methodology

The main objective of this project is to understand the natural mixing behavior of dumped waste rock and paste backfill, and to develop a numerical tool that can be used to evaluate and predict the natural mixture of the two materials under diverse conditions varying from laboratory to field. It is achieved by the realization of the following sub-objectives (SO):

SO 1. Experimental investigation of the natural mixing behavior of waste rock and paste backfill by laboratory tests

- To conduct a series of laboratory tests to examine the effects of solids content of paste backfill, waste rock particle size, and waste rock falling height on the natural mixing behavior of the two materials

SO 2. Development and incorporation of a component in an existing numerical model in order to be able to simulate the settlement behavior of waste rock particles in paste backfill slurry

- To propose and implement a drag force model into a DEM (discrete element method) code
- To validate the proposed numerical model against analytical solutions
- To test the applicability and predictability of the numerical model against experimental results

SO 3. To apply the validated and calibrated numerical model to predict the natural mixing behavior of dumped waste rock and paste backfill by taking into account the scale effects of stope geometry and particle sizes of waste rock

- To conduct natural mixing tests of dumped waste rock and paste backfill with different scales (various maximum particle sizes of waste rock and mold sizes)
- To reproduce the experimental results under various conditions by numerical prediction

1.3 Hypotheses

The thesis started with several hypotheses. The main ones can be listed as follows:

1) The mixture of waste rock and cemented paste backfill can result in higher strength than a single material among paste backfill and waste rock;

2) The mining behavior of dumped waste and paste backfill is affected by the solids content of paste backfill and the particle size and falling height of waste rock;
3) The mixing behavior of dumped waste rock and paste backfill in underground mines can be evaluated qualitatively and quantitatively by numerical modeling as long as:
   - The used numerical model is correctly validated against analytical solutions to make sure that the numerical model is exempt from any errors or bugs.
   - The numerical model is correctly used to ensure stable and reliable numerical results.
   - The numerical model is correctly calibrated against reliable experimental results.
   - The calibrated numerical model is tested to be able to predict additional experimental results, which were not used in the numerical model calibration process.
   - The calibrated and validated numerical model can take into account the size effect associated with the particle size of waste rock.

1.4 Contributions

Through the realization of the three previously presented SO, we are the first ones who have shown how the mixing behavior of dumped waste rock and paste backfill is influenced by the paste backfill solids content, waste rock particle size, and waste rock failing height. We are also the first ones who have proposed a quantitative definition to describe the mixing degree of the two materials. Development and incorporation of a component in order for an existing DEM code to be able to simulate the natural mixing behavior between dumped waste rock and paste backfill is another important contribution of this project. In addition, we are the first ones to show how to make particle size distribution curve cuts and construct an optimal numerical model to minimize the time of calculation and ensure stable and reliable numerical results. We also find that the rolling resistance coefficient does not significantly change as the maximum particle size of scalped samples increases. The successful application of the numerical model to reproduce the experimental results at different scales by calibration and prediction processes concluded the Ph.D. thesis. All these works resulted in three articles published in peer-reviewed journals, one conference article with peer-review, and two journal articles ready to be submitted:

Journal article 1:

Yuyu Zhang & Li Li (2023) Experimental study on the natural mixing behaviour of waste rocks poured in a paste backfill, *International Journal of Mining, Reclamation and Environment*, 37:10, 953-977, DOI: 10.1080/17480930.2023.2235847. This article is presented in Chapter 3.

Journal article 2:

Yuyu Zhang & Li Li (2024) Introduction and implementation of fluid forces in a DEM code for simulating particle settlement in fluids, *Powder Technology*, Volume 433, 2024, 119238, https://doi.org/10.1016/j.powtec.2023.119238. This article is presented in Chapter 4.

Journal article 3:

Yuyu Zhang & Li Li (2024) Optimization of discrete element method model to obtain stable and reliable numerical results of mechanical response of granular materials, *Minerals*, 2024, 14 (8), 758, https://doi.org/10.3390/min14080758 (registering DOI). This article is presented in Chapter 5.

Conference article:

Yuyu Zhang & Li Li. (2023) Natural mixing behavior of waste rocks poured in a paste backfill, in *Paste 2023: Proceedings of the 25th International Conference on Paste, Thickened and Filtered Tailings*, Banff, Calgary, Canada, pp. 213 – 219.

The project contributed to a better understanding of the natural mixing behavior of dumped waste rock and paste backfill under various conditions. The experimental results provide a fundamental understanding of the factors that affect the natural mixing behavior of waste rock and paste backfill. The proposed framework for constructing an optimal numerical model ensures the stability and reliability of the numerical results, thereby increasing people's confidence in numerical modeling in geotechnical engineering. The developed numerical model serves as a useful tool to investigate the natural mixing behavior of dumped waste rock and paste backfill under various conditions from laboratory to field.

1.5 Outline of the thesis

The Ph.D. thesis is presented as an article-based format.

Chapter 1 provides an introduction to show the background and problematic, objectives, contributions and the contents of the thesis.

Chapter 2 presents a literature review related to the project, including the underground mining methods and backfills, the mechanical mixtures of waste rock and paste backfill, and the numerical methods for simulating the particle-fluid systems.

Chapter 3 (Article 1) presents the primary test results of mixing waste rock and paste backfill in the laboratory with small particle sizes of waste rock and small-scale models. The effects of particle size of waste rock, falling height of waste rock and the solids content of paste backfill on the natural mixing behavior of waste rock poured into paste backfill are investigated. A definition of mixing degree is proposed to quantitatively describe the mixing quality of the mixture.

Chapter 4 (Article 2) presents the development and implementation of a new component in an existing numerical code developed based on discrete element method (DEM) to simulate the settlement of particles in fluids. The new numerical model, called f-EDEM, is validated against the analytical solution developed for the settling of spheres in the viscous fluids. The applicability and predictability of the validated numerical model are examined by reproducing and predicting the experimental results of pouring spheres into paste backfill.

Chapter 5 (Article 3) presents a methodology for building an optimal DEM model to minimize the time of calculation and ensure stable and reliable numerical results. The importance of numerical model validation against analytical solutions is shown: ensuring that the used numerical code does not have any errors and ensuring that the new-user masters well the necessary steps to obtain stable and reliable numerical results. An optimal numerical model that minimizes the time of calculation and ensures stable and reliable numerical results for the mechanical behaviors of granular materials can only be obtained through diverse sensitivity analyses, including time step and PSD cut. The reduction of Young’s modulus can also be optimized to shorten the time of calculation, but not suggested because reducing the stiffness of particles changes the physical problem. Calibration is usually necessary. But one needs to minimize the number of parameters determined by numerical calibration process. It should be applied exclusively to model parameters that do not have any physical meaning or cannot be measured. All the model parameters having clear physical meanings should be measured or estimated with a high level of confidence. The numerical model, along with the material parameters and calibrated model parameters, constitutes a calibrated numerical model.

The validity and predictability of the calibrated numerical model are examined against additional experimental results.

Chapter 6 presents calibration and validation of a numerical model against repose angle tests of waste rock having different maximum particle sizes. A first series of laboratory tests was realized on waste rock samples prepared by applying the scalping down technique. Numerical reproduction of these test results needs the calibration of rolling resistance coefficient because all the other model parameters have been obtained by measurement. As one clearly sees an increase in the repose angle with increasing $d_{\max}$, a change in the calibrated rolling resistance coefficient was expected when the value of $d_{\max}$ changes. However, the numerical results showed that the calibrated rolling resistance coefficient is constant and independent on the variation of $d_{\max}$. This is contradictory to the increase of repose angle with increasing $d_{\max}$ because the rolling resistance coefficient and repose angle are two intrinsic properties of granular material. More analyses on this contradiction reveal that the measured repose angle of granular material depends on the used quantity of granular material and on the opening diameter at the base of funnel. Stable, reliable, and representative test results can be obtained only when the used quantity of material is sufficient and the opening diameter at the base of funnel is large enough. Sensitivity analyses are necessary to determine the minimum required quantity of used material and the minimum required base opening of funnel. Another series of laboratory tests realized by using large enough quantity of waste rock and a funnel having a large enough base opening finally shows that the repose angle of waste rock samples prepared by applying the scalping down technique does not change significantly with the variation of $d_{\max}$. These results confirm once again that the scalping down technique is suitable for preparing scaled down waste rock samples, at least for repose angle tests. The calibrated numerical model EDEM can be used to analyze the geotechnical behavior of infrastructures made of granular materials like waste rock.

Chapter 7 presents the application of the validated and calibrated (i.e. with calibrated model parameters) numerical model obtained in Chapter 6 to predict the natural mixing behavior of dumped waste rock and paste backfill under various conditions. Laboratory tests, starting from small scales with smaller maximum particle sizes of waste rock to large scales with larger maximum particle sizes of waste rock, were conducted. The validated and calibrated numerical model is applied to reproduce the test results by prediction. The applicability and predictability of the validated numerical model for predicting the natural mixing behavior of dumped waste rock and paste backfill are successfully examined because quite good qualitative and quantitative agreements between the experimental results and numerical predictions were obtained. In addition, the analyses on the less good correlations between the numerical and experimental results revealed that some details neglected during the laboratory tests could have non-negligible impacts on the agreements. This shows once again that numerical modeling can be very useful as long as it is correctly conducted, instead of looking for good correlations between the numerical and experimental results at any price.

Chapter 8 provides a summary and general discussion on the main results of this thesis.

Chapter 9 presents the main conclusions and recommendations for further studies.

CHAPTER 2 LITERATURE REVIEW

This chapter first reviews the waste rock and tailings generated by underground mining operations, including the transportation processes and the associated energy consumption, as well as the physical properties of waste rock and tailings. Next, it provides an overview of underground mining methods and typical mine backfills, including hydraulic fill, rockfill, and paste backfill. Following this, the chapter investigates the mixtures of waste rock and tailings slurry (and paste backfill) used for backfilling underground stopes. Finally, the chapter presents the most commonly used numerical methods for simulating the particle-fluid systems, specifically the discrete element method coupling computational fluid dynamics method (DEM - CFD) and discrete element method coupling smoothed particle hydrodynamics method (DEM - SPH).

2.1 Mining wastes

Waste rock and tailings are the major by-products generated throughout the various stages of mining operations, ranging from mine exploration to mine closure. Effective management hand handing of these materials is crucial to mitigate potential environmental impacts.

2.1.1 Waste rock produced by the operations of development to access orebody

Accessing an underground orebody requires the excavation of various development working, such as shafts, drifts, raises, declines, etc. (Figure 2.1). The primary method for accessing an underground orebody is through a vertical drift known as shaft (Hamrin 1980). The shaft is typically equipped with elevators to transport workers, machines and materials, etc. The horizontal developed tunnels of underground mines are known as drifts (Hamrin 1980; Abzalov 2016). The size and shape of the drifts depend on their intended purpose for operations (e.g., transportation, ventilation or exploration, etc.).

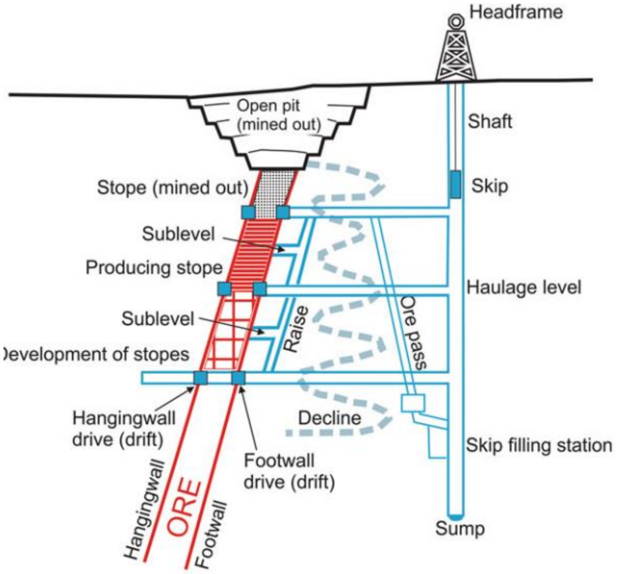

Figure 2.1: An underground mining with tunnels and openings to access orebody (reproduced of Abzalov 2016 with permission)

During the excavation of these development workings, a substantial amount of rocks must be removed from the original rock masses. These rocks, which typically lack sufficient mineral concentration and economic value, are referred to as waste rock. The volume of waste rock removed depends on several factors, including the geometry and position of ore body, the employed mining method and the stability of the original rock mass, etc.

2.1.2 Waste rock transportation: associated energy consumption and operation costs

Once the waste rock has been removed from its original place, it must be transported to its final disposal location, either underground or on the ground surface. In underground mines, the transportation system for waste rock is a critical component of the operation. The transportation of waste rock through drifts or declines is known as haulage, while the movement along the vertical path is referred to as hoisting (Tatiya 2005). Figure 2.2 presents a general classification of an underground mining transportation system reported by Tatiya (2005).

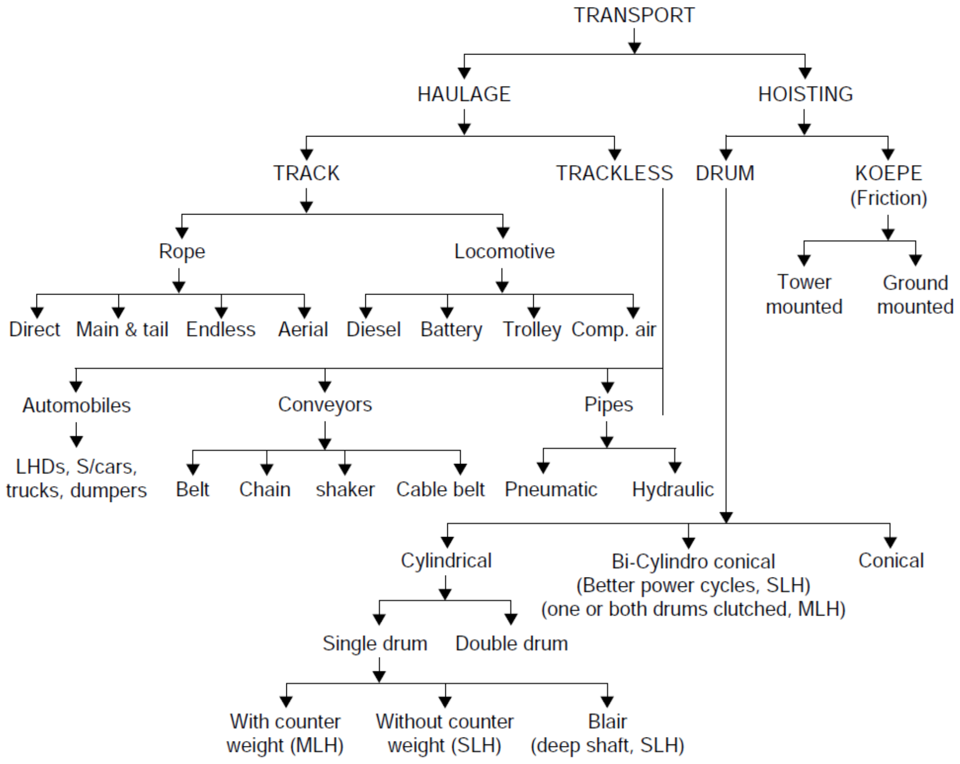

Figure 2.2: A schematic presentation of an underground mining transportation system (reproduced of Tatiya 2005 with permission)

Haulage system

The horizontal haulage system can be classified into track and trackless systems (see Figure 2.2). The track haulage system includes rope and locomotive haulage, which can run on trails. The trackless system includes various vehicles (e.g., shuttle cars, dump trucks, etc.), conveyors, and the pipeline.

Hoisting system

The hoisting system in underground mines operations through vertical and inclined shafts to establish a crucial connection between the underground and the ground surface. There are two primary types of hoisting systems: drum hoist and friction hoist. Drum hoists are characterized by a drum while friction hoists are characterized by the friction between the hoisting cable and drive wheel (Tatiya 2005). The selection of an appropriate waste rock transportation system depends on several factors, such as the mining method, rock properties, safety considerations, production requirements (Tatiya 2005).

In a typical underground mining operation, both horizontal and vertical transportation systems can be used to transport waste rock. The transportation of waste rock is a significant component of the mining operations, contributing substantially to both energy consumption and operational costs (Fabio 2011; Salama 2014; Greberg & Salama 2015; Skawina 2017). It has been reported that the costs of underground transportation of waste rock constitute a considerable percentage of the total mining cost in most mines and may even exceed the costs of mine backfilling in some cases (Salama 2014; Skawina 2017). Energy consumption in typical mining operations accounts for 20 to 40% of the total operational costs (Fabio 2011; Skawina 2017).

Table 2.1 presents an example of the operations costs associated with the transportation of waste rock for an underground mine, as estimated by Lee & Gu (2017). The transportation costs, including both hoisting and haulage, for waste rock could reach up to $4.5 per ton. For a mine with a waste rock to ore ratio of 1:4, and an annual mining rate of million ton, the costs of waste rock transportation could reach $4.5 million in yearly operating costs. In addition, all these operations need substantial consumption of energy.

Table 2.1: The estimated costs for the transportation of waste rock (Lee & Gu 2017)

Cost of waste rock hoisting	CAD 2.0/ton
Cost of haulage to dump	CAD 2.5/ton
Cost of waste dump placement	CAD 1.5/ton
Total waste rock disposal	CAD 6.0/ton
Cost of paste backfill	CAD 10.0/ton

2.1.3 Waste rock properties

Physical properties of waste rock

Generally, waste rock (Figure 2.3) produced by mining operations exhibits a wide range of particle sizes, from clay-sized particles as small as a few microns to large boulders as several meters in diameter (James et al. 2013; Qiu & Pabst 2023). The PSD curve of waste rock can vary significantly from one mine to another due to differences in material properties and the methods for drilling and blasting (Dwumfour et al. 2020). The typical coefficient of uniformity (C_u) of waste rock is 20 or higher (Aubertin et al. 2002; Gamache-Rochette 2004; Maknoon 2016). The on-site density of waste rock typically ranges from 1600 to 2000 kg/m^3 (Hustrulid et al. 2000). The specific gravity of waste rock particles varies between 2.6 and 4.8 or even higher (Kesimal et al. 2004; Bussière 2007; Maknoon 2016).

Figure 2.3: A photo of waste rock with a wide range of particle sizes (reproduced of Smith et al. 2013 with permission)

Hydraulic properties of waste rock

The hydraulic conductivity of waste rock can vary significantly due to the wide range of PSD, void ratio and particle shapes, etc. To measure the conductivity of waste rock in the laboratory, constant head tests are typically conducted. Experimental tests indicate that the saturated conductivity of waste rock generally varies around 10^{-3} m/s (Peregoedova 2012). Field tests and laboratory tests suggest that the hydraulic conductivity of waste rock is typically ranges from 10^{-5} to 10^{-3} m/s (Lessard 2011; Aubertin 2013; Yang 2016; Smith 2021).

2.1.4 Tailings and its properties

Tailings are a by-product of mill processing. The tailings are a granular material which typically contains clay, silty and sand sized particles (Smith 2021). In most cases, tailings are discharged into impoundments, where they are allowed to be settled and consolidated (see Figure 2.4).

Figure 2.4: A photo of deposit of mill tailings slurry (reproduced of Bussière 2007 with permission)

Physical properties

The PSD of tailings is primarily influenced by the milling process, which can be different from mines and milling methods. Figure 2.5 presents the typical PSD of tailings reported by Saw & Villaescusa (2013). The particle size of tailings generally ranges from 3 to 400 µm. More specifically, the particle size of gold tailings typically ranges from 3 to 100 µm, while metal tailings can range from 10 to 400 µm (Potvin et al. 2005).

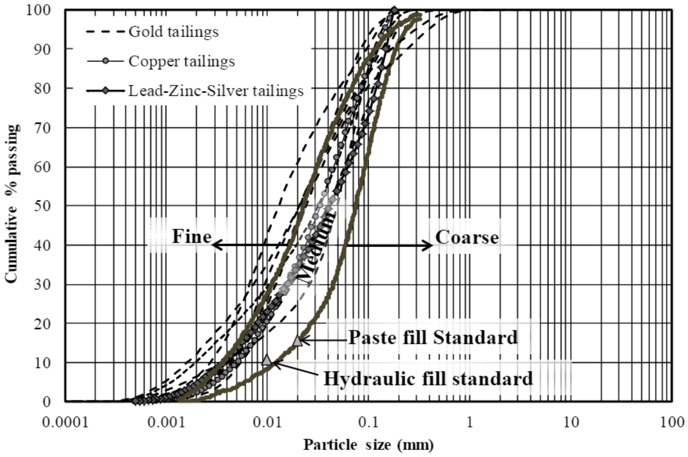

Figure 2.5: Typical PSD curves of tailings (reproduced of Saw & Villaescusa 2013 with permission)

Figure 2.6 presents the PSD curves for tailings from nine hard rock mines in Canada (Bussière 2007). The particle size of tailings in these mines ranges from 0.1 to 400 µm, containing more fine particles compared to those reported by Potvin et al. (2005). The value of D_{10} ranges from 0.001 to 0.004 mm, while D_{60} ranges from 0.01 to 0.05 mm. The C_u value ranges from 8 to 18 (Bussière 2007). According to the Unified Soil Classification System, tailings in these hard rock mines are classified as sandy silts of low plasticity (Bussière 2007).

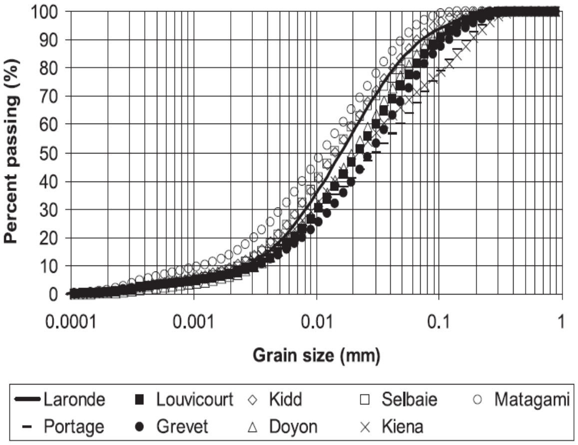

Figure 2.6: PSD curves of tailings of hard rocks mines in Canada (reproduced of Bussière 2007 with permission)

Hydraulic properties

The hydraulic conductivity of tailings is significantly influenced by its PSD curve. Higher clay content leads to lower permeability of tailings (Potvin et al. 2005). The saturated hydraulic conductivity for hard rock tailings with fine particles typically ranges from 1×10^{-6} to 1×10^{-8} m/s, while from 1×10^{-4} to 1×10^{-6} m/s for tailings with coarse particles (Bussière 2007; Smith 2021). In addition to particle size, the void ratio also impacts the permeability of tailings. The decrease of void ratio results in smaller pore sizes, which reduces the permeability of tailings. More details regarding the relationship between the hydraulic conductivity and void ratio of tailings can be found in Bussière (2007).

Mechanical properties

The strength parameters of tailings, such as the friction angle and cohesion, can be determined through direct shear tests or triaxial tests conducted in the laboratory. Experimental results indicate that the drained friction angle for saturated hard rock tailings ranges usually from 30° to 42°, with the cohesion value closes to 0 kPa (Pettibone & Kealy 1971; Matyas et al. 1984; Qiu & Sego 2001; Bussière 2007). The particle size has minimal impact on the friction angle and cohesion (Bussière 2007). Results from the consolidated undrained tests show that the undrained friction angle of tailings varies from 14° to 25°, which are significantly lower than the drained values (Vick 1990). The undrained cohesion for these tailings ranges from 0 to 100 kPa (Vick 1990; Bussière 2007).

2.2 Underground mining methods and backfills

2.2.1 Mining methods

Once an orebody has been identified, selecting the most appropriate mining method becomes crucial. The selection process depends on several factors, including the size and shape of the orebody, the strength of the ore, the content and distribution of the deposit, and the surrounding geological conditions (Hamrin 1980; Brady & Brown 2007). Figure 2.7 presents the classification of underground mining methods of Brady & Brown (2007). These mining methods are divided into three major categories: self-supported, artificially supported and unsupported.

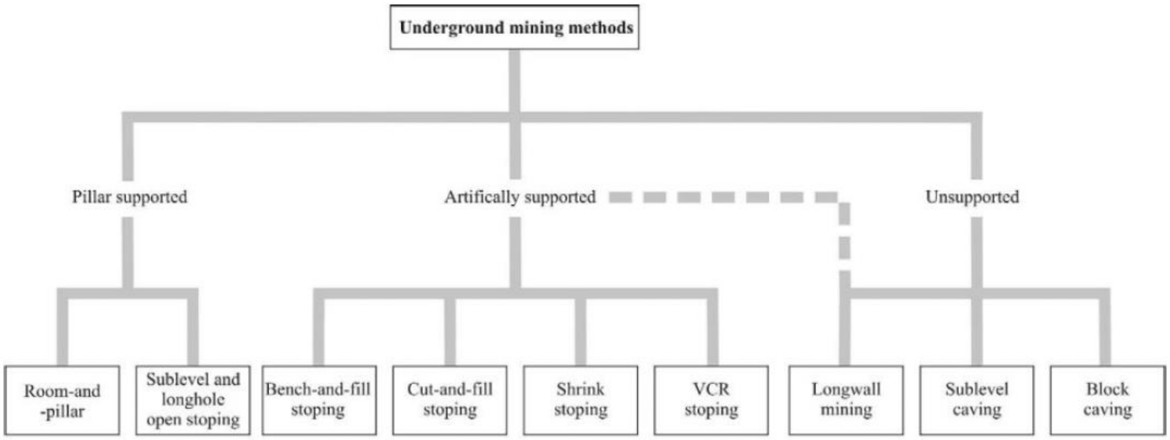

Figure 2.7: Underground mining methods (reproduced of Brady & Brown 2007 with permission)

2.2.1.1 Self-supported method

Room-and-pillar mining method

The room-and-pillar mining method (Figure 2.8) is suitable for ore deposits with a flat-bedded shape and limited thickness (Hamrin 1980). This method involves leaving pillars of ore to naturally support the hanging wall after the rooms are excavated (Bullock 2011). Generally, the room-and-pillar mining method has a relatively low ore recovery rate because a substantial number of ore pillars are left in place to serve as supporting structures. More variations of the room-and-pillar methods can be found in Hamrin (1980). In general, backfilling the voids for this mining method is not necessary unless the pillars need to be recovered. In such cases, backfill can provide ground support and helps control the back-floor convergence (Lane et al. 1999; Tesarik et al. 2009; Yang 2016).

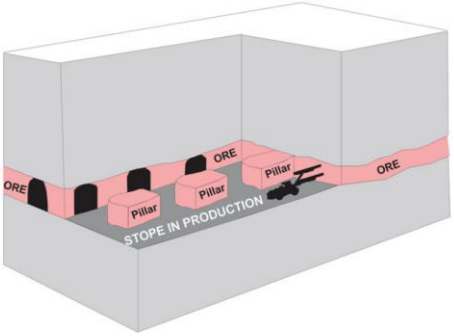

Figure 2.8: Room-and-pillar mining method (reproduced of Abzalov 2016 with permission)

Sublevel stoping

The sublevel stoping method (Figure 2.9) is commonly used in underground mining operations for ore deposits characterized by a steep dip, regular shape, consistent boundaries, and relatively high strength (Hamrin 1980). The most commonly used variations of this mining method include big-hole stoping, shrinkage stoping, and vertical crater retreat (VCR).

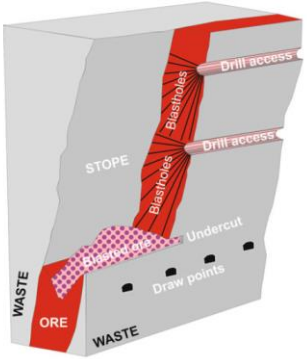

Figure 2.9: A schematic presentation of sublevel stoping (reproduced of Abzalov 2016 with permission)

2.2.1.2 Artificially supported methods

Artificially supported mining methods are often employed in mining operations where the surrounding rock structures are weak. In these mining methods, backfills are essential for controlling the stability of the rocks, limiting void exposure, and providing work platforms for the workers. The artificially supported methods include the cut-and-fill mining method and its variations (Potvin et al. 2005; Brady & Brown 2007).

Cut-and-fill

Cut-and-fill (Figure 2.10) is one of the mining methods for steeply dipping orebodies, especially those with irregular ore zones. In the cut-and-fill mining method, the ore is removed in horizontal slices, starting from the bottom undercut and progressing upward. The method is relatively expensive due to the use of backfilling materials and is therefore typically ideal for mining orebodies with high-grade mineralization. Backfills often serve as working platforms for workers to perform further excavation and help stabilize the surrounding rocks. In practice, the cut-and-fill method is divided into overhand cut-and-fill and underhand cut-and-fill method depending on the mining conditions.

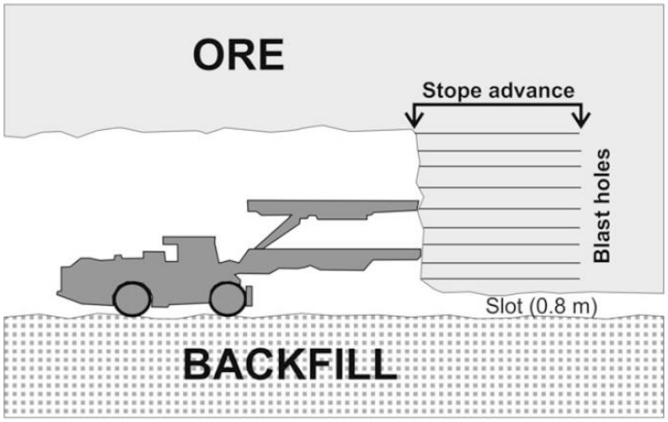

Figure 2.10: Schematic diagram of cut-and-fill method (reproduced of Abzalov 2016 with permission)

Variations of cut-and-fill methods

In general, there are three types of variations of cut and fill method: Avoca mining method, drift and fill method, and post pillar mining method.

The Avoca mining method involves dividing the orebody into horizontal slices or levels. Mining begins at the top and progresses downward. Ore is extracted from one level with the remaining ore and waste rock left in place. Along with the extraction, the stope is backfilled with waste rock from the opposite of the stope, ensuring stability and providing safe working platform (Bullock 2011).

The drift-and-fill method (Figure 2.11) involves the excavation of drifts (horizontal voids) within the ore body, which are then backfilled once the ore has been removed. This method is suitable for orebodies with a large width. In this mining method, the drifts are created side by side and then backfilled with cemented backfills. Then, the secondary drifts, containing the remaining ore pillars, can be recovered. The drifts in this method can have various shapes to adapt to different mining conditions (Bullock 2011; Wang 2021).

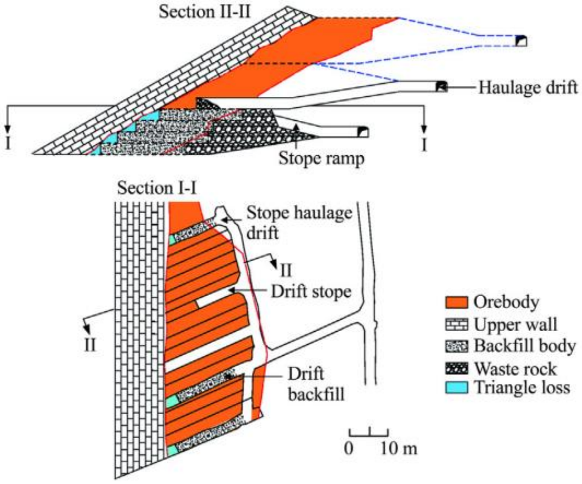

Figure 2.11: Section views of the drift and fill method in a mine (reproduced of Shuai et al. 2021 with permission)

The post-pillar (or as post room-and-pillar) is a combination of room-and-pillar and cut-and-fill stoping. It is often applied to orebodies with large thickness and width. In this method, the ore is removed in horizontal slices, starting from the bottom and progressing upward, with pillars left in the stope to support the roof. Backfill is commonly used in this method to fill the voids and enhance the support capacity of the pillars.

2.2.1.3 Unsupported methods

Unsupported mining methods refer to the mining techniques where the roof and hanging wall are not supported by anything other than the natural rock. In these methods, backfills are usually necessary to fill the stopes. The unsupported mining methods include block caving, sublevel caving, and longwall mining method.

The block caving mining method (Figure 2.12) is applied to ore deposits with large dimensions, low-grade mineralization, and where the surface subsidence is permissible (Hamrin 1980). This technique uses gravity in conjunction with internal rock stresses to break the rock mass into small pieces that can pass through draw points where the ore is handled. Generally, no drilling and blasting are required for ore production.

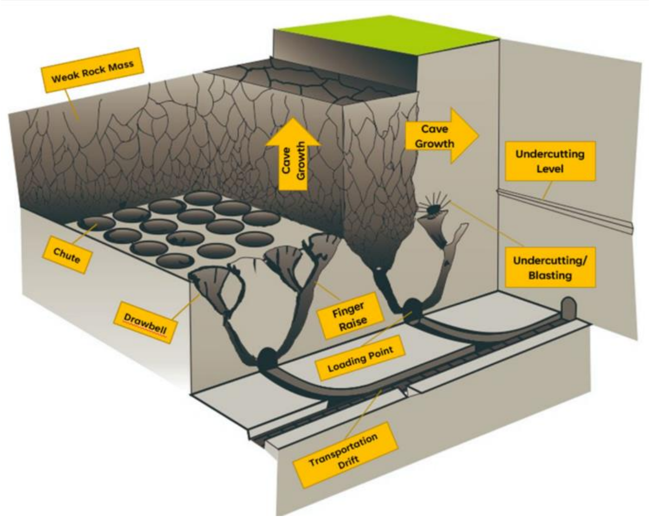

Figure 2.12: Block caving mining method (reproduced of Melati et al. 2023 with permission)

The sublevel caving method is used in large and steep orebodies. The surrounding rock must have sufficient strength to ensure the sublevel drifts remain stable (Hamrin 1980; Brady & Brown 2007). In this method, ore is removed by developing sublevels within the orebody. The hanging wall must be fractured and collapsed to form the cave while the ground surface must allow to subside. Surface subsidence continues as the mining operations advance.

The longwall mining method typically applies to ore deposits with thin thickness and large horizontal extent (Hamrin 1980; Wang 2021). This method extracts ore along a straight front, creating a large open stoping area that provides a safe working space for workers and equipment.

The hanging wall is allowed to subside. The roof along the longwall face is supported, and these supports move forward as mining advances, allowing the roof behind to collapse in a controlled manner.

2.2.2 Mining backfills

Mine backfill is employed to fill mined-out stopes and enhance the flexibility of ore extraction and recovery. The primary advantages of backfilling include improved surround rock stability, increased ore recovery rate, and reduced ore dilution (Hassani & Archibald 1998; Li & Aubertin 2012; Li 2014a, 2014b; Yang et al. 2017a). The most commonly used backfills in the mining industry include hydraulic fill, cemented paste backfill and rockfill.

2.2.2.1 Hydraulic fill

Hydraulic fill (Figure 2.13) is typically composed of deslimed tailings (referred to as tailings with fine particles are removed) (Sivakugan et al. 2005; Dalcé et al. 2019). It is prepared as a slurry, which is then transported through boreholes and pipelines to underground stopes (Potvin et al. 2005; Sivakugan et al. 2005; Yang 2016). To meet the transportation requirements, it often contains a substantial amount of water, which needs to be drained after placement. Therefore, the drainage process is essential to ensure the stability and consolidation of the hydraulic fill.

Figure 2.13: A photo of hydraulic fill in an underground mine (reproduced of Cacciuttolo & Marinovic 2023 with permission)

Physical properties

Fine particles are removed to make hydraulic fill to have high permeability. The maximum particle size of hydraulic fill is typically less than 1 mm, with less than 10% by weight of fine particles smaller than 10 µm (Potvin et al. 2005). Hydraulic fill can generally classified as silty sand or sandy silt according to the unified soil classification system (Stevens 1982). The uniformity coefficient C_u (= D_{60} / D_{10}) typically ranges from 5 to 10. Figure 2.14 presents the PSD curves of 25 different hydraulic fills in Australian mines as reported by Sivakugan et al. (2006).

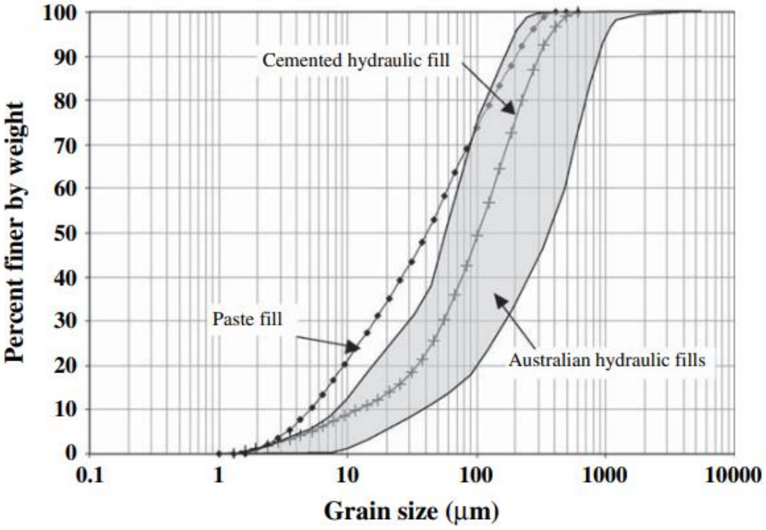

Figure 2.14: Typical PSD curves of different hydraulic fills in Australia mines (reproduced of Sivakugan et al. 2006 with permission)

The specific gravity of hydraulic fill ranges from 2.8 to 4.4 reported by Rankine (2005). Hydraulic fill is typically transported at pulp solids content by mass of 65 to 70% or in terms of water content typically ranging from 30 to 45% (Rankine et al. 2006). Experimental results show that maintaining a water content within this range can result in a relatively dense fill (Rankine et al. 2006).

Hydraulic properties

To minimize the potential failures of hydraulic fill induced by liquefaction, it is crucial to drain water as quickly as possible after its placement in stopes. Therefore, it must have high hydraulic conductivity. Generally, its conductivity ranges from 10^{-6} to 10^{-5} m/s (Hassani & Archibald 1998; Grice 2001; Potvin et al. 2005; Rankine 2005), which is higher than the conductivity of fine tailings typically ranging from 1×10^{-6} to 1×10^{-8} m/s as reported by Bussière (2007). This higher conductivity is attributed to the removal of fine particles.

In the mining industry, a few researches reported that the hydraulic conductivity of hydraulic fill should be larger than 2.8×10^{-5} m/s to ensure adequate drainage (Herget & De Korompay 1978). Experimental tests before backfilling are necessary to verify that the fill has sufficient drainage ability.

Mechanical properties

The strength of hydraulic fill depends on several factors, including binder content, binder type, curing conditions, and water content. For a given water content and curing time, the unconfined compressive strength (UCS) of cemented hydraulic fill is closely related to the cement content (Darling 2011; Saw & Villaescusa 2013). The cohesion can increase from 0.1 to 1.5 MPa as the cement content rises from 3 to 17% after 112 days (Askew et al. 1978). The mechanical properties of cemented hydraulic fill are also influenced by segregation, erosion and piping. These factors can affect the uniformity and stability of the fills, necessitating careful consideration during the design and placement process.

2.2.2.2 Rockfill

Rockfill is made of coarse granular materials, which can be waste rock, quarry rock, or other sources. A rockfill can be used to fill underground stope is shown in Figure 2.15. This type of fill can be categorized into consolidated fill and unconsolidated fill based on the presence or absence of binders (Hassani & Archibald 1998). Unconsolidated fill without any binders is usually used in secondary stopes where further exposure of backfill is not necessary. Consolidated rockfill with binder, also known as cemented rockfill, is often used in primary stopes where further exposure of the backfill is required (Hassani & Archibald 1998; Potvin et al. 2005). The addition of binders enhances the strength and stability, making it suitable for supporting the stope and facilitating mining operations for ore recovery.

Figure 2.15: A photo of rockfill produced in the laboratory (reproduced of Sainsbury et al. 2021) with permission)

Physical properties

Rockfill is classified as unmodified rockfill if it does not undergo any particle grading modification (Potvin et al. 2005). Unmodified rockfills are cohesionless and cannot maintain stability during the excavation of adjacent stopes, making them unsuitable for use in primary stopes. In practice, waste rock usually needs to be well-graded to enhance particle interlocking. The typical particle size can range from 1 to 100 mm. The C_u of rockfill typically ranges from 8 to 18 (Bussière 2007). The dry density ranges from 1500 to 2300 kg/m^3, with a void ratio ranging from 0.48 to 0.85 (Williams & Walker 1985; Williams & Kuganathan 1992; Wang 2021). To design the PSD of this fill, the Talbot grading technique (Talbot et al. 1923) is commonly applied.

When a cemented rockfill is dumped into a stope, the fine particles tend to accumulate at the center of the fill cone, resulting in a high cement content cone, while larger particles roll down to the edge of the cone. This leads to poorly cemented rockfill at the outer zones of the cone (Kugan & Ian 2001). The cones formed by cemented rockfill typically have slope of around 38 to 40 degrees (Kugan & Ian 2001). The separation between fine and coarse particles is known as segregation, which results in a non-homogenous distribution of cemented rockfill in the stopes. Zones with poorly or non-cemented rockfill may become unstable during the excavation of adjacent stopes. To reduce segregation problems, it is desirable to limit the maximum particle size to around 50 mm, as reported by Kugan & Ian (2001).

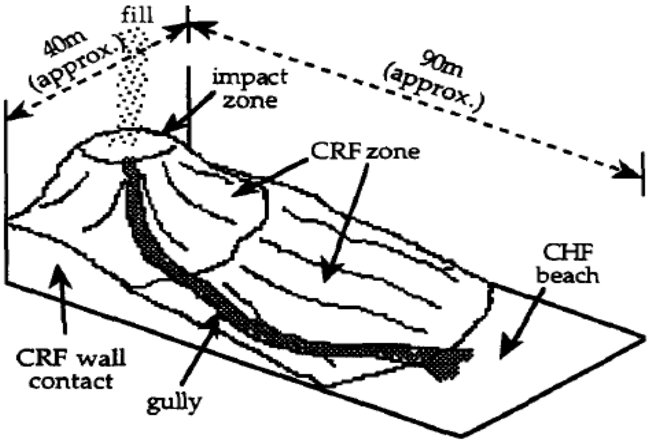

Figure 2.16: Segregation of a cemented rockfill (reproduced of Kugan & Ian 2001)

Mechanical properties

The friction angle of uncemented rockfill typically ranges from 35° to 55° (Potvin et al. 2005). The elastic modulus increases with the addition of binder (Yu & Counter 1983; Pierce et al. 1998). The strength is influenced by several factors, including PSD, binder content, rock type, angularity of fill particles, placement technology, and water content, etc. The binder content is the primary factor affecting the strength of cemented rockfill. With the typical cement range of 4 to 8%, the UCS varies between 1 to 10 MPa (Hedley 1995; Annor 1999). In practice, the strength of placed cemented rockfill can be lower than the strength obtained from laboratory tests due to factors such as segregation, quality control, and scale effects.

Hydraulic properties

Rockfill generally exhibits higher hydraulic conductivity compared to hydraulic fill and paste backfill due to the presence of large waste rock particles. Its hydraulic conductivity can be influenced by several factors, including PSD, particle shape, and void ratio. The hydraulic conductivity of rockfill typically ranges from 4×10^{-5} to 3×10^{-3} m/s (Lessard 2011; Peregoedova 2012; Aubertin 2013). Given its high hydraulic conductivity, rockfill presents fewer drainage issues when placed in stopes compared to hydraulic fill and paste backfill. This characteristic makes rockfill particularly advantageous in mining operations, where efficient drainage is crucial for maintaining stability and preventing waste-related problems.

2.2.2.3 Cemented paste backfill

To improve recovery in mill processing, tailings have become increasing finer. However, disposing of these fine tailings has become challenging, as they can lead to low recovery rates of hydraulic fill and drainage issues in stopes (Potvin et al. 2005). To address this problem, Robinsky (1975) proposed the concept of paste backfill (Figure 2.17) in the mid-1970s (Rankine & Sivakugan 2007; Cui & Fall 2015; Sun et al. 2018; Qi & Fourie 2019). The first real paste backfill was produced at the Bad Grund Mine in Germany in 1970 (Rankine & Sivakugan 2007). Following the successful implementation of several paste backfill practices in Canada and Australia during the 1990s, paste backfill technology was widely accepted and became a popular underground mining backfilling method.

Figure 2.17: A photo of cemented paste backfill in an underground mine (reproduced of Cacciuttolo & Marinovic 2023 with permission)

Physical properties

Paste backfill allows full stream tailings to be densified and dewatered to a solids content by mass of 70 to 85% before backfilling (Potvin et al. 2005). It has a relatively low water content, typically between 10 to 25% (Meggyes & Debreczeni 2006). The mining industry has demonstrated that a sufficient amount of fine particles is essential for paste backfill to avoid settlement and particle segregation during transportation (Landriault 1995; Meggyes & Debreczeni 2006; Sheshpari 2015). In general, paste backfill should contain at least 15% of particles passing 20 μm to retain water and maintain plug flow (Potvin et al. 2005). The C_u of paste backfill usually ranges from 10 to 20, which is higher than the value of hydraulic fill. By maintaining a proper particle size distribution and adequate fine particles, paste backfill can ensure stable, homogenous flow during transportation and effective filling in underground mine stopes. This reduces the risk of segregation and settlement, thereby improving the overall stability and effectiveness of the backfill.

Mechanical Properties

In the mining industry, it is a common practice to add binders to paste backfill to mitigate the risk of liquefaction in stopes. The binders typically used for paste backfill include cement, slag, fly ash, or their mixtures, with content ranging from 2 to 10% (Potvin et al. 2005; Sheshpari 2015). The strength of cemented paste backfill is influenced by several factors, including the binder content, solids content, curing time, curing stress, settlement and drainage (Belem et al. 2000; Belem & Benzaazoua 2007; Belem et al. 2016; Cui & Fall 2016, 2017, 2018). Experimental tests indicate that both the UCS and the elastic modulus of paste backfill increase with higher binder content. Adding binders not only enhances the strength and stability of paste backfill but also improves its overall performance in mining operations. The UCS of cemented paste backfill can reach around 4.15 MPa reported by Johnson et al. (2015). The cohesion of cemented paste backfill increases from 240 to 680 kPa at 21 curing days (Veenstra 2013; Wang 2021). The measured elastic modulus of cemented paste backfill ranges from 1.1 to 3.59 GPa at the Lucky Friday Mine (Johnson et al. 2015; Wang 2021).

Hydraulic Properties

The hydraulic conductivity of paste backfill typically ranges from 1×10^{-8} to 1×10^{-6} m/s (Bussière, 2007). This value is lower than the hydraulic conductivity of hydraulic fill, which generally ranges from 1×10^{-6} to 1×10^{-5} m/s (Hassani & Archibald 1998; Grice 2001; Potvin et al. 2005; Rankine 2005). The primary reason for this difference is the absence of clay particles in the classified tailings used for hydraulic fill, which increases its permeability compared to paste backfill. As a result, cemented paste backfill usually takes a longer time to drain and consolidate compared with hydraulic fill. Experimental results indicate that the hydraulic conductivity of cemented paste backfill can be influenced by several factors, including the binder types, particle size distributions, curing time, and the stress level.

Rheological Properties

Paste backfill is often regarded as a non-segregating and uniform fill with negligible water drainage after placement. The transportation process of paste backfill is entirely controlled by its rheological properties (Belem & Benzaazoua 2007; Jiang et al. 2016). Understanding the rheological properties, such as yield stress and viscosity, is crucial for the design of paste backfill.

The yield stress is defined as the minimum stress required to overcome the material's resistance to initiate flow (Uhlherr et al. 2002; Yilmaz & Fall 2017). The yield stress of non-Newtonian fluid is a critical parameter for the design and operation of paste backfill systems. If the applied stress is less than the yield stress, the paste backfill will not flow, and any deformation will recover upon removal of the stress. Once the applied stress exceeds the yield stress, the backfill will flow and behave like a liquid. The measured yield stress of paste backfills ranges from 100 to 800 Pa (Gawu & Fourie 2004; Yilmaz & Fall 2017). For most mining operations, the operating yield stress ranges from 50 to 500 Pa to ensure the effective transportation of cemented paste backfill (Sivakugan et al. 2015; Niroshan et al. 2018). Figure 2.18 presents the relationship between the yield stress and the solids content of several different mine tailings (Sofrá & Boger 2002).

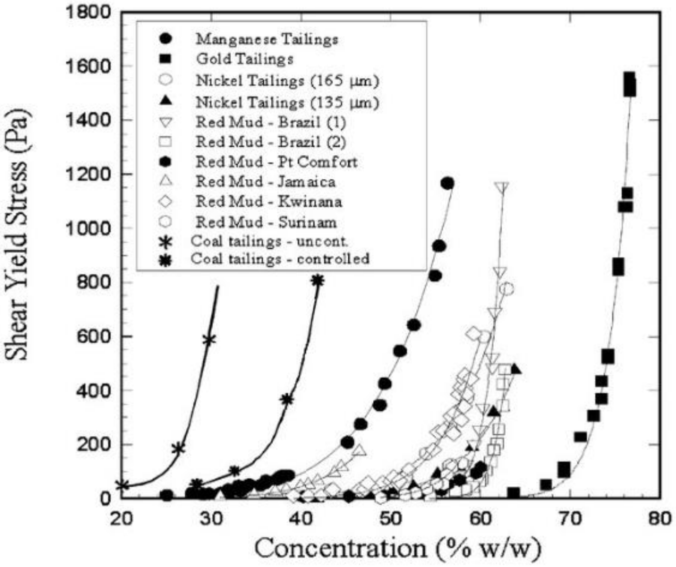

Figure 2.18: The relationship between the yield stress and the solids concentration (reproduced of Sofrá & Boger 2002 with permission)

The most common and convenient method to measure the yield stress of paste backfill is the ASTM slump cone test (Figure 2.19). A high slump value indicates a low-stiff paste backfill, while a low value suggests a stiff fill. An ideal slump value for paste backfill should be between 175 and 250 mm (Meggyes & Debreczeni 2006).

Figure 2.19: A photo of slump test to measure the yield stress of paste backfill (reproduced of Behera et al. 2020 with permission)

2.3 Mixtures of waste rock and tailings backfill for mine stopes

Despite the popularity of using traditional backfills composed of a single type of material, such as hydraulic fill, rock fill, and cemented paste backfill, many mines also utilize mixtures of two types of materials (such as waste rock and tailings) as backfilling materials. These mixtures are expected to have better mechanical and hydrological properties compared to traditional single material backfills.

2.3.1 Mechanical mixtures of waste rock and tailing backfill

The mechanical mixture refers to the mixture with a special equipment such as concrete mixer where waste rock and tailings backfill are blended under controlled conditions. In this process, the waste rock is typically crushed and well-graded. The mixing process is usually conducted on the ground surface. After being mixed, the mixture is transported to the underground stope by trucks, conveyor, or borehole.

Rocky paste fill at Mount Isa Mine

Kugan & Ian (2001) reported the use of a rocky paste fill (RPF) at the Mount Isa Mine in Australia (Figure 2.20). The RPF is produced by mixing the cemented tailings with graded rockfill to fill the stopes. In this process, fine rockfill particles were retained in the mixture to aid dewatering of the cemented tailings and to create a non-segregating cohesive paste. The maximum rockfill particle size was limited to 50 mm to avoid segregation problems. The solids content of cemented tailings was 70 to 74%.

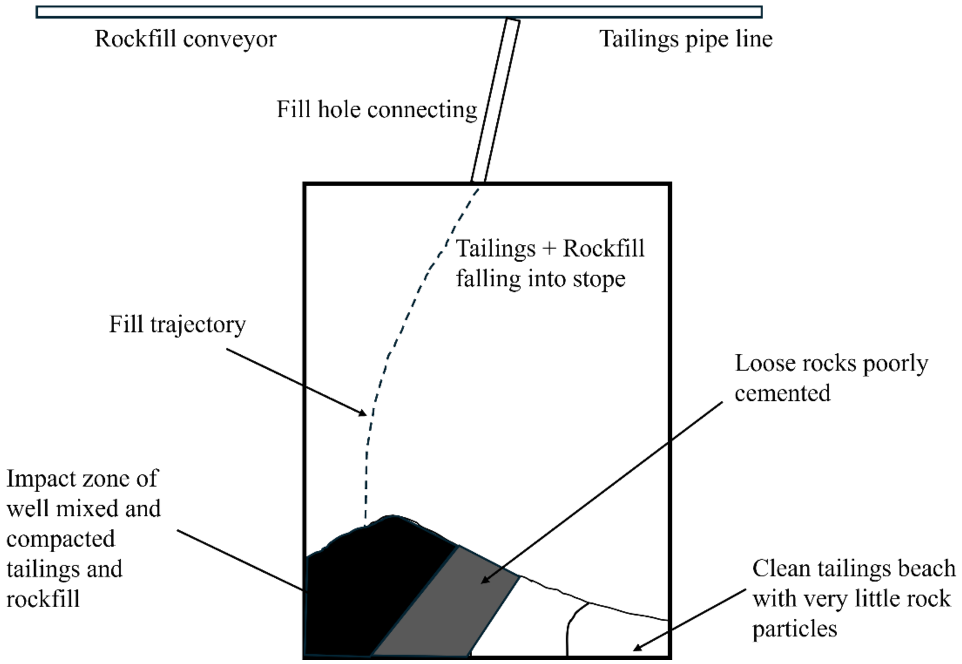

Figure 2.20: Schematic presentation of mixing rockfill and cemented tailings at the Mount Isa Mine (Modified based on Kugan & Ian 2001)

Strength test results indicate that the RPF can achieve an UCS of 1.07 MPa at 28 days with a mix ratio of rockfill to cemented tailings of 2:1. Drop tests suggest that RPF is a homogeneous fill that can easily flow to any horizontal part of the stope, behaving like lava, without forming segregation zones. The advantages of RPF at Mount Isa Mine includes:

- RPF is a homogeneous fill that can flow to any horizontal part of the stope without forming segregation zones.
- RPF releases little to no water after placement, thereby avoiding additional water pressure problems.
- RPF can achieve higher strength with a smaller amount of binders compared to hydraulic fill and paste backfill.

RPF at Olympic Dam Mine

Baldwin & Grice (2000) reported the use of a RPF at Olympic Dam Mine, operated by WMC Resources Ltd in Australia. The fill is prepared in a surface mixing plant using various combinations of tailings, sand, binder, and crushed waste rocks. The solids content of the tailings was around 50 to 53%. The binder used is a mixture of Portland cement and fly ash in ratios ranging from 1:2 to 1:3. Before backfilling, the binder, tailings, and crushed waste rocks are mixed in a pug mill at an average mixing rate of 300 m³/hour. The well-mixed fill is then transported by truck to the fill hole to fill the stope with depth range from 350 to 500 meters.

The strength of RPF at Olympic Dam Mine is designed to range from 0.5 to 5 MPa, with strength decreasing by 0.5 MPa from the bottom to the top of the stope. The main advantages of RPF in Olympic dam mine are summarized as follows:

- The RPF is a homogeneous mixture with minimal segregation.
- The slump value of the RPF is around 150 to 180 mm, indicating good flow characteristics.
- The RPF can achieve strengths ranging from 0.5 MPa to 5 MPa, providing robust support in the stope.

Paste aggregate fill (PAF) at Randgold's Loulo Mine

Lee & Gillot (2014) reported the use of a high strength PAF at Randgold's Loulo mine in Mali. The PAF was composed of 50% tailings and 50% aggregate (waste rocks). The solids content of the tailings was 75%. Waste rocks were crushed into smaller sizes using crushers, then mixed with tailings and cement in a mixer. After mixing, the mixture was transported via pipes to the underground stopes. The strength results indicate that the PAF, composed of 50% tailings and 50% waste rocks, developed the highest strength within the same timeframe. It can reach 7 MPa after 28 days of curing and eventually up to 9.5 MPa after 90 days.

Waste rock-tailings fill at Tong Keng Mine

Sun et al. (2018) reported the use of a waste rock-tailings fill at Tong Keng Mine in China. This method involved the mixtures of waste rocks, tailings, and cement to backfill subsidence areas at the mine. The maximum particle size of waste rock used was 20 mm, smaller than the waste rocks used at Mount Isa Mine, as reported by Kugan & Ian (2001). The schematic diagram for this method is provided in the Figure 2.21.

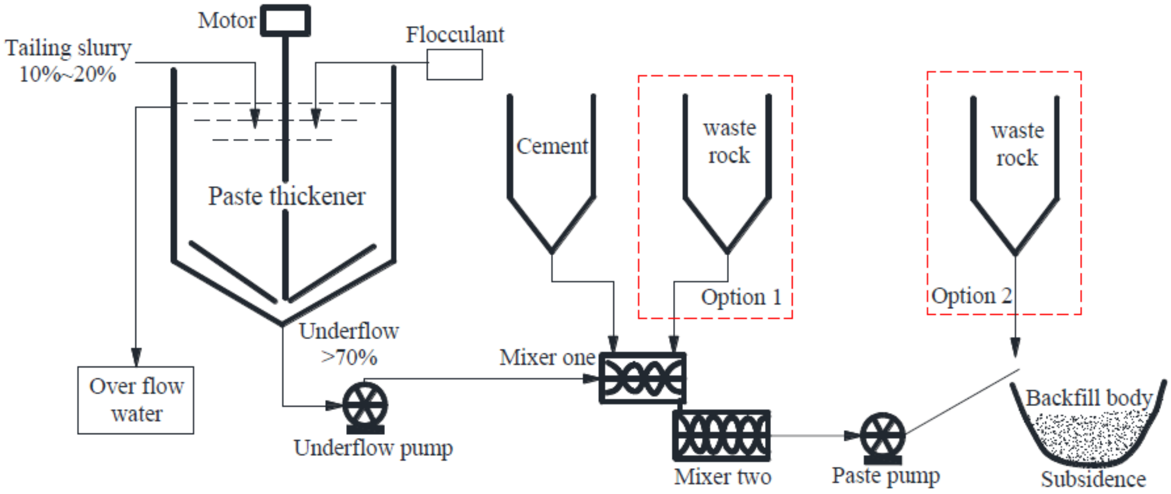

Figure 2.21: Schematic diagram of waste rock-tailings fill at Tong Keng Mine (reproduced of Sun et al. 2018 with permission)

The solids content of the tailings for the mixtures ranges from 81 to 83%, higher than the tailings used at Mount Isa and Randgold's Loulo mines (Kugan & Ian 2001; Lee & Gillot 2014). The content of cement and waste rocks ranged from 2 to 5% and 25 to 35% by dry mass, respectively. The strength of the mixtures could reach 3 MPa after 28 days. Additionally, the hydraulic conductivity was tested to be between 1×10^{-6} to 1×10^{-5} m/s. The main advantages of this type of fill are summarized as follows:

- The waste rock-tailings fill can develop a high strength of 3 MPa with a very small amount of binders.
- The mixture has relatively high hydraulic conductivity, which facilitates drainage and reduces potential water pressure issues.

Hane et al. (2017) investigated the strength of the mixtures of cemented tailings with crushed waste rock (Figure 2.22), referred to as paste aggregate fill (PAF) by conducting a series of UCS tests. Three classes of crushed waste rock were prepared. The crushed waste rock in the PAF mixtures accounts for 8 to 45% by the total mass of dry tailings and crushed waste rock. Test results indicate that the addition of crushed waste rock to cemented tailings allows significantly improved the UCS of the mixtures after 28 and 90 days of curing.

Figure 2.22: A process for preparing the paste aggregate fill (reproduced of Hane et al. 2017 with permission)

Jehring & Bareither (2016) evaluated the effect of tailings composition on the shear strength of co-mixed waste rock and tailings (WR&T). Crushed waste rock was mixed with four types of tailings: fine-graded garnet, coarse-grained garnet, copper and soda ash. Triaxial tests were conduced on the tailings, waste rock and the mixtures to determine the shear strength parameters. The results indicate that the undrained friction angle of waste rock is 37°, the tailings range from 34° to 41°, and the mixture range from 38° to 40°. The tailings affect the shear behavior of the mixture when the mixture ratio smaller than the optimum mixture ratio (R_{opt}), while the waste rock has a significant effect when the mixture ratio is larger than R_{opt}.

2.3.2 Natural mixtures of waste rock and paste backfill

The conception of natural mixtures refers to the formation of mixtures by pouring waste rock into a stope being filled with cemented paste backfill. In this type of mixture, the waste rock is neither crushed nor graded before being dumped in the stope. The waste rock and paste backfill naturally mix in the stope without needing any special equipment. This practice avoids the haulage and hoist of underground produced waste rock from underground to the ground surface, reducing energy consumption and operational costs associated with waste rock transportation from underground to the surface. Although this practice is quite common in underground mines (Canada), it is scarcely documented in the literature.

Lee & Gu (2017) reported numerous potential advantages of natural mixtures of waste rock and paste backfill. These advantages include maintaining the strength of the fill mass by incorporating waste rock, eliminating waste rock transportation costs, reducing the rehandling costs of waste rock (such as crushing and grading), and allowing simultaneous disposal of waste rock and paste backfill. They also proposed a prototype of a co-disposal machine for dumping waste rock into the paste backfill in a stope. However, the natural mixing behavior of waste rock and paste backfill is not investigated in their works.

Veenstra & Grobler (2021) presented a design methodology for maximizing waste rock disposal by depositing it in the primary stopes of the Dead Bullock Soak underground mine in Australia. They proposed an encapsulation filling method, where the waste rock is isolated from exposure by being surrounded by cemented paste backfill. Numerical modeling was conducted to determine the optimal location and shape for waste rock deposits within the stope. The stability of the mixture was also evaluated using numerical models. A case study of a paste-waste stope was presented, showing positive initial trial results, and additional stopes are being identified and ranked as potential paste-waste targets. However, in this work, they do not show how the poured waste rocks are mixed with the paste backfill in a stope. Until now, the study on the natural mixing behavior of waste rocks poured in a paste backfill is still absent.

2.4 Numerical modeling methods

Understanding the natural mixing behavior of waste rock and paste backfill in a stope is often challenging due to several scale factors. First, the particle size of on-site waste rock can be very large. Second, the mine stopes usually have very large dimensions, from tens to hundreds of meters. Conducting experimental tests to investigate the mixing behavior of waste rock and paste backfill in a real-size mold with real particle size of field samples is impractical due to financial and safety constraints. Numerical modeling is thus indispensable, enabling engineers to predict the mixing behavior of waste rock and paste backfill in an underground mine stope under various conditions.

Numerical method for simulating granular materials behaviors

Waste rock is a typical granular material, and its movement behavior is usually simulated using the discrete element method (DEM). The DEM method was first proposed by Cundall to study the discontinuous behavior of solid particles (Cundall & Strack 1979). DEM is a Lagrangian method that uses Newton's second law to simulate the movement of particles. In DEM, solid particles exhibit two types of motion: translational and rotational. The motion of solid particles is governed by Newton's second law.

Numerical methods for simulating fluids

Paste backfill is a high density non-Newtonian fluid. Its behavior can be simulated using numerical methods designed for fluid dynamics. Two numerical methods are used for simulating fluid behavior.

Computational Fluid Dynamics (CFD) modeling is a technique built on principles of fluid mechanics. The fluid motion is governed by the locally averaged Navier-Stokes equation, which can be solved using the traditional finite element method (Malik & Puigjaner 2002). This approach divides the fluid domain into a mesh, and the equations are solved for each element of the mesh to simulate fluid behavior.

Smoothed Particle Hydrodynamics (SPH) is a fully Lagrangian and mesh-free method first proposed by Gingold & Monaghan (1977). In the SPH method, the fluid is primarily represented as a series of particles. Each particle carries various field variables, such as density, pressure, and position, and moves according to the Lagrangian material velocity. The motion of the fluid particles is also governed by the locally averaged Navier-Stokes equations, but the fluid is treated as a collection of discrete particles rather than a continuous mesh, which can be advantageous for simulating complex fluid interactions and free surface flows.

2.4.1 Numerical methods for simulating particle-fluid systems

Studying the mixing behavior of dumped waste rock and paste backfill needs a numerical model that can handle with a particle-fluid system. Coupled DEM-CFD or DEM-SPH methods are often used to simulate such system. In these coupled methods, the movement of particles is simulated by the DEM, while the fluid is simulated using CFD or SPH methods. The particle-fluid interaction forces are transferred through the coupling processes.

2.4.1.1 Drag force models

Before simulating the movement of particles in a fluid, it is crucial to understand the drag force experienced by the particles. The drag force is a critical factor influencing particle motion and interactions within the fluid. Various drag force models are used to calculate the drag forces for particles in different fluids. These models account for factors such as particle size, shape, fluid properties, and flow conditions.

Particle settling in Newtonian fluids

For a spherical particle settling in a Newtonian fluid, the drag force acting on the particle is the sum of two parts: the viscous drag force due to friction and the form drag force due to boundary layer separation (He et al. 2001). The drag force can be generally expressed as (Di Felice 1994):

$$F_d = \frac{1}{2}\rho_f v^2 A C_d \tag{2.1}$$

where F_d (N) is the drag force; ρ_f (kg/m^3) is the density of fluid; v (m/s) is the settling velocity of particle; A (m^2) is the cross-section area of a spherical particle; C_d is a drag coefficient, which related to the Reynolds number, R_e (Chhabra 2006; Okesanya et al. 2020):

$$R_e = \frac{\rho_f v d}{\eta} \tag{2.2}$$

where η (Pa.s) is the viscosity of fluid; d (m) is the diameter of the particle.

For a particle settling in Newtonian fluid with a low Reynolds number, the relationship between the drag coefficient and Reynolds number can be expressed as (Stokes 1851):

$$C_d = \frac{24}{R_e} \tag{2.3}$$

The drag force can then be expressed as (Stokes 1851):

$$F_d = 3\pi\eta v d \tag{2.4}$$

Particle settling in non-Newtonian fluids

For the drag force of a spherical particle settling in a non-Newtonian fluid, the influence of yield stress must be considered. The drag force acting on a moving spherical particle in such fluid is given by Dedegil (1987) as follows:

$$F_d = (\frac{\pi}{2}d)^2\tau_y + \frac{1}{2}C_d\rho_f v^2 A \tag{2.5}$$

where τ_y (Pa) is the yield stress, which is the minimum required shear stress to start flowing a non-Newtonian fluid.

To obtain the drag force of sphere in a non-Newtonian fluid, the relationship between the drag coefficient C_d and Reynolds number R_e must be established. Several relationships between C_d and R_e have been proposed in the literature.

Ansley & Smith (1967) proposed an equation to express the drag coefficient for a non-Newtonian fluid:

$$C_d = 24X\frac{1+B_i}{R_e} \tag{2.6}$$

where X is a drag-correction factor; k is the shear rate constant; B_i is the Bingham number.

Turton & Levenspiel (1986) introduces a five-constants drag coefficient formula:

$$C_d\ (R_e < 2\times10^5) = \frac{24}{R_e}(1+0.173R_e^{0.657}) + \frac{0.413}{1+16300R_e^{-1.09}} \tag{2.7}$$

Dedegil (1987) established a $C_d - R_e$ relationship based on the tests of 121 spheres settling in clays with six different densities conducted by Valentik & Whitmore (1965):

$$C_d = \begin{cases} \dfrac{24}{R_e}, & R_e < 8 \\ \dfrac{22}{R_e} + 0.25, & 8 \le R_e \le 150 \\ 0.4, & R_e > 150 \end{cases} \tag{2.8}$$

Schiller (1993) introduced a formula for the drag coefficient with three constants:

$$C_d\ (R_e < 800) = \frac{24}{R_e}(1+0.15R_e)^{0.687} \tag{2.9}$$

Brown & Lawler (2003) proposed a drag coefficient solution based on a large number of experimental datasets:

$$C_d\ (R_e < 2\times10^5) = \frac{24}{R_e}(1+0.15R_e)^{0.681} + \frac{0.407}{1+8710R_e^{-1}} \tag{2.10}$$

Cheng (2009) proposed a drag coefficient by using the data provided by Brown and Lawler (2003) to a wide range of Reynolds number:

$$C_d\ (2 \times 10^{-3} < R_e < 2 \times 10^5) = \frac{24}{R_e}(1 + 0.27R_e)^{0.43} + 0.47[1 - \exp\,(-0.04R_e^{0.38})] \tag{2.11}$$

Okesanya et al. (2020) conducted a series of tests of spherical particles settling in Carbopol polymers fluids and proposed a generalized drag model for particle settling in all types of viscoplastic fluids:

$$C_d = \frac{24}{R_e}(1 + 0.12R_e)^{0.35} + 0.398[1 - \exp\,(-0.01R_e^{0.9282})] \tag{2.12}$$

All the above-mentioned C_d – R_e relationships are empirical based on laboratory tests. These selected formulas stand out from others because they are applicable across a relatively wide range of Reynolds number. However, all the models were developed for spherical particles. Their validity for non-spherical particles remains unknown.

2.4.1.2 Coupled DEM-CFD method

CFD-DEM coupling refers to the interaction of computational fluid dynamics (CFD) and discrete element method (DEM). The first CFD-DEM method was proposed by Tsuji et al. (1993) to describe bubble formation in a 2D gas-solid fluidized bed. This method has been successfully applied to simulate meso-scale fluidization, particle settling, pneumatic conveying, pipe flow, and other processes. The CFD-DEM method solves Newton's second law equations for particle motion using DEM and employs the locally averaged Navier-Stokes equation for the fluid phase. Fluid-particle coupling is achieved by exchanging interaction forces, such as drag and buoyancy, between the two phases during computation. The CFD-DEM method can be divided into two categories: the unresolved method and the resolved method. In the unresolved method, the particle size must be smaller than the CFD mesh size. In contrast, the resolved CFD-DEM method imposes no such limitation, allowing the particle size to be larger than the CFD mesh size.

For the unresolved CFD-DEM approach, the particle is assumed to not completely fill a cell in CFD. The motion of incompressible-fluid is governed by the volume-averaged Navier-Stokes equations, which are expressed as (Kloss et al. 2012):

$$\frac{\partial \alpha_f}{\partial t} + \nabla \cdot \left(\alpha_f \boldsymbol{u}_f\right) = 0 \tag{2.13}$$

$$\frac{\partial(\alpha_f \boldsymbol{u}_f)}{\partial t} + \nabla \cdot \left(\alpha_f \boldsymbol{u}_f \boldsymbol{u}_f\right) = -\alpha_f \nabla \frac{p}{\rho_f} - \boldsymbol{R}_{pf} + \nabla \cdot \boldsymbol{\tau} \tag{2.14}$$

where α_f is the volume fraction occupied by the fluid, ρ_f is the density of the fluid, $\boldsymbol{u}_f$ is the velocity vector of the fluid, p is the pressure, $\boldsymbol{\tau}$ is the stress tensor for the fluid, $\boldsymbol{R}_{pf}$ is the momentum exchanges with the particle phase, t is the time.

For the resolved CFD-DEM approach, the particles are allowed to be bigger than the computational grid in the CFD code. As a result, the particles can cover multiple cells. The governing equations of the fluid domain are incompressible Navier-Stokes equations. The equations of motions can be summarized as (Shirgaonkar et al. 2009):

$$\rho_f \left(\frac{\partial \boldsymbol{u}}{\partial t} + \boldsymbol{u} \cdot \nabla \boldsymbol{u}\right) = \nabla \cdot \boldsymbol{\sigma} \tag{2.15}$$

The continuity equation:

$$\nabla \cdot \boldsymbol{u} = 0 \tag{2.16}$$

The boundary condition:

$$\boldsymbol{u} = \boldsymbol{u}_{\partial\Omega} \tag{2.17}$$

The interface conditions on the fluid-solid boundary:

$$\boldsymbol{u} = \boldsymbol{u}_i \text{ and } \boldsymbol{\sigma} \cdot \widehat{\boldsymbol{n}} = \boldsymbol{t}_{\partial\Omega} \tag{2.18}$$

The initial condition:

$$\boldsymbol{u}(\boldsymbol{x}, t = 0) = \boldsymbol{u}_{\boldsymbol{0}}(\boldsymbol{x}) \tag{2.19}$$

where $\boldsymbol{\mu}$ is the velocity, $\widehat{\boldsymbol{n}}$ is the outward normal unit vector, $\boldsymbol{t}_{\partial\Omega}$ is the traction vector acting from the fluid on the solid body surface. $\boldsymbol{u}_i$ is the velocity of the solid-fluid interface, $\boldsymbol{u}_{\boldsymbol{0}}$ is the initial velocity, $\boldsymbol{\sigma}$ is the stress tensor inside the fluid.

Kloss et al. (2012) introduced a CFD-DEM framework to simulate coupled fluid-granular systems. Their simulations utilized two open-source software packages, OpenFOAM and LIGGGHTS.

They proposed two distinct approaches: the unresolved CFD-DEM and the resolved CFD-DEM methods. The unresolved CFD-DEM approach is designed for scenarios where particle sizes are smaller than the computational mesh, whereas the resolved CFD-DEM approach is suitable for cases where particle sizes exceed the computational grid. The validation of the unresolved CFD-DEM model was achieved through simulations of a single spout fluidized bed.

Zhao & Shan (2013) reported a coupled CFD-DEM model to simulate the behavior of a sandpile in water. In their study, two open-source software packages, DEM (LIGGGHTS) and CFD (OpenFOAM), were used to simulate the fluid-particle system. The interaction forces between solid particles and fluid include buoyancy and drag forces. The numerical method is validated first against an analytical solution developed for the settlement of a single spherical particle in water. The results indicate that the numerical model can successfully reproduce the settling velocity of sphere at different times. After validation, the model was applied to examine the behavior of a sand pile in water (Figure 2.23).

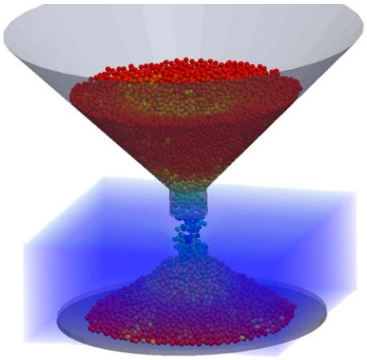

Figure 2.23: Physical model of the formation of a sand pile in water simulated using coupled DEM-CFD method (reproduced of Zhao & Shan 2013 with permission)

Zhao et al. (2014) reported a three-dimensional numerical model for simulating the settlement of spherical particles in water by coupling DEM with CFD. The simulations employed two open-source software packages: ESySParticle for DEM and OpenFOAM for CFD. The DEM-CFD model was validated by simulating the sedimentation of a single particle in water, for which an analytical solution is available. The results show that the simulation results match very well with the analytical solution for the settling velocity of a single spherical particle at different times. It was then applied to simulate the granular batch sedimentation with 6000 particles. The segregation of particles at different locations can be well captured by the numerical model (Figure 2.24).

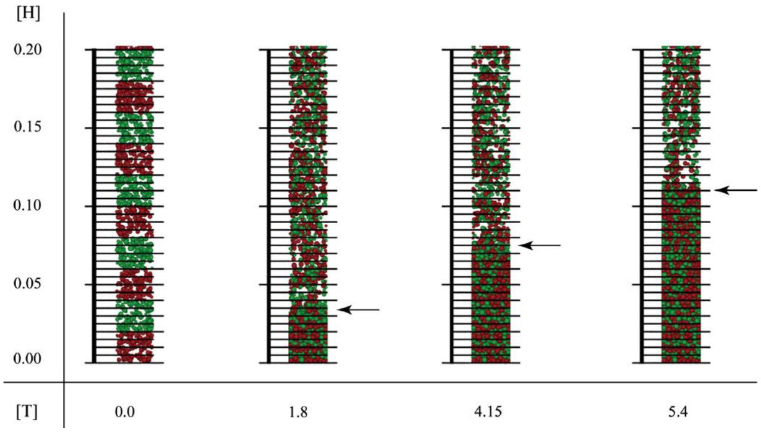

Figure 2.24: Sedimentation of particles simulated by the coupling DEM-CFD model (reproduced of Zhao et al. 2014 with permission)

Zhang & Yin (2018) developed a CFD-DEM model for simulating slurry infiltration and filter cake formation. The simulations were realized by using two open-source codes: LIGGGHTS and OpenFOAM. The simulations results indicated that the sedimentation behaviors of the slurry particles and filter cake formation phenomenon can be well captured by using the coupled CFD-DEM method.

Fonceca Junior et al. (2021) introduced a methodology for simulating particle-fluid interactions using the resolved CFD-DEM coupling method. This method explicitly accounts for the body force acting on the fluid phase when calculating the local momentum balance equations. The model was employed to simulate the settling velocity of a sphere under confined conditions. The numerical results suggest that the velocity of the sphere consistently decreases as the distance between the confining walls is reduced.

Nguyen et al. (2021) proposed a resolved CFD-DEM coupling model to simulate particulate flows. The model was validated through three simulations: flow past a single particle, flow through a periodic array, and a particle approaching a plane wall. It was then applied to predict the relative viscosity of suspensions and fluidized beds with uniform density and binary mixture particles (Figure 2.25). The results suggest that the numerical model is capable of simulating particulate flow across a range of densities, from dilute to relatively dense systems.

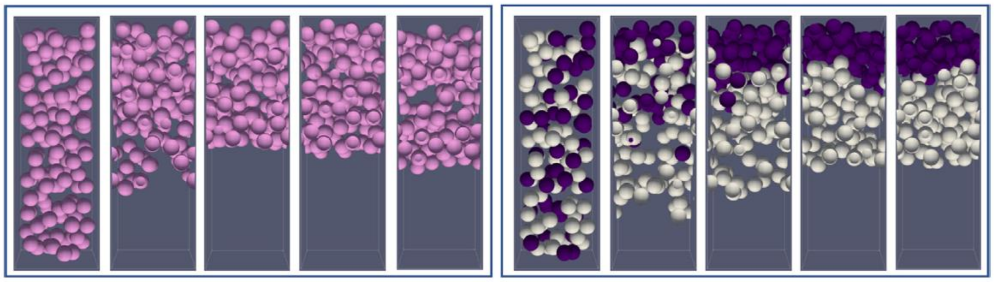

Figure 2.25: Application of numerical model to simulate fluidization of particles (reproduced of Nguyen et al. 2021 with permission)

Shen et al. (2022) developed a resolved coupling CFD-DEM model to simulate interactions between two-phase fluids and irregularly shaped particles. The numerical model was implemented using the open-source C++ library code CFDEM. Validation was achieved by simulating several benchmark cases, including a single particle settling in a two-phase fluid, the settling of two particles, and particles with irregular shapes. The model was further applied to simulate dam break wave impact on a rock pile. The numerical results showed good agreement with experimental results, indicating the effectiveness of the numerical model.

Puderbach et al. (2021) proposed a resolved coupling CFD-DEM model for simulating the filter cake formation during solid-liquid separation. The model enables 4-way coupling which considers particle-fluid and the particle-particle interactions. The model was first validated with an empirical model with a single particle settling in the transition regime of the fluid-particle flow. It was then applied to simulate the filtration process (161 particles). The good agreement between the numerical results and test results demonstrates the proposed resolved model has a great potential for analyzing and optimizing cake filtration processes.

Casarin et al. (2022) presented a two-way coupling CFD-DEM method to simulate particle sedimentation in a quiescent Bingham fluid. The numerical model was validated against experimental results for particle settling in a Bingham fluid (clay) conducted by Valentik & Whitmore (1965). The results confirm that the two-way CFD-DEM coupling scheme is effective for simulating particle settling in viscoplastic fluids, particularly when the particle size is larger than the fluid cell.

Ferreira et al. (2023) developed an unresolved CFD-DEM model to simulate liquid fluidized beds. The simulations were conducted using Lethe, a FEM-based CFD and DEM code capable of CFD-

DEM coupling. The numerical model was validated by comparing test results of pressure drop and bed porosity. The comparison between numerical and experimental results indicates that the model can accurately predict the interphase momentum changes in real systems.

Zhang et al. (2023) employed a resolved CFD-DEM model to simulate the free-settling of polyhedral particles in water. The numerical model is validated against the experimental tests of ellipsoidal particles settling in water. The results indicate that the settling velocity of ellipsoidal particles can be well predicted by the proposed numerical model. The results also demonstrate that the particle shape has a big influence on the fluid resistance, rotational motion and fluid disturbance.

2.4.1.3 Coupled DEM-SPH method

The coupling of SPH and DEM enables a unified Lagrangian particle-based approach, well-suited for applications involving free surfaces and strong fluid-particle interactions. The coupled SPH-DEM model has been utilized to address various engineering problems, including solid-liquid flows, hydraulic fracturing, and particle sedimentation.

Sun et al. (2013) reported a three-dimensional simulation of solid-liquid flow using the DEM-SPH method. The coupled DEM-SPH model was validated against laboratory results of a three-dimensional dam-break flow and solid-liquid flow in a rotating tank. The simulation results closely matched the experimental results at various time intervals. The temporal evolutions of both the solid bed and the liquid flow were accurately captured using the coupled DEM-SPH model.

Robinson et al. (2013) reported a two-way coupled SPH-DEM model to simulate the grain dispersion influenced by liquid injection. In the simulation, the solid particles had a density of 1160 kg/m^3 and diameter of 1.1×10^{-3} m, respectively. The liquid particles had a density of 1000 kg/m^3 and a viscosity of 8.9×10^{-4} Pa. s. The model was validated through experimental dispersion tests. The simulation results suggest that the coupled SPH-DEM model accurately captured the laboratory results of grain dispersion at different liquid flow rates of 400 ml/min and 100 ml/min.

He et al. (2018) reported on a GPU-based coupled SPH-DEM method for simulating particle-fluid flow with free surfaces. The model was validated against laboratory results of a two-phase dam break, as reported by Sun et al. (2013). The water tank used in the laboratory had dimensions of 200 × 150 × 150 mm, and the total mass of spherical particles was 200 g. The simulation results showed good agreement with the experimental results at various time points. The coupled SPH-DEM model was then used to predict particle-fluid flow in a rotating cylindrical drum with a diameter and length of 100 mm. The simulation involved 7755 solid particles, each with a diameter of 2.7 mm. The model accurately captured the width of the particle bed. These results demonstrate that the coupled SPH-DEM model has significant potential for solving fluid-particle systems in industrial applications.

Xu et al. (2019) reported a coupled SPH-DEM to analyze the fluid-particle interaction in granular materials. Two GPU based open-source software of DualSPHysics (SPH software) and Blaze-DEM (DEM software) are coupled in the simulation processes. Three benchmarks of water-entry of a single particle (Figure 2.26), water-entry of a spinning sphere and collision of two submerged spheres are selected to validate the SPH-DEM model. The result indicates that the decrease of the SPH particle size results in better simulation results which are closer to the experiment results. However, the smaller the SPH particle size, the larger number of SPH particles will be needed which leads to the increase simulation time.

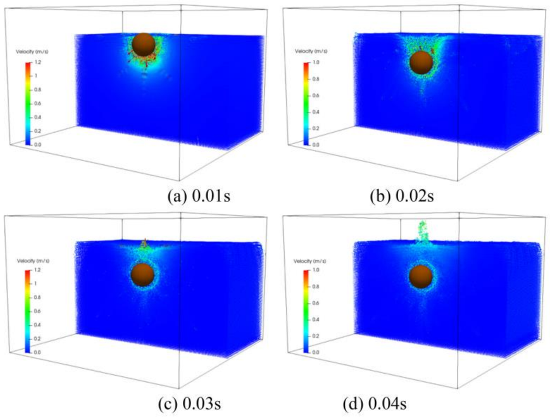

(a) 0.01s (b) 0.02s

(c) 0.03s (d) 0.04s

Figure 2.26: Velocity of water-entry of a single sphere at different times obtained by coupled SPH-DEM model (reproduced of Xu et al. 2019 with permission)

Wu et al. (2020) developed a coupled SPH-DEM model to simulate the behavior of mineral slurries. The simulations utilized the LAMMPS code. In the simulations, the viscosity of mineral slurries with solids content of 80%, 65%, 50% and 30% were analyzed. The numerical results were then validated against viscometry tests conducted on slurries with the same four solids contents. The findings demonstrated that the proposed numerical model effectively predicts the rheological properties of mineral slurries. Furthermore, the results indicate that the DEM parameters have minimal impacts on the rheology of the slurries, particularly at lower solids content.

Peng et al. (2021) presented a fully resolved three-dimensional SPH-DEM numerical model to simulate the suspensions with non-Newtonian fluids and particles with irregular shapes. The fluid phase was modelled by SPH with a regularized Bingham model, while the particles were simulated using the DEM method. To enhance the simulation speed, graphic unit processors (GPU) were utilized in the simulations. The numerical model is validated first against an analytical solution developed for the water-entry problem of spheres with different densities. The results indicate that the numerical model can correctly predict the evolution of the water-entry depth of the spheres (Figure 2.27). Subsequently, the numerical model was applied to simulate the concrete flows with various rock shapes. A good agreement between the experiments results and numerical results is obtained.

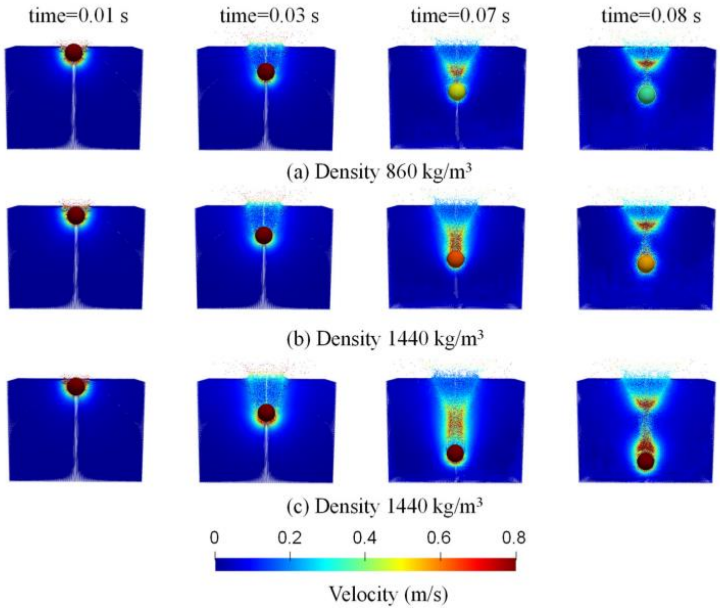

Figure 2.27: Numerical model of water entry of the spheres with different densities (reproduced of Peng et al. 2021 with permission)

Zhu et al. (2021) developed an algorithm to simulate the high shear mixing process of a granular flow with a high proportion of solids particles. The algorithm involves the two-way coupling of SPH and DEM. The model is verified first by a benchmark case of a solid particle moving in a liquid (Figure 2.28). It was then applied to simulate the behavior of liquid flowing through a porous media. Good agreements between the numerical results and the analytical results demonstrate the numerical model is successfully validated.

Figure 2.28: Numerical model of a single particle settling in a fluid represented by the SPH particles (reproduced of Zhu et al. 2021 with permission)

2.5 Summary

Underground mines generate significant quantities of waste rock. Traditionally, most of the underground produced waste rock needs to be transported from underground to ground surface, leading to significant energy consumption and operation costs. Re-using this material as rockfill or RPF requires additional handling processes, such as crushing and grading, mechanical mixing, and transportation. All these operations need additional operation costs and energy consumption.

A growing practice in Canada is to directly dump the underground produced waste rock into mine stopes being filled with cemented paste backfill. The approach allows the waste rock and paste backfill to be mixed naturally without the need of special mixers and mechanical mixing, thus significantly reducing the energy consumption and operational costs associated with the transportation of waste rock. However, studies on the natural mixture of dumped waste rock and paste backfill are absent in the literature. The natural mixing behavior of waste rock and paste backfill needs to be investigated through laboratory tests and numerical modeling.

Understanding the natural mixing behavior of waste rock and paste backfill in a stope is a challenge due to the large dimensions of stopes and the large sizes of field waste rock. Numerical modeling is therefore necessary to take into account scale effects related to stope dimensions and waste rock particle sizes. According to the literature, coupled DEM-SPH and DEM-CFD methods are commonly used to simulate the mixture of particles and fluids (referred to as a fluid-particle system). None of them, however, can be directly used to simulate the mixing behavior of dumped waste rock and paste backfill.

The coupled DEM-SPH method is limited to small-scale engineering problems due to the extremely high computational time and costs. In each simulation step of the SPH method, neighboring particles must be searched and their effects on the current particle accounted for. These search and update calculations require enormous computation time when simulating fluids represented by large quantities of particles (Valdez-Balderas et al. 2013; Ohno et al. 2017; Park et al. 2020; Domínguez et al. 2021). When the SPH solver is coupled with DEM, the calculation time can increase significantly due to the additional particles associated with the DEM code.

The unresolved DEM-CFD approach can become problematic with large particle sizes of waste rock because the CFD mesh size must be larger than the maximum diameter of the particles (Kloss et al. 2012; Peng et al. 2014; Zhang & Yin 2018; Casarin et al. 2022; Ferreira et al. 2023). This requirement may result in overly coarse CFD meshes when simulating systems with very large particles, leading to reduced accuracy and potentially unreliable numerical results. Additionally, strong interaction processes, such as transporting fluid forces from CFD to DEM, can sometimes contribute to numerical instabilities (Casarin et al. 2022).

Further refinement and development of a numerical model are required to simulate the natural mixing behavior of dumped waste rock and paste backfill.

CHAPTER 3 ARTICLE 1: EXPERIMENTAL STUDY ON THE NATURAL MIXING BEHAVIOUR OF WASTE ROCKS POURED IN A PASTE BACKFILL

Yuyu Zhang and Li Li

The article has been published in *International Journal of Mining, Reclamation and Environment*, 37:10, 953-977, DOI: 10.1080/17480930.2023.2235847

Abstract:

Underground produced waste rocks are typically hoisted and stored on ground surface as waste rock piles. The practice requires energy consumption for transporting the waste rocks from underground to ground surface and generates additional operation costs. An alternative practice is to directly pour the waste rocks into mine stopes being filled with paste backfill. However, the natural mixing behavior of waste rocks poured in a paste backfill has never been studied. To fill this gap, a series of physical model tests have been for the first time performed in the laboratory to understand the natural mixing behavior of waste rocks and paste backfill. The definitions of solids content by mass of waste rocks and mixing degree are for the first time proposed to quantitatively evaluate the mixing behavior between the poured waste rocks and paste backfill. The test results show that the penetration of waste rocks into paste backfill and mixing degree of poured waste rocks with paste backfill can be improved through the use of paste backfill of low solids content, large particle sizes of waste rocks, or/and through the increase of falling height of poured waste rocks. The proposed definitions of solids content by mass of waste rocks and mixing degree can be used as good indicators to quantitatively evaluate the mixing quality of the natural mixture.

Keywords: Underground mines; Mine backfill; Waste rocks; Paste backfill; Mixing degree; Natural mixture

3.1 Introduction

Underground mines produce a substantial amount of waste rocks during the development work in order to access ore bodies. Traditionally, these waste rocks need to be transported and hoisted to ground surface because there are no enough underground spaces for storing them. However, the transportation and haulage of waste rocks require large energy consumption and additional operation costs. The lack of enough trucks and haulage systems to transport waste rocks is another problem of this practice.

An alternative practice for industry is to directly pour the underground-produced waste rocks into mine stopes being filled with cemented paste backfill (main body) after the plug pour. These waste rocks are dumped into the cemented paste backfill at 1:1 ratio using a scoop right after excavation. No special crushing and sieving required before dumping. Once poured into paste backfill, the waste rocks mix with the cemented paste backfill in a natural way, without any need for mechanical mixing. This alternative practice can significantly reduce the energy consumption and operation costs associated with the hoisting and transportation of waste rocks from underground to ground surface (Lee & Gu 2017). In addition, if the waste rocks have a full mixing with the cemented paste backfill, the mixture can have mechanical properties much better than those of individual paste backfill and waste rocks (Qiu et al. 2020, 2022).

Despite these advantages, this practice also involves some risks. If the poured waste rocks are not fully mixed with the cemented paste backfill, the cohesionless waste rocks without any paste backfill may fail and collapse upon a side-exposure associated with the excavation of an adjacent stope. The failed mass could lead to ore dilution or even ore loss (Henning 2007). It is thus necessary to have a good understanding of the natural mixing behavior between the two materials.

However, almost all the existing studies related to backfills have been given on one single type of backfill, including the extensive works conducted by Li and other researchers (Aubertin et al. 2003; Béket Dalcé et al. 2019; El Mkadmi et al. 2014; Jaouhar et al. 2018; Jaouhar & Li 2019; Keita et al. 2021a, 2021b; Li et al. 2003; Li et al. 2005; Li & Aubertin 2012; Li 2014a, 2014b; Li & Aubertin 2014; Liu et al. 2017a, 2017b, 2018; Pagé et al. 2019; Qin et al. 2021a, 2021b; Sobhi et al. 2017; Sobhi & Li 2017; Wang et al. 2021a, 2021b; Wang & Li 2022; Yan et al. 2020; Yan et al. 2022a, 2022b; Yang et al. 2017, 2018; Zhai et al. 2021; Zheng & Li 2020; Zheng et al. 2019, 2020a, 2020b, 2020c).

One can only see a few publications related to the mixtures of graded waste rocks and tailings (Wickland & Wilson 2005; Wilson 2001; Wilson et al. 2008) or the graded waste rocks and cemented hydraulic fill (Kuganathan & Sheppard 2001). The abovementioned mixtures require the waste rocks and tailings or hydraulic fill to be mechanically mixed in pipes or special mixing machines. Crushing and sieving are also necessary to limit the sizes of waste rocks. These mechanical mixtures are thus completely different from the natural mixture of waste rocks poured in a paste backfill. Recently, Veenstra & Grobler (2021) present a concept, by which a waste rocks structure is built and wrapped by cemented paste backfill. It can also allow the maximum use of waste rocks and avoid the transportation and hoist of waste rocks from underground to ground surface. However, they do not show how the poured waste rocks are mixed with the paste backfill in a stope.

Until now, the study on the natural mixing behavior of waste rocks poured in a paste backfill is absent. To fill this gap, in this paper, a series of physical model tests have been for the first time performed in laboratory to show the natural mixing behavior of waste and paste backfill. The definitions of solids content by mass of waste rocks and mixing degree are proposed for the first time to quantitatively describe the natural mixture between waste rocks and paste backfill. The effects of some key influencing factors on the natural mixing behavior between the two materials are investigated and discussed.

3.2 Laboratory tests

3.2.1 Materials

In this study, an uncemented paste backfill made of full tailings was used to facilitate the investigation of the natural mixing behavior between the waste rocks and paste backfill. The tested tailings were taken from a mine located at the northwest of Québec, Canada. Figure 3.1 illustrates the particle size distribution curve of the tailings. It has a maximum particle size of 0.63 mm, containing approximately 77% of particles smaller than 80 µm and 36% smaller than 20 µm. The backfill made of such tailings meets the criterion of paste backfill in terms of particle size distribution (contains at least 15% of particle smaller than 20 µm) (Hassani & Archibald 1998; Potvin et al. 2005; Zheng & Li 2020).

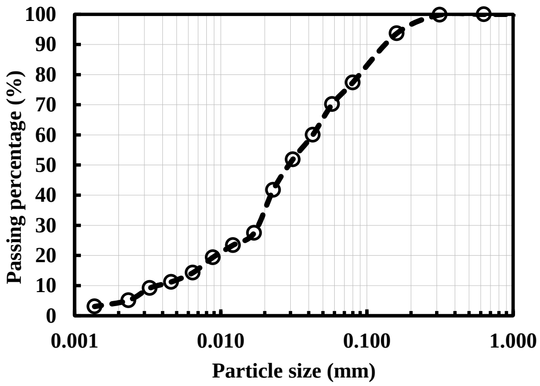

Figure 3.1: Particle size distribution curve of the tested tailings

The tested tailings were first dried in an oven for 24 hours. The dried tailings were then poured into water to make a paste backfill (Figure 3.2a). A full mixing between the tailings and water was guaranteed by the use of an electric stirring rod, as shown in Figure 3.2b.

(a) (b)

Figure 3.2: Procedures for making a homogenous paste backfill: (a) addition of dried tailings into water; (b) mixing with an electric stirring rod

The tested paste backfills were prepared with three solids contents by mass of 70, 72.5, and 75%, respectively. With a solids content by mass of 70%, the paste backfill looks like a liquid, as shown in Figure 3.3a. At a solids content by mass of 72.5%, the paste backfill still looks like a liquid (Figure 3.3b), but much thicker than the previous paste backfill with a solids content by mass of 70%. At a solids content by mass of 75%, the paste backfill becomes thick and viscous, looking like a paste (Figure 3.3c).

(a) (b) (c)

Figure 3.3: Pictures of paste backfills having solids contents by mass of: (a) 70%, (b) 72.5%, and (c) 75%, respectively

The tested waste rocks were taken from the same mine from where the tailings were taken. Sieving was performed to obtain waste rocks samples with particle sizes in the range of 2.5 to 5.0, 5.0 to 8.0, and 8.0 to 9.5 mm, as shown in Figure 3.4. They were named as small, medium and large particle size waste rocks samples, and tinted of blue (Figure 3.5a), green (Figure 3.5b) and yellow (Figure 3.5c) colors, respectively. The coloring of waste rocks samples is necessary to better observe the mixing state between waste rocks and paste backfill after cutting the backfill mass formed by pouring the waste rocks into the paste backfill.

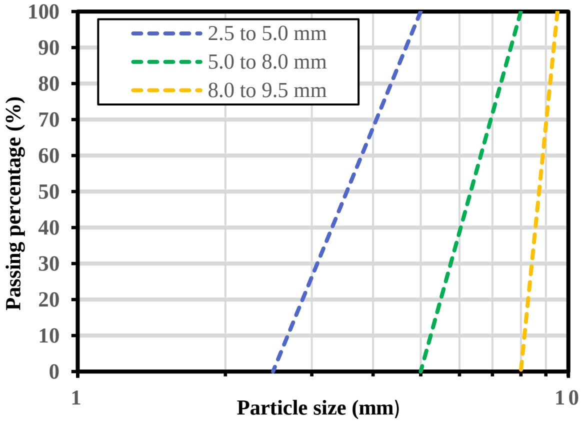

Figure 3.4: Particle size distribution curves of the tested waste rocks

(a) (b) (c)

Figure 3.5: Tinted waste rocks samples with different particle sizes: (a) small particle sizes in the range of 2.5 to 5.0 mm; (b) medium particle sizes in the range of 5.0 to 8.0 mm; (c) large particle sizes in the range of 8.0 to 9.5 mm

3.2.2 Testing procedure

Figure 3.6 shows a schematic presentation (Figure 3.6a) and a picture (Figure 3.6b) of the physical model, used to study the natural mixing behavior of waste rocks poured in a paste backfill. On Figure 3.6a, H_{paste} represents the height of the paste backfill before any pouring of waste rocks; P is the solids content by mass of paste backfill; H_f is the falling height of waste rocks. The box of 16.5 cm long, 20 cm large and 25 cm high was used to simulate an underground mine stope in reduced scale (see Figure 3.6b). It is made of wood studs to ease the later box disassembling and sample cut. Its inside walls were covered with waterproof plastic sheet to prevent any water seepage. A funnel was fixed at the top center of the mold to control the falling height, position of pouring, and quantity of waste rocks. The funnel has a diameter of 19 cm on top, a diameter of 4.0 cm at the end with the exit tube, and an overall height of 12 cm. In this study, the tested waste rocks were poured through the funnel at the center area of the mold. All tests were done by using a total mass of waste rocks M_{wr} = 1000 g and an initial height of paste backfill H_{paste} = 10 cm. In this study, no plug is poured into the mold before the pouring of paste backfill.

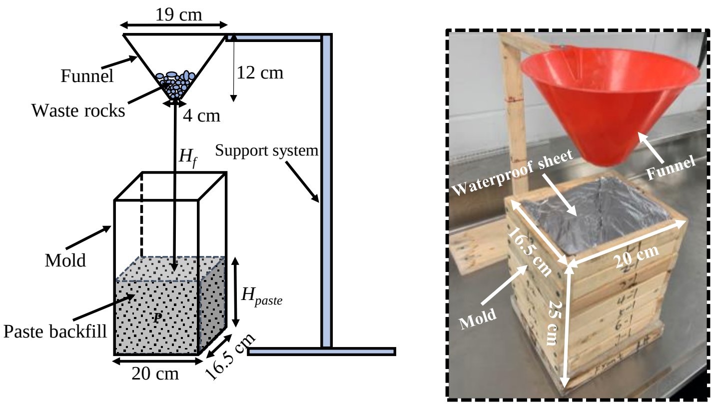

(a) (b)

Figure 3.6: A physical model to study the natural mixing behavior of waste rocks poured in a paste backfill: (a) schematic presentation; (b) a picture

Table 3.1 shows the test program to evaluate the effects of solids content by mass (P) of paste backfill, particle sizes (d_{wr}) of waste rocks and falling height (H_f) of waste rocks on the natural mixing behavior between the two materials.

Table 3.1: Test program of natural mixing between waste rocks and paste backfill

Cases	d_{wr} (mm)	H_f (cm)	P (%)
Case 1	2.5 to 5.0	15	70
Case 2	2.5 to 5.0	15	72.5
Case 3	2.5 to 5.0	15	75
Case 4	5.0 to 8.0	15	72.5
Case 5	8.0 to 9.5	15	72.5
Case 6	2.5 to 5.0	45	72.5
Case 7	2.5 to 5.0	75	72.5

After the pouring of waste rocks into the paste backfill, the natural mixture was left to settle down and dry. When it became hard enough, the wood studs were disassembled with the mixture was then cut into small blocks. Figure 3.7 shows the schematic presentation of the cut procedure of a mixture. The mixture was divided into three layers along the Z direction. Each layer was further cut into 12 small blocks of 5.5 cm long, 5 cm large and 3 cm high. The position of each small block is identified by its layer number along with Z direction and its numbers in X and Y directions.

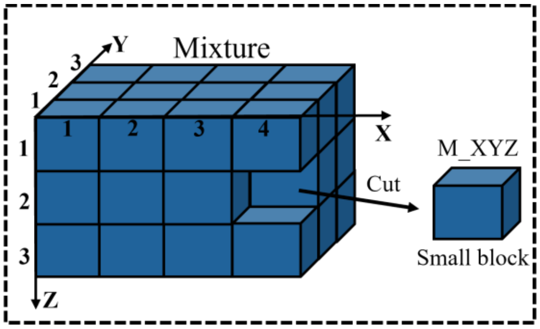

Figure 3.7: Schematic presentation of the cut procedure of the mixture

The obtained small blocks were then placed in an oven to make them completely dried. After 24 hours of drying, each block was gently crushed by hand and placed in a container, followed by a sieving analysis. The masses of waste rocks and paste backfill of each block were then obtained due to the large contrast in particle size distribution between the tested waste rocks and paste backfill. These steps are illustrated in Figure 3.8 showing the state of dried blocks (Figure 3.8a), a crushed block (Figure 3.8b), and sieving analysis (Figure 3.8c), respectively.

(a) (b) (c)

Figure 3.8: Procedure for obtaining the particle size distribution curves of a small block: (a) small blocks after 24 hours of oven-drying; (b) hand-crushed mixture of a dried block; (c) sieving analysis

3.3 Test results and interpretation

3.3.1 Qualitative analysis

3.3.1.1 Effect of the solids content by mass of paste backfill

Figure 3.9 presents a top view of the mixtures after the pour of small particle size of waste rocks in the paste backfills having three different solids contents by mass of 70 (Case 1), 72.5 (Case 2), and 75% (Case 3), respectively (see Table 3.1 for more details). At a solids content by mass of 70%, the waste rocks easily penetrated into the paste backfill and almost all the poured waste rocks sunk into the paste backfill with only a few tracks left on the top surface of the mixture (Figure 3.9a). At a solids content by mass of 72.5%, the penetration of waste rocks into the paste backfill became difficult and the drag force against the sinking of waste rocks particles would be stronger than in the paste backfill of 70%. Subsequently, a large amount of waste rocks remained on the top surface without mixing with any paste backfill (Figure 3.9b). When the solids content of the paste backfill further increases to 75%, the waste rocks are difficult to penetrate into and sink in the paste backfill. Accordingly, the major part of the poured waste rocks remained on the top surface of the mixture (Figure 3.9c).

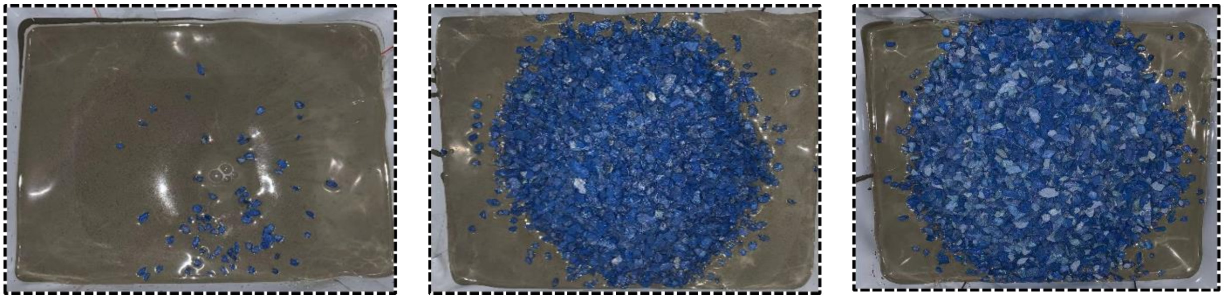

(a) (b) (c)

Figure 3.9: Top views of the mixtures after the pour of waste rocks in the paste backfills having solids contents by mass of: (a) 70% (Case 1); (b) 72.5% (Case 2); (c) 75% (Case 3)

Figure 3.10 presents the views of the internal structures of the mixtures between the poured small particle size waste rocks and the paste backfills having a solids content by mass of 70% (Figure 3.10a), 72.5% (Figure 3.10b), and 75% (Figure 3.10c), respectively. With a solids content of 70%, one sees the presence of waste rocks along the whole depth with all the particles entirely wrapped of paste backfill (Figure 3.10a). The mixture between the waste rocks and paste backfill has a texture looking like a concrete. When the solids content increases to 72.5%, one sees a large pocket of waste rocks along the depth of 0 to 3 cm in the form of an inverse cone or a volcano crater without any mix with paste backfill (Figure 3.10b). Along the depth of 3 to 9 cm, one sees the presence of waste rocks entirely wrapped of paste backfill, indicating a good mixture. At a solids content of 75%, one can see the waste rocks also in the form of an inverse cone or volcano crater along the depth of 0 to 3 cm. No waste rocks submerged into the paste backfill along the depth of 3 to 9 cm (Figure 3.10c). The results along with those presented in Figure 3.9 indicate that a good mixture between poured waste rocks and paste backfill exists only when the paste backfill has a low solids content. When the solids content of paste backfill is high, the quantity of unmixed waste rocks increases. The mixing behavior between the poured waste rocks and paste backfill varies in space (depth).

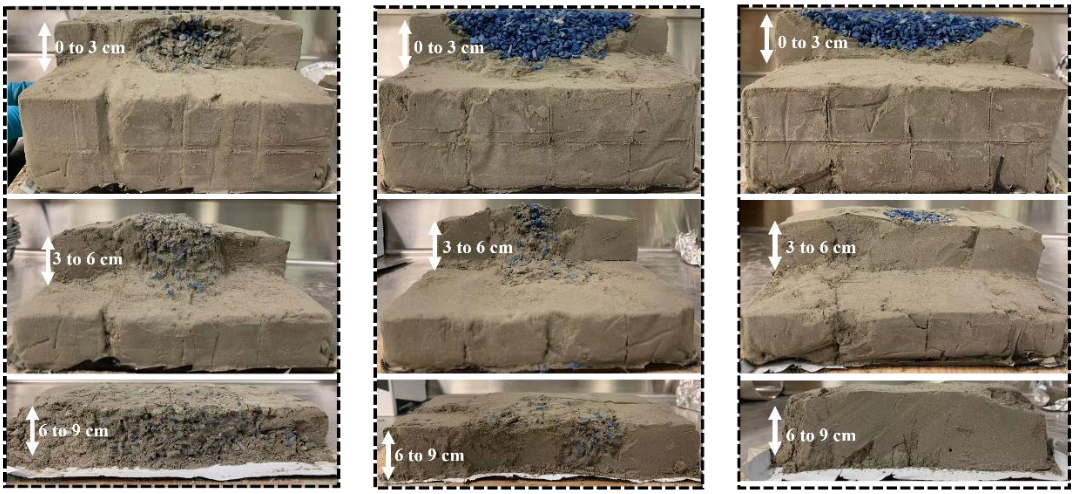

(a) (b) (c)

Figure 3.10: Internal structures of the mixtures after the pour of waste rocks in the paste backfills having solids contents by mass of: (a) 70% (Case 1); (b) 72.5% (Case 2); (c) 75% (Case 3)

Figure 3.11 presents the particle size distribution (PSD) curves of the tested tailings and waste rocks (WR) along with the PSD of the small blocks issued from the cut of mixture generated by pouring small particle size waste rocks into paste backfills having a solids content by mass of 70 (Figure 3.11a), 72.5 (Figure 3.11b) and 75% (Figure 3.11c), respectively. At a solids content by mass of 70% (Figure 3.11a), the mass of paste backfill for each block increases as the increase of mixture depths (from Layer 1 to 3). The high amount of paste backfill in each block indicates the waste rocks are well mixed with paste backfill. When the solids content by mass of paste backfill increase to 72.5% (Figure 3.11b), the PSD curves of the two center blocks (M_221 and M_321) at layer 1 overlap with the PSD curve of waste rocks, indicating an absence of paste backfill in the blocks. At a solids content by mass of 75% (Figure 3.11c), the PSD curves of two center blocks (M_221 and M_321) at layer 1 also overlap with that of waste rocks, once again indicating an absence of paste backfill in these blocks. These results confirm that, for a given mass, particle sizes and falling height of waste rocks, the quantity of unmixed waste rocks can be expected to increase as the solids content of paste backfill increases.

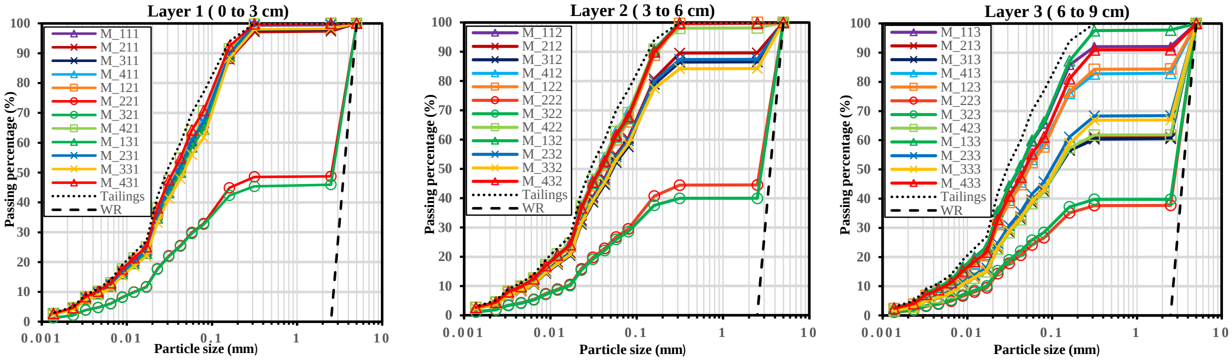

(a)

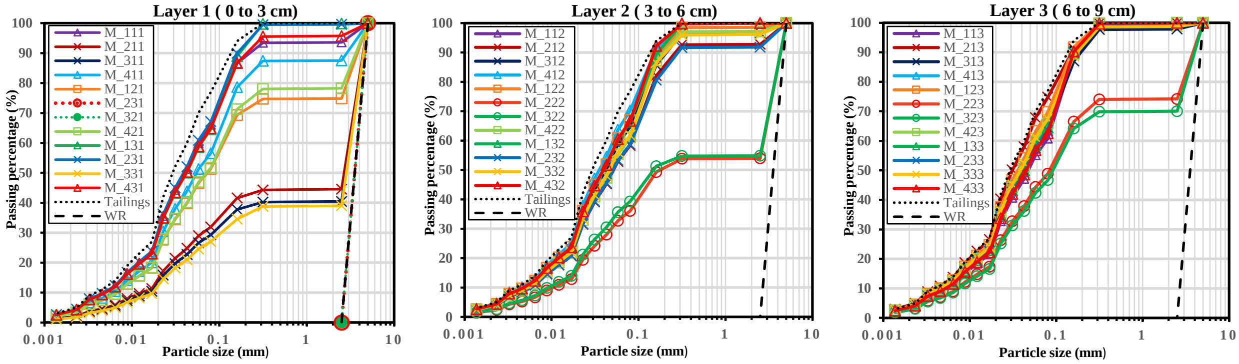

(b)

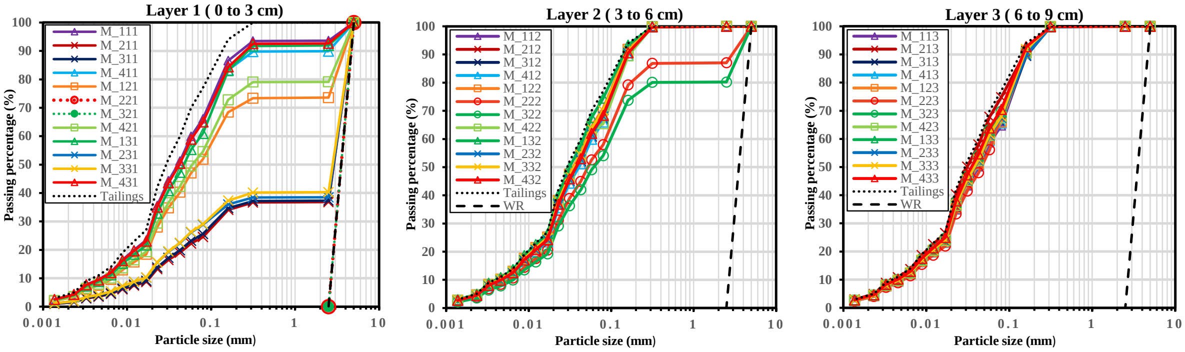

(c)

Figure 3.11: Particle size distribution (PSD) curves of small blocks after the pour of waste rocks in the paste backfills having solids contents by mass of: (a) 70% (Case 1); (b) 72.5% (Case 2); (c) 75% (Case 3)

3.3.1.2 Effect of the particle size of waste rocks

Figure 3.12 presents the top views of the mixtures after the pour of small particle sizes waste rocks (Case 2), medium particle sizes waste rocks (Case 4) and large particle sizes waste rocks (Case 5) in the paste backfills having a solids content by mass of 72.5%, respectively. One sees that a large quantity of waste rocks stayed on the top surface for the case of small particle size waste rocks (Figure 3.12a), while only a small portion of waste rocks remained on the top surface for the case of large particle size waste rocks (Figure 3.12c). With the medium particle size waste rocks, a quantity intermediate between the two previous cases were observed on the top surface of the mixture (Figure 3.12b). These results indicate that large particle sizes of waste rocks are preferred in terms of penetration of poured waste rocks in a given paste backfill.

(a) (b) (c)

Figure 3.12: Top views of the mixtures after the pour of waste rocks with: (a) small particle sizes (Case 2); (b) medium particle sizes (Case 4); (c) large particle sizes (Case 5)

Figure 3.13 presents the internal structures of the mixtures after the pouring of waste rocks with small particle sizes waste rocks (Figure 3.13a), medium particle sizes waste rocks (Figure 3.13b) and large particle sizes waste rocks (Figure 3.13c), exposed after a few vertical cuts. In all cases, the waste rocks were poorly mixed with paste backfill in the center part of the paste backfill along the depth of 0 to 3 cm, while the waste rocks are all wrapped by paste backfill along the depth of 3 to 9 cm.

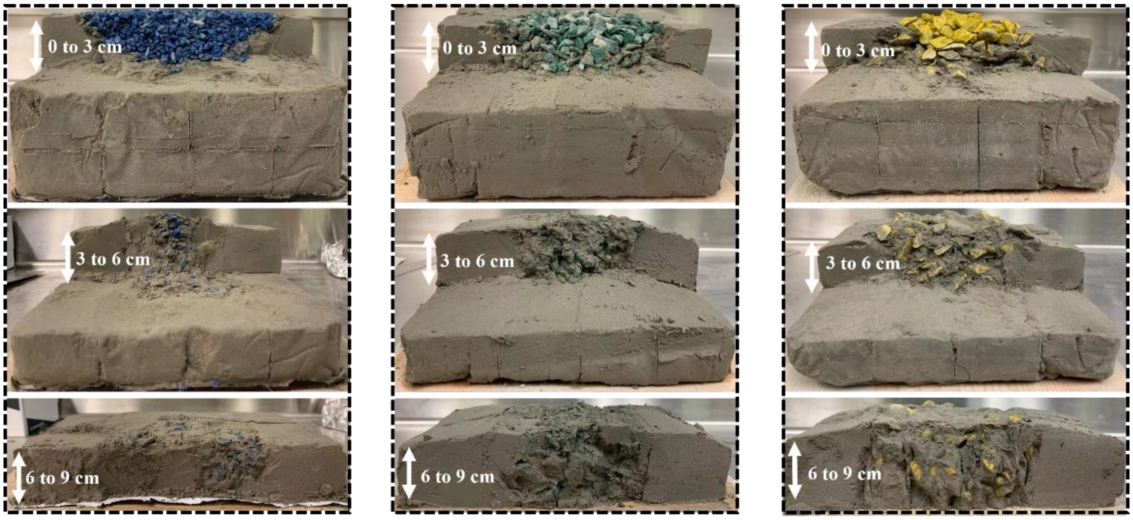

(a) (b) (c)

Figure 3.13: Internal structures of the mixtures after the pour of waste rocks with: (a) small particle sizes (Case 2); (b) medium particle sizes (Case 4); (c) large particle sizes (Case 5)

The PSD curves of small blocks after the pour of waste rocks with small particle sizes has already been presented in Figure 3.11b (Case 2). Figure 3.14 only presents the PSD curves of small blocks after the pour of waste rocks with medium particle sizes (Figure 3.14a) and large particle sizes (Figure 3.14b), respectively. For waste rocks with medium particle sizes (Figure 3.14a), the two center blocks at layer 1 (M_221 and M_321) contain 8.7 and 5.6% of paste backfill, respectively, suggesting a little presence of paste backfill in these blocks. For waste rocks with large particle sizes (Figure 3.14b), the mass of paste backfill at the corresponding two center blocks increases to 16.5 and 13.1 %, respectively. The PSD curves of other blocks for waste rocks with medium and large sizes are similar. These results suggest that, for paste backfill with a high solids content, the increase of waste rocks particle sizes can help to improve the mixing behavior between the two materials.

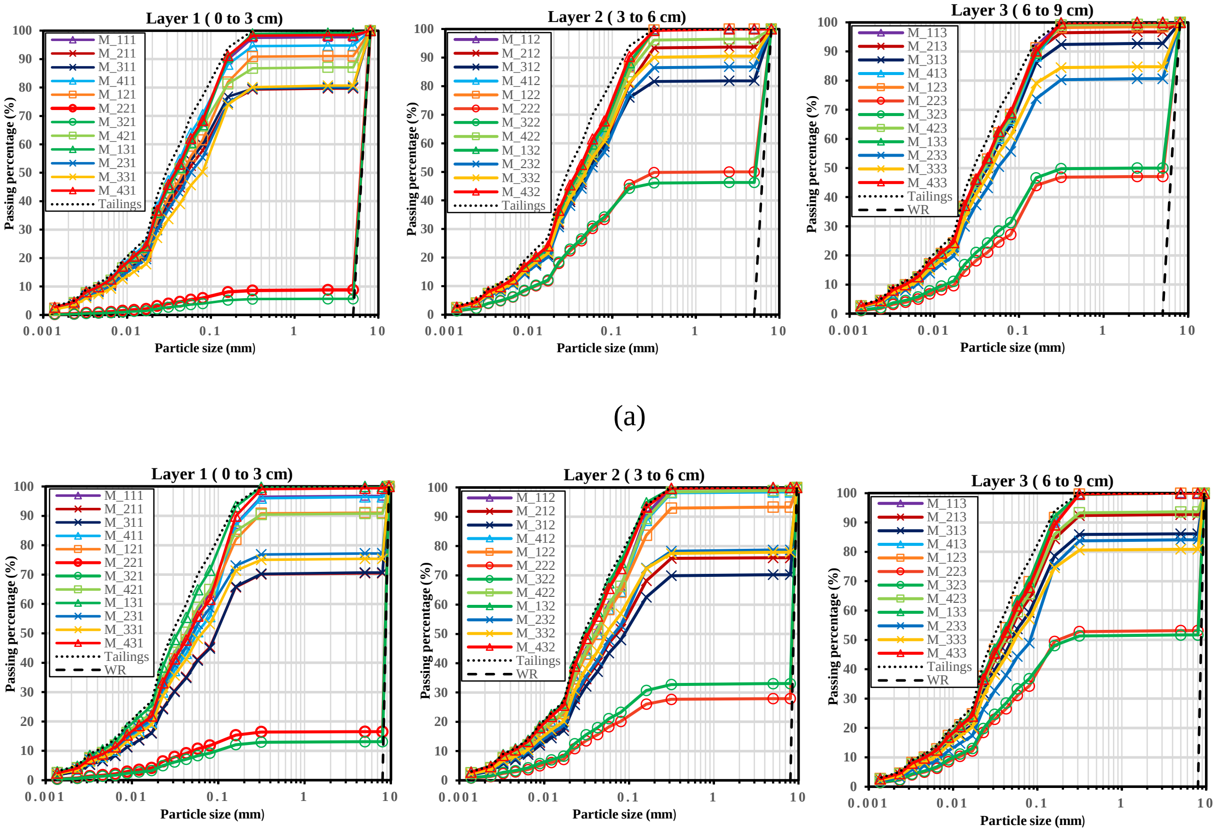

(a)

(b)

Figure 3.14: Particle size distribution (PSD) curves of small blocks after the pour of waste rocks with: (a) medium particle sizes of 5.0 to 8.0 mm (Case 4); (b) large particle sizes of 8.0 to 9.5 mm (Case 5)

3.3.1.3 Effect of the falling height of waste rocks

Figure 3.15 presents the top views of the mixtures after the pour of waste rocks in the paste backfill having a solids content by mass of 72.5% at falling heights of 15 (Case 2), 45 (Case 6) and 75 cm (Case 7), respectively. One sees a large amount of waste rocks remaining on the top surface of the mixture at a falling height of 15 cm (Figure 3.15a). The mass of waste rocks on the top surface of the mixture decreases with the falling height increases to 45 cm (Figure 3.15b). When the falling height further increases to 75 cm, almost all the waste rocks sunk into the paste backfill, resulting in a very small quantity of waste rocks particles on the top surface of the mixture (Figure 3.15c).

(a) (b) (c)

Figure 3.15: Top views of the mixtures after the pour of waste rocks in the paste backfills having a solids content by mass of 72.5% at falling heights of: (a) 15 cm (Case 2); (b) 45 cm (Case 6); (c) 75 cm (Case 7)

Figure 3.16 presents the internal structures of the mixtures after the pouring of waste rocks at falling heights of 15 (Figure 3.16a), 45 (Figure 3.16b) and 75 cm (Figure 3.16c), respectively. From Fig. 16a, one notes that the quantity of submerged waste rocks inside the paste backfill are small when the waste rocks are poured at the falling height of 15 cm. However, the quantity of submerged waste rocks increase as the falling heights increases to 45 cm (Figure 3.16b). All the waste rocks are submerged into the paste backfill as the falling heights increases to 75 cm (Figure 3.16c). The submerged waste rocks are entirely wrapped by the paste backfill, suggesting a good mixture.

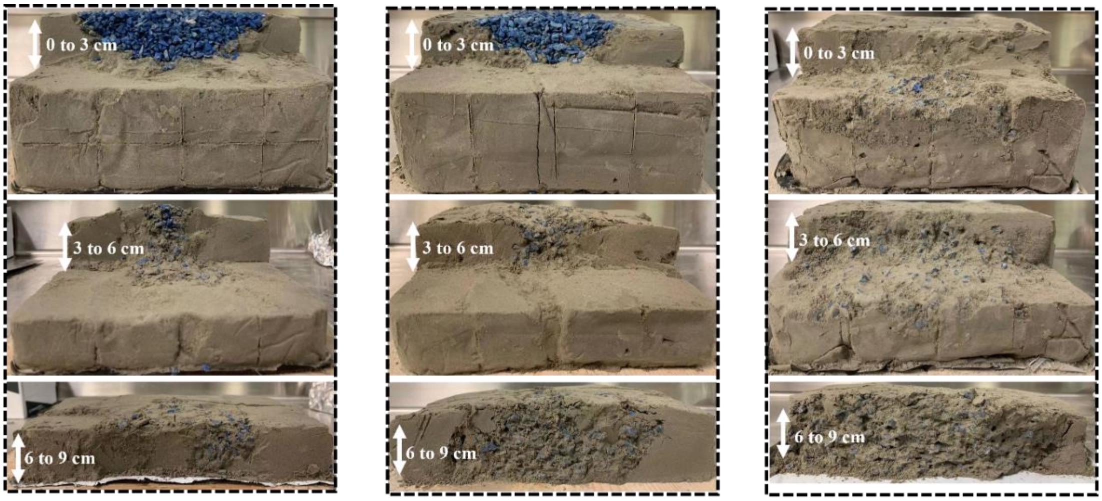

(a) (b) (c)

Figure 3.16: Internal structures of the mixtures after the pour of waste rocks at falling heights of: (a) 15 cm (Case 2); (b) 45 cm (Case 6); (c) 75 cm (Case 7)

The PSD curves of small blocks after the pour of waste rocks at the falling height of 15 cm has been shown in Figure 3.11b (Case 2). Figure 3.17 presents the PSD curves of small blocks after the pour of waste rocks at falling heights of 45 (Figure 3.17a) and 75 cm (Figure 3.17b), respectively. At a falling height of 45 cm, one sees that the center blocks at layer 1 (M_221 and M_321) contain around 19.1%, suggesting a little amount of paste backfill in these blocks. At a falling height of 75 cm, the two center blocks at layer 1 (M_221 and M_321) contain about 80% of paste backfill, indicating the presence of large quantity of paste backfill. The results along with the findings of falling height at 15 cm (Figure 3.11b) indicate, for paste backfill with a high viscosity, the mixing behavior between the two materials can be improved by increasing the falling height of waste rocks.

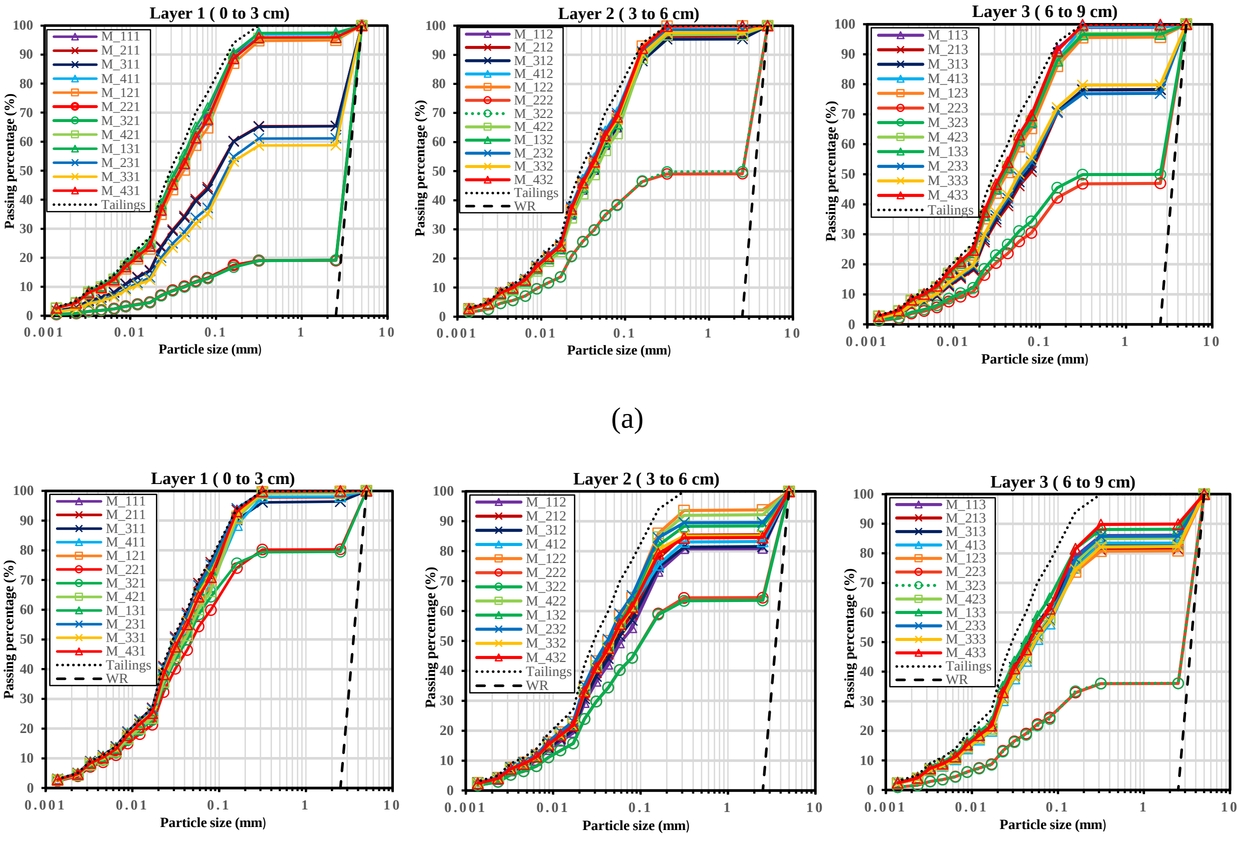

(a)

(b)

Figure 3.17: Particle size distribution (PSD) curves of small blocks after the pour of waste rocks at falling heights of: (a) 45 cm (Case 6); (b) 75 cm (Case 7)

3.3.2 Spatial distribution of mixing degree between waste rocks and paste backfill

In section 3.3.1, the mixing behavior between the poured waste rocks and paste backfill has been presented in a qualitative way. It gave a global and general picture of the internal structure of a mixture. However, it does not allow a quantitative description on the mixing degree of mixture or a spatial description on the mixing degree of the mixture between the two materials. To overcome these limitations, one first needs the definition of a parameter that can be used to quantitatively evaluate the degree of mixture between two different materials. As such definition is absent in the literature, one first proses a definition of waste rocks content by mass as follows:

$$C = \frac{M_{wr}}{M_{wr} + M_{paste.dried}} \tag{3.1}$$

where C is the solids content by mass of waste rocks of a mixture, M_{wr} and M_{paste} are the masses of waste rocks and dried paste backfill in the mixture, respectively. When $M_{wr} = 0$, the mixture does not contain any waste rocks and the solids content by mass of waste rocks C is equal to 0%. When $M_{paste.dried} = 0$, the mixture does not contain any paste backfill and the solids content by mass of waste rocks C is equal to 100%.

The solids content by mass of waste rocks can give an idea on the portion of waste rocks, but fail to describe the mixing degree between paste backfill and waste rocks. If one considers that a full mixture between the two materials is reached when the voids of waste rocks are fully filled with paste backfill. The mixing degree of the mixture between the two materials can be defined as follows:

$$S = \frac{V_{paste.dried}}{V_v} \tag{3.2}$$

where S is the mixing degree of a mixture, $V_{paste.dried}$ is the volume of dried paste backfill in a mixture, V_v is the voids volume of waste rocks.

The volume of dried paste backfill in a mixture can then be obtained by:

$$V_{paste.dried} = \frac{M_{paste.dried}}{\rho_{paste.dried}} \tag{3.3}$$

where $M_{paste.dried}$ is the mass of dried paste backfill in a mixture; $\rho_{paste.dried}$ is the density of dried paste backfill in a mixture, defined as follows:

$$\rho_{paste.dried} = \rho_s * (1 - n_{paste.dried}) \tag{3.4}$$

where ρ_s is the particle density of tailings particles; $n_{paste.dried}$ is the porosity of dried paste backfill, expressed as:

$$n_{paste.dried} = \frac{e_f}{1 + e_f} \tag{3.5}$$

where e_f is the final void ratio of dried paste backfill determined from shrinkage test curve (Qin et al. 2021b; Saleh-Memba et al. 2016).

The voids volume of waste rocks in a mixture can be obtained by:

$$V_v = V_{wr} * n_{wr} \tag{3.6}$$

where V_v is the voids volume of waste rocks, n_{wr} is the porosity of waste rocks; V_{wr} is the volume of waste rocks, obtained as follows:

$$V_{wr} = \frac{M_{wr}}{\rho_{wr}} \tag{3.7}$$

where M_{wr} is the mass of waste rocks in a mixture, ρ_{wr} is the density of waste rocks.

Substituting equations (3.3) to (3.7) into equation 3.2, the mixing degree of a mixture becomes:

$$S = \frac{M_{paste.dried} * \rho_{wr}}{\rho_s \left(1 - \frac{e_f}{1 + e_f}\right) * M_{wr} * n_{wr}} \tag{3.8}$$

If the mass of dried paste backfill, $M_{paste.dried}$ equals to zero, the mixing degree of the mixture, S, equals to zero. The mixing degree of the mixture increases as the mass of dried paste backfill of the mixture increases. When the mass of paste backfill increases to a degree by which all the void volume of waste rocks is filled with paste backfill, the mixing degree of the mixture, S, equals to 100%. If the mass of paste backfill increases further, the void volume and porosity of the waste rocks increase. Equation (3.8) cannot be applied by considering n_{wr} as a constant. The mixing degree of the mixture can either be considered as 100% or inapplicable.

Figures 3.18 and 3.19 respectively shows the spatial distributions of solids contents by mass of waste rocks C and mixing degree S of the mixtures for Cases 1 to 7. Details on the direct measurements and calculations of the solids content by mass of waste rocks and mixing degree for each small block are presented in Appendix I, while the correction and estimation of the solids content by mass of waste rocks and mixing degree of the mixture for the small blocks near the interfaces between waste rocks and paste backfill are presented in Appendix II.

From Figure 3.18, one sees the solids content by mass of waste rocks varies from 50 to 60% inside the center area of the mixture (Case 1), suggesting most waste rocks are presented in these areas. For Cases 2, 3, 4 and 6, the solids content by mass of waste rocks ranges from 90 to 100% on the top part of the mixtures, indicating a high amount of waste rocks with the absence of paste backfill in these areas. One can find that the spatial distributions of the solids contents by mass of waste rocks agree well with the observations and qualitative analyses shown in Figures 3.9 to 3.17. The solids content by mass of waste rocks can give a quantitative description on the portion of waste rocks for each of the mixture, thus can be used as an indicator to describe the mixing behavior of the mixture.

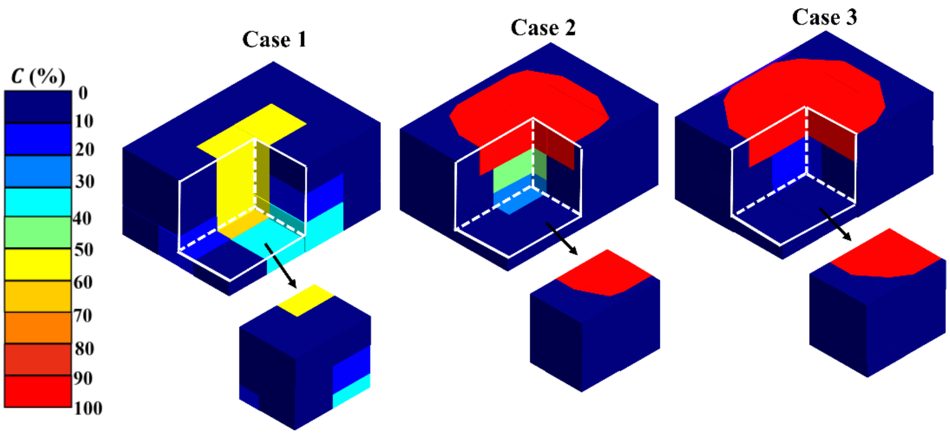

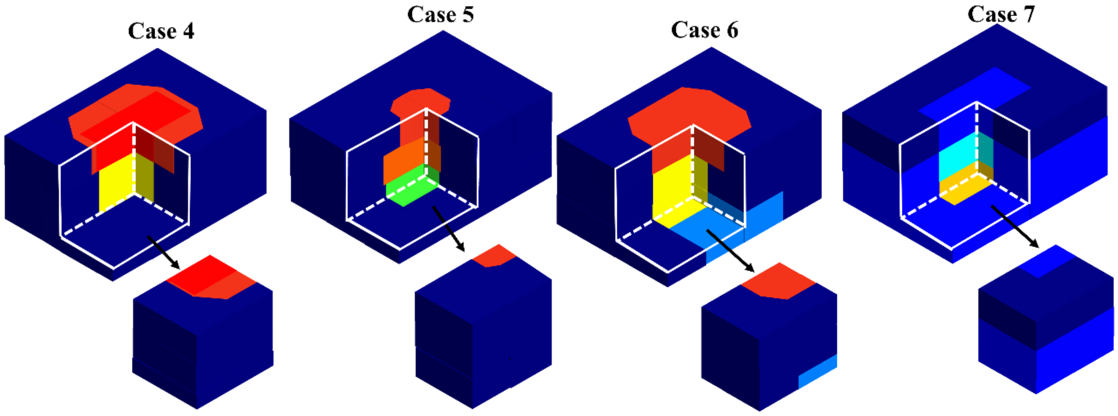

Figure 3.18: The spatial distributions of solids content by mass of waste rocks C for Cases 1 to 7

Figure 3.19 shows that the spatial mixing quality between the poured waste rocks and paste backfill of a mixture is presented in a quantitative way. For Cases 1 and 7, the mixing degree of the mixtures equals to 100%, indicating the waste rocks are fully mixed with the paste backfill. For Cases 2, 3 and 4, the mixing degree on the top part of the mixtures vary from 0 to 20%, suggesting the waste rocks are poorly mixed with the paste backfill in these areas. For Cases 5 and 6, the mixing degree on the top ranges from 30 to 50%, which also confirms the waste rocks are not fully mixed with the paste backfill. The mixing degree reaches 100% at the bottom parts of the mixtures for all cases.

Both figures indicate that the portions of pure waste rocks can be decreased by using paste backfill of low solids content, waste rocks of large particle sizes and large falling height. The proposed definition of solids content by mass of waste rocks *C* and mixing degree *S* can be used to quantitatively describe the natural mixing behavior between poured waste rocks and paste backfill.

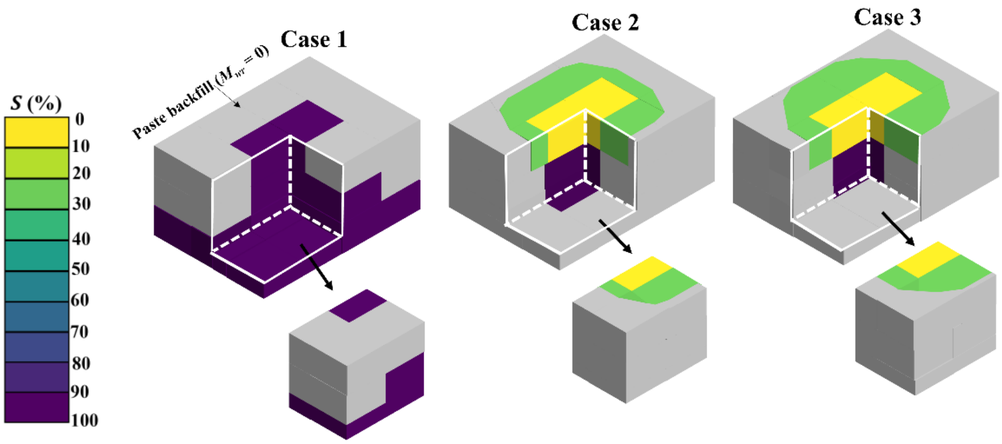

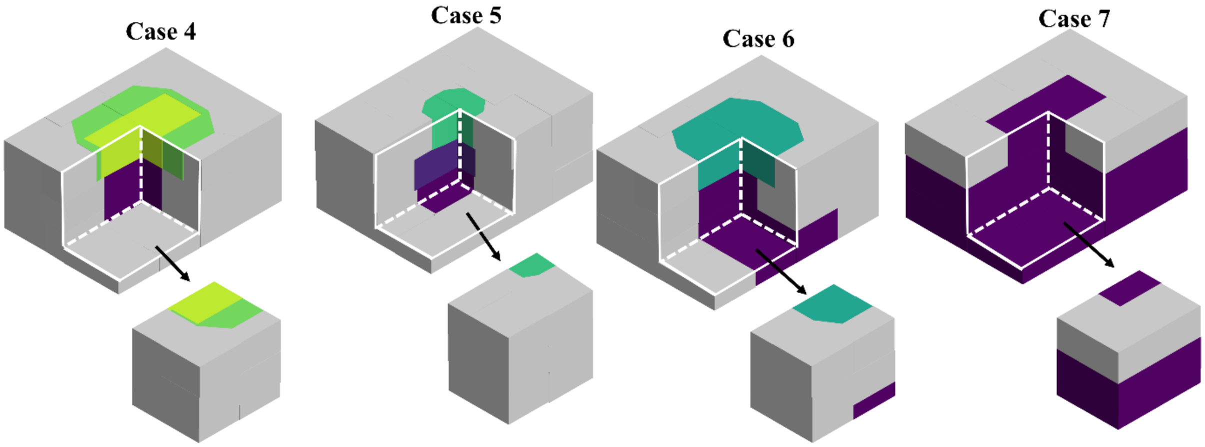

Figure 3.19: The spatial distributions of mixing degree S for Cases 1 to 7

3.4 Discussion

A series of physical model tests were performed to investigate the natural mixing behavior of waste rocks poured in a paste backfills. The effects of solids content of paste backfill, particle size of waste rocks, and falling height of waste rocks on the natural mixing behavior of poured waste rocks and paste backfill is for the first time evaluated. Two definitions used to quantitatively describe the nature mixing behavior of waste rocks and paste backfill were also proposed for the first time. The test results can be used to understand the natural mixing behavior of poured waste rocks with a paste backfill in a mine stope.

Nevertheless, it should be noted that the experimental work presented in this study is preliminary and involves several limitations. As a very preliminary stage without any references (neither in published works nor for a specific mine or stope), the solids contents of paste backfill, sizes and falling height of waste rocks, and box sizes were chosen in an arbitrary way. No scale factors can be considered because the on-site conditions are unknown. In the future, more experimental and field works are necessary by considering the scale effect factors. The use of non-cemented paste backfill constitutes another limitation of the test program presented in Table 1. The effect of binder on the natural mixing behavior of waste rocks and cemented paste backfill will be investigated in the following works. More experimental tests will also be conducted to obtain the rheology parameters (e.g., viscosity and yield stress) used to describe the flowability of cemented paste backfill. These are part of our ongoing works and will be part of our future publications.

In the study, the mass of waste rocks was used as a control variable for the sake of simplicity in laboratory tests. However, volume of waste rocks is a better variable than mass of waste rocks because it allows to consider the capacity of paste backfill holding the waste rocks. The control variable of waste rocks volume will be applied in the future works. In addition, the waste rocks were poured into the paste backfill from the top center of the mold. This does not always correspond to the field conditions where waste rocks are commonly dumped in a stope being filled with waste rocks from an over-cut at a stope edge. More experimental work is thus necessary to investigate the effect of pouring position on the mixing behavior between poured waste rocks and paste backfill.

Another limitation of this study is associated with the cut size of small block. The same size was used for all the small blocks. This results in inaccurate descriptions of the solids content by mass of waste rocks and mixing degree of the mixture, especially near the interfaces between waste rocks and paste backfill. In future studies, the blocks around the interfaces between waste rocks and paste backfill should be cut in dimensions as small as possible to obtain a more accurate description of the mixing degree between the two materials.

Despite the above-mentioned limitations, the experimental results and the analyses presented in this study result in a better understanding of the natural mixing behavior between the poured waste rocks and paste backfill. The results along with the proposed definitions of solids content by mass of waste rocks and mixing degree of the mixture of this study pave the way for future work on the natural mixing behavior of waste rocks and paste backfill.

3.5 Conclusions

In this study, the natural mixing behavior of waste rocks poured in a paste backfill has been, for the first time, investigated through laboratory tests. The definitions of solids content by mass of waste rocks and mixing degree of mixtures were for the first time proposed to quantitatively describe the mixture between the poured waste rocks and paste backfill. The main findings are summarized as follows:

1. For a given mass, particle sizes and falling height of waste rocks, the quantity of unmixed waste rocks can be expected to increase as the solids content of paste backfill increases.
2. The mixing behavior between the poured waste rocks and paste backfill varies in space of a mixture.

3. The mixing degree of poured waste rocks and paste backfill can be improved through the use of paste backfill of low solids content, large particle sizes of waste rocks, or through the increase of falling height of poured waste rocks.
4. The proposed definitions of solids content by mass of waste rocks and mixing degree of the mixtures seem to be appropriate describe the spatial mixing behavior of the waste rocks and paste backfill. They can be used as good indicators to quantitatively evaluate the mixing quality of the natural mixture.

3.6 Appendix I: Solids content by mass of waste rocks C and mixing degree S of the small blocks

Table 3.2 presents the solids content by mass of waste rocks and mixing degree of the mixtures using the proposed equations (3.1) and (3.8). In the calculations, the final void ratio e_f of dried paste backfill is determined by using the shrinkage test results conducted by Saleh-Memba et al. (2016).

Table 3.2: Calculated solids content by mass of waste rocks *C* and mixing degree *S* of small blocks based on direct measurements

Case 1	Blocks	M_{wr} (kg)	$M_{paste.dried}$ (kg)	ρ_s (kg/m^3)	e_f	C	S
Layer 1	M_111	0.0007	0.1267	2710	0.6	0.5%	/
	M_211	0.0027	0.0985	2710	0.6	2.6%	/
	M_311	0.0020	0.0967	2710	0.6	2.0%	/
	M_411	0.0000	0.1255	2710	0.6	0.0%	/
	M_121	0.0000	0.1052	2710	0.6	0.0%	/
	M_221	0.0673	0.0639	2710	0.6	51.3%	100%
	M_321	0.0479	0.0407	2710	0.6	54.0%	100%
	M_421	0.0001	0.1057	2710	0.6	0.09%	/
	M_131	0.0001	0.1132	2710	0.6	0.09%	/
	M_231	0.0004	0.0978	2710	0.6	0.4%	/
	M_331	0.0017	0.0921	2710	0.6	1.8%	/
	M_431	0.0000	0.1282	2710	0.6	0.0%	/
Layer 2	M_112	0.0002	0.1556	2710	0.6	0.1%	/

Table 3.2: Calculated solids content by mass of waste rocks *C* and mixing degree *S* of small blocks based on direct measurements (continued)

Case 1	Blocks	M_{wr} (kg)	$M_{paste.dried}$ (kg)	ρ_s (kg/m^3)	e_f	C	S
Layer 2	M_212	0.0122	0.1055	2710	0.6	10.3%	100.%
	M_312	0.0160	0.1029	2710	0.6	13.4%	100%
	M_412	0.0004	0.1360	2710	0.6	0.2%	/
	M_122	0.0000	0.0944	2710	0.6	0.0%	/
	M_222	0.0988	0.0793	2710	0.6	55.4%	100%
	M_322	0.0780	0.0520	2710	0.6	60.0%	100%
	M_422	0.0016	0.0860	2710	0.6	1.8%	/
	M_132	0.0001	0.1021	2710	0.6	0.1%	/
	M_232	0.0191	0.1330	2710	0.6	12.5%	100%
	M_332	0.0176	0.0945	2710	0.6	15.7%	100%
	M_432	0.0002	0.1053	2710	0.6	0.19%	/
Layer 3	M_113	0.0130	0.1515	2710	0.6	7.9%	100%
	M_213	0.0544	0.0853	2710	0.6	38.9%	100%
	M_313	0.0479	0.0735	2710	0.6	39.4%	100%
	M_413	0.0279	0.1355	2710	0.6	17.0%	100%
	M_123	0.0161	0.0871	2710	0.6	15.6%	100%
	M_223	0.1113	0.0673	2710	0.6	62.3%	100%
	M_323	0.1036	0.0684	2710	0.6	60.2%	100%
	M_423	0.0487	0.0789	2710	0.6	38.1%	100%
	M_133	0.0035	0.1510	2710	0.6	2.2%	100%
	M_233	0.0672	0.1455	2710	0.6	31.5%	100%
	M_333	0.0558	0.1130	2710	0.6	33.0%	100%
	M_433	0.0136	0.1380	2710	0.6	8.9%	100%

Table 3.2: Calculated solids content by mass of waste rocks *C* and mixing degree *S* of small blocks based on direct measurements (continued)

Case 2	Blocks	M_{wr} (kg)	$M_{paste.dried}$ (kg)	ρ_s (kg/m^3)	e_f	C	S
Layer1	M_111	0.0092	0.1347	2710	0.6	6.4%	3085.8%
	M_211	0.0846	0.0679	2710	0.6	55.5%	169.2%
	M_311	0.0791	0.0537	2710	0.6	59.6%	143.1%
	M_411	0.0169	0.1186	2710	0.6	12.5%	1479.1%
	M_121	0.0364	0.1082	2710	0.6	25.2%	626.5%
	M_221	0.1200	0.0000	2710	0.6	100.0%	0.0%
	M_321	0.1290	0.0000	2710	0.6	100.0%	0.0%
	M_421	0.0326	0.1170	2710	0.6	21.8%	756.4%
	M_131	0.0054	0.1333	2710	0.6	3.9%	5202.7%
	M_231	0.0891	0.0672	2710	0.6	57.0%	159.0%
	M_331	0.0943	0.0600	2710	0.6	61.1%	134.2%
	M_431	0.0072	0.1615	2710	0.6	4.3%	4727.5%
Layer 2	M_112	0.0000	0.1346	2710	0.6	0.0%	/
	M_212	0.0101	0.1297	2710	0.6	7.2%	100%
	M_312	0.0044	0.1273	2710	0.6	3.3%	/
	M_412	0.0000	0.1532	2710	0.6	0.0%	/
	M_122	0.0023	0.1588	2710	0.6	1.4%	/
	M_222	0.0707	0.0829	2710	0.6	46.0%	100%
	M_322	0.0716	0.0869	2710	0.6	45.2%	100%
	M_422	0.0038	0.1315	2710	0.6	2.8%	/
	M_132	0.0000	0.1457	2710	0.6	0.0%	/
	M_232	0.0143	0.1602	2710	0.6	8.2%	100%
	M_332	0.0056	0.1407	2710	0.6	3.8%	/
	M_432	0.0000	0.1495	2710	0.6	0.0%	/
Layer 3	M_113	0.0000	0.1380	2710	0.6	0.0%	/
	M_213	0.0002	0.1731	2710	0.6	0.1%	/
	M_313	0.0025	0.1164	2710	0.6	2.1%	/

Table 3.2: Calculated solids content by mass of waste rocks *C* and mixing degree *S* of small blocks based on direct measurements (continued)

Case 2	Blocks	M_{wr} (kg)	$M_{paste.dried}$ (kg)	ρ_s (kg/m^3)	e_f	*C*	*S*
Layer 3	M_413	0.0000	0.1161	2710	0.6	0.0%	/
	M_123	0.0000	0.1390	2710	0.6	0.0%	/
	M_223	0.0367	0.1055	2710	0.6	25.8%	100%
	M_323	0.0347	0.0811	2710	0.6	30.0%	100%
	M_423	0.0000	0.1376	2710	0.6	0.0%	/
	M_133	0.0000	0.1384	2710	0.6	0.0%	/
	M_233	0.0017	0.1361	2710	0.6	1.2%	/
	M_333	0.0017	0.1308	2710	0.6	1.3%	/
	M_433	0.0000	0.0985	2710	0.6	0.0%	/

Table 3.2: Calculated solids content by mass of waste rocks *C* and mixing degree *S* of small blocks based on direct measurements (continued)

Case 3	Blocks	M_{wr} (kg)	$M_{paste.dried}$ (kg)	ρ_s (kg/m^3)	e_f	*C*	*S*
Layer1	M_111	0.0169	0.1341	2710	0.6	11.1%	1672.4%
	M_211	0.1398	0.0814	2710	0.6	63.2%	122.7%
	M_311	0.1399	0.0833	2710	0.6	62.6%	125.5%
	M_411	0.0138	0.1229	2710	0.6	10.1%	1877.0%
	M_121	0.0351	0.0977	2710	0.6	26.4%	586.6%
	M_221	0.1591	0.0000	2710	0.6	100%	0.0%
	M_321	0.1555	0.0000	2710	0.6	100%	0.0%
	M_421	0.0274	0.1038	2710	0.6	20.8%	798.4%
	M_131	0.0123	0.1398	2710	0.6	8.0%	2395.5%
	M_231	0.1399	0.0875	2710	0.6	61.5%	131.9%
	M_331	0.1315	0.0887	2710	0.6	59.7%	142.2%
	M_431	0.0116	0.1462	2710	0.6	7.3%	2656.3%
Layer 2	M_112	0.0000	0.1532	2710	0.6	0.0%	/

Table 3.2: Calculated solids content by mass of waste rocks C and mixing degree S of small blocks based on direct measurements (continued)

Case 3	Blocks	M_{wr} (kg)	$M_{paste.dried}$ (kg)	ρ_s (kg/m^3)	e_f	C	S
Layer 2	M_212	0.0000	0.1334	2710	0.6	0.0%	/
	M_312	0.0000	0.1196	2710	0.6	0.0%	/
	M_412	0.0000	0.1493	2710	0.6	0.0%	/
	M_122	0.0000	0.1224	2710	0.6	0.0%	/
	M_222	0.0133	0.0895	2710	0.6	12.9%	100%
	M_322	0.0193	0.0783	2710	0.6	19.7%	100%
	M_422	0.0000	0.1515	2710	0.6	0.0%	/
	M_132	0.0000	0.1191	2710	0.6	0.0%	/
	M_232	0.0000	0.1318	2710	0.6	0.0%	/
	M_332	0.0000	0.1291	2710	0.6	0.0%	/
	M_432	0.0000	0.1391	2710	0.6	0.0%	/
Layer 3	M_113	0.0000	0.1417	2710	0.6	0.0%	/
	M_213	0.0000	0.1319	2710	0.6	0.0%	/
	M_313	0.0000	0.1323	2710	0.6	0.0%	/
	M_413	0.0000	0.1314	2710	0.6	0.0%	/
	M_123	0.0000	0.1445	2710	0.6	0.0%	/
	M_223	0.0000	0.1320	2710	0.6	0.0%	/
	M_323	0.0000	0.1120	2710	0.6	0.0%	/
	M_423	0.0000	0.1274	2710	0.6	0.0%	/
	M_133	0.0000	0.1344	2710	0.6	0.0%	/
	M_233	0.0000	0.1323	2710	0.6	0.0%	/
	M_333	0.0000	0.1402	2710	0.6	0.0%	/
	M_433	0.0000	0.1479	2710	0.6	0.0%	/

Table 3.2: Calculated solids content by mass of waste rocks *C* and mixing degree *S* of small blocks based on direct measurements (continued)

Case 4	Blocks	M_{wr} (kg)	$M_{paste.dried}$ (kg)	ρ_s (kg/m^3)	e_f	*C*	*S*
Layer1	M_111	0.0034	0.1445	2710	0.6	2.3%	/
	M_211	0.0232	0.0908	2710	0.6	20.3%	806.1%
	M_311	0.0230	0.0916	2710	0.6	20.0%	820.2%
	M_411	0.0066	0.1199	2710	0.6	5.2%	/
	M_121	0.0125	0.1276	2710	0.6	8.9%	2102.4%
	M_221	0.1380	0.0133	2710	0.6	91.2%	19.8%
	M_321	0.1236	0.0074	2710	0.6	94.3%	12.3%
	M_421	0.0189	0.1276	2710	0.6	12.9%	1390.5%
	M_131	0.0012	0.1515	2710	0.6	0.7%	/
	M_231	0.0202	0.0815	2710	0.6	19.8%	831.0%
	M_331	0.0170	0.0710	2710	0.6	19.3%	860.2%
	M_431	0.0023	0.1447	2710	0.6	1.5%	/
Layer 2	M_112	0.0000	0.1416	2710	0.6	0.0%	/
	M_212	0.0082	0.1218	2710	0.6	6.3%	100%
	M_312	0.0253	0.1142	2710	0.6	18.1%	100%
	M_412	0.0000	0.1394	2710	0.6	0.0%	/
	M_122	0.0000	0.1181	2710	0.6	0.0%	/
	M_222	0.0646	0.0646	2710	0.6	50.0%	100%
	M_322	0.0685	0.0590	2710	0.6	53.7%	100%
	M_422	0.0049	0.1349	2710	0.6	3.5%	/
	M_132	0.0000	0.1194	2710	0.6	0.0%	/
	M_232	0.0169	0.1110	2710	0.6	13.2%	100%
	M_332	0.0117	0.1117	2710	0.6	9.4%	100%
	M_432	0.0000	0.0950	2710	0.6	0.0%	/
Layer 3	M_113	0.0000	0.1448	2710	0.6	0.0%	/
	M_213	0.0046	0.1368	2710	0.6	3.2%	/
	M_313	0.0108	0.1383	2710	0.6	7.2%	100%

Table 3.2: Calculated solids content by mass of waste rocks C and mixing degree S of small blocks based on direct measurements (continued)

Case 4	Blocks	M_{wr} (kg)	$M_{paste.dried}$ (kg)	ρ_s (kg/m^3)	e_f	C	S
Layer 3	M_413	0.0000	0.1655	2710	0.6	0.0%	/
	M_123	0.0022	0.1449	2710	0.6	1.5%	/
	M_223	0.0976	0.0869	2710	0.6	52.9%	100%
	M_323	0.0822	0.0821	2710	0.6	50.0%	100%
	M_423	0.0010	0.1472	2710	0.6	0.6%	/
	M_133	0.0000	0.1691	2710	0.6	0.0%	/
	M_233	0.0336	0.1399	2710	0.6	19.3%	100%
	M_333	0.0255	0.1418	2710	0.6	15.2%	100%
	M_433	0.0000	0.1584	2710	0.6	0.0%	/

Table 3.2: Calculated solids content by mass of waste rocks C and mixing degree S of small blocks based on direct measurements (continued)

Case 5	Blocks	M_{wr} (kg)	$M_{paste.dried}$ (kg)	ρ_s (kg/m^3)	e_f	C	S
Layer1	M_111	0.0042	0.1258	2710	0.6	3.2%	/
	M_211	0.0395	0.0751	2710	0.6	34.4%	391.6%
	M_311	0.0375	0.0627	2710	0.6	37.4%	344.4%
	M_411	0.0046	0.1236	2710	0.6	3.5%	/
	M_121	0.0116	0.1125	2710	0.6	9.3%	100%
	M_221	0.0855	0.0169	2710	0.6	83.5%	40.7%
	M_321	0.0841	0.0127	2710	0.6	86.8%	31.1%
	M_421	0.0101	0.0996	2710	0.6	9.2%	100%
	M_131	0.0000	0.1181	2710	0.6	0.0%	/
	M_231	0.0326	0.1105	2710	0.6	22.7%	698.1%
	M_331	0.0247	0.1062	2710	0.6	18.8%	885.5%
	M_431	0.0009	0.1447	2710	0.6	0.6%	/
Layer 2	M_112	0.0000	0.1339	2710	0.6	0.0%	/
	M_212	0.0342	0.1083	2710	0.6	24.0%	100%

Table 3.2: Calculated solids content by mass of waste rocks C and mixing degree S of small blocks based on direct measurements (continued)

Case 5	Blocks	M_{wr} (kg)	$M_{paste.dried}$ (kg)	ρ_s (kg/m^3)	e_f	C	S
Layer 2	M_312	0.0454	0.1071	2710	0.6	29.7%	100%
	M_412	0.0022	0.1420	2710	0.6	1.5%	/
	M_122	0.0078	0.1087	2710	0.6	6.7%	/
	M_222	0.0958	0.0371	2710	0.6	72.0%	80%
	M_322	0.0950	0.0400	2710	0.6	70.3%	86.7%
	M_422	0.0014	0.1336	2710	0.6	1.0%	/
	M_132	0.0000	0.1157	2710	0.6	0.0%	/
	M_232	0.0352	0.1299	2710	0.6	21.3%	100%
	M_332	0.0380	0.1338	2710	0.6	22.1%	100%
	M_432	0.0000	0.1121	2710	0.6	0.0%	/
Layer 3	M_113	0.0000	0.1591	2710	0.6	0.0%	/
	M_213	0.0103	0.1309	2710	0.6	7.2%	100%
	M_313	0.0215	0.1337	2710	0.6	13.8%	100%
	M_413	0.0000	0.1704	2710	0.6	0.0%	/
	M_123	0.0000	0.1535	2710	0.6	0.0%	/
	M_223	0.0787	0.0894	2710	0.6	46.8%	100%
	M_323	0.0768	0.0821	2710	0.6	48.3%	100%
	M_423	0.0104	0.1518	2710	0.6	6.4%	100%
	M_133	0.0000	0.1490	2710	0.6	0.0%	/
	M_233	0.0317	0.1677	2710	0.6	15.9%	100%
	M_333	0.0320	0.1354	2710	0.6	19.1%	100%
	M_433	0.0000	0.1678	2710	0.6	0.0%	/

Table 3.2: Calculated solids content by mass of waste rocks C and mixing degree S of small blocks based on direct measurements (continued)

Case 6	Blocks	M_{wr} (kg)	$M_{paste.dried}$ (kg)	ρ_s (kg/m^3)	e_f	C	S
Layer1	M_111	0.0034	0.1170	2710	0.6	2.8%	/
	M_211	0.0354	0.0669	2710	0.6	34.6%	389.2%
	M_311	0.0379	0.0714	2710	0.6	34.6%	388.0%
	M_411	0.0034	0.1110	2710	0.6	2.9%	/
	M_121	0.0054	0.1007	2710	0.6	5.0%	/
	M_221	0.1200	0.0283	2710	0.6	80.9%	48.6%
	M_321	0.0880	0.0209	2710	0.6	80.8%	48.9%
	M_421	0.0052	0.1150	2710	0.6	4.3%	/
	M_131	0.0030	0.1191	2710	0.6	2.4%	/
	M_231	0.0444	0.0699	2710	0.6	38.8%	324.2%
	M_331	0.0485	0.0691	2710	0.6	41.2%	293.4%
	M_431	0.0064	0.1512	2710	0.6	4.0%	/
Layer 2	M_112	0.0000	0.1404	2710	0.6	0.0%	/
	M_212	0.0044	0.1236	2710	0.6	3.4%	/
	M_312	0.0063	0.1316	2710	0.6	4.5%	/
	M_412	0.0000	0.1423	2710	0.6	0.0%	/
	M_122	0.0001	0.1199	2710	0.6	0.08%	/
	M_222	0.0650	0.0628	2710	0.6	50.8%	100%
	M_322	0.0670	0.0666	2710	0.6	50.1%	100%
	M_422	0.0038	0.1239	2710	0.6	2.9%	/
	M_132	0.0000	0.1187	2710	0.6	0.0%	/
	M_232	0.0017	0.1284	2710	0.6	1.3%	/
	M_332	0.0026	0.1130	2710	0.6	2.2%	/
	M_432	0.0000	0.1166	2710	0.6	0.0%	/
Layer 3	M_113	0.0017	0.1704	2710	0.6	0.9%	/
	M_213	0.0380	0.1365	2710	0.6	21.7%	100%
	M_313	0.0454	0.1634	2710	0.6	21.7%	100%

Table 3.2: Calculated solids content by mass of waste rocks *C* and mixing degree *S* of small blocks based on direct measurements (continued)

Case 6	Blocks	M_{wr} (kg)	$M_{paste.dried}$ (kg)	ρ_s (kg/m^3)	e_f	C	S
Layer 3	M_413	0.0015	0.1928	2710	0.6	0.7%	/
	M_123	0.0069	0.1523	2710	0.6	4.3%	/
	M_223	0.1161	0.1028	2710	0.6	53.0%	100%
	M_323	0.1200	0.1197	2710	0.6	50.0%	100%
	M_423	0.0052	0.1698	2710	0.6	2.9%	/
	M_133	0.0050	0.1457	2710	0.6	3.3%	/
	M_233	0.0413	0.1379	2710	0.6	23.0%	100%
	M_333	0.0408	0.1611	2710	0.6	20.2%	100%
	M_433	0.0002	0.1874	2710	0.6	0.1%	/

Table 3.2: Calculated solids content by mass of waste rocks *C* and mixing degree *S* of small blocks based on direct measurements (continued)

Case 7	Blocks	M_{wr} (kg)	$M_{paste.dried}$ (kg)	ρ_s (kg/m^3)	e_f	C	S
Layer1	M_111	0.0008	0.1563	2710	0.6	0.5%	/
	M_211	0.0027	0.1252	2710	0.6	2.1%	/
	M_311	0.0034	0.0901	2710	0.6	3.6%	/
	M_411	0.0027	0.1387	2710	0.6	1.9%	/
	M_121	0.0003	0.1382	2710	0.6	0.2%	/
	M_221	0.0327	0.1332	2710	0.6	19.7%	100%
	M_321	0.0300	0.1163	2710	0.6	20.5%	100%
	M_421	0.0008	0.0980	2710	0.6	0.8%	/
	M_131	0.0001	0.1205	2710	0.6	0.08%	/
	M_231	0.0002	0.1192	2710	0.6	0.1%	/
	M_331	0.0001	0.1038	2710	0.6	0.1%	/
	M_431	0.0001	0.1172	2710	0.6	0.09%	/

Table 3.2: Calculated solids content by mass of waste rocks *C* and mixing degree *S* of small blocks based on direct measurements (continued)

Case 7	Blocks	M_{wr} (kg)	$M_{paste.dried}$ (kg)	ρ_s (kg/m^3)	e_f	C	S
Layer 2	M_112	0.0240	0.1011	2710	0.6	19.1%	/
	M_212	0.0165	0.0970	2710	0.6	14.5%	100%
	M_312	0.0215	0.0948	2710	0.6	18.4%	100%
	M_412	0.0248	0.1231	2710	0.6	16.7%	100%
	M_122	0.0067	0.1008	2710	0.6	6.2%	100%
	M_222	0.0535	0.0970	2710	0.6	35.5%	100%
	M_322	0.0544	0.0948	2710	0.6	36.4%	100%
	M_422	0.0121	0.1422	2710	0.6	7.8%	100%
	M_132	0.0162	0.1238	2710	0.6	11.5%	100%
	M_232	0.0135	0.1162	2710	0.6	10.4%	100%
	M_332	0.0200	0.1148	2710	0.6	14.8%	100%
	M_432	0.0220	0.1204	2710	0.6	15.4%	100%
Layer 3	M_113	0.0201	0.1250	2710	0.6	13.8%	100%
	M_213	0.0176	0.0768	2710	0.6	18.6%	100%
	M_313	0.0167	0.0821	2710	0.6	16.9%	100%
	M_413	0.0281	0.1421	2710	0.6	16.5%	100%
	M_123	0.0269	0.1137	2710	0.6	19.1%	100%
	M_223	0.2011	0.1134	2710	0.6	63.9%	100%
	M_323	0.1810	0.1021	2710	0.6	63.9%	100%
	M_423	0.0234	0.1341	2710	0.6	14.8%	100%
	M_133	0.0300	0.2235	2710	0.6	11.8%	100%
	M_233	0.0185	0.1118	2710	0.6	14.2%	100%
	M_333	0.0358	0.1671	2710	0.6	17.6%	100%
	M_433	0.0225	0.1996	2710	0.6	10.1%	100%

3.7 Appendix II: Estimation of the mass of pure paste backfill in the blocks around the interfaces

In the tests, the mixtures were cut into small blocks with the same size. It was noted that the small blocks along the interfaces between waste rocks and paste backfill are too large, as shown in Figure 3.20. Pure paste backfill (not mixed with any waste rocks) outside of interfaces were artificially added to the parts of mixture, resulting in the mass and portion of mixture inside the interfaces were diluted. Subsequently, the solids contents by mass of waste rocks *C* and the mixing degree *S* based on the direct measurements and calculations presented in Table 3.2 of Appendix I can be very inaccurate, especially around the interfaces between the waste rock and paste backfill.

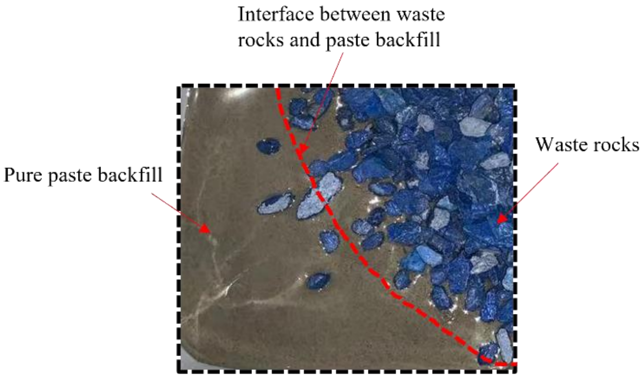

Figure 3.20: Photo of a small block along the interface between waste rocks and paste backfill

In this study, corrections were made by excluding the mass of pure paste backfill $M'_{paste.dried}$, estimated based on observation of pictures, as shown in Figure 3.21. The solids contents by mass of waste rocks and the mixing degree of the mixture based on these corrections are presented in Table 3.3.

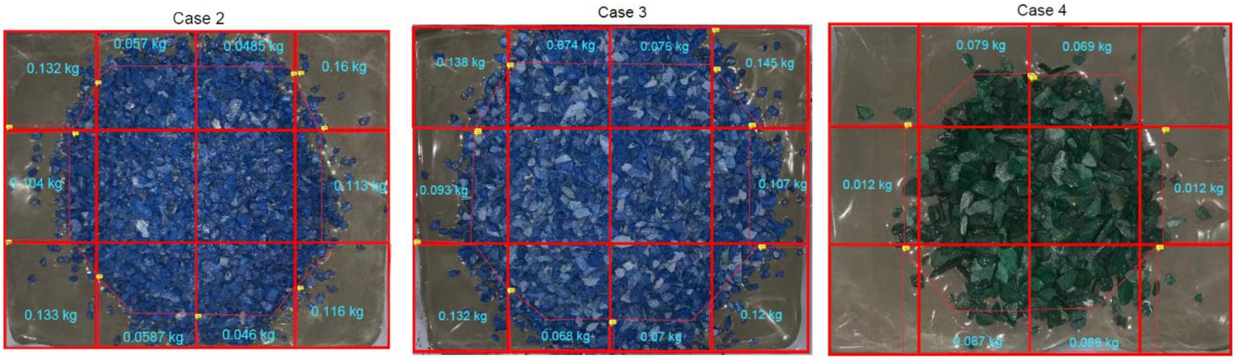

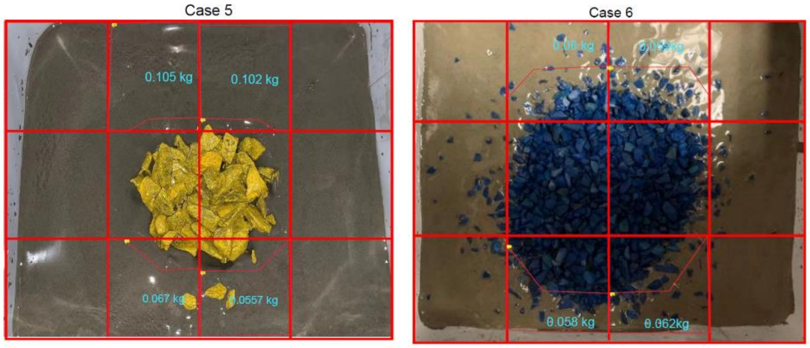

Figure 3.21: Estimation of the mass of pure paste backfill in each block at layer 1

Table 3.3: Corrections of the solids content by mass of waste rocks *C* and mixing degree *S* of the blocks

Case 2	Blocks	M'_{paste} (kg)	$M'_{paste.dried}$ (kg)	$M_{paste.dried}$ (kg)	C	S
Layer 1	M_111	0.185	0.1338	0.0009	91.2%	20%
	M_211	0.081	0.0587	0.0092	90.2%	23%
	M_311	0.063	0.0460	0.0077	91.1%	21%
	M_411	0.161	0.1169	0.0017	90.6%	22%
	M_121	0.144	0.1047	0.0035	91.2%	20%
	M_421	0.157	0.1139	0.0031	91.3%	20%
	M_131	0.183	0.1328	0.0005	91.4%	20%
	M_231	0.080	0.0577	0.0095	90.3%	22%
	M_331	0.067	0.0485	0.0115	89.1%	26%
	M_431	0.222	0.1606	0.0009	89.2%	25%

Table 3.3: Corrections of the solids content by mass of waste rocks *C* and mixing degree *S* of the blocks (continued)

Case 3	Blocks	M'_{paste} (kg)	$M'_{paste.dried}$ (kg)	$M_{paste.dried}$ (kg)	C	S
Layer 1	M_111	0.176	0.1320	0.0021	89.1%	26%
	M_211	0.091	0.0682	0.0132	91.3%	20%
	M_311	0.094	0.0703	0.0130	91.5%	20%
	M_411	0.162	0.1213	0.0016	89.6%	24%
	M_121	0.125	0.0939	0.0038	90.2%	23%
	M_421	0.134	0.1007	0.0031	89.8%	24%
	M_131	0.184	0.1384	0.0014	89.5%	25%
	M_231	0.099	0.0745	0.0130	91.4%	20%
	M_331	0.102	0.0763	0.0124	91.4%	20%
	M_431	0.193	0.1450	0.0012	90.3%	22%

Table 3.3: Corrections of the solids content by mass of waste rocks *C* and mixing degree *S* of the blocks (continued)

Case 4	Blocks	M'_{paste} (kg)	$M'_{paste.dried}$ (kg)	$M_{paste.dried}$ (kg)	C	S
Layer 1	M_211	0.121	0.0879	0.0029	88.7%	26%
	M_311	0.122	0.0888	0.0028	89.2%	25%
	M_121	0.174	0.1262	0.0014	89.6%	24%
	M_421	0.173	0.1251	0.0025	88.4%	27%
	M_231	0.109	0.0792	0.0023	89.6%	24%
	M_331	0.095	0.0690	0.0020	89.2%	25%

Table 3.3: Corrections of the solids content by mass of waste rocks *C* and mixing degree *S* of the blocks (continued)

Case 5	Blocks	M'_{paste} (kg)	$M'_{paste.dried}$ (kg)	$M_{paste.dried}$ (kg)	*C*	*S*
Layer 1	M_211	0.094	0.0679	0.0072	84.6%	37%
	M_311	0.077	0.0557	0.0070	84.2%	39%
	M_231	0.145	0.1052	0.0053	86.0%	33%
	M_331	0.141	0.1022	0.0040	85.9%	34%

Table 3.3: Corrections of the solids content by mass of waste rocks *C* and mixing degree *S* of the blocks (continued)

Case 6	Blocks	M'_{paste}(kg)	$M'_{paste.dried}$(kg)	$M_{paste.dried}$(kg)	*C*	*S*
Layer 1	M_211	0.081	0.0587	0.0082	81.2%	47%
	M_311	0.086	0.0626	0.0088	81.1%	48%
	M_231	0.083	0.0605	0.0094	82.5%	43%
	M_331	0.082	0.0598	0.0093	83.8%	40%

Acknowledgments

The authors acknowledge the financial support from the Natural Sciences and Engineering Research Council of Canada (NSERC RGPIN-2018-06902), Natural Sciences and Engineering Research Council of Canada (NSERC ALLRP 580767 - 22), Fonds de recherche du Québec – Nature et technologies (FRQNT 2017-MI-202860), Mitacs Elevate Postdoctoral Fellowship (IT12569), and industrial partners of the Research Institute on Mines and the Environment (RIME UQAT – Polytechnique; http://rime-irme.ca).

References

Aubertin, M, 2013, ‘Waste rock disposal to improve the geotechnical and geochemical stability of piles’, paper presented at the 23rd World Mining Congress (WMC 2013), Montréal, pp. 8.

Aubertin, M, Li, L, Arnoldi, S, Belem, T, Bussière, B, Benzaazoua, M & Simon, R 2003, ‘Interaction between backfill and rock mass in narrow stopes’, *Soil and rock America*, vol. 1, no. 2, pp. 1157-1164.

Dalcé, JB, Li, L & Yang, P 2019, ‘Experimental study of uniaxial compressive strength (UCS) distribution of hydraulic backfill associated with segregation’, *Minerals*, vol. 9, no. 3, pp. 147.

Elimelech, M., Gregory, J., Jia, X., & Williams, R. A. (1995). ‘Chapter 4 - Colloidal hydrodynamics and transport’, in M. Elimelech, J. Gregory, X. Jia, & R. A. Williams (Eds.), *Particle Deposition & Aggregation*, pp. 68-109.

El Mkadmi, N, Aubertin, M & Li, L 2014, ‘Effect of drainage and sequential filling on the behaviour of backfill in mine stopes’, *Canadian Geotechnical Journal*, vol. 51, no. 1, pp. 1-15.

Hassani, F & Archibald, J 1998, *Mine Backfill*, Canadian Institute of Mining, Metallurgy and Petroleum, Montreal.

Henning, J, 2007. *Evaluation of Long-Hole Mine Design Influences on Unplanned Ore Dilution*, Ph.D. thesis, McGill University.

Jaouhar, E M & Li, L 2019, ‘Effect of drainage and consolidation on the pore water pressures and total stresses within backfilled stopes and on barricades’, *Advances in Civil Engineering*, vol. 2019, pp. 1-19.

Jaouhar, E M, Li, L & Aubertin, M 2018, ‘An analytical solution for estimating the stresses in vertical backfilled stopes based on a circular arc distribution’, *Geomechanics and Engineering*, vol. 15, no. 3, pp. 889-898.

Keita, A M T, Jahanbakhshzadeh, A & Li, L 2021a, ‘Numerical analysis of the stability of arched sill mats made of cemented backfill’, *International Journal of Rock Mechanics and Mining Sciences*, vol. 140, no. 4, article 104667.

Keita, A M T, Jahanbakhshzadeh, A & Li, L 2021b, ‘Numerical analysis of the failure mechanisms of sill mats made of cemented backfill’, *International Journal of Geotechnical Engineering*, vol. 16, no. 7, pp. 802-814.

Kuganathan, K & Sheppard, I 2001, ‘A non-segregating ‘rocky paste fill’ (RPF) produced by co-disposal of cemented de-slimed tailings slurry and graded rockfill’, in D Stone (ed.), *Proceedings of the Seventh International Symposium on Mining with Backfill*, Society for Mining, Metallurgy and Exploration, Englewood, pp. 27–41.

Lee, C & Gu, F 2017, ‘An examination of improvements in co-disposal of waste rock with backfill’, in A Wu & R Jewell (eds), *Paste 2017: Proceedings of the 20th International Seminar on Paste and Thickened Tailings*, University of Science and Technology Beijing, Beijing, pp. 338-345.

Li, L 2014a, ‘Analytical solution for determining the required strength of a side-exposed mine backfill containing a plug’, *Canadian Geotechnical Journal*, vol. 51, no. 5, pp. 508-519.

Li, L 2014b, ‘Generalized solution for mining backfill design’, *International Journal of Geomechanics*, vol. 14, no. 3, article 04014006.

Li, L & Aubertin, M 2012, ‘A modified solution to assess the required strength of exposed backfill in mine stopes’, *Canadian Geotechnical Journal*, vol. 49, no. 8, pp. 994-1002.

Li, L & Aubertin, M 2014, ‘An improved method to assess the required strength of cemented backfill in underground stopes with an open face’, *International Journal of Mining Science and Technology*, vol. 24, no. 4, pp. 549-558.

Li, L, Aubertin, M & Belem, T 2005, ‘Formulation of a three-dimensional analytical solution to evaluate stresses in backfilled vertical narrow openings’, *Canadian Geotechnical Journal*, vol. 42, no. 6, pp. 1705-1717.

Li, L, Aubertin, M, Simon, R, Bussière, B & Belem, T 2003, ‘Modeling arching effects in narrow backfilled stopes with FLAC’, in R Brummer, P Andrieux, C Detournay & R Hart (eds), *Proceedings of 3rd international symposium on FLAC and FLAC3D numerical modelling in geomechanics*, A. A. Balkema, a member of Swets & Zeitlinger Publishers, Sudbury, pp. 211–219.

Liu, G, Li, L, Yang, X & Guo, L 2017a, ‘Numerical analysis of stress distribution in backfilled stopes considering interfaces between the backfill and rock walls’, *International Journal of Geomechanics*, vol. 17, no. 2, article 06016014.

Liu, G, Li, L, Yang, X & Guo, L 2018, ‘Required strength estimation of a cemented backfill with the front wall exposed and back wall pressured’, *International Journal of Mining and Mineral Engineering*, vol. 9, no. 1, pp. 1-20.

Liu, G, Li, L, Yao, M, Landry, D, Malek, F, Yang, X & Guo, L 2017b, ‘An investigation of the uniaxial compressive strength of a cemented hydraulic backfill made of alluvial sand’, *Minerals*, vol. 7, no. 1, pp. 4.

Pagé, P, Li, L, Yang, P & Simon, R 2019, ‘Numerical investigation of the stability of a base-exposed sill mat made of cemented backfill’, *International Journal of Rock Mechanics and Mining Sciences*, vol. 114, no. 2, pp. 195-207.

Potvin, Y, Thomas, E, & Fourie, A 2005, *Handbook on Mine Fill*, Australian Centre for Geomechanics, Perth.

Qin, J, Zheng, J & Li, L 2021a, ‘An analytical solution to estimate the settlement of tailings or backfill slurry by considering the sedimentation and consolidation’, *International Journal of Mining Science and Technology*, vol. 31, no. 3, pp. 463-471.

Qin, J, Zheng, J & Li, L 2021b, ‘Experimental study of the shrinkage behaviour of cemented paste backfill’, *Journal of Rock Mechanics and Geotechnical Engineering*, vol. 13, no. 3, pp. 545-554.

Qiu, H, Zhang, F, Liu, L, H, D & T, B 2020, ‘Influencing factors on strength of waste rock tailing cemented backfill’. *Geofluids*, pp. 1-7.

Qiu, H, Zhang, F, Sun, W, Liu, L, Zhao, Y & Huan, C 2022, ‘Experimental study on strength and permeability characteristics of cemented rock-tailings backfill’. *Frontiers in Earth Science*.

Saleh-Mbemba, F., Aubertin, M., Mbonimpa, M 2016, ‘Experimental characterization of the shrinkage and water retention behaviour of tailings from hard rock mines’, *Geotechnical and Geological Engineering*, vol. 34, pp. 251–266.

Sobhi, MA & Li, L 2017, ‘Numerical investigation of the stresses in backfilled stopes overlying a sill mat’, *Journal of Rock Mechanics and Geotechnical Engineering*, vol. 9, no. 3, pp. 490-501.

Sobhi, MA, Li, L & Aubertin, M 2017, ‘Numerical investigation of earth pressure coefficient along central line of backfilled stopes’, *Canadian Geotechnical Journal,* vol. 54, no. 1, pp. 138-145.

Veenstra, RL & Grobler, JJ 2021, ‘Paste-waste design and implementation at Newmont Goldcorp’s Tanami Operation’, in F Hassani, J Palarski, V Sokoła-Szewioła & G Strozik (eds), *Minefill 2020-2021: Proceedings of the 13th International Symposium on Mining with Backfill*, CRC Press, Katowice, pp. 382-397.

Wang, R & Li, L 2022, ‘Time-dependent stability analyses of side-exposed backfill considering creep of surrounding rock mass’, *Rock Mechanics and Rock Engineering*, vol. 55, no. 4, pp. 2255-2279.

Wang, R, Zeng, F & Li, L 2021a, ‘Applicability of constitutive models to describing the compressibility of mining backfill: a comparative study’, *Processes*, vol. 9, no. 12, article 2139.

Wang, R, Zeng, F & Li, L 2021b, ‘Stability analyses of side-exposed backfill considering mine depth and extraction of adjacent stope’, *International Journal of Rock Mechanics and Mining Sciences*, vol. 142, no. 6, article 104735.

Wickland, BE & Wilson, GW 2005, ‘Self-weight consolidation of mixtures of mine waste rock and tailings’, *Canadian Geotechnical Journal*, vol. 42, no. 2, pp. 327-339.

Wilson, G 2001, ‘Co-disposal of tailings and waste rock’, *Geotechnical News*, vol. 19, no. 2, pp. 44-49.

Wilson, GW, Wickland, B & Miskolczi, J 2008, ‘Design and performance of paste rock systems for improved mine waste management’, in AB Fourie (ed.), *Rock Dumps 2008: Proceedings of the First International Seminar on the Management of Rock Dumps, Stockpiles and Heap Leach Pads*, Australian Centre for Geomechanics, Perth, pp. 107-116.

Yan, B, Zhu, W, Hou, C, Yilmaz, E, & Saadat, M 2020. ‘Characterization of early age behavior of cemented paste backfill through the magnitude and frequency spectrum of ultrasonic P-wave’, *Construction and Building Materials*, 249, 118733.

Yan, B, Jia, H, Yilmaz, E, Lai, X, Shan, P, & Hou, C 2022a. ‘Numerical investigation of creeping rockmass interaction with hardening and shrinking cemented paste backfill’, *Construction and Building Materials*, 340, 127639.

Yan, B, Jia, H, Yilmaz, E, Lai, X, Shan, P, & Hou, C 2022b. ‘Numerical study on microscale and macroscale strength behaviors of hardening cemented paste backfill’, *Construction and Building Materials*, 321, 126327.

Yang, P, Li, L & Aubertin, M 2018, ‘Theoretical and numerical analyses of earth pressure coefficient along the centreline of vertical openings with granular fills’, *Applied Sciences*, vol. 8, no. 10, article 1721.

Yang, P, Li, L, Aubertin, M, Brochu-Baekelmans, M & Ouellet, S 2017, ‘Stability analyses of waste rock barricades designed to retain paste backfill’, *International Journal of Geomechanics*, vol. 17, no. 3, article 04016079.

Zhai, Y, Yang, P & Li, L 2021, ‘Analytical solutions for the design of shotcreted waste rock barricades to retain slurried paste backfill’, *Construction and Building Materials*, vol. 307, article 124626.

Zheng, J & Li, L 2020, ‘Experimental study of the “short-term” pressures of uncemented paste backfill with different solid contents for barricade design’, *Journal of Cleaner Production*, vol. 275, article 123068.

Zheng, J, Li, L & Li, Y 2019, ‘Total and effective stresses in backfilled stopes during the fill placement on a pervious base for barricade design’, *Minerals*, vol. 9, no. 1, pp. 38.

Zheng, J, Li, L & Li, Y 2020a, ‘A solution to estimate the total and effective stresses in backfilled stopes with an impervious base during the filling operation of cohesionless backfill’, *International Journal for Numerical and Analytical Methods in Geomechanics*, vol. 44, no. 11, pp. 1570-1586.

Zheng, J, Li, L & Li, Y 2020b, ‘Solutions to estimate the excess PWP, settlement and volume of draining water after slurry deposition. Part I: impervious base’, *Environmental Earth Sciences*, vol. 79, no. 6, article 124 (2020).

Zheng, J, Li, L & Li, Y 2020c, ‘Solutions to estimate the excess PWP, settlement and volume of draining water after slurry deposition. Part II: pervious base’, *Environmental Earth Sciences*, vol. 79, no. 11, article 275 (2020).

CHAPTER 4 ARTICLE 2: INTRODUCTION AND IMPLEMENTATION OF FLUID FORCES IN A DEM CODE FOR SIMULATING PARTICLE SETTLEMENT IN FLUIDS

Yuyu Zhang and Li Li

The article has been published in *Powder Technology*, Volume 433, 2024, 19238, https://doi.org/10.1016/j.powtec.2023.119238.

Abstract:

Simulations of a problem involving particles and fluid usually require coupling a discrete element method (DEM) with computational fluid dynamics (CFD) or smoothed particle hydrodynamics (SPH). The former suffers from the accuracy or even reliability problem induced by mesh size while the latter suffers from small size model and high computation time and cost. To overcome part of these problems, fluid forces have been formulated and directly implemented in a DEM code, resulting in a new model, named f-EDEM. Using this model, the settlement of particles in a fluid can be simulated by a single DEM code without the need of coupling with a CFD or SPH solver. In this study, the formulation and implementation of fluid forces into the DEM code are presented. The proposed f-EDEM model is first validated against an analytical solution. The applicability and ability of the f-EDEM model are examined by reproducing and predicting some laboratory results. The comparisons between the numerical, analytical and experimental results indicate that the f-EDEM model is successfully validated and has the required capacity for simulating the settlement of single and multiple particles in both Newtonian and some of non-Newtonian (Bingham plastic) fluids. The results also indicate that the time step recommended by most DEM manuals can be excessively small, resulting in a high computational cost. It is thus necessary to perform sensitivity analysis of time steps to obtain an optimal numerical model, which ensures stable and reliable numerical result with the shortest time of computation.

Keywords: Discrete element method (DEM); Particle settlement; Bingham plastic fluids; Fluid forces.

4.1 Introduction

Particle settlement in fluids is a phenomenon frequently encountered in several domains, such as mineral slurries, debris flows, natural muds, landslides, and lava flows (Bokharaeian et al., 2021;

Nguyen et al., 2021). Understanding and quantifying the particles settlement is thus necessary for the design and control of such systems. Obviously, this would be extremely difficult, if not totally impossible through analytical solution due to the large number of particles and the extremely complex interactions between particles and particles as well as between particles and fluid. Alternatively, numerical modeling can be considered as a versatile way to evaluate the interaction between particles and fluid.

There are two major numerical approaches that can be employed to simulate the movement of particles in fluids. The first one couples discrete element method (DEM) with computational fluid dynamics (CFD) method. The movement of an individual particle is explicitly tracked by solving the Newton's second law using DEM (Cundall & Strack, 1979), while the flow of fluid is described by the Navier-Stokes equation in CFD (Fonceca Junior et al., 2021; Jajcevic et al., 2013; Tsuji et al., 1993; Zhao & Shan, 2013). The fluid related forces such as drag and buoyance forces are calculated by the CFD solver and then taken as input parameters for the DEM code. This approach has been applied to simulate gas-solid fluidization, pneumatic conveying, cyclones and pipeline flow (Picabea et al., 2022; Zhao & Shan, 2013; Zhu et al., 2008). The approach (un-resolved DEM-CFD method), however, can become problematic with large size particles because the CFD mesh size must be larger than the maximum diameter of particles (Casarin et al., 2022; Ferreira et al., 2023; Kloss et al., 2012; Peng et al., 2014; Zhang & Yin, 2018). The requirement may result in overly coarse CFD meshes when simulating particles containing very large ones. The accuracy reduces and the numerical results can become unreliable. Moreover, the strong interaction processes (e.g., transport fluid forces from CFD to DEM) between the two codes can sometimes contribute to numerical instabilities (Casarin et al., 2022). In addition, for a simple one-way simulation (only the fluid affects the flow of particles), the velocity fields data calculated by the CFD solver can be imported into some DEM codes. This allows the movement of particles induced by the fluid to be captured in DEM but does not necessarily require coupling the two codes at the same time. At current state, several commercial DEM codes can support this approach to different levels of complexity (e.g., Altair EDEM, Ansys Rocky, ThreeParticle).

The second approach is to couple DEM with the smoothed particle hydrodynamics (SPH) method. SPH is a mesh-free method, in which the fluid is discretized into a set of particles (Gingold & Monaghan, 1977; Platzer & Fimbinger, 2021) to simulate complicated free-surface flow and splashing without any problem of convergences (Cleary & Prakash, 2004; Cleary et al., 2006; He et al., 2018; Moreira et al., 2020; Peng et al., 2021; Robb et al., 2016; Wu et al., 2020). The coupled DEM-SPH method has thus been majorly used to simulate the free flows, such as debris flows, landslides and dam breaks (Cleary, 2015; Robinson et al., 2013; Trujillo-Vela et al., 2020; Zhou & Li, 2022). However, application of coupled DEM-SPH method is limited to small scale engineering problems due to the extremely high computational time and costs. In each simulation step of SPH method, the neighboring particles must be searched and their effects on the current particle must be taken into account. Such search and update calculations require enormous computation time when simulating the fluid represented by large quantities of particles (Domínguez et al., 2021; Ohno et al., 2017; Park et al., 2020; Valdez-Balderas et al., 2013). Once the SPH solver needs to be coupled with DEM, the calculation time can further increase significantly due to the additional particles associated with the DEM code.

The previous analysis on existing numerical methods elucidates that coupling two different numerical codes may suffer from a problem of numerical stability/reliability or from a problem of computation time/cost when dealing with the movement of particles in a fluid. In order to overcome (at least partly) these problems, a new component has been developed and implemented on a commercialized DEM code, after taking into account the drag and buoyance forces of fluid. The settlement of particles in both Newtonian and some non-Newtonian (e.g., Bingham plastic) fluids can thus be simulated using a single DEM code without any need of coupling with a CFD or SPH solver. In this study, the development is presented. The developed numerical model is validated against an analytical solution. The applicability and power of the numerical model is tested by the reproduction and prediction of experimental results.

4.2 Governing equations and forces

In this study, a DEM based commercial software, named Altair EDEM was used for numerical simulations. In DEM code, the translational and rotational accelerations of a particle are ruled by Newton’s second law. The velocity and position of an individual particle are calculated and updated through numerical integration over a considered time step. The governing equation, which controls the movement of a particle in a fluid, is expressed as the following equation based on the DEM theory proposed by Cundall & Strack (1979):

$$m\frac{v}{dt} = F_g + F_c + F_f \tag{4.1}$$

where m and v are the mass and translational velocity of the particle, respectively; t is time; F_g is the gravitational force; F_c is the contact force between particles; F_f are the fluid forces acting on the particles (presented later).

The rotation motion of a particle is described as follows (Cundall & Strack, 1979):

$$I\frac{dw}{dt} = M \tag{4.2}$$

where I is the moment of inertia, w is the angular velocity, M is the contact torque acting on a particle.

The gravity force, F_g, acting on a spherical particle is expressed as follows:

$$F_g = \frac{1}{6}\pi\rho_p d^3 g \tag{4.3}$$

where ρ_p is the density of particle, d is the diameter of particle, g is the acceleration of gravity.

The contact forces, F_c, between particles are determined based on Hertz-Mindin (H-M) contact model due to its accuracy and efficiency in contact force calculations (Hertz, 1882; Mindlin, 1949). Particles are assumed to be rigid. Small overlaps are allowed to represent particle deformations during collisions. By using contact detection algorithms, the accelerations, velocities and positions of particles can be calculated using Newton's second laws of motion. More details on contact forces of the H-M model can be found in many references (e.g., Capozzi et al., 2019; Dhaouadi et al., 2021; Salamat & Genç, 2023).

In DEM code, the gravity force and contact force have often been taken into account and built in, whereas the fluid forces, F_f (in Equation 4.1), are not incorporated because the fluid is not considered. In this study, interaction between particles and fluid are concerned and the fluid forces are taken into account by considering buoyance force and drag force.

The buoyance force F_b (N) acting on a spherical particle fully submerged in a fluid can be expressed by considering the Archimedes' principle as follows (Britannica, 2023):

$$F_b = \frac{1}{6}\pi\rho_f d^3 g \tag{4.4}$$

where ρ_f is the density of fluid, d is the diameter of particle, g is the acceleration of gravity.

Regarding the drag force, one has to consider if the fluid is a Newtonian fluid or non-Newtonian fluid. In a Newtonian fluid, the general form of drag force acting on a spherical particle settling in the fluid can be expressed as (Di Felice, 1994):

$$F_d = \frac{1}{2}\rho_f v^2 A C_d \tag{4.5}$$

where F_d is the drag force; v is the settling velocity of particle; A is the cross-section area of a spherical particle; C_d is a drag coefficient, which depends on the shape and surface state of the particle and on the particle Reynolds number R_e, is expressed as follows (Chhabra, 2006; Okesanya et al., 2020):

$$R_e = \frac{\rho_f v d}{\eta} \tag{4.6}$$

where η is the viscosity of a Newtonian fluid.

For a spherical particle settling in a laminar flow region with very small Reynolds number. The drag force can be expressed based on Stokes law (Stokes, 1844):

$$F_d = 3\pi\eta v d \tag{4.7}$$

Substituting equation (4.7) into (4.5), one can obtain the relationship between the drag coefficient and Reynolds number of a sphere in stokes flow (Concha Arcil, 2009):

$$C_d = \frac{24}{R_e} \tag{4.8}$$

For the drag force of a spherical particle in a non-Newtonian fluid with a yield stress, the influence of yield stress must be considered. The drag force acting on a moving spherical particle in such fluid is given by Dedegil (1987) as follows:

$$F_d = (\frac{\pi}{2}d)^2\tau_y + \frac{1}{2}C_d\rho_f v^2 A \tag{4.9}$$

where τ_y is the yield stress, which is the minimum required shear stress to start flowing a non-Newtonian fluid.

The Reynolds number of particle in a non-Newtonian fluid can be expressed as follows after a generalization of Equation (4.6) for Newtonian fluid (Dedegil, 1987; Machač et al., 1995):

$$R_e' = \frac{\rho_f v d}{\eta_a} \tag{4.10}$$

where R_e' is the particle Reynolds number in a non-Newtonian fluid; η_a is the apparent viscosity of a non-Newtonian fluid, determined as the slope of shear stress, τ, and shear rate , $\dot{\gamma}$, as follows (He et al., 2001):

$$\eta_a = \frac{\tau}{\dot{\gamma}} \tag{4.11}$$

The particle to fluid shear rate, $\dot{\gamma}$, is defined as follows (Dedegil, 1987; He et al., 2001):

$$\dot{\gamma} = \frac{v}{d} \tag{4.12}$$

In this study, the non-Newtonian fluid with a yield stress is considered as a Bingham plastic fluid with its shear stress τ is described by the Bingham model (Blackery & Mitsoulis, 1997):

$$\tau = \tau_y + \eta_B\frac{v}{d} \tag{4.13}$$

where η_B is the plastic viscosity of a Bingham fluid.

Substituting equations (4.11), (4.12), (4.13) into equation (4.10) results in an expression for the particle Reynolds number of a sphere in a Bingham plastic fluid as follows (Dedegil, 1987):

$$R_e' = \frac{\rho_f v^2}{\left[\tau_y + \eta_B(\frac{v}{d})\right]} \tag{4.14}$$

To establish a relationship between the drag coefficient, C_d, and Reynolds number, R'_e of a particle in a Bingham plastic fluid, the settlement of a particle in such fluid is analyzed. When a particle is released into the fluid, its velocity increases upon the influence of gravity, a constant buoyance force, and a small but increasing drag force associated with the increasing velocity of settlement. The acceleration of settlement decreases as the sinking velocity and associated drag force increase. The sinking velocity reaches a maximum and constant value, usually called terminal velocity, when an equilibrium is achieved between the gravity force, the buoyance, and drag forces:

$$F_b + F_d - F_g = 0 \tag{4.15}$$

Substituting equations (4.3), (4.4) and (4.9) into equation (4.15) leads to:

$$\frac{1}{6}\pi\rho_p d^3 g - \frac{1}{6}\pi\rho_f d^3 g - \left(\frac{\pi}{2}d\right)^2 \tau_y - \frac{1}{2}C_d \rho_f v_{ter}^2 A = 0 \tag{4.16}$$

where v_{ter} is the terminal velocity of a particle settling in a fluid; A is the cross-section area of a spherical particle.

The drag coefficient of a particle can then be expressed as follows:

$$C_d = \frac{2}{v_{ter}^2 \rho_f}\left[\frac{2}{3}\left(\rho_p - \rho_f\right)dg - \pi\tau_y\right] \tag{4.17}$$

Substituting the velocity v of equation (4.14) by the terminal velocity v_{ter} leads to an expression for the particle Reynolds number R'_e as follows:

$$R'_e = \frac{\rho_f v_{ter}^2}{\left[\tau_y + \eta_B\left(\frac{v_{ter}}{d}\right)\right]} \tag{4.18}$$

A relationship between C_d and R'_e can then be established through the terminal velocity v_{ter} included in both of equations (4.17) and (4.18). In this study, the C_d – R'_e relationship is determined based on the test results of Valentik & Whitmore (1965), who conducted spheres settling tests in clay suspensions. The tests were realized with 121 spheres settling in clay suspensions having six different densities. The terminal velocity v_{ter} of each sphere in the clay suspension was well recorded. Figure 4.1 shows the variation of drag coefficient C_d of each sphere at its terminal velocity as a function of the corresponding particle Reynolds number R'_e.

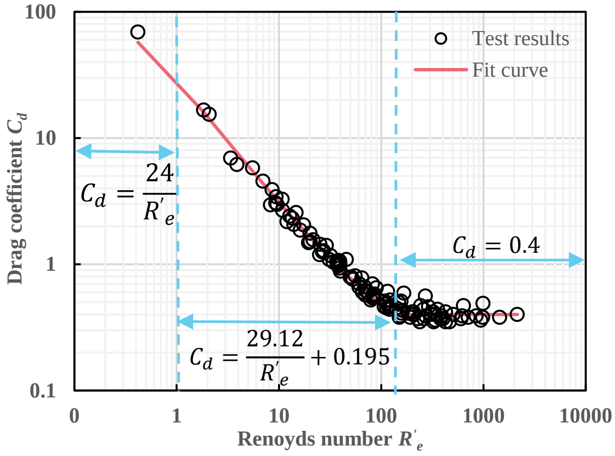

Figure 4.1: Variation of drag coefficient C_d as a function of the corresponding particle Reynolds number R_e of each sphere with the settling test results of Valentik & Whitmore (1965)

Applying the curve-fitting technique on the test results shown in Figure 4.1 leads to a $C_d - R'_e$ relationship for sphere settling in clay suspensions as follows:

$$C_d = \begin{cases} \dfrac{24}{R'_e}, & R'_e < 1 \\ \dfrac{29.12}{R'_e} + 0.195, & 1 \le R'_e \le 150 \\ 0.4, & R'_e > 150 \end{cases} \tag{4.19}$$

This equation will be used to describe the $C_d - R'_e$ relationship for spheres settling in a Bingham plastic fluid. It should be noted here, the proposed $C_d - R_e'$ relationship (equation (4.19)) is different from the one proposed by Dedegil (1987). This is because the shear stress τ used by Dedgil (1987) is taken from the shear stress and shear rate curve conducted by Valentik & Whitmore (1965). However, in this study, the shear stress τ is applied based on Bingham model (equation (4.13)) which leads to the difference of the particle Reynolds number R_e'.

4.3 Implementation and ability of the f-EDEM model

As mentioned, this work is developed based on a commercialized DEM code, named Altair EDEM. An advantage of this code is the possibility of introducing user-defined-force-models, external couplings and particle-generation factories through API (standing for Application Programming Interface). To implement the fluid forces into EDEM, the buoyance force (equation (4.4)) and drag force (equations (4.5) and (4.9)) were translated and compiled into a DLL (standing for Dynamic Loading Library) module through Visual Studio C++ programming. The DLL module can be loaded and run by EDEM to take into account the fluid forces as plug-in particle body forces (Figure 4.2). In the simulation, the fluid forces are automatically applied to the particles once they enter inside the pre-determined fluid area. This development results in a new model, named f-EDEM for modeling particle settlement in fluids.

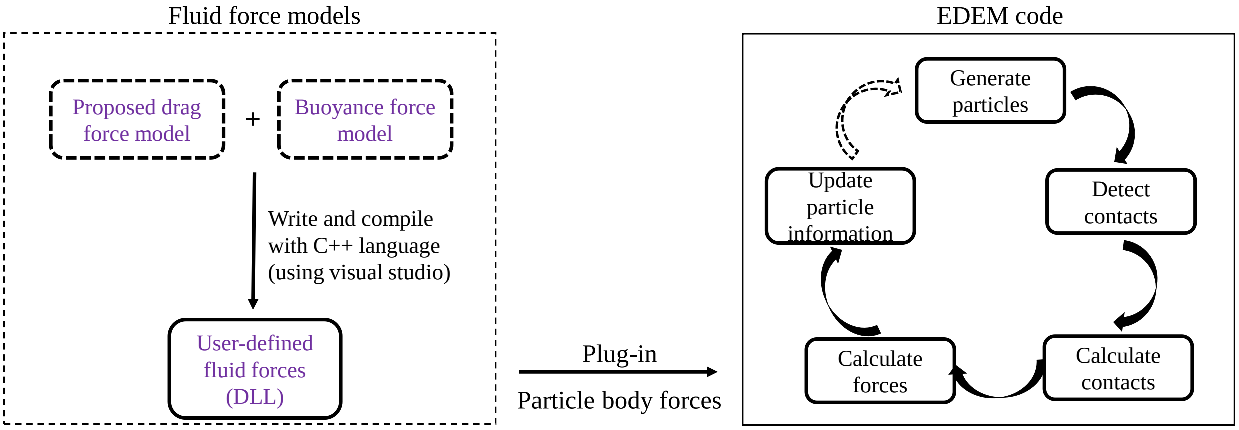

Figure 4.2: Flowchart of fluid forces programming and implementation in EDEM

Before any applications of a numerical model, the validation against analytical solutions must be done in order to ensure that the numerical code does not contain any errors and the user can correctly use the numerical code (Li, 2022). To do so, both of the numerical model and physical model should not contain any uncertainty. In this regard, the comparison between numerical and experimental results to obtain a good agreement, usually through the process of calibration (i.e., adjustment of some parameters), is not a validation because the experiment results contain always more or less uncertainty. No one can guarantee whether the calibrated parameters are reliable or unreliable. The comparisons are thus a process of calibration, useful to test the applicability or power of the numerical model, but questionable as a validation of the numerical model (Li, 2022).

In this study, the validation of the f-EDEM model will be done against the settlement of a single spherical particle in water. Figure 4.3 presents the physical model of a spherical particle, settling down in water with an initial speed of zero. The drag force acting on the particle is expressed by

Stokes drag (equation (4.7)), the settlement of the spherical particle in water is thus governed by the following equation (Zhao et al., 2014):

$$\frac{1}{6}\pi d^3 \rho_p \frac{dv}{dt} = \frac{1}{6}\pi d^3 (\rho_p - \rho_w) g - 3\pi d \mu_w v \tag{4.20}$$

where d (m) is the diameter of particle, ρ_p (kg/m^3) is the density of particle, ρ_w is the density of water, μ_w (Pa.s) is the viscosity of water, v (m/s) is the settling velocity of the particle.

Integrating equation (4.20) and considering the initial condition of $v = 0$ at $t = 0$ lead to an expression for the terminal velocity of particle v_{ter} as follows (Stokes, 1844; Concha Arcil, 2009):

$$v_{ter} = \frac{d^2 (\rho_p - \rho_w) g}{18 \mu_w} \tag{4.21}$$

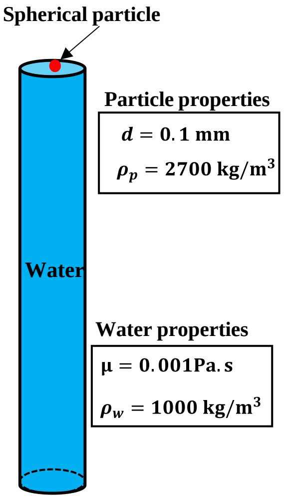

Figure 4.3: Physical model of the settlement of a spherical particle in the water

The validation of the f-EDEM model is realized by considering the physical parameters given in Table 4.1.

Table 4.1: Physical parameters and considered time for the settlement of a spherical particle in water

Particle diameter, d_p (mm)	0.1
Particle density, ρ_p (kg/m^3)	2700
Poisson's ratio of particle, ν	0.25
Young's modulus of particle, E (GPa)	30
Water density, ρ_w(kg/m^3)	1000
Water viscosity, μ_w (Pa. s)	0.001

Figure 4.4 presents the numerical model of the physical model presented in Figure 4.3, built with EDEM by considering the physical parameters given in Table 4.1.

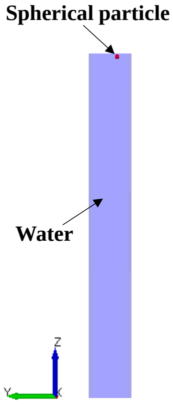

Figure 4.4: Numerical model of Figure 4.3 by considering the physical parameters given in Table 4.1, built with EDEM

In order to obtain stable and reliable numerical results, sensitivity analysis of time step is necessary. In this regard, a time step equaling to 10 to 20% of the Rayleigh time T_R is commonly recommended in DEM simulations (Washino et al., 2016). The Rayleigh time T_R is expressed by the following equation (Li et al., 2005; Rackl & Hanley, 2017; Burns et al., 2019):

$$T_R = \frac{\pi r_p}{0.8766 + 0.163n}\sqrt{\frac{\rho_p}{G}} \tag{4.22}$$

where r_p is the particle radius, ν is the Poisson's ratio of particle, ρ_p is the particle density, G is the shear modulus of particle. Considering the physical parameters given in Table 4.3 with $r_p = d_p/2$ = 0.1 mm/2 = 0.05 mm and $G = \frac{E}{2(1+n)}$ = 12 GPa and applying equation (4.22) lead to a value of T_R = 8.12×10^{-8} s. With 20% of T_R, the recommended time step is 1.62×10^{-8} s.

Figure 4.5 presents the variation of the settling velocity of the particle at t = 0.001 s as a function of time step. One sees that the numerical results become stable when the time step is smaller than 2.5×10^{-5} s. The numerical results do not change any more significantly as the time step further decreases. The optimal time step is thus around 2.5×10^{-5} s; a value of 1.0×10^{-5} s was taken to be somehow conservative. These values are much larger than the time step of 1.62×10^{-8} s, recommended and commonly used in DEM simulations (20% of T_R). For such case, the application of the recommended and commonly used time step can result in unnecessary costs of simulation time. For a much more complicated situation with much more particles, it is unknown if the time step determined by using 20% of T_R is too large or too small. The former case results in instable and unreliable numerical results while the latter case generates useless waste of time and cost calculations. None of them is desirable. The good and reliable way is to always conduct sensitivity analysis of time step, case by case, to find the optimal time step in order to ensure stable and reliable numerical result with the shortest time of calculations.

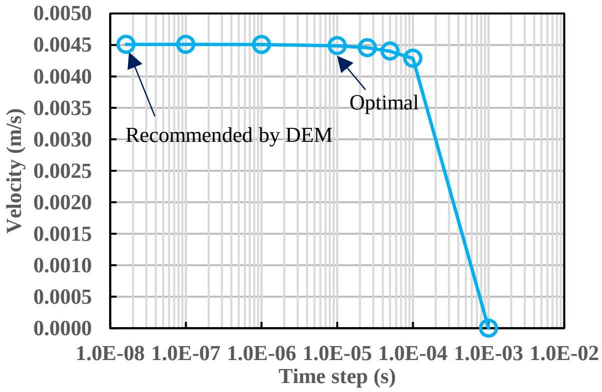

Figure 4.5: The variation of settling velocity (t = 0.001 s) of spherical particle as a function of time step

Figure 4.6 presents the variation of settling velocity of the particle in the water with time, obtained by applying the analytical solution (Equation (4.20)) and numerical model with the optimal time step of 1×10^{-5} s. A perfect agreement is obtained between the analytical and numerical results. The f-EDEM model can thus be considered as validated by the analytical solution. It remains to test the applicability or power of the numerical model against experimental results.

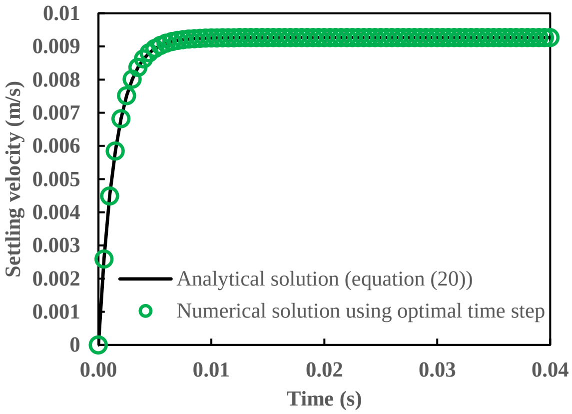

Figure 4.6: Variation of settling velocity of the particle as a function of time, obtained by applying the analytical solution (Equation (4.20)) and f-EDEM model with the optimal time step of 1×10^{-5} s

4.4 Application and ability of the f-EDEM model

In this section, the f-EDEM model is employed to reproduce and predict the experimental results regarding the settlement of particles in different fluids. The applicability and ability of the f-EDEM model are examined by comparing the numerical results with the laboratory results.

4.4.1 Application of the f-EDEM model to numerically reproduce the tests of spheres settling in clay

In this part, the applicability or power of the f-EDEM model is tested by reproducing and predicting the experimental results obtained by Valentik & Whitmore (1965), who conducted several tests of spheres settling in clay suspensions. Figure 4.7 shows a schematic presentation of the physical model used by Valentik & Whitmore (1965) for testing the settlement of a sphere in clay suspensions. The clay suspensions were poured in a vertical tank of 3 m high. A sphere was released from a vacuum tube into the clay suspension. The terminal velocity of the sphere in the suspension was recorded using detectors fixed outside the tank. The diameters of spheres range from 9.5 to 57 mm and their densities were changed by adding fine lead shot to a sealed opening in the sphere.

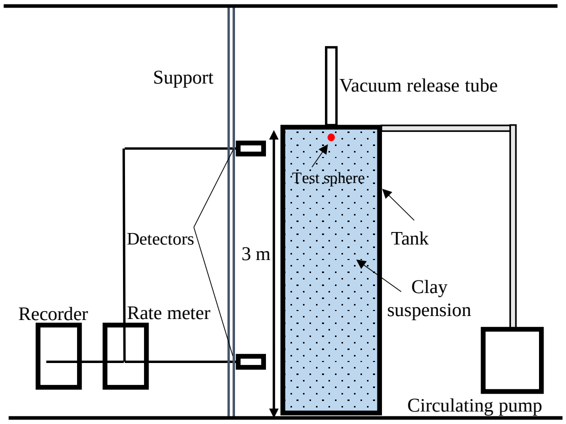

Figure 4.7: A schematic presentation of the physical model of Valentik and Whitmore (1965) for testing the settlement of a sphere in clay suspensions

The detailed physical parameters for the clay suspensions and the corresponding particle Reynolds number R'_e as well as the drag coefficient C_d of spheres are shown in Tables 4.2 and 4.3, respectively.

Table 4.2: Physical parameters of clays suspensions used in the tests (Valentik & Whitmore, 1965)

	Density $\rho_{\_clay}$ (kg/m^3)	Plastic viscosity η_B (Pa. s)	Yield stress τ_y (Pa)
Clay suspension 1	1280	0.0131	30.5
Clay suspension 2	1254	0.0095	22.5
Clay suspension 3	1226	0.0081	17.5
Clay suspension 4	1207	0.0067	13
Clay suspension 5	1184	0.0054	8.5
Clay suspension 6	1149	0.004	4

Table 4.3: Physical parameters of spheres and the corresponding particle Reynolds number R'_e and drag coefficients C_d by applying equations (4.18) and (4.17), respectively

	Diameter of sphere $d_{\_sphere}$ (m)	Density of sphere $\rho_{\_sphere}$ (kg/m^3)	Terminal velocity v_{ter} (m/s)	Particle Reynolds number R'_e	Drag coefficient C_d
Suspension 1	0.0159	6450	0.1	0.42	69.03
	0.019	5832	0.21	1.84	16.65
	0.019	6032	0.365	5.5	5.80
	0.019	6513	0.65	17.5	2.05
	0.019	7290	0.98	39.4	1.06
	0.0254	4804	0.41	7.0	4.55
	0.0254	5237	0.78	25.2	1.44
	0.0254	5544	0.98	39.6	1.00
	0.0254	6142	1.3	69.4	0.66
	0.0254	7034	1.63	108.5	0.51
	0.0317	8195	2.28	211.6	0.40
	0.0381	3431	0.48	9.6	2.98
	0.0381	3603	0.57	13.5	2.32
	0.0381	3742	0.72	21.6	1.56
	0.0381	3990	0.88	32.2	1.17
	0.0381	4025	0.95	37.5	1.02
	0.0381	4479	1.16	55.7	0.81
	0.0381	7160	2.25	207.2	0.42
	0.0444	7712	2.52	260.2	0.44
	0.0508	2673	0.305	3.9	6.16
	0.0508	2909	0.58	14.0	2.07
	0.0508	3416	1.21	60.8	0.66
	0.0571	2728	0.51	10.9	2.67
	0.0571	2981	0.81	27.4	1.28

Table 4.3: Physical parameters of spheres and the corresponding particle Reynolds number R'_e and drag coefficients C_d by applying equations (4.18) and (4.17), respectively (continued)

	Diameter of sphere $d_{\_sphere}$ (m)	Density of sphere $\rho_{\_sphere}$ (kg/m^3)	Terminal velocity v_{ter} (m/s)	Particle Reynolds number R'_e	Drag coefficient C_d
	0.0571	3124	0.94	36.8	1.05
	0.0571	3621	1.25	65.0	0.78
	0.0571	3958	1.47	89.7	0.65
Suspension 2	0.0127	6698	0.395	8.6	3.90
	0.0159	6450	0.73	29.1	1.41
	0.019	7290	1.54	127.8	0.46
	0.0254	6123	1.5	122.3	0.52
	0.0381	2937	0.48	12.8	2.41
	0.0381	3214	0.83	38.0	0.97
	0.0381	3815	1.4	107.6	0.46
	0.0381	4179	1.66	150.8	0.38
	0.0381	7160	2.5	338.9	0.36
	0.0444	7712	2.56	356.6	0.44
	0.0508	2437	0.41	9.3	3.06
	0.0508	2673	0.85	40.0	0.88
	0.0508	4083	1.83	183.8	0.41
	0.0571	2352	0.54	16.2	1.86
	0.0571	2765	1.14	71.8	0.61
	0.0571	4003	2.04	228.5	0.37
	0.0095	6749	0.37	9.4	3.43
	0.0159	6732	1.1	82.1	0.70
	0.019	4199	0.54	20.2	1.76
	0.0254	2795	0.22	3.4	6.93
	0.0254	3179	0.54	20.2	1.51

Table 4.3: Physical parameters of spheres and the corresponding particle Reynolds number R'_e and drag coefficients C_d by applying equations (4.18) and (4.17), respectively (continued)

	Diameter of sphere $d_{\_sphere}$ (m)	Density of sphere $\rho_{\_sphere}$ (kg/m^3)	Terminal velocity v_{ter} (m/s)	Particle Reynolds number R'_e	Drag coefficient C_d
Suspension 3	0.0254	3704	1.01	70.2	0.57
	0.0254	6123	1.88	239.4	0.35
	0.0317	3005	0.7	34.0	1.04
	0.0317	8195	2.4	389.9	0.39
	0.0381	2786	0.46	14.7	2.57
	0.0444	2295	0.53	19.6	1.48
	0.0444	2987	1.28	113.3	0.45
	0.0508	2183	0.6	25.1	1.19
	0.0508	2493	1.07	79.4	0.52
	0.0508	3002	1.49	153.5	0.39
	0.0508	4000	1.95	261.7	0.37
	0.0571	2229	0.75	39.2	0.93
	0.0571	2706	1.33	122.6	0.46
Suspension 4	0.0095	6751	0.716	45.8	0.98
	0.0159	6432	1.29	148.3	0.50
	0.019	3560	0.65	38.5	0.99
	0.019	4035	0.97	85.1	0.55
	0.019	7290	1.75	271.5	0.39
	0.0254	2711	0.15	2.1	15.39
	0.0254	2779	0.54	26.8	1.25
	0.0254	3210	0.88	70.6	0.62
	0.0254	3649	1.15	120.0	0.46
	0.0317	2865	0.76	53.0	0.87
	0.0381	2702	0.97	86.2	0.58

Table 4.3: Physical parameters of spheres and the corresponding particle Reynolds number R'_e and drag coefficients C_d by applying equations (4.18) and (4.17), respectively (continued)

	Diameter of sphere $d_{\_sphere}$ (m)	Density of sphere $\rho_{\_sphere}$ (kg/m^3)	Terminal velocity v_{ter} (m/s)	Particle Reynolds number R'_e	Drag coefficient C_d
	0.0444	2415	0.95	82.9	0.57
	0.0508	2222	0.95	83.0	0.54
	0.0571	1910	0.58	31.1	1.09
	0.0571	2098	0.9	74.6	0.60
	0.0571	2595	1.45	192.7	0.38
	0.0571	3707	1.88	322.7	0.42
Suspension 5	0.0095	6751	0.94	115.8	0.61
	0.0127	3332	0.28	10.8	3.27
	0.0159	3150	0.53	38.3	1.07
	0.0159	6432	1.58	327.1	0.35
	0.019	2887	0.67	61.2	0.70
	0.019	3891	1.1	162.6	0.43
	0.019	7290	1.89	468.0	0.35
	0.0254	2018	0.295	12.0	2.17
	0.0254	2394	0.61	51.1	0.79
	0.0254	2544	0.78	83.1	0.55
	0.0254	3041	1.08	158.2	0.41
	0.0254	4604	1.52	310.0	0.40
	0.0254	6123	1.79	427.2	0.42
	0.0317	2420	0.94	120.8	0.44
	0.0381	2309	0.95	123.8	0.47
	0.0381	7160	2.52	848.9	0.39
	0.0571	1711	0.69	65.8	0.60
	0.0571	2204	1.22	204.5	0.40

Table 4.3: Physical parameters of spheres and the corresponding particle Reynolds number R'_e and drag coefficients C_d by applying equations (4.18) and (4.17), respectively (continued)

	Diameter of sphere $d_{\_sphere}$ (m)	Density of sphere $\rho_{\_sphere}$ (kg/m^3)	Terminal velocity v_{ter} (m/s)	Particle Reynolds number R'_e	Drag coefficient C_d
	0.0571	2801	1.57	337.5	0.40
Suspension 6	0.0095	6751	1.26	402.6	0.37
	0.0127	3319	0.76	156.5	0.51
	0.0127	6693	1.4	507.1	0.40
	0.0159	2984	0.86	201.5	0.42
	0.0159	6432	1.54	621.1	0.39
	0.019	2516	0.82	185.2	0.41
	0.019	3838	1.26	427.7	0.35
	0.019	6032	1.64	711.2	0.38
	0.019	7290	1.9	942.7	0.36
	0.0254	1708	0.42	49.8	0.79
	0.0254	2009	0.71	140.9	0.45
	0.0254	3006	1.18	382.2	0.37
	0.0254	4102	1.49	602.4	0.37
	0.0254	6023	1.92	984.5	0.38
	0.0381	2000	0.77	166.9	0.59
	0.0381	2310	1.02	291.1	0.46
	0.0381	5932	2.31	1445.2	0.38
	0.0444	2003	0.93	243.3	0.47
	0.0571	1314	0.17	8.3	2.95
	0.0571	1481	0.63	112.8	0.49
	0.0571	2007	0.98	271.2	0.56
	0.0571	2832	1.51	638.1	0.47
	0.0571	3879	1.89	993.2	0.49
	0.0571	6002	2.8	2146.8	0.40

Figure 4.8 illustrates the numerical model to simulate the settlement of spheres in the clay suspensions built with EDEM. The geometry of the numerical model is the same as the physical model shown in Figure 4.7. The physical parameters for the numerical model can be found in Tables 4.2 and 4.3.

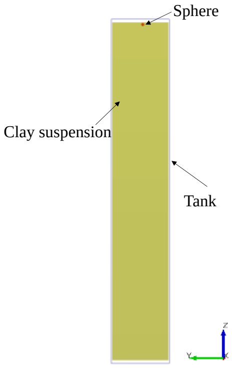

Figure 4.8: Numerical model for reproducing the settling of spheres in the clay suspensions built with EDEM

Once again, sensitivity analysis is necessary to determine the optimal time step. Figure 4.9 shows the variation of the terminal velocity v_{ter} of spheres as a function of time step. It is seen that the numerical results become stable once the time step is equal to or smaller than 1×10^{-1} s for spheres with four different diameters. Further reductions of time step do not significantly change the simulation results.

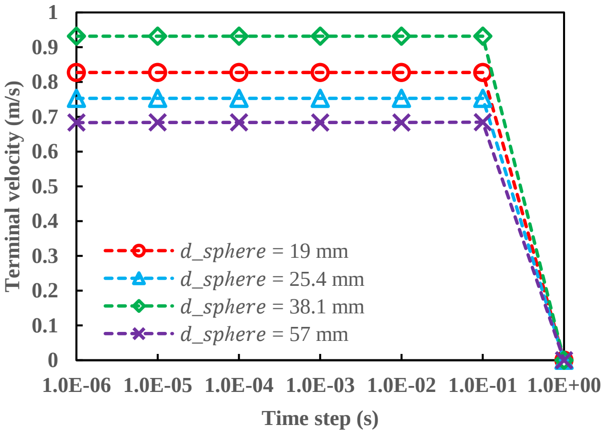

Figure 4.9: The variation of terminal settling velocity v_{ter} of spheres as a function of time step

Figure 4.10 illustrates the variation of the settling velocity of spheres at *t* = 0.01 s as a function of time step. The numerical results become stable when the time step is reduced to 1×10^{-4} s, a value much smaller than the optimal time step of 1×10^{-1} s for simulating the terminal velocity. This is because the settling velocity changes rapidly with time at the beginning and tends to become constant when it is close to the terminal velocity. The time step should be small enough to capture the rapid change of velocity with time at the beginning of settlement. When the velocity is close to the terminal velocity, the velocity changes with time becomes small and a large time step can become enough to capture the velocity change with time. To ensure the numerical results are stable for the spheres at all different times, the optimal time step is determined as 1×10^{-5} s.

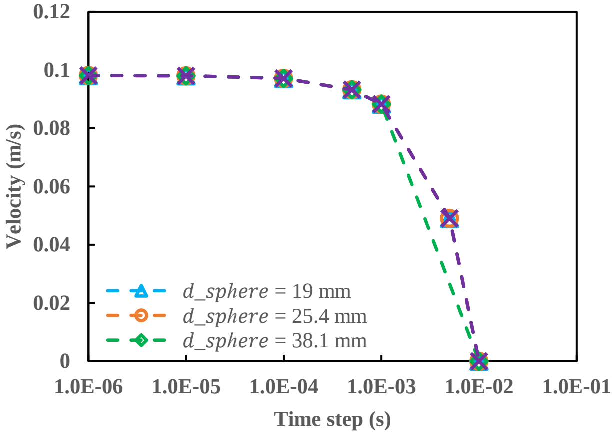

Figure 4.10: The variation of settling velocity of spheres (*t* = 0.01 s) as a function of time step

Figure 4.11 presents the variation of the terminal velocities of spheres as a function of sphere density for different diameters of spheres settling in clay suspensions 1 to 6 (Figures 4.11a to 4.11f), obtained by laboratory tests and f-EDEM model by considering the optimal time step of 1×10^{-5} s. One sees that the agreements between the experimental results and numerical predictions are very good for all the spheres in different clay suspensions. These results confirm that the f-EDEM model can be applied (i.e. is applicable or has the required power) to simulate the settlements of spheres in clay suspensions.

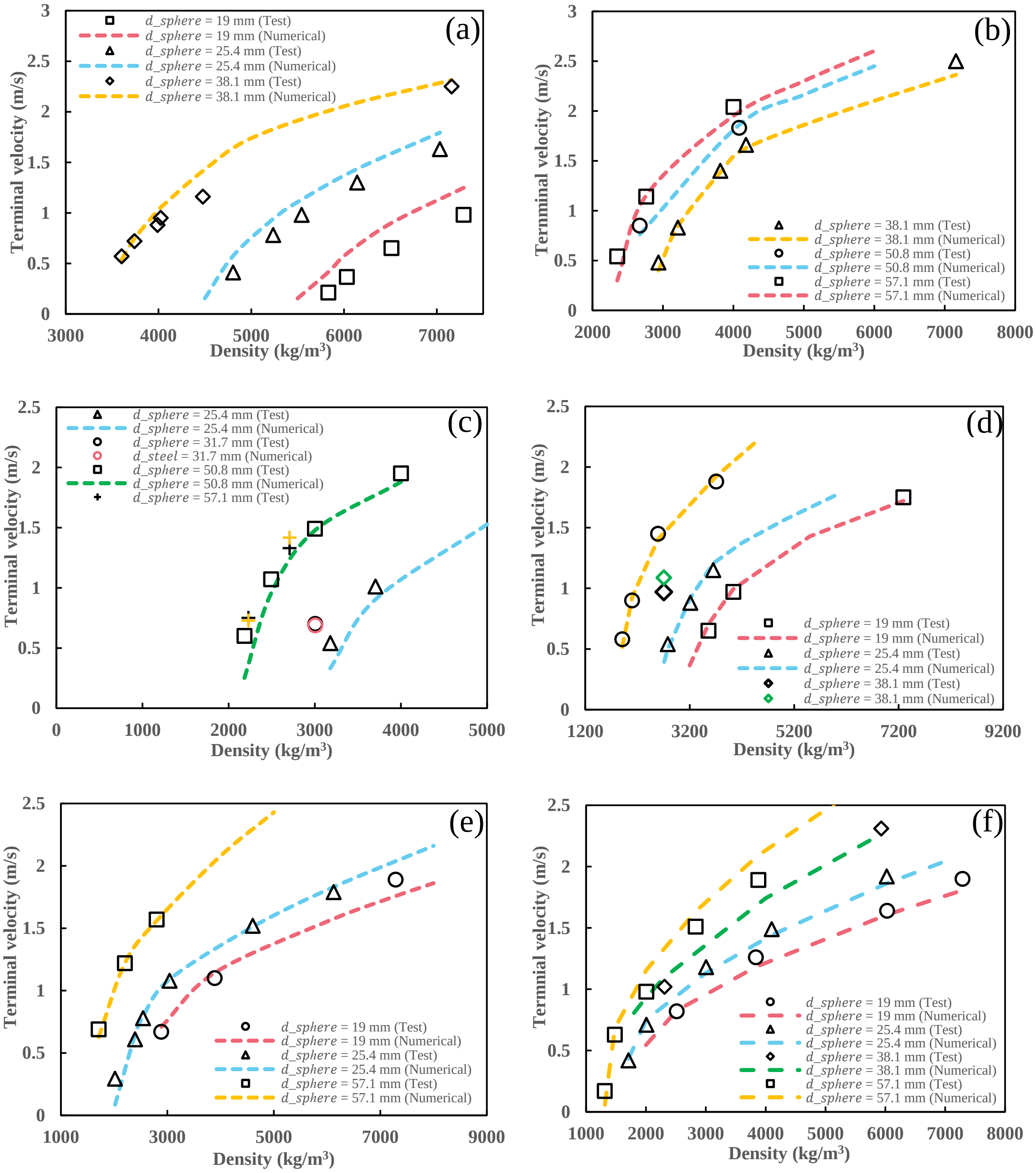

Figure 4.11: Variation of the terminal velocities of spheres as a function of sphere density for different diameters of spheres settling in clay suspensions 1 to 6, obtained by the test and f-EDEM model with the optimal time step of 1×10^{-5} s: (a) suspension 1; (b) suspension 2; (c) suspension 3; (d) suspension 4; (e) suspension 5; (f) suspension 6

4.4.2 Application of the f-EDEM model to numerically reproduce tests of steel balls falling into a paste backfill

To further exam the applicability of f-EDEM model to simulate the settlement of particles in other non-Newtonian fluids, a series of particle settlement tests have been realized in the laboratory with steel balls and a paste backfill, which is usually characterized as a Bingham plastic fluid (Potvin et al., 2005). The number of calibration parameters is minimized through the measurements as long as possible of the material parameters of the tested steel balls and paste backfill. Typical values are taken from the literature for the Young's modulus and Poisson's ratio of steel balls as well as the rolling resistance coefficient of steel ball of 12.6 in diameter. This results in Table 4.4, by which one sees that the calibration is necessary only on the plastic viscosity of the tested paste backfill. The yield stress of the tested paste backfill was obtained through slump tests (see details given Appendix I), whereas the restitution coefficient between the steel balls was measured by conducting steel ball drop tests (see details given Appendix II) and the static friction coefficient between the steel balls was measured through tilt tests with a steel block and a steel plate (see details given in Appendix III).

Table 4.4: Physical parameters for the tests of steel ball falling into a paste backfill

Steel ball parameters	Diameter, d_{steel} (mm)	8, 12.6, 16	Measured
	Density, ρ_{steel} (kg/m^3)	8135	Measured
	Falling height, H_f (mm)	0, 105, 150,	Measured
	Young's modulus, E (GPa)	200	Marinack et al., 2013
	Poisson's ratio, ν	0.3	Marinack et al., 2013
Paste backfill parameters	Solids content, P (%)	75	Measured
	Yield stress, τ_y (Pa)	136	Measured
	Viscosity, η_B (Pa.s)	0.7	Calibrated
Interaction parameters between steel	Restitution coefficient, μ_e	0.612	Measured
	Static friction coefficient, μ_s	0.341	Measured
	Rolling resistance coefficient, μ_r	0.002	Minkin & Sikes, 2018

Figure 4.12 presents a schematic presentation and a picture of the physical model used to test the penetration of a single steel ball in the tested paste backfill (see details given in Zhang & Li, 2023 for the preparation of the paste backfill). The prepared paste backfill was poured into a cylinder of 75 mm in diamter and 150 mm high, quickly followed by the release of a steel ball at a predetermined falling height H_f. Three steel balls were used in the tests with each having a diameter of 8, 12.6, or 16 mm, respectively. Each steel ball was dropped into the paste backfill from six different falling heights (see Table 4.4). Once the steel ball falled into the paste backfill, the mold was fixed on the table and remained untouched until the paste backfill became hard enough for cut. During the waiting time, any movements or vibrations, which are subjetive to affect the physical model, were not allowed.

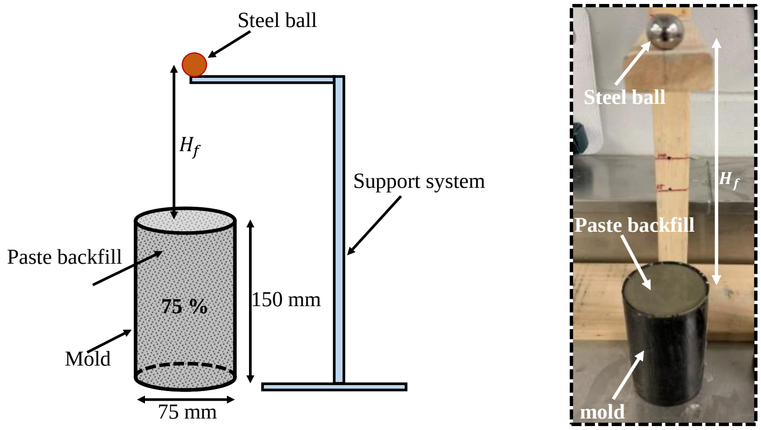

(a) (b)

Figure 4.12: Tests of a steel ball falling into a paste backfill: (a) schematic presentation; (b) physical model

Figure 4.13 shows a typical specimen (Figure 4.13a) of hardended paste backfill taken out from the mold and and the steel ball of 16 mm in diameter (Figure 4.13b) exposed after gently cut of the paste backfill. The settling distance of the steel ball within the paste backfill was measured using an electronic digital caliper (Figure 4.13b). The procedure was repteated for different steel balls and different predetermined falling heights.

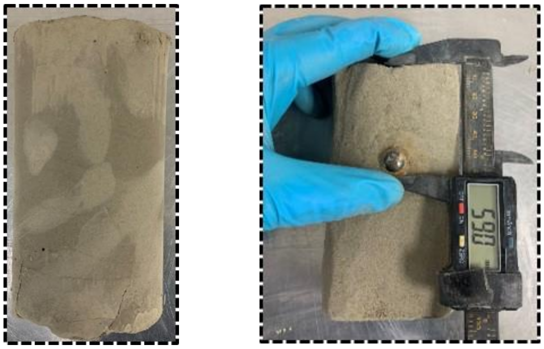
(a) (b)

Figure 4.13: Measurement of settling distance of a steel ball within the paste backfill: (a) hardened paste backfill sample taken out from the mold; (b) measuring the settling distance of steel ball within the paste backfill

Figure 4.14 presents a numerical model of the physical model presented in Figure 4.12 built with EDEM. The physical parameters can be found in Table 4.4, expect the viscosity of the paste backfill, which needs to be obtained by numerical calibration against the experiment results. Sensitivity analyses of time step presented in Figure 4.15 indicate that the optimal time step for all the three steel balls is around 1×10^{-5} s. A value of 5×10^{-6} s was retained for being more conservative.

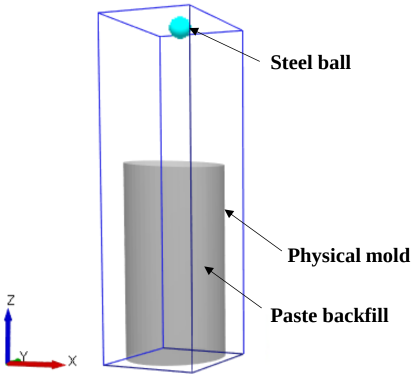

Figure 4.14: Numerical model of the physical model presented in Figure 4.12 for reproducing the settlement of a single steel ball within the paste backfill built with EDEM

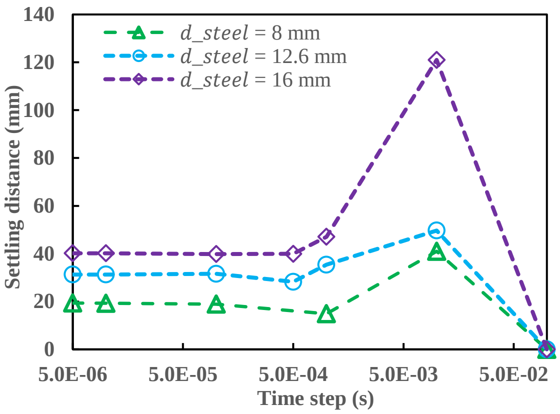

Figure 4.15: The variation of settling distance of steel balls as a function of time step

To calibrate the viscosity of the paste backfill, the test results obtained by using the steel ball of 12.6 mm in diameter dropped into paste backfill at a falling height of 255 mm will be reproduced by f-EDEM model. This leads to a viscosity 0.7 Pa.s by which the best agreement between the experimental and numerical results is achieved. This viscosity of paste backfill is then used to predict the other test results obtained with the same steel ball dropped at different falling heights and those obtained with the two other steel balls dropped at different failling heights.

Figure 4.16 shows the variation of the settling distance of a steel ball in the paste backfill as a function of falling height, obtained by laboratory results and calculated by f-EDEM model by using the physical parameters shown in Table 4.4 along with the calibrated viscosity of 0.7 Pa.s for the paste backfill. It can be seen that the agreement between the numerical and experimental results for the case of steel ball of 12.6 mm dropped at a falling height of 255 mm is almost perfect because these tests results were used to calibrate the viscosity of the paste backfill. For the tests with the same steel ball dropped at different heights and for tests with the other two steel balls (8 and 16 mm in diameter, respectively) dropped at different falling heights, the agreements between the experimental results and those predicted by using the calibrated f-EDEM model remain quite good, except for the settlement of the steel ball of 16 mm in diameter dropped at falling heights of 105 and 150 mm, respectively. In general, the agreements between the experimental results and numerical results predicted by applying the f-EDEM model are good. The f-EDEM model can thus be considered as capable of simulating the settlement of a single steel ball in the paste backfill.

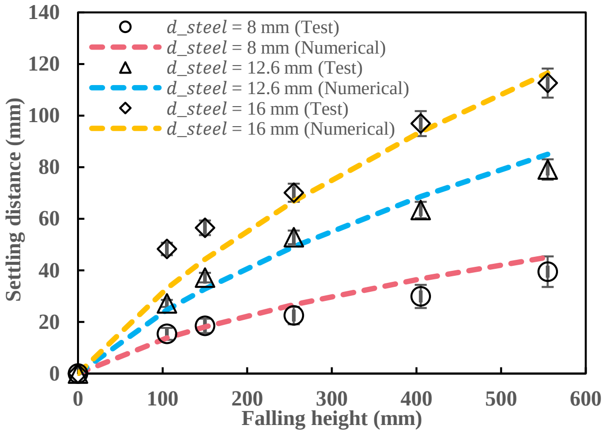

Figure 4.16: Variation of settling distance of steel balls as a function of falling height, obtained by test and f-EDEM model with optimal time step of 5×10^{-6} s

To further show the applicability of the f-EDEM model, additional falling tests have been performed with 68 steel balls having a diameter of 12.6 mm initially held in a funnel, dropped at a falling height of 15 cm into the same paste backfill as that one used for falling tests with a single steel ball (see details given in Table 4.4). Figure 4.17 shows a schematic presentation (Figure 4.17a) and a picture (Figure 4.17b) of the physical model.

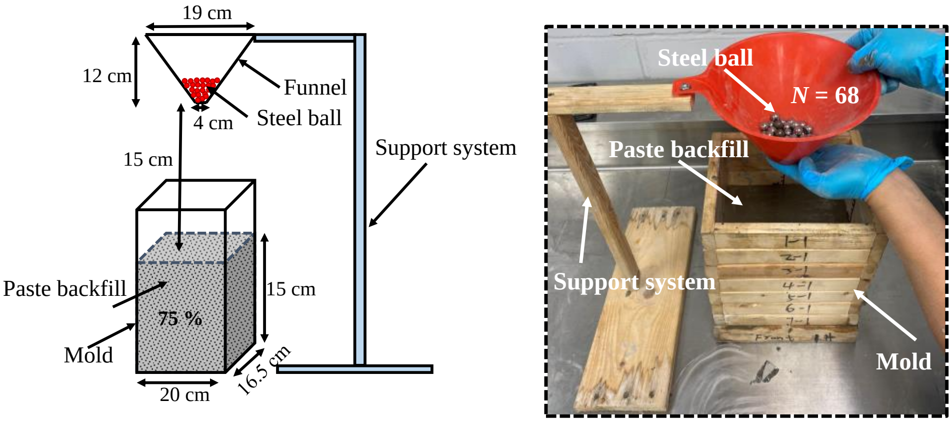

(a) (b)

Figure 4.17: Physical model used for the falling tests with 68 steel balls of 12.6 mm in diameter, initially held in a funnel and dropped into the paste backfill at a falling height of 15 cm: (a) schematic presentation; (b) a picture

Once again, the mold was left untouched on the table for a couple of weeks after having poured the steel balls into the paste backfill. During the waiting time, no vibrations and movements were allowed. When the paste backfill became hard enough, the mold was removed and the hardened paste backfill was gently cut layer by layer to obtain the spatial position in terms of *X*, *Y* and *Z* coordinates of each steel ball, as shown in Figure 4.18.

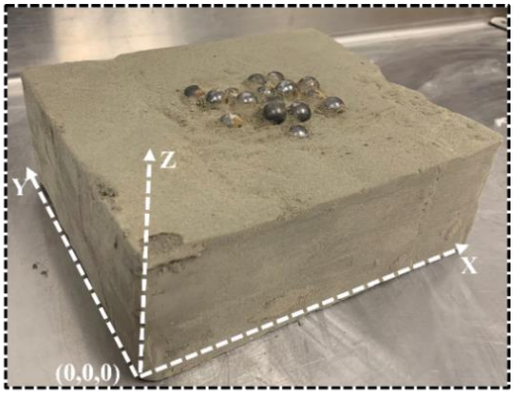

Figure 4.18: Identifying the spatial distributions of steel balls in the paste backfill

Figure 4.19 presents the numerical model of Figure 4.17, built with EDEM. It is worth mentioning that all the required parameters for the numerical model have been determined as shown in Table 4.4 with the viscosity of 0.7 Pa.s for the paste backfill obtained by calibration process against the experimental results of falling tests with a single steel ball of 12.6 mm dropped at a falling height of 255 mm. Subsequently, all the numerical results presented hereafter are numerical predictions.

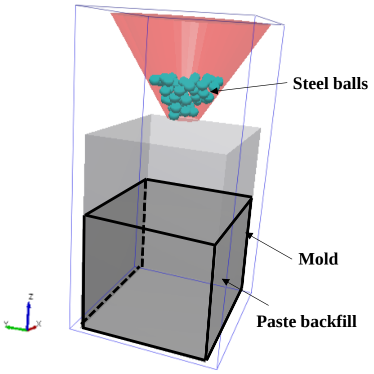

Figure 4.19: Numerical model for reproducing the test of multiple steel balls falling into a paste backfill

Figure 4.20 illustrates the variation of steel ball number, N, at $t = 0.5$ s as a function of time step $\varDelta T$. One sees that only one steel ball was generated when the time step is 2.43×10^{-5} s. The number of steel ball $N = 4$ when the time step decreases to 2.08×10^{-5} s. Once the time step is reduced to 1.04×10^{-5} s or smaller, the number of steel ball becomes stable ($N = 68$). The optimal time step is thus taken as 1.04×10^{-5} s. This value is larger than 20% T_R (1.39×10^{-6} s), a value recommended by most DEM simulations. The results once again confirm that sensitivity of time step is always necessary to conduct case by case to find the optimal time step in order to ensure stable and reliable numerical result with the shortest time of calculations.

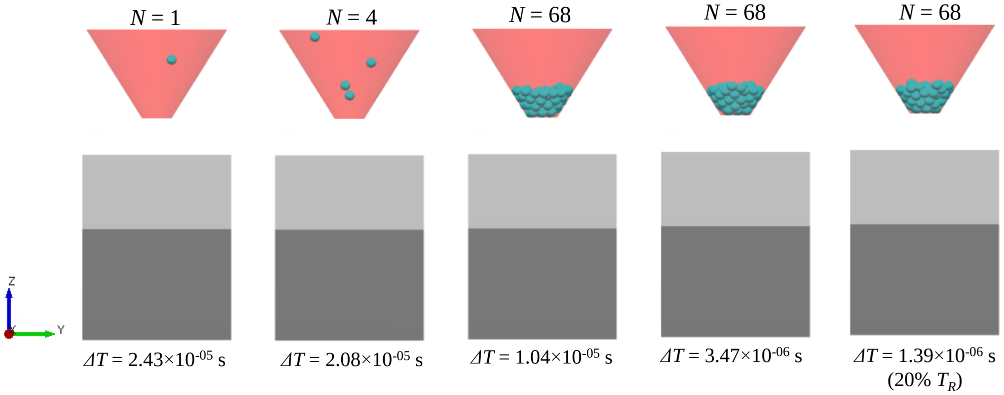

Figure 4.20: Variation of steel ball number N at $t = 0.5$ s with the change of time step $\varDelta T$

Figure 4.21 presents the distributions of steel balls in the vertical direction (along Z axis) in the paste backfill, obtained by laboratory tests (Figure 4.21a, plotted by inputting the measured coordinates X, Y and Z of each sphere in Python) and predicted by f-EDEM model with the optimal time step of 1.04×10^{-5} s (Figure 4.21b). Both the experimental and numerical results indicate that all the steel balls remain in suspending within the paste backfill along the vertical heights from $Z = 8.5$ to 13.5 cm. The only way to explain this phenomenon is to attribute it to the loss of kinematic energy of steel balls because of the large drag force provided by the paste backfill with high viscosity and yield stress. The steel balls quickly experience deceleration as soon as they penetrate into paste backfill. They can stop moving and remain in suspending probably because the mass of the steel ball is not large enough to overcome the drag force in the paste backfill when the settling velocity falls to zero. Moreover, some steel balls can penetrate deeper in the paste backfill due to the hit and impact of upper steel balls fallen later. In general, a good agreement between the experimental and numerical results is obtained, as shown by Figures 4.21a and 4.21b.

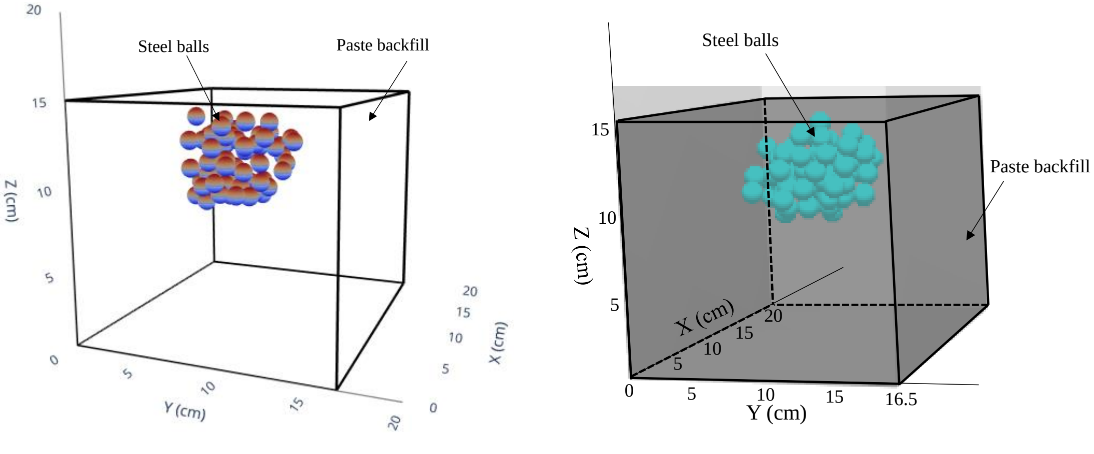

(a) (b)

Figure 4.21: Distributions of steel balls in the vertical direction (along Z axis) in the paste backfill, obtained by laboratory tests and predicted by f-EDEM model with the optimal time step of 1.04×10^{-5} s: (a) test results; (b) numerical results

To further evaluate the quality of agreement between the experimental and numerical modeling with the f-EDEM model, the horizontal distributions of the steel balls at different vertical heights are also examined. Figure 4.22 shows the distributions of steel balls at a horizontal plane varying from Z = 13.5 to 8.5 cm (Figures 4.22a to 4.22f), obtained by the laboratory tests and predicted by the numerical modeling with the f-EDEM model. It should be noted that the numerical results are presented in terms of probability. This is because it is very difficult, if not impossible, to reproduce exactly the initial spatial position of each individual particle. The initial spatial position of each individual particle remains undefined in the laboratory tests, while the individual particles are randomly generated by the f-EDEM model. These differences in initial spatial positions of particles can result different collisions during their movements. The settlements and spatial distributions can thus be different from one simulation to another. To reduce the uncertainty associated with the initial generation of particles, the simulations were repeated 15 times. The number of presence of particle in each cluster was then counted, resulting in the presence probability of a particle, as shown in Figures 4.22a to 4.22f.

All the numerical results indicate that the steel balls are highly probable to be present in the small center area while the probability of presence reduces to 40% or less along the perimeter of the center area. The high probabilities in the center area are confirmed by the experimental results.

Along the perimeters of center area, the observed presence of particles cannot confirm or disaffirm the numerical results with a probability of 40%. However, the agreements between the numerical and experimental results are quite good in term of the perimeter positions for all the planes varying from Z = 12.5 to 9.5 cm, except in the plane of Z = 8.5 cm, in which the positions of perimeter particles are slightly different from those predicted by the numerical modeling (Figure 4.22f). In general, the agreements between the experimental results and numerical predictions are quite good, considering numerous uncertainties in the laboratory tests. The ability and applicability of the f-EDEM model in simulating the settlement of multiple steel balls in paste backfill are also confirmed.

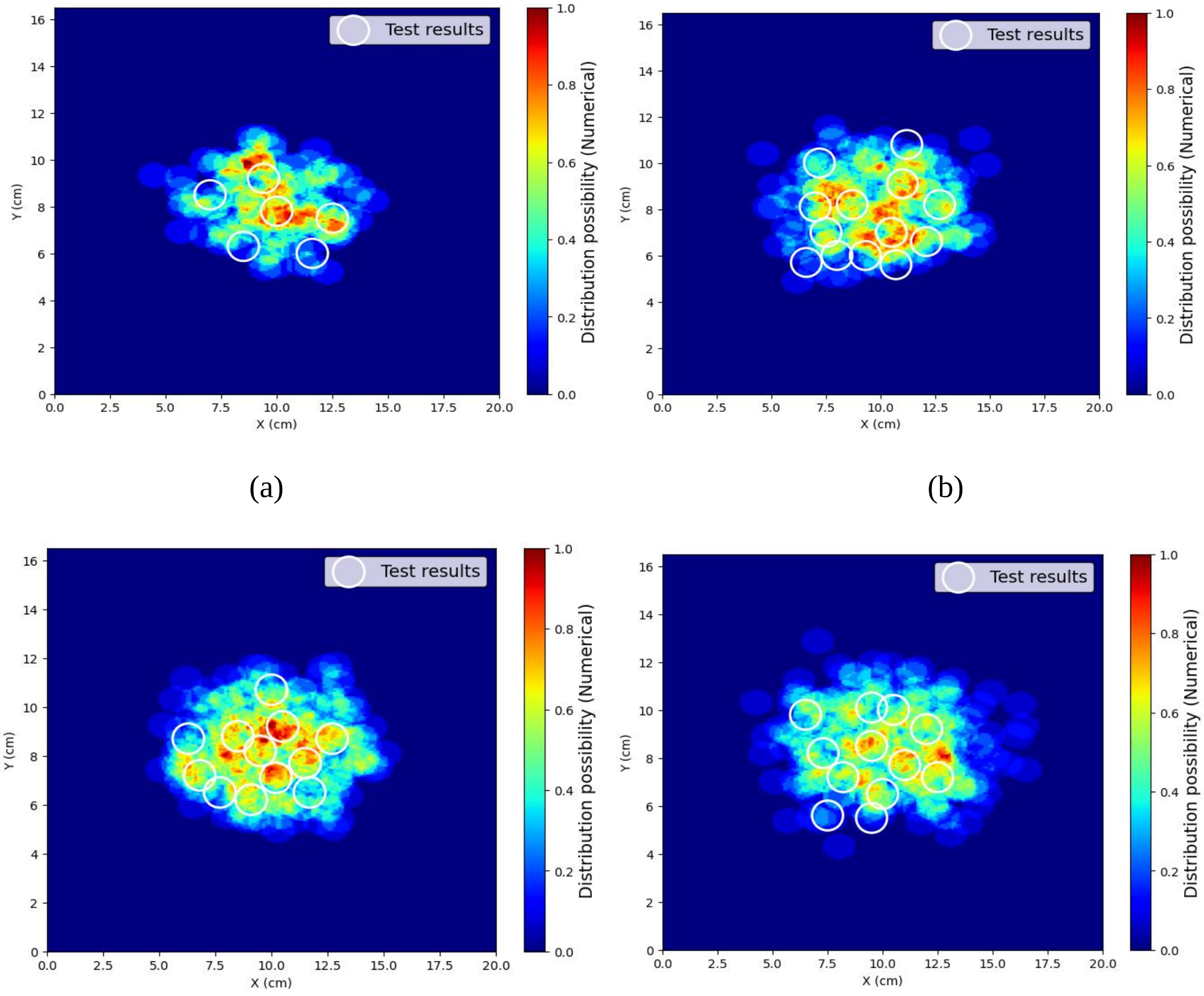

(a)

(b)

(c)

(d)

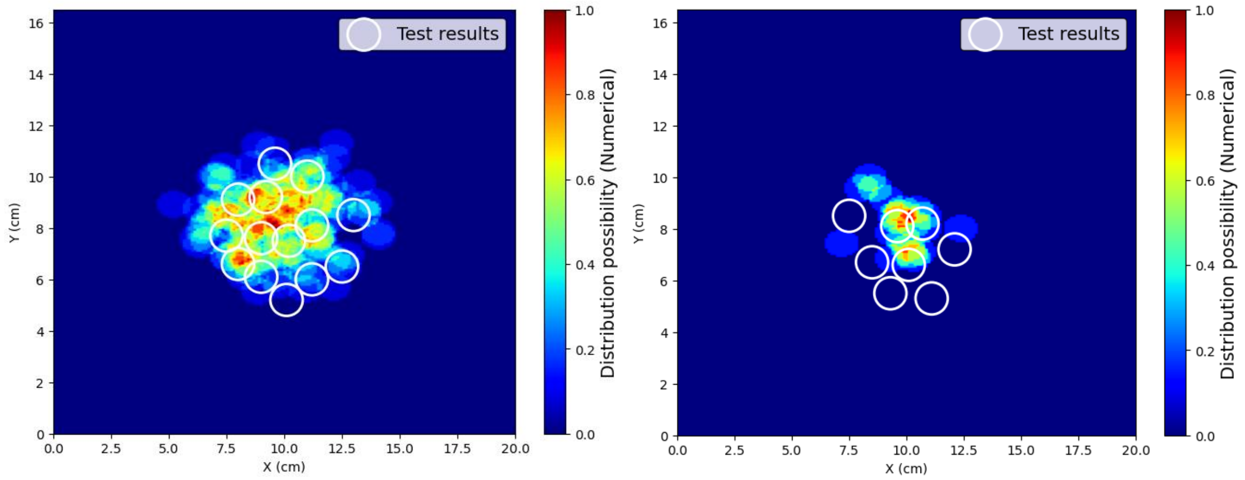

(e) (f)

Figure 4.22: The distributions of steel balls at a horizontal plane varying from Z = 13.5 to 8.5 cm, obtained by the laboratory tests and predicted by the f-EDEM model: (a) Z = 13.5 cm; (b) Z = 12.5 cm; (c) Z = 11.5 cm; (d) Z = 10.5 cm; (e) Z = 9.5 cm; (f) Z = 8.5 cm

4.5 Discussion

In this study, the formulation and implementation of fluid forces have been realized in the EDEM code via a user-defined-force-model to simulate the settlement of spherical particles in different fluids. This results in a new model, called f-EDEM model. The f-EDEM model has been validated against an analytical solution while its ability and applicability have been confirmed through the numerical reproductions of several experimental results. It can thus be used to solve several engineering problems associated with the settlement of particles in fluids. However, one needs to keep in mind that this study involves several limitations.

In this study, the fluids (e.g., clay suspension and paste backfill) were represented by the buoyance and drag forces. The numerical model does not correspond to the real situation with the physical presence of the simulated fluid. In the simulation, the flow velocity of the fluid is set to be always zero (fluid at rest). The slip velocity between the particle and fluid thus be considered equals the settling velocity of particle. However, the model is not able to take into account the effects of particle movement on the motion of fluid (e.g., the splash of fluid after the particle is dropped) because the flow of fluid cannot be described in the simulation. In this situation, the accuracy of slip velocity between the particle and fluid can be influenced. For the cases with even more complicated interactions, such as two-way simulations (the fluid flow affects the particles movement and the particles in turn affect the motion of fluid) or the particle-related inner stream flow (fluid flow between the particles), the coupling with CFD solver will be necessary as these simulations requires the Navier-Stokes equation to describe the flow of the fluids. More work is thus needed to render the model able to simulate these complicated cases in our future study. In addition, the sedimentation or consolidation of clay suspensions and paste backfill cannot be taken into account using the proposed model.

By comparing the numerical and the test results, the applicable particle density obtained by this study ranges from 1314 to 8135 kg/m^3 and the particle diameter ranges from 8 to 57.1 mm. Particles out of these specific ranges will need to be examined by conducting more numerical simulations and lab tests.

The ability of f-EDEM model to simulate the settlement of particles in part of Bingham plastic fluids (e.g., clay suspensions and paste backfill) has been confirmed by reproducing and predicting the experimental results. However, the drag force model is not a generalized model for simulating the settlement of particles in all non-Newtonian fluids. The applicability of f-EDEM model to simulate the settling of particles in other Bingham plastic fluids remains to be examined by comparing the numerical results with more physical test results. In addition, the proposed drag model is developed for particles with spherical shapes. For simulations using spheres to represent non-spherical particles (e.g., rock particles), one needs to make sure that the shape-related effects can be neglected due to the relatively small errors coming from the particle-shape-approximation (as spheres) and have insignificant influences on the overall simulation results. Otherwise, the shape effects will need to be addressed and considered by changing some other parameters. This will be part of our future works and publications.

Another limitation of the f-EDEM model is related to the consideration of fully submerged particles. This can be considered reasonable with small particles. When the dropped particles are large, the changes of submergence of the particle from the moment of contact with the top surface of the fluid to fully submerged state cannot be captured by the f-EDEM model. More work is thus necessary to take into account this aspect in the future.

4.6 Conclusions

In this study, fluid forces have been formulated and directly implemented in EDEM code, resulting in a new model, named f-EDEM. Using this model, the settlement of particles in fluids can be simulated by a single DEM code without the need of coupling with a CFD or SPH solver. The good agreement between the analytical solution and numerical results of the settling velocity of a particle in water indicates that the f-EDEM model was successfully validated. Further comparisons and good agreements between the experiment results and numerical reproduction of spheres settling in clay suspensions and steel balls settling in paste backfill indicate that the f-EDEM model is applicable and has the ability of simulating the settlements of particles in Newtonian and some Bingham plastic fluids. In addition, this study shows that the time step recommended by the manual of most DEM codes (10 to 20% of Rayleigh time) can be excessively small, leading to a high computational cost. It is always necessary to conduct sensitivity analysis of time step, case by case, to find the optimal time step in order to ensure stable and reliable numerical result with the shortest time of calculations.

4.7 Appendix I: Measurement of yield stress of paste backfill by slump tests

Slump tests were conducted to measure the yield stress of paste backfill using the method proposed by Pashias and Boger (1996). The test procedures are presented in Figure 4.23. A cylinder model was chosen for the tests because this geometry is considered as the most accurate model to predict the yield stress of mine backfill based on the study of Clayton et al. (2003). The cylinder model is made of Polyvinyl chloride and has an inner diameter of 152 mm and a height of 152 mm (Figure 4.23a). In the tests, the paste backfill with solids content by mass of 75% was first poured into the cylinder mold. The mold was then gently lifted in a vertical direction. The slump height S of paste backfill was measured using a ruler (Figure 4.23b). The tests were repeated three times to minimize the test errors.

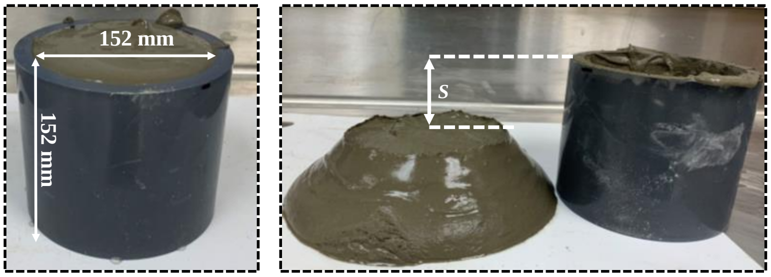

(a) (b)

Figure 4.23: Slump tests: (a) cylinder mold filled with paste backfill; (b) measure the slump height

The yield stress of paste backfill is then calculated based on the cylinder model theory given by Pashias and Boger (1996). First, a relationship between the dimensionless slump height and dimensionless yield stress can be expressed as:

$$S' = 1 - 2\tau_y'\left[1 - \ln 2\tau_y'\right] \tag{4.23}$$

where S' is the dimensionless slump height, τ_y' is the dimensionless yield stress.

The dimensionless variables can be expressed as:

$$S' = S/H \tag{4.24}$$

where S is the slump height, H is the height of cylinder model.

$$\tau_y' = \tau_y/\rho_{\_paste}gH \tag{4.25}$$

where τ_y is the yield stress, $\rho_{\_paste}$ is the density of paste backfill.

Based on equations (4.23) to (4.25), the yield stress τ_y of paste backfill can be calculated. Table 4.5 presents the test parameters and calculated yield stress of paste backfill.

Table 4.5: Slump test results

Model height, H (mm)	Model inner diameter, D (mm)	Paste backfill density, $\rho_{\_paste}$ (kg/m^3)	Slump height, S (mm)	Yield stress, τ_y (Pa)	Average yield stress (Pa)
152	152	1843	102	135	136
152	152	1843	103	131	
152	152	1843	100	143	

4.8 Appendix II: Determination of restitution coefficient between steel balls through steel ball drop tests

The restitution coefficient between steel balls were determined by conducting the tests of a steel ball re-bounce in a steel plate (Figure 4.24). In the tests, a steel ball with diameter $d_{\_steel}$ = 8 mm was drop into a steel plate at a pre-determined falling height H_f. The re-bounce height H_r of steel ball in the plate was recorded using a high-speed camera. The steel ball was dropped at five different falling heights with each test was repeated five times to minimize the test errors.

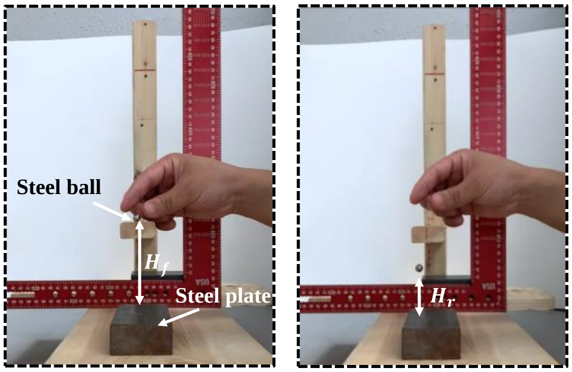

(a) (b)

Figure 4.24: Steel ball drop tests: (a): drop the steel ball at falling height of H_f (b): measure the re-bounce height H_r of steel ball

The restitution coefficient μ_e is then calculated by Sandeep et al. (2021):

$$\mu_e = \sqrt{\frac{H_r}{H_f}} \tag{4.25}$$

The physical parameters and test results are presented in Table 4.6.

Table 4.6: Physical parameters and results of a steel ball re-bounce tests

Steel ball diameter $d_{\_steel}$ (mm)	Steel ball density $\rho_{\_steel}$ (kg/m^3)	Steel ball falling height H_f (mm)	Steel ball re-bounce height H_r (mm)	Restitution coefficient μ_e	Average
8	8135	95	37.0	0.624	0.612
		188	72.0	0.619	
		252	90.9	0.601	
		318	118.0	0.609	
		398	146.9	0.608	

A numerical model (Figure 4.25) was constructed to reproduce the test results by using the average restitution coefficient (μ_e = 0.612). The input physical parameters of the numerical model can be found in Table 4.6.

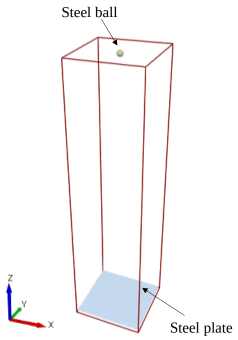

Figure 4.25: Numerical model for reproducing the test of steel ball drop in a steel plate

Figure 4.26 presents the comparisons between the test results and numerical results of re-bounce height of steel ball at different falling heights. It is seen that the numerical results match perfectly with the test results at each falling height. The results confirm that the numerical model can precisely predict the re-bounce height of steel ball at different falling heights by using the measured restitution coefficient.

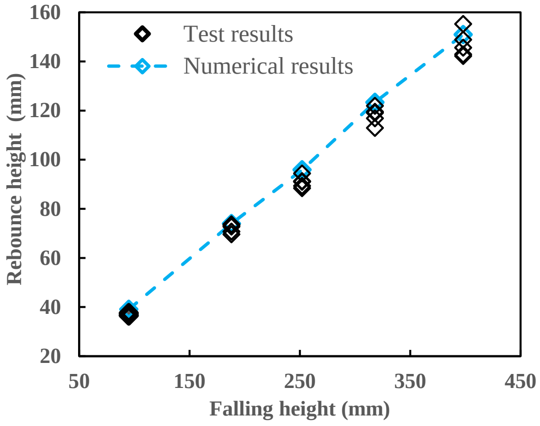

Figure 4.26: Variation of re-bounce height of steel with the falling height, obtained by test results and numerical results

4.9 Appendix III: Determination of the static friction coefficient between steel balls through tilt tests

The static friction between the steels were estimated by conducting the tilt test with a steel block and a steel plate (Figure 4.27). In the test, the steel plate was slightly lifted to a height H_l at where the steel block started to move. The lift height H_l was then recorded. The test was repeated five times to reduce the measurement error.

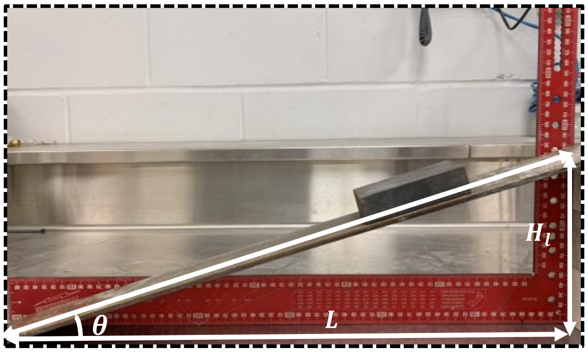

Figure 4.27: The tilt test with a steel block and a steel plate

The static friction coefficient is calculated by (Ibrahim Dickey et al., 2011):

$$\mu_s = \frac{H_l}{L} \tag{4.26}$$

where μ_s is the static friction coefficient, H_l is the lift height, L is distance between the vertex at the angle θ and the vertex at the vertical angle.

The detailed test results are presented in Table 4.7.

Table 4.7: Test results of a steel block slide on a steel plate

Trials	L (cm)	H_l (cm)	μ_s	Average
1	600	205	0.342	0.341
2	600	205	0.342	
3	600	202	0.337	
4	600	202	0.337	
5	600	208	0.347	

Acknowledgements

The authors acknowledge the financial support from the Natural Sciences and Engineering Research Council of Canada (NSERC RGPIN-2018-06902), Natural Sciences and Engineering Research Council of Canada (NSERC ALLRP 580767 - 22), Fonds de recherche du Québec –

Nature et technologies (FRQNT 2017-MI-202860), and industrial partners of the Research Institute on Mines and the Environment (RIME UQAT – Polytechnique; http://rime-irme.ca).

References

Blackery, J., & Mitsoulis, E. (1997). Creeping motion of a sphere in tubes filled with a Bingham plastic material. Journal of Non-Newtonian Fluid Mechanics, 70(1), 59-77. https://doi.org/https://doi.org/10.1016/S0377-0257(96)01536-4

Bokharaeian, M., Naderi, R., & Csámer, Á. (2021). Numerical experimental comparison of mudflow by smoothed particle hydrodynamics (SPH). International Review of Applied Sciences and Engineering, 13(1), 22-28. https://doi.org/10.1556/1848.2021.00263

Burns, S. J., Piiroinen, P. T., & Hanley, K. J. (2019). Critical time step for DEM simulations of dynamic systems using a Hertzian contact model. International Journal for Numerical Methods in Engineering, 119(5), 432-451. https://doi.org/10.1002/nme.6056

Capozzi, L. C., Barresi, A. A., & Pisano, R. (2019). Supporting data and methods for the multi-scale modelling of freeze-drying of microparticles in packed-beds. Data Brief, 22, 722-755. https://doi.org/10.1016/j.dib.2018.12.061

Casarin, J., Franco, A., Germer, E., & Pivovarski, R. (2022). Numerical simulation of the particle settling in a Bingham fluid using the two-way coupling CFD-DEM scheme. Journal of Theoretical and Applied Mechanics, 409-422. https://doi.org/10.15632/jtam-pl/150239

Chhabra, R. (2006). Bubbles, drops, and particles in non-Newtonian fluids. https://doi.org/10.1201/9781420015386

Clayton, S., Grice, T. G., & Boger, D. V. (2003). Analysis of the slump test for on-site yield stress measurement of mineral suspensions. International Journal of Mineral Processing, 70(1-4), 3-21. https://doi.org/10.1016/s0301-7516(02)00148-5

Cleary, P. W. (2015). Prediction of coupled particle and fluid flows using DEM and SPH. Minerals Engineering, 73, 85-99. https://doi.org/10.1016/j.mineng.2014.09.005

Cleary, P. W., & Prakash, M. (2004). Discrete-element modelling and smoothed particle hydrodynamics: potential in the environmental sciences. Philos Trans A Math Phys Eng Sci, 362(1822), 2003-2030. https://doi.org/10.1098/rsta.2004.1428

Cleary, P. W., Sinnott, M., & Morrison, R. (2006). Prediction of slurry transport in SAG mills using SPH fluid flow in a dynamic DEM based porous media. Minerals Engineering, 19(15), 1517-1527. https://doi.org/10.1016/j.mineng.2006.08.018

Concha Arcil, F. (2009). Settling velocities of particulate systems. KONA Powder and Particle Journal, 27, 18-37. https://doi.org/10.14356/kona.2009006

Cundall, P. A., & Strack, O. D. L. (1979). A discrete numerical model for granular assemblies. Géotechnique, 29(1), 47-65. https://doi.org/10.1680/geot.1979.29.1.47

Dedegil, M. Y. (1987). Drag coefficient and settling velocity of particles in non-Newtonian suspensions. Journal of Fluids Engineering, 109(3), 319-323. https://doi.org/10.1115/1.3242667

Dhaouadi, W., Marteau, E., Kolvenbach, H., Choukroun, M., Molaro, J. L., Hodyss, R., & Schulson, E. M. (2021). Discrete element modeling of planetary ice analogs: mechanical behavior upon sintering. Granular Matter, 24(1). https://doi.org/10.1007/s10035-021-01167-6

Di Felice, R. (1994). The voidage function for fluid-particle interaction systems. International Journal of Multiphase Flow, 20(1), 153-159. https://doi.org/https://doi.org/10.1016/0301-9322(94)90011-6

Domínguez, J., Fourtakas, G., Altomare, C., Canelas, R., Tafuni, A., García Feal, O., Martínez-Estévez, I., Mokos, A., Vacondio, R., Crespo, A., Rogers, B., Stansby, P., & Gesteira, M. (2021). State-of-the-art SPH solver DualSPHysics: from fluid dynamics to multiphysics problems.

Ferreira, V. O., Geitani, T. E., Silva, D., Blais, B., & Lopes, G. C. (2023). In-depth validation of unresolved CFD-DEM simulations of liquid fluidized beds. Powder Technology, 426. https://doi.org/10.1016/j.powtec.2023.118652

Fonceca Junior, J., Maza, D., & Hidalgo, R. (2021). Modeling particle-fluid interaction in a coupled CFD-DEM framework. EPJ Web of Conferences, 249, 09004. https://doi.org/10.1051/epjconf/202124909004

Gingold, R. A., & Monaghan, J. J. (1977). Smoothed particle hydrodynamics: theory and application to non-spherical stars. Monthly Notices of the Royal Astronomical Society, 181(3), 375-389. https://doi.org/10.1093/mnras/181.3.375

He, Y., Bayly, A. E., Hassanpour, A., Muller, F., Wu, K., & Yang, D. (2018). A GPU-based coupled SPH-DEM method for particle-fluid flow with free surfaces. Powder Technology, 338, 548-562. https://doi.org/10.1016/j.powtec.2018.07.043

He, Y. B., Laskowski, J. S., & Klein, B. (2001). Particle movement in non-Newtonian slurries: the effect of yield stress on dense medium separation. Chemical Engineering Science, 56(9), 2991-2998. https://doi.org/https://doi.org/10.1016/S0009-2509(00)00479-6

H. Hertz. (1882) “Uber die beruhrung fester elastischer korper (On the contact of elastic solids),” J Reine Angew Math, Vol. 92, pp. 156-171.

Ibrahim Dickey, R. D., Jackson, R. L., & Flowers, G. T. (2011). Measurements of the static friction coefficient between tin surfaces and comparison to a theoretical model. Journal of Tribology, 133(3). https://doi.org/10.1115/1.4004338

Jajcevic, D., Siegmann, E., Radeke, C., & Khinast, J. G. (2013). Large-scale CFD–DEM simulations of fluidized granular systems. Chemical Engineering Science, 98, 298-310. https://doi.org/10.1016/j.ces.2013.05.014

Kloss, C., Goniva, C., König, A., Amberger, S., & Pirker, S. (2012). Models, algorithms and validation for opensource DEM and CFD-DEM. Progress in Computational Fluid Dynamics, 12, 140-152. https://doi.org/10.1504/PCFD.2012.047457

Li, L. (2022). Special issue on numerical modeling in civil and mining geotechnical engineering. Processes, 10(8). https://doi.org/10.3390/pr10081571

Li, Y., Xu, Y., & Thornton, C. (2005). A comparison of discrete element simulations and experiments for ‘sandpiles’ composed of spherical particles. Powder Technology, 160(3), 219-228. https://doi.org/10.1016/j.powtec.2005.09.002

Machač, I., Ulbrichová, I., Elson, T. P., & Cheesman, D. J. (1995). Fall of spherical particles through non-Newtonian suspensions. Chemical Engineering Science, 50(20), 3323-3327. https://doi.org/https://doi.org/10.1016/0009-2509(95)00168-5

Marinack, M. C., Musgrave, R. E., & Higgs, C. F. (2013). Experimental investigations on the coefficient of restitution of single particles tribology transactions, 56(4), 572-580. https://doi.org/10.1080/10402004.2012.748233

Mindlin, R.D. (1949) Compliance of elastic bodies in contact. Transactions of the ASME, Journal of Applied Mechanics, 16, 259-268.

Minkin, L., & Sikes, D. (2018). Coefficient of rolling friction - lab experiment. American Journal of Physics, 86(1), 77-78. https://doi.org/10.1119/1.5011957

Moreira, A. B., Leroy, A., Violeau, D., & Taveira-Pinto, F. d. A. (2020). Overview of large-scale smoothed particle hydrodynamics modeling of dam hydraulics. Journal of Hydraulic Engineering, 146(2). https://doi.org/10.1061/(asce)hy.1943-7900.0001658

Nguyen, G. T., Chan, E. L., Tsuji, T., Tanaka, T., & Washino, K. (2021). Resolved CFD–DEM coupling simulation using volume penalisation method. Advanced Powder Technology, 32(1), 225-236. https://doi.org/10.1016/j.apt.2020.12.004

Ohno, K., Nitta, T., & Nakai, H. (2017). SPH-based fluid simulation on GPU using verlet list and subdivided cell-linked list. 2017 Fifth International Symposium on Computing and Networking (CANDAR).

Okesanya, T., Kuru, E., & Sun, Y. (2020). A new generalized model for predicting the drag coefficient and the settling velocity of rigid spheres in viscoplastic fluids. SPE Journal, 25(06), 3217-3235. https://doi.org/10.2118/196104-PA

Park, S.-H., Jo, Y. B., Ahn, Y., Choi, H. Y., Choi, T. S., Park, S.-S., Yoo, H. S., Kim, J. W., & Kim, E. S. (2020). Development of multi-GPU–based smoothed particle hydrodynamics code for nuclear thermal hydraulics and safety: potential and challenges. Frontiers in Energy Research, 8. https://doi.org/10.3389/fenrg.2020.00086

Pashias, N., Boger, D. V., Summers, J. M., & Glenister, D. J. (1996). A fifty cent rheometer for yield stress measurement. Journal of Rheology, 40, 1179-1189.

Peng, C., Zhan, L., Wu, W., & Zhang, B. (2021). A fully resolved SPH-DEM method for heterogeneous suspensions with arbitrary particle shape. Powder Technology, 387, 509-526. https://doi.org/10.1016/j.powtec.2021.04.044

Peng, Z., Doroodchi, E., Luo, C., & Moghtaderi, B. (2014). Influence of void fraction calculation on fidelity of CFD-DEM simulation of gas-solid bubbling fluidized beds. AIChE Journal, 60(6), 2000-2018. https://doi.org/10.1002/aic.14421

Picabea, J., Maestri, M., Cassanello, M., Salierno, G., De Blasio, C., Cardona, M. A., Hojman, D., & Somacal, H. (2022). Validation of CFD-DEM simulation of a liquid–solid fluidized bed by dynamic analysis of time series. Particuology, 68, 75-87. https://doi.org/10.1016/j.partic.2021.11.003

Platzer, F., & Fimbinger, E. (2021). Modelling pasty material behaviour using the discrete element method. Multiscale Science and Engineering, 3(2), 119-128. https://doi.org/10.1007/s42493-021-00064-7

Potvin, Y., Thomas, E., Fourie, A., & Australian Centre for, G. (2005). Handbook on mine fill. Australian Centre for Geomechanics Nedlands, Western Australia.

Rackl, M., & Hanley, K. J. (2017). A methodical calibration procedure for discrete element models. Powder Technology, 307, 73-83. https://doi.org/https://doi.org/10.1016/j.powtec.2016.11.048

Robb, D. M., Gaskin, S. J., & Marongiu, J.-C. (2016). SPH-DEM model for free-surface flows containing solids applied to river ice jams. Journal of Hydraulic Research, 54(1), 27-40. https://doi.org/10.1080/00221686.2015.1131203

Robinson, M., Luding, S., & Marco Ramaioli, M. (2013). Grain sedimentation with SPH-DEM and its validation.

Salamat, J., & Genç, B. (2023). Numerical simulation of granular flow in concrete batching plant via discrete element method. The European Journal of Research and Development, 3(2), 11-28. https://doi.org/10.56038/ejrnd.v3i2.219

Sandeep, C. S., Senetakis, K., Cheung, D., Choi, C. E., Wang, Y., Coop, M. R., & Ng, C. W. W. (2021). Experimental study on the coefficient of restitution of grain against block interfaces for natural and engineered materials. Canadian Geotechnical Journal, 58(1), 35-48. https://doi.org/10.1139/cgj-2018-0712

Stokes, G. G. (1844). On the effect of the internal friction of fluids on the motion of pendulums. Pitt Press. https://books.google.ca/books?id=C1PLzgEACAAJ

Trujillo-Vela, M. G., Galindo-Torres, S. A., Zhang, X., Ramos-Cañón, A. M., & Escobar-Vargas, J. A. (2020). Smooth particle hydrodynamics and discrete element method coupling scheme for the simulation of debris flows. Computers and Geotechnics, 125, 103669. https://doi.org/https://doi.org/10.1016/j.compgeo.2020.103669

Tsuji, Y., Kawaguchi, T., & Tanaka, T. (1993). Discrete particle simulation of two-dimensional fluidized bed. Powder Technology, 77(1), 79-87. https://doi.org/https://doi.org/10.1016/0032-5910(93)85010-7

Valdez-Balderas, D., Domínguez, J. M., Rogers, B. D., & Crespo, A. J. C. (2013). Towards accelerating smoothed particle hydrodynamics simulations for free-surface flows on multi-GPU clusters. Journal of Parallel and Distributed Computing, 73(11), 1483-1493. https://doi.org/10.1016/j.jpdc.2012.07.010

Valentik, L., & Whitmore, R. L. (1965). The terminal velocity of spheres in Bingham plastics. British Journal of Applied Physics, 16(8), 1197. https://doi.org/10.1088/0508-3443/16/8/320

Washino, K., Chan, E. L., Miyazaki, K., Tsuji, T., & Tanaka, T. (2016). Time step criteria in DEM simulation of wet particles in viscosity dominant systems. Powder Technology, 302, 100-107. https://doi.org/10.1016/j.powtec.2016.08.018

Wu, D., Chen, W., Glowinski, D., & Wheeler, C. (2020). Modelling mineral slurries using coupled discrete element method and smoothed particle hydrodynamics. Powder Technology, 364, 553-561. https://doi.org/10.1016/j.powtec.2020.02.011

Zhang, Y., & Li, L. (2023). Experimental study on the natural mixing behaviour of waste rocks poured in a paste backfill. International Journal of Mining, Reclamation and Environment, 1-25. https://doi.org/10.1080/17480930.2023.2235847

Zhang, Z., & Yin, T. (2018). A coupled CFD–DEM simulation of slurry infiltration and filter cake formation during slurry shield tunneling. Infrastructures, 3(2). https://doi.org/10.3390/infrastructures3020015

Zhao, J., & Shan, T. (2013). Coupled CFD–DEM simulation of fluid–particle interaction in geomechanics. Powder Technology, 239, 248-258. https://doi.org/10.1016/j.powtec.2013.02.003

Zhao, T., Houlsby, G. T., & Utili, S. (2014). Investigation of granular batch sedimentation via DEM–CFD coupling. Granular Matter, 16(6), 921-932. https://doi.org/10.1007/s10035-014-0534-0

Zhou, S., & Li, L. (2022). Numerical investigation on the impact of tailings slurry on catch dams built at the downstream of a breached tailings pond. Processes, 10(5). https://doi.org/10.3390/pr10050898

Zhu, H. P., Zhou, Z. Y., Yang, R. Y., & Yu, A. B. (2008). Discrete particle simulation of particulate systems: A review of major applications and findings. Chemical Engineering Science, 63(23), 5728-5770. https://doi.org/10.1016/j.ces.2008.08.006

CHAPTER 5 ARTICLE 3: OPTIMIZATION OF DISCRETE ELEMENT METHOD MODEL TO OBTAIN STABLE AND RELIABLE NUMERICAL RESULTS OF MECHANICAL RESPONSE OF GRANULAR MATERIALS

Yuyu Zhang and Li Li

The article has been published in *Minerals*, 2024, 14 (8), 758; https://doi.org/10.3390/min14080758 (registering DOI)

Abstract

Discrete element method (DEM) is largely used to simulate the geotechnical behavior of granular materials. However, numerical modeling with this type of code is expensive and time consuming, especially when fine particles are involved. This leads researchers to make use of different approaches to shorten the time of calculation without verifying the stability and reliability of numerical results even though compromise between time of calculation and accuracy is commonly claimed. The particle size distribution (PSD) curve of studied granular material is completely ignored or arbitrarily cut. It is unclear if the ensued numerical results are still representative of the studied granular materials. Additionally, one can see a large number of numerical models established on a base of calibration by ignoring the physical meaning and even measured values of some model parameters. The representativeness and reliability of the ensued numerical results are questionable. All these partly contribute to reducing the public's confidence in numerical modeling. In this study, a methodology is illustrated to obtain an optimal DEM model, which minimizes the time of calculation and ensures stable and reliable numerical results for the mechanical behavior of a waste rock. The results indicate that the PSD curve of studied waste rock can indeed be cut by excluding a portion of fine particles, while the Young's modulus of waste rock particles can also be decreased to accelerate the numerical calculations. A physical explanation on why the time of calculation can be shortened by reducing the Young's modulus of waste rock particles is for the first time given. Nevertheless, the PSD cut, reduction of Young's modulus, and time step must be determined through their sensitivity analyses to ensure stable and reliable results with the shortest time of calculation. In addition, it is important to minimize the number of model parameters determined through the process of calibration, especially when they have physical meanings and can be obtained by measurement. In this study, the only model parameter having a clear physical meaning but difficult to measure is the rolling resistance coefficient. Its value has to be obtained through a process of calibration against some experimental results obtained by repose angle tests on a waste rock. The validity and predictability of the calibrated numerical model have been successfully verified against additional experimental results.

Keywords: Discrete element method (DEM); DEM model validation; Optimal cut of PSD curve; Optimal time step; Optimal Young's modulus; Predictability of DEM model.

5.1 Introduction

In several industries such as chemical engineering, powder engineering and geotechnical engineering, one usually needs to deal with granular materials (Kuo et al. 2002; Jing 2003, O'Sullivan 2011; Lu et al. 2015; Svanberg et al. 2020; Qiu and Pabst 2022). Over the years, one sees increasing use of discrete element method (DEM; Cundall and Strack 1979) to analyze the mechanical behavior of granular materials in geotechnical engineering. The main advantage of DEM is that the movements of individual particles along with the interactions between particles can be captured.

Despite the advantages of DEM model compared to continua models, its application suffers from the requirement of huge and expensive sources of computation (Malone and Xu 2008; Siegmann et al. 2021). For a poorly graded and coarse granular material, the narrow particle size distribution (PSD) curve can be readily reproduced by DEM models and the time of computing can also be reasonable. For many cases, especially in geotechnical engineering with granular geomaterials like rockfill or waste rock, the PSD curves can be very wide with fine particles as small as a few microns and coarse particle as large as several centimeters or even meters (Aubertin 2013; James et al. 2013; Deiminiat and Li 2022; Deiminiat et al. 2020, 2022, 2023). Numerical reproduction of the full PSD curve by DEM model becomes extremely heavy, if not totally impossible. The time of computing can also be extremely long (Radeke et al. 2010; Feng and Owen 2014; Roessler and Katterfeld 2018) even with powerful computing technologies, such as multi-graphical units processors and parallel computing (Cleary et al. 2017; Tian et al. 2017). This partly explains the few and very limited application of DEM model to treat full-scale industrial problems in geotechnical engineering because the full consideration of the PSD curves of actual granular materials is still impossible (Roessler and Katterfeld 2018; Houhamdi et al. 2022).

Subsequently, an approach commonly adopted in DEM modeling is to exclude a portion of fine particles in an arbitrary way (e.g., Brosh et al. 2014; Utili et al. 2015; Thoeni et al. 2019; Wang et al. 2021; Taha et al. 2022). The computation time can be significantly reduced, but the stability, reliability, and representativeness of the obtained numerical results are questionable.

Another widely used approach to shorten the time of DEM computing is to reduce the stiffness of particles, rather than using the actual value of particle stiffness (Malone and Xu 2008). Physically, reducing particle stiffness means that the simulated particles are softer than those of actual material. The system could indeed reach a static equilibrium faster than that of actual material. This explains why the time of calculation to equilibrium can be shortened. But the interactions between particles and the intermediate responses in terms of forces and deformation should be different from those of the actual materials. Surprisingly, several studies showed that the same results can be obtained by reducing the stiffness of particles (e.g., Kuo et al. 2002; Härtl and Ooi 2008; Kobayashi et al. 2013; Yan et al. 2015; Washino et al. 2018). If all these are true, can we reduce the value of particle stiffness as small as a value close to zero? If not, what is the minimum value to ensure stable, reliable and representative numerical results?

In DEM modeling, time step is another factor that can affect the stability and reliability of numerical results. A too small-time step leads to unnecessarily long time of calculation, whereas a too large time step can result in unstable and unreliable numerical results (Burns and Hanley 2016; Burns et al. 2019). Optimal time step should be determined to minimize the time of computing and to ensure stable and reliable numerical results (Zhang and Li 2024). However, it is seldom mentioned in published works with DEM modeling. Probably, the default time step value given in most DEM codes based on Rayleigh time is used (Li et al. 2005; Washino et al. 2016; Rackl and Hanley 2017). It is however unclear if the default value is always optimal to minimize the time of computing and to ensure stable and reliable numerical results.

Finally, one notes that numerous DEM simulations were realized without making distinction between calibration and prediction. In addition, little efforts were made to minimize the number of model parameters determined through the process of calibration. It is thus not rare to see the determination of some model parameters such as particle density, Poisson’s ratio, static friction coefficient, etc. in an arbitrary way or through a process of calibration even though these model parameters have clear physical meaning and can be readily obtained thorough laboratory tests. The uncertainty of the numerical model is high, and the credibility of the numerical results is low because good agreements between numerical and experimental results can be achieved by different combinations of these calibrated model parameters. All these along with the previously mentioned practices contribute to compromise the public’s confidence in numerical modeling, a phenomenon quite special in geotechnical engineering (Li 2022).

In this study, a commercialized DEM code, named EDEM (Altair EDEM 2022) was chosen to simulate the mechanical behavior of a coarse granular material made of waste rock. The above-mentioned aspects will be addressed in order to present a methodology for constructing an optimal numerical model, which ensures stable and reliable numerical results with the minimum time of computing. The determination of model parameters is also addressed to reduce the uncertainty of numerical modeling. All the model parameters that have physical meanings and have been obtained by laboratory tests or by considering typical values. The only model parameter having a clear physical meaning but difficult to measure is the rolling resistance coefficient. Its value has to be obtained through a process of calibration against some experimental results obtained by repose angle tests on a waste rock. The validity and predictability of the calibrated numerical model have been successfully verified against additional experimental results.

5.2 Validation of the EDEM

Before conducting any numerical modeling, it is important for any new users to undergo sufficient training to know how to make use of a numerical model to produce stable and reliable numerical results. This training can be achieved through the process of numerical model validation against analytical solutions. This step, usually considered as unnecessary by a large number of researchers, is crucial, especially for new users, to learn how to use the code correctly, to identify any errors or limitations in the numerical model, and to learn how to obtain an optimal numerical model, which ensures stable and reliable numerical results with the shortest time of calculation (Li 2022).

In this study, the validation of the EDEM code was realized against the analytical solutions developed for calculating the normal and tangential forces at the contact between two spheres, a process similar to the works conducted by Chung and Ooi (2011).

Figure 5.1 shows the physical model of two identical spheres moving with an initial speed of 10 m/s in an opposite direction with their centers aligned in a plane parallel to their moving direction.

In the figure, R is the radius of the spheres, E, the Young's modulus, ρ, the density, and ν, the Poisson's ratio.

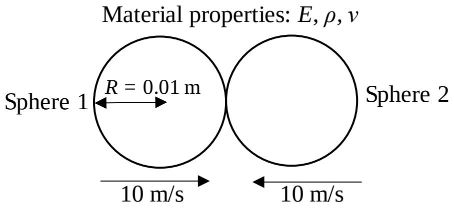

Figure 5.1: A physical model of two identical spheres moving with an initial speed of 10 m/s in an opposite direction with their centers aligned in a plane parallel to their moving direction (taken from Chung and Ooi 2011)

Table 5.1 shows the physical and mechanical property parameters of spheres, used for the validation of the EDEM model. It needs to be noted here, the purpose of validation is to examine if the numerical model can produce the same results as the analytical solution, as long as the numerical model and analytical solution use the same given parameters values. The parameters values used for validation can thus be arbitrary and even fictive.

Table 5.1: Physical parameters of two identical spheres having a radius of 0.01 m collided with an initial speed of 10 m/s in an opposite direction

Material of particles	Young's modulus, E (Pa)	Density, ρ (kg/m^3)	Poisson's ratio, ν
Material 1	2.0×10^{11}	7750	0.3
Material 2	4.8×10^{10}	2800	0.2
Material 3	2.0×10^{10}	2500	0.25

An analytical solution for calculating the normal contact force between two spheres, F_n, has been given as follows (Hertz 1882; Timoshenko et al. 1951):

$$F_n = \frac{4}{3}\delta_n^{\frac{3}{2}} \frac{E_1 E_2}{E_2(1-\nu_1^2) + E_1(1-\nu_2^2)} \sqrt{\frac{R_1 R_2}{R_1 + R_2}} \tag{5.1}$$

where δ_n is the overlap of normal contact; E_1 and E_2 are the Young's modulus of sphere 1 and sphere 2, respectively; ν_1 and ν_2 are the Poisson's ratios of sphere 1 and sphere 2, respectively; R_1 and R_2 are the radius of sphere 1 and sphere 2, respectively.

As a special case with two identical spheres having $E = E_1 = E_2$, $\nu = \nu_1 = \nu_2$, and $R = R_1 = R_2$, Eq. 1 reduces to:

$$F_n = \frac{\sqrt{2R}}{3}\delta_n^{\frac{3}{2}} \frac{E}{1-\nu^2} \tag{5.2}$$

Figure 5.2 presents a numerical model of EDEM to reproduce the physical model presented in Fig. 1 along with the material parameters given in Table 5.1. As the problem does not contain any uncertainty in terms of geometrical (radius) and material properties (density, Young's modulus and Poisson's ratio) for both physical and numerical models, a perfect agreement between numerical and analytical solutions can be expected as long as the numerical results are stable and reliable. This requires sensitivity analyses of model parameters in order for obtaining an optimal numerical model, which ensures stable and reliable numerical results with shortest time of computing.

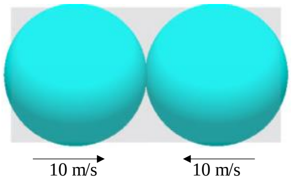

Figure 5.2: Numerical model of the physical model presented in Figure 5.1, built with EDEM by considering the parameters given in Table 5.1

For this simple problem with two spheres, the only need for optimization of the numerical model is to perform sensitivity analysis of time step to find the optimal time step. For one hand, time step should be as large as possible to shorten the time of computing. On the other hand, the stability and reliability of numerical results cannot be guaranteed if the time step is not small enough. The optimal time step corresponds to the largest time step, which can ensure stable and reliable numerical results with the shortest time of computation.

Figure 5.3 presents the variation of the normal contact force F_n (Figure 5.3a) and normal contact overlap δ_n (Figure 5.3b) of the spheres as function of time step for the three cases presented in Table 5.1. For spheres with material 1, the numerical results (both normal contact force and normal overlap) become stable when the time step is smaller than 1.08×10^{-7} s. Further reduction of time step does not lead to any change in the numerical results. The optimal time step for material 1 is thus determined as 1.08×10^{-7} s. Similarly, for the cases of material 2 and 3, the optimal time steps are determined as 1.29×10^{-7} and 1.91×10^{-7} s, respectively. It is noted that the optimal time step changes as the sphere material changes. Sensitivity analysis of time step is thus necessary, case by case, to ensure stable and reliable numerical results with the shortest time of calculations.

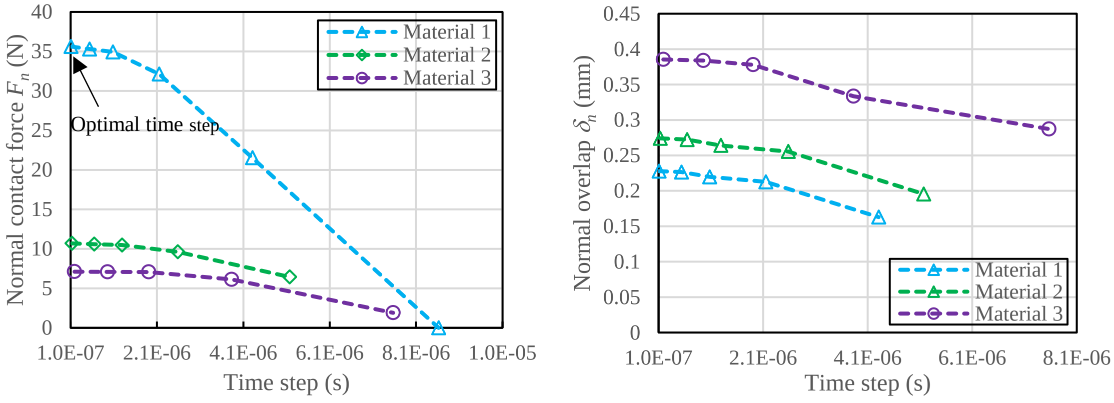

(a) (b)

Figure 5.3: Variation of (a) normal contact force and (b) normal contact overlap as function of time step for the case of spheres with different materials

Figure 5.4 presents the variation of normal contact force F_n as function of normal contact overlap δ_n, both obtained by the numerical modeling with the optimal time step. On the figure is plotted also the variation of the normal contact force F_n predicted by applying the analytical solution (Equation (5.2)) as function of normal contact overlap δ_n. Perfect agreements are obtained between the analytical and numerical results for all the three cases of Table 5.1. The validity of the EDEM model is thus verified, at least partly.

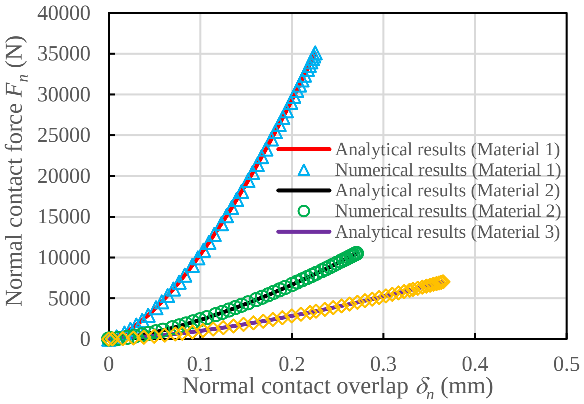

Figure 5.4: Variation of normal contact force F_n as function of normal contact overlap δ_n, both obtained by the numerical modeling with the optimal time step and predicted by applying the analytical solution (equation (5.2))

Figure 5.5 presents another physical model with two identical spheres moving with an initial speed of 10 m/s in opposite direction with their centers not aligned with their movement direction. The same spheres geometry and materials properties presented in Table 5.1 are used here.

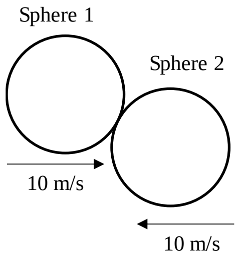

Figure 5.5: A physical model of two identical spheres moving with an initial speed of 10 m/s in an opposite direction with their centers not aligned with their movement direction

The analytical solution for calculating the tangential force at the contact between the two spheres, F_t, can be expressed as follows (Mindlin 1949; Mindlin and Deresiewicz 1953):

$$F_t = -S_t \delta_t \tag{5.3}$$

where δ_t is the tangential overlap; S_t is the tangential stiffness expressed as:

$$S_t = \frac{8G_1G_2}{G_2(2-\nu_1)+G_1(2-\nu_2)}\sqrt{\frac{R_1R_2}{R_1+R_2}\delta_n} \tag{5.4}$$

where G_1 and G_2 are the shear modulus of sphere 1 and sphere 2, respectively. As a special case with two identical spheres having $G = G_1 = G_2$, $\nu = \nu_1 = \nu_2$, and $R = R_1 = R_2$, Eq. 4 reduces to:

$$S_t = \frac{2G}{2-\nu}\sqrt{2R\delta_n} \tag{5.5}$$

where G is expressed as follows:

$$G = \frac{E}{2(1+\nu)} \tag{5.6}$$

Figure 5.6 shows a numerical model of the physical model presented in Figure 5.5, built with EDEM by considering the parameters given in Table 5.1.

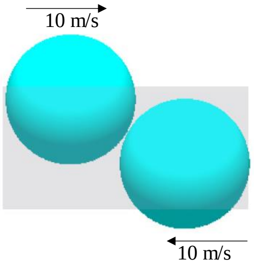

Figure 5.6: Numerical model of the physical model presented in Figure 5.5, built with EDEM by considering the parameters given in Table 5.1

Sensitivity analyses of time step lead to optimal time steps of 1.08×10^{-7}, 1.29×10^{-7}, and 1.91×10^{-7} s for the cases of Materials 1, 2, and 3, respectively. Figure 5.7 presents the variation of the tangential contact force F_t as a function of tangential contact overlap δ_t, both obtained by numerical modeling with the optimal time step. The tangential contact force F_t as a function of tangential contact overlap δ_t, predicted by applying the analytical solution (equation (5.5)) is also plotted on the figure. The perfect agreement between the numerical and analytical results indicate once again that the EDEM model is validated against analytical solutions.

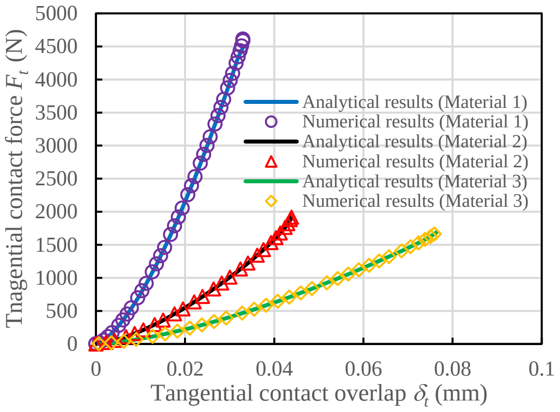

Figure 5.7: Variation of the tangential contact force F_t as a function of tangential contact overlap δ_t, both obtained by the numerical modeling with the optimal time step and predicted by applying the analytical solution (equation (5.5))

5.3 Application of the EDEM code for simulating the mechanical behavior of granular material

In the previous section, the validity of EDEM code has been verified against analytical solutions. In this section, the power or applicability of the numerical model will be tested through the numerical reproduction of experimental results.

In this study, two series of tests performed with a waste rock taken from a mine located at the northwest of Québec, Canada. The test results will be reproduced by numerical modeling with the EDEM code. The experimental results obtained by the first series of tests will be used to calibrate the rolling resistance coefficient of waste rock particle, an unmeasurable model parameter. The experimental results obtained by the second series of tests are then used to test the predictability of the calibrated numerical model.

Figure 5.8 presents the PSD curve of the tested waste rock in terms of accumulated percentage by mass (Figure 5.8a) and percentage by particle number (Figure 5.8b) after excluding oversized and undersized particle in order for the particle sizes in the range of 0.315 to 8.0 mm. Figure 5.8b shows the variation of percentage of particle numbers as function of particle size in form of histogram. It can be fitted to a Gaussian curve by applying the normal distribution function (Berger and Hrenya 2014):

$$f(d) = \frac{1}{\sigma\sqrt{2\pi}} \exp\,[-\frac{(d-\mu)^2}{2\sigma^2}] \tag{5.7}$$

where *f(d)* is the probability function of particle diameter, *d*; μ is the mean diameter of particles; σ is the standard deviation.

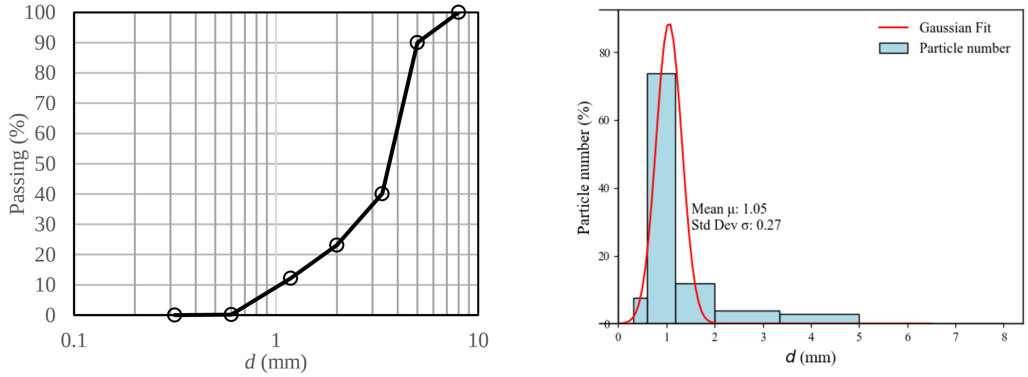

(a) (b)

Figure 5.8: PSD curves of tested waste rock in terms of: (a) accumulated percentage by mass and (b) percentage by particle number

The first series of tests were conducted to obtain the repose angle of the tested waste rock. Figure 5.9 shows a schematic presentation (Figure 5.9a) and pictures (Figure 5.9b) of waste rock repose angle tests. The tests were perfomed with a total mass of 300.5 g of waste rock, placed in a funnel having an open diameter of 19 cm on top, an open diameter of 4.0 cm at the base, and an overall height of 12 cm (Figure 5.9a). The tests were realized by gently (around 0.01 m/s) lifting the funnel in the vertical direction until the empty of the funnel, resulting in the formation of a waste rock pile on the table (Figure 5.9b). The height *H* and the diameter *D* of the waste rock pile were measured, respectively. The repose angle can then be calculated. The test was repeated five times and one obtains by measurmeent an average repose angle θ of 36.41° for the tested waste rock.

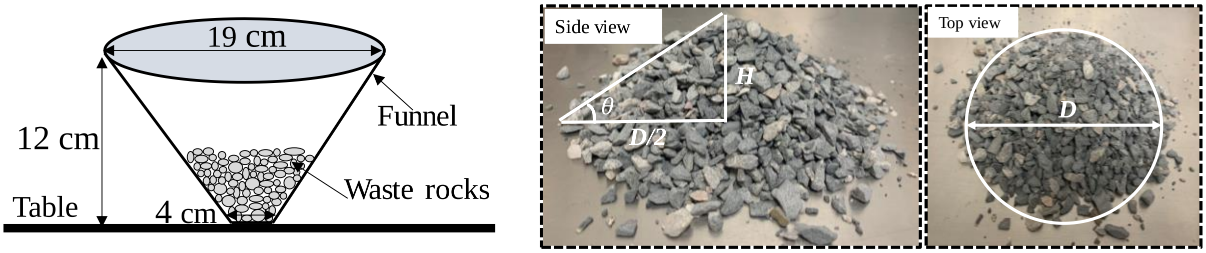

(a) (b)

Figure 5.9: Waste rock repose angle test: (a) schematic presentation; (b) pictures of a repose angle test

Table 5.2 presents the material parameters necessary for the EDEM model. Once again, the parameters which have clear physical meanings need be determined or estimated by conducting experimental tests instead of being considered as arbitrary parameters obtained by calibration process. In Table 5.2, the particle density of tested waste rock was measured in our laboratory. The Young’s modulus, Poisson’s ratio and static friction coefficient of the tested waste rock were measured by Major and Knupp (2008). The restitution coefficient of tested waste rock was determined by the drop tests results conducted by Sandeep et al. (2021). The rolling resistance coefficient of waste rock is unknown. This parameter is used to consider the shape effects of the non-spherical waste rock particle and has to be calibrated against the experimental results. The calibration of rolling resistance coefficient will be introduced after.

Table 5.2: Model and material parameters necessary for EDEM model

	Model and material parameter	Values	Determination
Waste rock particle parameter	Particle density, ρ (kg/m^3)	2760	Measured
	Young's modulus, E (GPa)	46.8	Measured[†]
	Poisson's ratio, ν	0.19	Measured[†]
Particle – particle interaction	Restitution coefficient, μ_e	0.79	Measured[‡]
	Static friction coefficient, μ_s	0.466	Measured[†]
	Rolling resistance coefficient, μ_r	--	Unknown

Note: [†]by Major and Knupp (2008) for the same waste rock; [‡] by Sandeep et al. (2021) for the same waste rock.

To numerically reproduce these experimental results, the first task is to generate waste rock particles that have a PSD same as that of the tested waste rock shown in Figure 5.8 in terms of percentage by mass (Figure 5.8a) and percentage by particle numbers (Figure 5.8b). It is possible in this study because the tested waste rock was obtained by intentionally excluding the oversized (large) and undersized (small) particles. For most cases, it is impossible to generate particles having the full PSD curve of studied material because the fine particles can be small in percentage by mass, but huge in percentage by particles numbers. PSD cut has to be done to exclude a portion of fine particles by assuming that the excluded fine particles do not have any effects on the mechanical behavior of the granular materials. However, its validity needs to be verified. In this study, a good manner of PSD curve will be shown through sensitivity analyses of PSD cut to ensure stable and reliable numerical results.

Figure 5.10 presents five possible cuts to the PSD of the tested waste rock: PSD 1, PSD 2, PSD 3, PSD 4 and PSD 5 with particle sizes ranging from 5.0 to 8.0 mm, 3.35 to 8.0 mm, 2.0 to 8.0 mm, 1.18 to 8.0 mm and 0.315 to 8.00 mm, respectively. PSD 5 is the same as the PSD of the tested waste rock with particle sizes ranging from 0.315 to 8.0 mm.

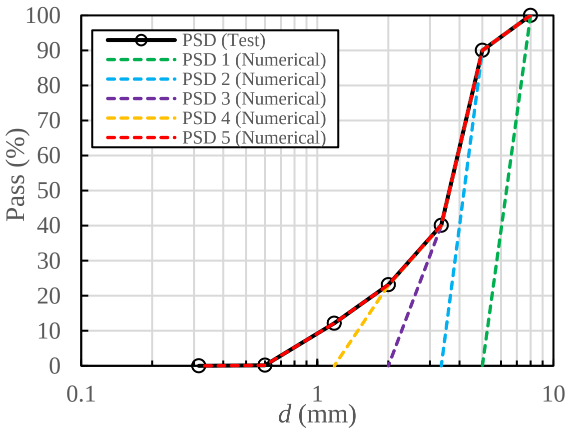

Figure 5.10: Different cuts of PSD curves of tested waste rock used in the numerical model

To generate particles with PSD 1 in EDEM model, one should note that the particles of PSD 1 have sizes varying between 5 and 8 mm. To generate the particles having sizes intermediate between 5 and 8 mm in EDEM, the Gaussian distribution with $\sigma/\mu = 0.25$ obtained from the full PSD of the tested waste rock is used. The same procedure had been applied in the generation of particles of two consecutive sieves for PSD 2 to 5. Figure 5.11 presents the number-weighted PSD generated by EDEM for PSD 1 to 5 using Gaussian distribution. The generated particle numbers are 727, 2578, 5571, 14438 and 44415 for PSD 1, PSD 2, PSD 3, PSD 4, and PSD 5, respectively. One notes that the particle number significantly increases as smaller fine particles are taken into account.

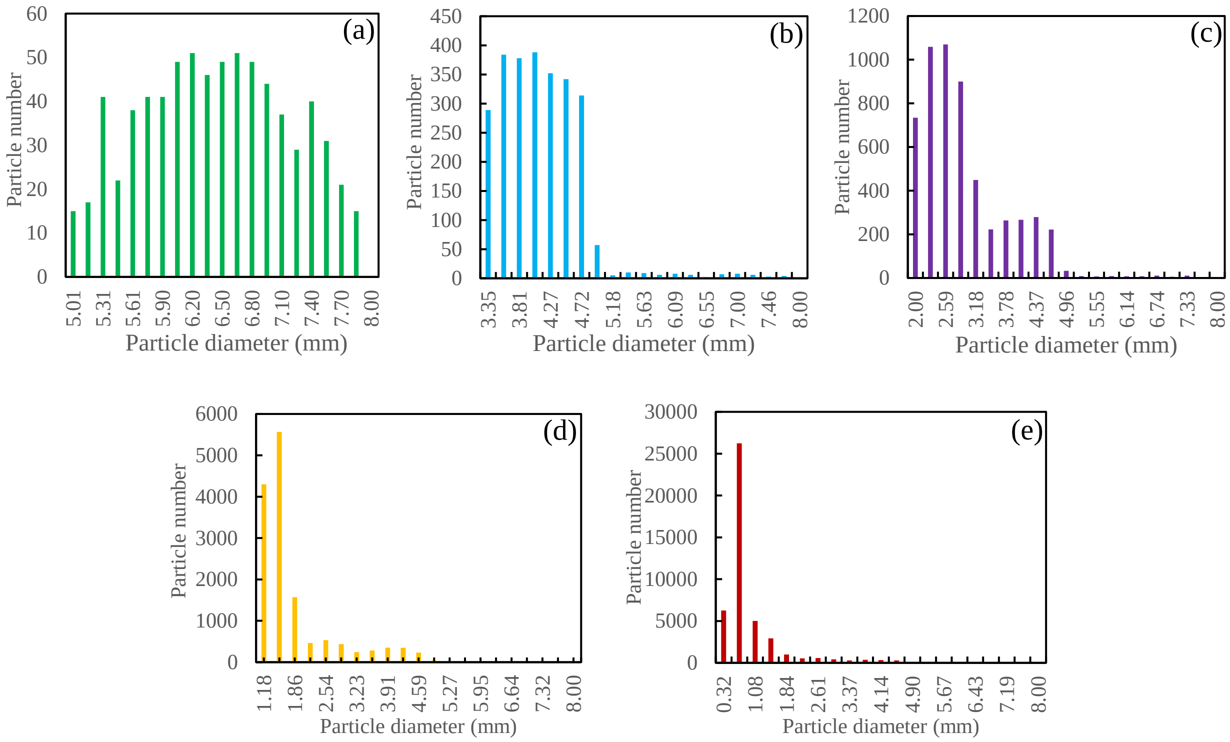

Figure 5.11: Particle number-weighted PSD generated by EDEM to reproduce the different cuts of PSD of the tested waste rock: (a) PSD 1; (b) PSD 2; (c) PSD 3; (d) PSD 4; (f) PSD 5

Figure 5.12 presents the numerical models with the waste rock particles generated by EDEM for the different cuts of PSD. The geometry of the numerical models is the same as the physical model shown in Figure 5.9a. The material and model parameters necessary for the EDEM model have been given in Table 5.2. Spherical particles were used in the simulations to represent the non-spherical waste rocks particles. The unmeasurable angularity of particles will be reflected by the calibration of the rolling resistance coefficient. On the figure is also plotted the numerical model with the waste rock particles generated by EDEM for the full PSD curve (PSD 5). One sees clearly that the particle distributions generated by applying PSD cut become closer to that generated by applying the full PSD curve of the tested waste rock as the excluded fine particle size decreases.

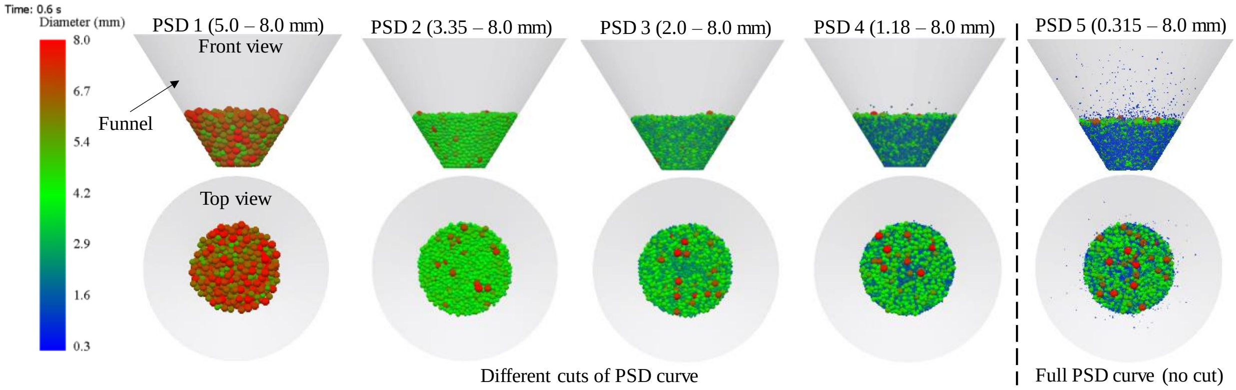

Figure 5.12: Numerical models with the waste rock particles generated by EDEM by applying four different PSD cuts and the full PSD of the tested waste rock

Once the waste rock particles are generated in EDEM model, the flow of particles can be simulated. Figure 5.13 shows the states of the particles generated by EDEM for the case of PSD 1 from the beginning to the end of repose angle test. The waste rock particles were first generated in the funnel by using the dynamic factory of EDEM with a generation rate of 2 kg/s (Figure 5.13a). After then, the funnel was lifted up with a speed of 0.01 m/s in the vertical direction. Figure 5.13b shows the formation of a waste rock pile on the table at an intermediate stage. Figure 5.13c shows the state of the waste rock pile at the end of numerical simulation. The repose angle θ of the waste rock pile was obtained by using the protractor tool in EDEM by clipping the waste rock pile in the center.

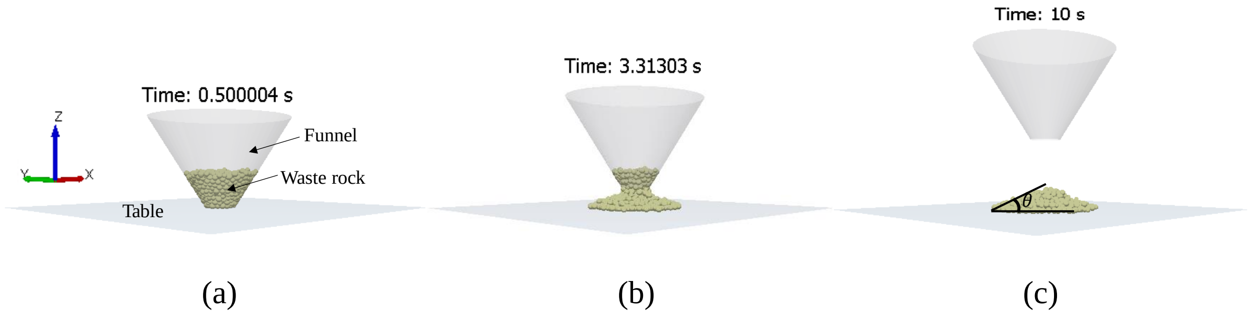

Figure 5.13: Numerical model built with EDEM for case of PSD 1: (a) initial state; (b) intermediate state; (c) final state

The same numerical modeling process for PSD 1 had been repeated for the cases of PSD 2 to 5. In all the cases, time step sensitivity analyses have been done first to ensure stable and reliable numerical results. Figure 5.14 presents the variations of repose angle of waste rock pile as function of time step, obtained by numerical modeling with EDEM for PSD 1 to 5 by using a rolling resistance coefficient of 0.05. For all the cases, the numerical modeling results in a repose angle of 0° when a large time step is used, meaning that all the particles were lost in the numerical simulation due to the overly large time step. For PSD 1, the numerical results become stable when the time step is equal to or smaller than 3.24×10^{-6} s. The optimal time step is thus determined as 3.24×10^{-6} s. Similarly, the optimal time steps are determined as 2.17×10^{-6}, 1.29×10^{-6}, 3.83×10^{-7} and 1.02×10^{-7} s for PSD 2, PSD 3, PSD 4, and PSD 5, respectively. One notes that the optimal time step decreases as the content of fine particles increases. In addition, one notes that the repose angles obtained by the EDEM model by using a rolling resistance coefficient of 0.05 are much smaller that the measured value of $\theta = 36.41°$.

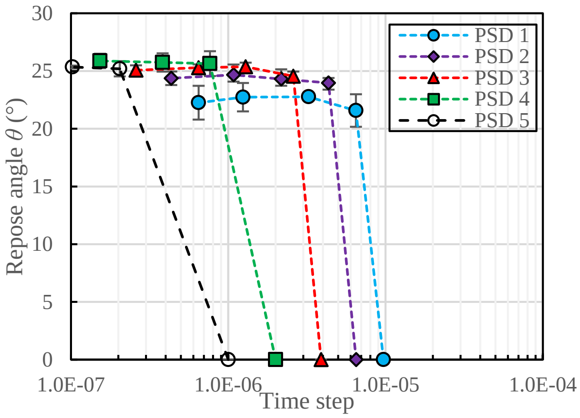

Figure 5.14: Variation of repose angle as function of time step, obtained by numerical simulations with the parameters shown in Table 5.2 and a rolling resistance coefficient of 0.05 for five different cuts of PSD

Figure 5.15 presents the variation of repose angle of waste rock pile as function of PSD cut, obtained by numerical simulations with the optimal time steps for three different rolling resistance coefficients μ_r. One notes that the repose angle of waste rock increases as the content of fine particles increases from PSD 1 to PSD 3. The repose angle becomes stable (constant) at PSD 3, indicating that including more and smaller fine particles does not have any effect on the repose angle of the tested waste rock. The repose angle of the tested waste rock with a full curve of PSD 5 (0.315 – 8.0 mm) can be obtained by using the curve of PSD 3 (2.0 – 8.0 mm) in the numerical model. The optimal cut of PSD thus corresponds to PSD 3 (2.0 – 8.0 mm).

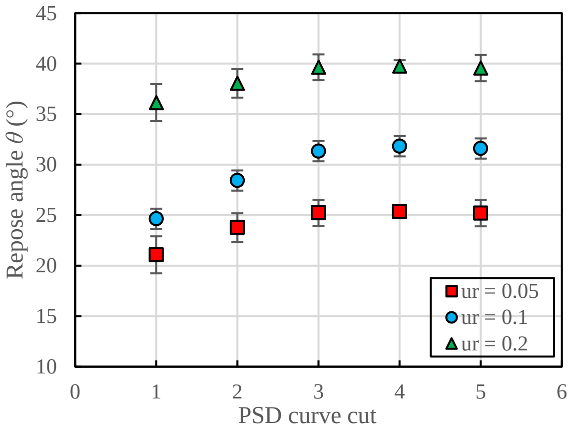

Figure 5.15: Variation of repose angle of waste rock piles as function of PSD cut, obtained by numerical simulations with the parameters shown in Table 5.2 along with the optimal time steps for three different rolling resistance coefficients μ_r

Figure 5.16a presents the variations of repose angle of waste rock with optimal cut of PSD 3 (2.0 – 8.0 mm) as function of time step, obtained by numerical model with different values for the Young's modulus of the tested waste rock. 4.68×10^{10} Pa corresponds to the measured value shown in Table 5.2, while 4.68×10^{3} Pa is obtained by reducing the measured Young's modulus by a factor of 10^{7}. The other input parameters for the EDEM numerical model are given in Table 5.2 along with a rolling resistance coefficient of 0.05. The optimal time steps are determined as 6.48×10^{-7}, 6.48×10^{-6}, 7.0×10^{-6}, 1.30×10^{-5}, 4.10×10^{-5} and 6.48×10^{-5} s for Young's modulus of 4.68×10^{10}, 4.68×10^{8}, 4.68×10^{7}, 4.68×10^{6}, 4.68×10^{5} and 4.68×10^{4} Pa, respectively. The results indicate that the optimal time step decreases as the Young's modulus of waste rock particles increases. This can be explained as follows from the dynamic physics of particles-particles and particles-ground surface interactions:

For particles having large Young's modulus values, the particles are harder. The jumping and inter hitting of particles can be faster and stronger. Long time is necessary to allow the system to settle down and reach a static equilibrium. But short time step is necessary to capture the intermediate responses of particles movement. When one attributes a much smaller value to the waste rock particles, the particles become much softer that those of actual material. The jumping and inter hitting of particles become much slower and weaker. A static equilibrium can be achieved quickly. This explains why the optimal time step becomes longer. More interestingly, this explains well why the time of calculation can be shortened through the reduction of Young’s modulus. Strictly said however, the use of smaller Young’s modulus than the actual value of waste rock particles means the simulation of another physical model, not anymore the original one even though the obtained repose angle can be very close to that obtained by using the actual Young’s modulus as long as the Young’s modulus is not reduced to a value smaller than 4.68×10^7 Pa. Beyond that value, the EDEM model can lead to underestimate of the repose angle, as shown in Figure 5.16b. The optimal Young’s modulus for this mechanical problem can thus be determined as 4.68×10^7 Pa. Numerical modeling with any values smaller than this optimal Young’s modulus cannot guarantee stable and reliable numerical results.

These results and analysis indicate that it is indeed advantageous to use reduced value for Young’s modulus to accelerate the numerical calculations for some specific mechanical problems. Nevertheless, the Young’s modulus of granular materials should not be decreased in an arbitrary way. Otherwise, the stability and reliability of the numerical results cannot be guaranteed. Similar findings have been reported by Lommen et al. (2014).

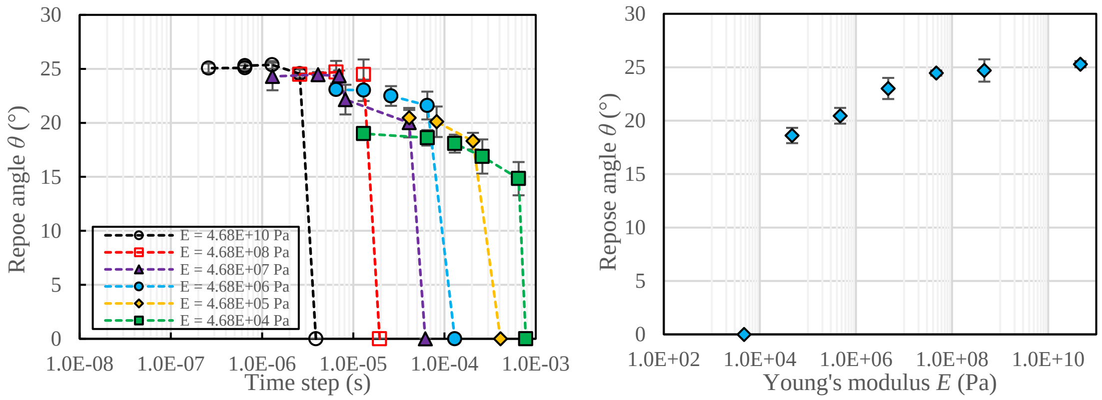

(a) (b)

Figure 5.16: (a) variations of repose angle as function of time step, obtained by numerical model by using the optimal cut of PSD 3 and a rolling resistance coefficient of 0.05 for different Young’s modulus; (b) variation of repose angle as a function of Young’s modulus using optimal time step

Figure 5.17 shows the variation of repose angle of waste rock piles as function of rolling resistance coefficients μ_r, obtained by numerical simulations with the optimal numerical model (i.e. with optimal cut of PSD 3 (2.0 – 8.0 mm), optimal Young’s modulus of 4.68×10^7 Pa and optimal time step of 4.10×10^{-6} s) determined by several sensitivity analyses. The figure is also plotted the measured repose angle of $\theta = 36.41°$ for the tested waste rock. One sees that the best agreement between the numerical and experimental results can be obtained by using a rolling resistance coefficient of $\mu_r = 0.16$.

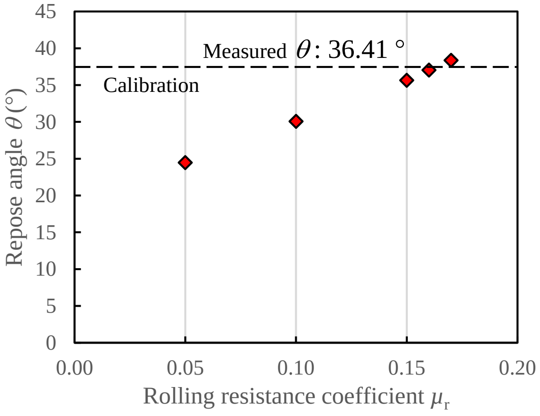

Figure 5.17: Variation of repose angle as function of rolling resistance coefficients μ_r, obtained by numerical simulations with the optimal numerical model (i.e. with optimal time step of 4.10×10^{-6} s, optimal Young's modulus of 4.68×10^{7} Pa, and optimal cut of PSD 3)

The material parameters given in Table 5.2 and the EDEM model along with the optimal cut of PSD 3 (2.0 – 8.0 mm), optimal Young's modulus of 4.68×10^{7} Pa and rolling resistance coefficient of $\mu_r = 0.16$ constitute the calibrated numerical model, which can be applied to predict the mechanical behavior of the tested waste rock in different testing conditions. Its validity and predictability will be verified against another series of tests realized to evaluate the effect of falling height H_F of waste rock on the repose angle of the tested waste rock.

Figure 5.18 shows a schematic presentation of the tests. A total mass of 300.5 g of waste rock was placed in the same funnel as the one used in the first series of tests. The waste rock was then dropped on the table at a falling height of H_F. Figure 5.19 presents the side and top views of waste rock piles generated by dropping the waste rock from three different falling heights. It can be seen that the repose angle θ decreases from 27.9° to 21.2° while the diameter D of waste rock piles increases from 14.5 to 15.5 cm as the falling height increases from 6 to 15.5 cm.

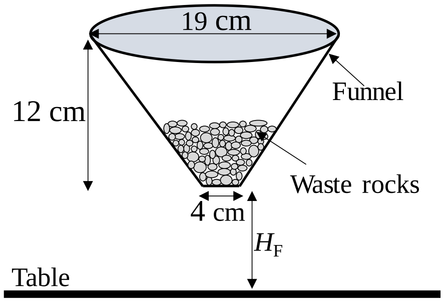

Figure 5.18: Schematic presentation of waste rock dropped at a falling height of H_F

(a) (b) (c)

Figure 5.19: Side and top views of waste rock piles generated by dropping waste rock from different falling heights: (a) H_F = 6 cm; (b) H_F = 10.5 cm; (c) H_F = 15.5 cm

Figure 5.20 presents the calibrated numerical model with the material parameters given in Table 5.2, rolling resistance coefficient $\mu_r = 0.16$, optimal Young's modulus of 4.68×10^7 Pa, optimal time step of 4.10×10^{-6} s and optimal cut of PSD 3 (2.0 – 8.0 mm) to predict the effects of falling height H_F on the repose angle of the tested waste rock. The geometry of the numerical model is the same as the physical model shown in Figure 5.18. In the simulations, waste rock particles were generated first in the funnel. The bottom was blocked with a plate attached to the bottom (Figure 5.20a). The vertical distance between the funnel bottom and the table is equal to the falling height of H_F. The plate was removed at the end of the generation of all the particles (Figure 5.20b). A waste rock pile was generated on the table once all the waste rock particles were dropped on the table (Figure 5.20c). The total simulation time was set to be 10 s.

(a) (b) (c)

Figure 5.20: Calibrated numerical model (with the material parameters given in Table 5.2, rolling resistance coefficient $\mu_r = 0.16$, optimal Young's modulus of 4.68×10^{7} Pa, optimal time step of 4.10×10^{-6} s and optimal cut of PSD 3) for predicting the effects of falling height H_F on the repose angle of waste rock: (a) initial state; (b) intermediate state; (c) final state

Figure 5.21 presents the side views (Figure 5.21a) and top views (Figure 5.21b) of waste rock piles, obtained by numerical modeling with the calibrated numerical model for different falling heights. The repose angle θ (Figure 5.21a) and the diameter D (Figure 5.21b) of waste rocks pile were estimated by using the protractor tool and ruler tool in EDEM, respectively.

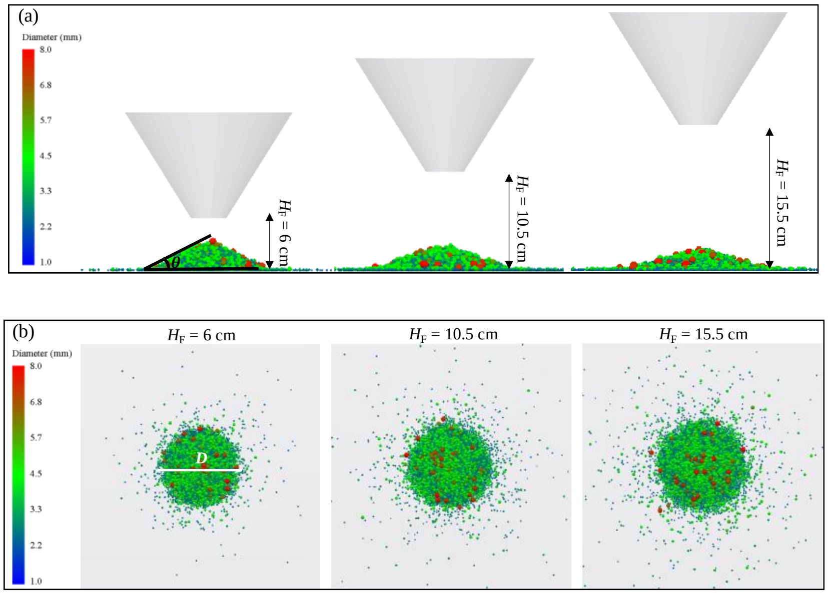

Figure 5.21: Views of waste rock piles with different falling heights H_F obtained by calibrated numerical model: (a) side views; (b) top views

Figure 5.22 presents the repose angles θ (Figure 5.22a) and diameter D (Figure 5.22b) of waste rock pile as function of falling height H_F, obtained by laboratory tests and predicted by numerical modeling with the calibrated model. Good agreements are obtained between the experimental results and numerical predictions for both the repose angle and diameter of waste rock piles for all the three different falling heights. These results indicate that the validity and predictability of the calibrated numerical model to simulate the mechanical behavior of granular materials have been successfully verified. It can be used to analyze the mechanical behavior of structures made of the tested waste rock under different conditions.

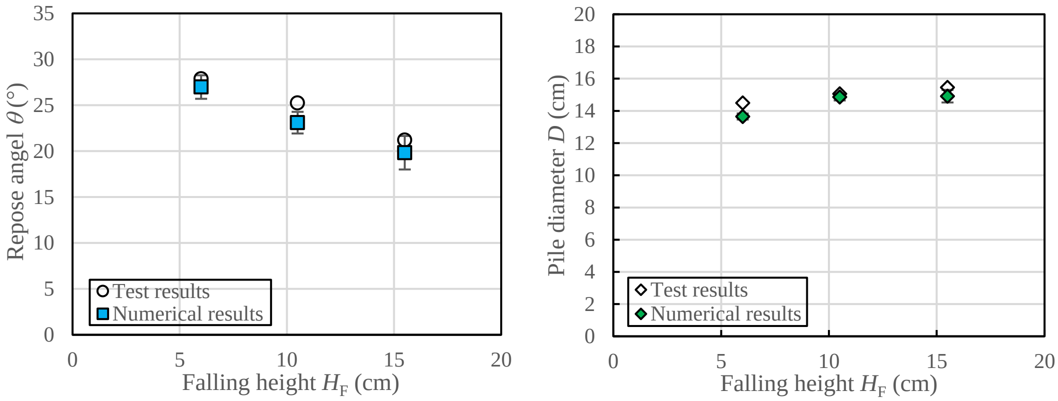

(a) (b)

Figure 5.22: Variations of: (a) repose angle θ and (b) pile diameter D as function of falling height H_F, obtained by laboratory tests and predicted by calibrated numerical model

5.4 Discussion

In this study, one has shown how to obtain an optimal numerical model with an optimal cut of PSD curve, an optimal time step and an optimal Young's modulus to ensure stable and reliable numerical results with the shortest calculation time. The validity of the EDEM numerical model has been verified against analytical solution, while the applicability of the numerical model has been confirmed by numerical reproduction and prediction of experimental results. The methodology can be applied to any other numerical codes based on the discrete element method for mechanical behavior analyses. Nevertheless, it should be kept in mind that the methodology also has certain limitations.

In the study, spherical particles were used in the EDEM simulation to represent the non-spherical waste rocks particles. The shape effect of waste rock particles was accounted for by calibrating the rolling resistance coefficient against the results of waste rock repose angle tests. However, the spherical particles may not fully capture the behavior of waste rock where the particle shape has a significant influence. Future studies should incorporate the actual shape of waste rock particles for simulations that are closer to reality.

Laboratory sieve analysis can determine the mass proportion of particles with standard sieve sizes. However, the actual particle size distributions (e.g., particle sizes and corresponding mass proportions) between two consecutive standard sieves are unknown due to the lack of intermediate sieves. Assumptions and approximations, such as Gaussian distribution used in this study, have to be made in the numerical model to generate particles between the two neighbor sieves. Therefore, PSD generated in EDEM may not fully correspond to the actual PSD of the tested waste rocks between the two consecutive sieves. More study is necessary to obtain more representative particle distribution between two neighboring sieves.

In this study, Young’s modulus of waste rock was artificially reduced in the numerical model to reduce the DEM simulation time. The numerical results did not significantly change when the Young’s modulus was larger than the optimal Young’s modulus determined by sensitivity analyses. These findings suggest that reducing Young’s modulus can be used in the DEM simulations for determining the repose angle of waste rock. However, it is unknown if this approach still applies to determining other behaviors of waste rock. It is generally recommended that the physical parameters of materials should not be altered in the numerical model, as these changes mean changes of physical problem, which do not correspond to the modeled problems.

This study aims to demonstrate how to achieve an optimal (particle size distribution) PSD cut by excluding fine particles. The methodology is only considered valid for mechanical behaviors (e.g., repose angle) because fine particles, where their sizes and quantities are negligible compared to the pores or void spaces crated by larger particles, can remain free within these spaces. This justifies performing PSD cuts by excluding some fine particles through sensitivity analysis. However, this methodology is not applicable for simulating the hydraulic and thermal behavior of granular materials, as these properties are significantly influenced by the sizes and quantities of fine particles. Additionally, it cannot be used in simulations where fine particles contribute to cohesive forces. For such analyses, a new methodology is required.

The total mass of waste rock used in this study is 300.5 g, with a maximum particle size of 8.0 mm. The mass and maximum particle size of waste rock are considerably smaller than those typically found in field conditions. The impact of waste rock particle size and mass on the repose angle of waste rock will be investigated in future studies.

5.5 Conclusions

The study proposes a methodology for constructing an optimal DEM numerical simulation to obtain stable and reliable numerical results of mechanical behaviors of granular materials with the shortest time of computing. The validation of numerical model against analytical solution is emphasized for new users. An optimal numerical model with an optimal PSD cut, optimal time step and optimal Young's modulus can be obtained by conducting sensitivity analyses. Calibration is only recommended for model parameters that cannot be measured or their measurements are not reliable. The numerical model, along with the material parameters and the calibrated model parameters, constitute a calibrated numerical model. The validity and predictability of the calibrated numerical model needs to be tested against additional experimental results. More conclusions and suggestions are summarized as follows:

- The good agreements between the numerical and analytical results for the normal contact force and tangential contact force between two spheres indicate the EDEM code is validated.
- To simulate the mechanical behavior of granular materials, a portion of fine particles can indeed be neglected to reduce the simulation time. However, the PSD cut for excluding fine particles cannot be done arbitrarily. Sensitivity analyses of PSD cut must be performed to obtain the optimal cut of PSD curve, ensuring stable and reliable numerical results.
- Young's modulus of granular materials can be reduced to reduce the required time step and accelerate the achievement of a static equilibrium state. The physical and mechanism of these has been for the first time explained. It is however very clear that the use of smaller Young's modulus than the actual value of waste rock particles means the simulation of another physical model, not anymore the original one even though the obtained repose angle can be very close to that obtained by using the actual Young's modulus as long as the Young's modulus is not reduced to a value smaller than a critical value. Optimal Young's modulus should be determined by performing its sensitivity analysis to ensure stable and reliable numerical results with shortest time of calculations.
- Sensitivity analyses of time step need to be done, case by case, to find the optimal time step, which ensures stable and reliable numerical results with the minimized time of simulation.

- In numerical modeling, calibration is recommended only for unmeasurable model parameters. Measured physical and mechanical parameters are suggested to be directly used in DEM model to reduce uncertainty of simulation and the number of calibrated parameters. They should not be simply neglected, changed or calibrated unless their measurements are unreliable due to human or instrumentation errors.
- The good agreements between the experimental results and numerical predictions indicate that the calibrated DEM model can be used to simulate the mechanical behavior of granular materials.

Acknowledgements

The authors acknowledge the financial support from the Natural Sciences and Engineering Research Council of Canada (NSERC RGPIN-2018-06902), Natural Sciences and Engineering Research Council of Canada (NSERC ALLRP 580767 - 22), and industrial partners of the Research Institute on Mines and the Environment (RIME UQAT – Polytechnique; http://rime-irme.ca).

References

Aubertin, M. (2013). "Waste rock disposal to improve the geotechnical and geochemical stability of piles. " 23rd World Mining Congress (WMC 2013). Montréal, Québec: 8-8.

Altair EDEM (2022). "Altair EDEM 2022.2 Release Notes." Altair Engineering Inc.

Berger, K. J. and C. M. Hrenya (2014). "Challenges of DEM: II. wide particle size distributions." Powder Technology 264: 627-633.

Brosh, T., H. Kalman and A. Levy (2014). "Accelerating CFD–DEM simulation of processes with wide particle size distributions." Particuology 12: 113-121.

Burns, S. J. and K. J. Hanley (2017). "Establishing stable time-steps for DEM simulations of non-collinear planar collisions with linear contact laws." International Journal for Numerical Methods in Engineering 110(2): 186-200.

Burns, S. J., P. T. Piiroinen and K. J. Hanley (2019). "Critical time step for DEM simulations of dynamic systems using a Hertzian contact model." International Journal for Numerical Methods in Engineering 119(5): 432-451.

Chung, Y. C. and J. Y. Ooi (2011). "Benchmark tests for verifying discrete element modelling codes at particle impact level." Granular Matter 13(5): 643-656.

Cleary, P. W., J. E. Hilton and M. D. Sinnott (2017). "Modelling of industrial particle and multiphase flows." Powder Technology 314: 232-252.

Cundall, P. A. and O. D. L. Strack (1979). "A discrete numerical model for granular assemblies." Géotechnique 29(1): 47-65.

Deiminiat, A. and L. Li (2022). "Experimental study on the reliability of scaling down techniques used in direct shear tests to determine the shear strength of rockfill and waste rocks." CivilEng 3(1): 35-50.

Deiminiat, A., L. Li and T. Pabst (2023). "Experimental study on specimen size effect and the minimum required specimen diameter to maximum particle size ratio for constant head permeability tests." Environmental Earth Sciences 82(14).

Deiminiat, A., L. Li and F. Zeng (2022). "Experimental study on the minimum required specimen width to maximum particle size ratio in direct shear tests." CivilEng 3(1): 66-84.

Deiminiat, A., L. Li, F. Zeng, T. Pabst, P. Chiasson, R. Chapuis and P. P. Rossi (2020). "Determination of the shear strength of rockfill from small-scale laboratory shear tests: a critical review." Advances in Civil Engineering 2020: 1-18.

Feng, Y. T. and D. R. J. Owen (2014). "Discrete element modelling of large scale particle systems—I: exact scaling laws." Computational Particle Mechanics 1(2): 159-168.

Härtl, J. and J. Y. Ooi (2008). "Experiments and simulations of direct shear tests: porosity, contact friction and bulk friction." Granular Matter 10(4): 263-271.

Hertz, H. (1882). "Ueber die Berührung fester elastischer Körper." Journal für die reine und angewandte Mathematik 1882(92): 156-171.

Houhamdi, S., E. Gallego Vazquez and K. Djeghaba (2022). "Particle size effect on DEM simulation of pressures applied on a cylindrical silo with hopper." Periodica Polytechnica Civil Engineering.

James, M., M. Aubertin and B. Bussière (2013). "On the use of waste rock inclusions to improve the performance of tailings impoundments." 18th International Conference on Soil Mechanics and Geotechnical Engineering. Paris, France: 735-738.

Jing, L. (2003). "A review of techniques, advances and outstanding issues in numerical modelling for rock mechanics and rock engineering." International Journal of Rock Mechanics and Mining Sciences 40(3): 283-353.

Kobayashi, T., T. Tanaka, N. Shimada and T. Kawaguchi (2013). "DEM–CFD analysis of fluidization behavior of Geldart Group A particles using a dynamic adhesion force model." Powder Technology 248: 143-152.

Kuo, H. P., P. C. Knight, D. J. Parker, Y. Tsuji, M. J. Adams and J. P. K. Seville (2002). "The influence of DEM simulation parameters on the particle behaviour in a V-mixer." Chemical Engineering Science 57(17): 3621-3638.

Li, L. (2022). "Special issue on numerical modeling in civil and mining geotechnical engineering." Processes 10(8).

Li, Y., Y. Xu and C. Thornton (2005). "A comparison of discrete element simulations and experiments for 'sandpiles' composed of spherical particles." Powder Technology 160(3): 219-228.

Lommen, S., D. Schott and G. Lodewijks (2014). "DEM speedup: stiffness effects on behavior of bulk material." Particuology 12: 107-112.

Lu, G., J. R. Third and C. R. Müller (2015). "Discrete element models for non-spherical particle systems: from theoretical developments to applications." Chemical Engineering Science 127: 425-465.

Major, G. and R. Knupp (2008). "Report on feasibility-level pit slope design criteria Osisko Canadian Malartic project." Golder Associates Inc.

Malone, K. F. and B. H. Xu (2008). "Determination of contact parameters for discrete element method simulations of granular systems." Particuology 6(6): 521-528.

Mindlin, R. D. (1949). "Compliance of elastic bodies in contact." Journal of Applied Mechanics 16: 259-268.

Mindlin, R. D. and H. Deresiewicz (1953). "Elastic spheres in contact under varying oblique forces." Journal of Applied Mechanics 20: 327-344.

O'Sullivan, C. (2011). "Particle-based discrete element modeling: geomechanics perspective." International Journal of Geomechanics 11(6): 449-464.

Qiu, P. and T. Pabst (2022). "Waste rock segregation during disposal: calibration and upscaling of discrete element simulations." Powder Technology 412.

Rackl, M. and K. J. Hanley (2017). "A methodical calibration procedure for discrete element models." Powder Technology 307: 73-83.

Radeke, C. A., B. J. Glasser and J. G. Khinast (2010). "Large-scale powder mixer simulations using massively parallel GPU architectures." Chemical Engineering Science 65(24): 6435-6442.

Roessler, T. and A. Katterfeld (2018). "Scaling of the angle of repose test and its influence on the calibration of DEM parameters using upscaled particles." Powder Technology 330: 58-66.

Sandeep, C. S., K. Senetakis, D. Cheung, C. E. Choi, Y. Wang, M. R. Coop and C. W. W. Ng (2021). "Experimental study on the coefficient of restitution of grain against block interfaces for natural and engineered materials." Canadian Geotechnical Journal 58(1): 35-48.

Siegmann, E., S. Enzinger, P. Toson, P. Doshi, J. Khinast and D. Jajcevic (2021). "Massively speeding up DEM simulations of continuous processes using a DEM extrapolation." Powder Technology 390: 442-455.

Svanberg, A., S. Larsson, R. Mäki and P. Jonsén (2020). "Full-scale simulation and validation of bucket filling for a mining rope shovel by using a combined rigid FE-DEM granular material model." Computational Particle Mechanics 8(4): 825-843.

Taha, H., N.-S. Nguyen, D. Marot, A. Hijazi and K. Abou-Saleh (2022). "A DEM study of the effect of the loss of fine particles on the mechanical behavior of gap-graded soils." Geomechanics for Energy and the Environment 31.

Thoeni, K., M. Servin, S. W. Sloan and A. Giacomini (2019). "Designing waste rock barriers by advanced numerical modelling." Journal of Rock Mechanics and Geotechnical Engineering 11(3): 659-675.

Tian, Y., S. Zhang, P. Lin, Q. Yang, G. Yang and L. Yang (2017). "Implementing discrete element method for large-scale simulation of particles on multiple GPUs." Computers & Chemical Engineering 104: 231-240.

Timoshenko, S., S. Timoshenko and J. N. Goodier (1951). Theory of Elasticity, by S. Timoshenko and J.N. Goodier. 2nd Edition, McGraw-Hill Book Company.

Utili, S., T. Zhao and G. T. Houlsby (2015). "3D DEM investigation of granular column collapse: evaluation of debris motion and its destructive power." Engineering Geology 186: 3-16.

Wang, L., M. Meguid and H. S. Mitri (2021). "Impact of ballast fouling on the mechanical properties of railway ballast: insights from discrete element analysis." Processes 9(8).

Washino, K., E. L. Chan, K. Miyazaki, T. Tsuji and T. Tanaka (2016). "Time step criteria in DEM simulation of wet particles in viscosity dominant systems." Powder Technology 302: 100-107.

Washino, K., E. L. Chan and T. Tanaka (2018). "DEM with attraction forces using reduced particle stiffness." Powder Technology 325: 202-208.

Yan, Z., S. K. Wilkinson, E. H. Stitt and M. Marigo (2015). "Discrete element modelling (DEM) input parameters: understanding their impact on model predictions using statistical analysis." Computational Particle Mechanics 2(3): 283-299.

Zhang, Y. and L. Li (2024). "Introduction and implementation of fluid forces in a DEM code for simulating particle settlement in fluids." Powder Technology 433.

CHAPTER 6 NUMERICAL AND EXPERIMENTAL STUDIES OF THE NATURAL MIXING BEHAVIOR BETWEEN A PASTE BACKFILL AND DUMPED WASTE ROCK IN STOPES FROM LABORATORY TO FIELD CONDITIONS. PART I: NUMERICAL MODEL CALIBRATION AND VALIDATION

Abstract:

Underground mines produce large quantities of waste rock. Transporting these waste rock from underground to ground surface requires substantial energy consumption and operation costs. An alternative approach is to dump the waste rock directly into stopes being filled with cemented paste backfill, thus reducing the transportation-related issues. However, this practice requires a good understanding of the natural mixing behavior of the dumped waste rock and paste backfill in a stope, as the cohesionless waste rock without any paste backfill may fail upon exposure. Achieving this understanding is challenging because it is impractical to perform laboratory tests under or similar to field conditions due to limited laboratory spaces and the overly large size of field waste rock. To partly overcome this problem, scaling down technique is often applied to remove large particles of waste rock, allowing small-scale tests to be conducted in the laboratory. However, the small-scale test results cannot be directly used to predict the natural mixing behavior of dumped waste rock and cemented paste backfill under various field conditions. In this case, numerical modeling has to be applied. In this study, both laboratory tests and numerical modeling are used to analyze the natural mixing behavior of dumped waste rock and paste backfill. To better present the results, the study is divided into two parts. This paper presents Part I of the study, which focuses on calibrating and validating a numerical model. In this part, repose angle tests are conducted on waste rock samples with different maximum particle sizes $d_{\max}$ prepared using the scalping down technique. The rolling resistance coefficients of waste rock with different values of $d_{\max}$ are calibrated based on the test results. A relationship between rolling resistance coefficient and $d_{\max}$ is obtained to predict the rolling resistance coefficient of waste rock with larger $d_{\max}$. The calibrated numerical model is applied to predict the repose angles of waste rock with larger $d_{\max}$ and different masses. The results indicate that the minimum required mass and specimen size ratio must be respected to obtain a reliable repose angle of waste rock. The scalping technique is valid for preparing waste rock samples for repose angle tests. The established relationship between repose angle and d_{max} can correctly predict the repose angle of waste rock with larger value of d_{max} (including large scale and on-site scale pile). The rolling resistance coefficient does not significantly change as d_{max} increases from smaller to larger values. The good agreements between the measured repose angles and those predicted by numerical modeling indicate that the calibrated numerical model can be used to analyze the geotechnical behavior of various sizes of infrastructures made of waste rock with different d_{max} under diverse conditions. It can also be used to investigate the natural mixing behavior of a paste backfill and dumped waste rock. The application of this validated numerical model for analyzing the natural mixing behavior is presented in Part II of the study.

Keywords: Waste rock pile; Underground mine; Repose angle; Scalping method; Natural mixing behavior; Rolling resistance coefficient

6.1 Introduction

Underground mines generate a substantial amount of waste rock to access ore bodies. Traditionally, most of the underground produced waste rock must be transported and hoisted to the surface to dispose as waste rock piles. Significant energy consumption and additional operational costs have to be engaged. In Canada and probably elsewhere, a quite common practice is to dump the underground produced waste rock directly into underground mine stopes being filled with cemented paste backfill. This approach can significantly reduce the amount of waste rock that needs to be transported to ground surface, therefore reducing the associated energy consumption and operational costs. In addition, if the dumped waste rock is fully mixed with the cemented paste backfill, the resulting mixture can exhibit superior mechanical properties compared to individual paste backfill and waste rock (Hane et al. 2017; Qiu et al. 2020; Qiu et al. 2022).

Despite the above-mentioned advantages, directly dumping waste rock in stopes being filled with cemented paste backfill can also present some risks. If the dumped waste rock does not fully mix with the cemented paste backfill or if the mixture between dumped waste rock and cemented paste backfill is poor, the cohesionless waste rock along with a portion of cemented paste backfill can fail and collapse upon side exposure during the excavation of an adjacent stope, leading to ore dilution, ore loss, and even other unexpected consequence. Therefore, it is crucial to have a good understanding of the natural mixing behavior between the dumped waste rock and paste backfill in stopes.

Until now, Zhang and Li (2023) are probably the first to have studied the natural mixture between dumped waste rock and a paste backfill through small laboratory tests. A small box was used to simulate a mine stope, while a waste rock excluding both very fine and large particles was used to mimic the field waste rock. This preliminary study provides a direct insight on the natural mixture between dumped waste rock and paste backfill. More experimental works need be conducted by using larger boxes with larger particles of waste rock to approach the field conditions. It is however impossible to perform laboratory tests under or similar to field conditions, not only due to limited spaces in laboratory, but also due to the oversize of field waste rock having largest particles or blocks of tens to hundreds of centimeters (James et al. 2013; Martin et al. 2019; Deiminiat et al. 2020; Deiminiat and Li 2022; Deiminiat et al. 2022; Qiu and Pabst 2023).

To partly overcome the problem associated with the oversized particles, four scaling down techniques have been proposed, named scalping, parallel, replacement, and quadratic (Marachi 1969; Marschi et al. 1972; Varadarajan et al. 2006; Hamidi et al. 2012; Ovalle et al. 2020; Deiminiat et al. 2020; Deiminiat and Li 2022; Deiminiat et al. 2022). Despite the popularity and wide application of parallel scaling down technique, Deiminiat et al. (2020) have shown that the parallel scaling down technique was not correctly validated, while the scalping and replacement down techniques were inadequately invalidated. The further studies of Deiminiat and Li (2022) have shown that the parallel scaling down technique is inadequate and the scalping scaling down technique is adequate to evaluate the shear strength of in situ large particle materials through extrapolation prediction. Theoretically, the shear strength of in situ waste rock can be obtained from laboratory tests by applying the scalping down technique.

To understand the natural mixing behavior between dumped waste rock and paste backfill, laboratory tests can also be done by applying the scalping down technique with waste rock having different maximum particle sizes $d_{\max}$. However, the natural mixing behavior of dumped waste rock and cemented paste backfill under different field conditions cannot be directly predicted through experimental work. The only possible way is to conduct numerical modeling to evaluate and predict the natural mixing behavior of dumped waste rock and paste backfill under field conditions with any particle sizes of waste rock and any dimensions of stopes. This requires a reliable and applicable numerical model, which cannot only be used to produce reliable numerical results, but also be able to correctly take into account the size effects of stope geometries and particle sizes of waste rock.

In this study, a numerical code based on discrete element method (DEM), named EDEM (EDEM 2022) is employed to analyze the natural mixing behavior of dumped waste rock and paste backfill. Its validity has been verified through a step of validation against some analytical solutions after several sensitivity analyses to ensure stable numerical results (Li 2022; Zhang and Li 2024). Its applicability to simulate the mechanical behavior of granular materials has also been tested through comparisons between stable and reliable numerical results and reliable experimental results. The details of these can be found in Zhang and Li (2024), who showed that it is important to reduce and minimize the number of model parameters determined by calibration, especially for those having clear physical meanings. Subsequently, particles' density, Young's modulus, and Poisson's ratio as well as particle-to-particle's static friction coefficient and restitution coefficient should be measured for as long as possible because they have clear physical meanings. The particle-to-particle's rolling resistance coefficient has also a clear physical meaning. It is expected to be dependent on the shapes and sizes of particles. But it is difficult and even impossible to measure. Its value has to be estimated based on a process of calibration.

To this end, a few small-scale laboratory tests with waste rock samples prepared by applying the scalping down technique (i.e. simply excluding the oversized particles larger than the chosen $d_{\max}$) can be performed. The experimental results obtained with samples having different values of $d_{\max}$ can be used to obtain different rolling resistance coefficients through a process of calibration by numerical modeling. This allows the establishment of a relationship between the calibrated rolling resistance coefficient and $d_{\max}$. The rolling resistance coefficient of any untested samples, including in situ waste rock, having larger values of $d_{\max}$ can then be obtained by prediction using interpolation or extrapolation techniques (Varadarajan et al. 2006; Gupta 2009; Abbas 2011; Frossard et al. 2012; Honkanadavar et al. 2016; Xu 2018; Zhang et al. 2019). The size effects associated with stope geometry and particle sizes of waste rock can then be taken into account and the mixing behavior of dumped waste rock and paste backfill in underground mine stopes under field conditions can be predicted.

To better present the results, the study is divided into two parts. In this part (Part I), a series of repose angle tests on waste rock samples prepared using the scalping down technique are conducted. The experimental results (resulted pile shapes and repose angles) obtained on waste rock samples having different values of $d_{\max}$ are then reproduced by numerical modeling. The rolling resistance of the studied waste rock is calibrated and predicted for the studied waste rock having different values of $d_{\max}$. The calibrated and validated numerical model can then be applied to predict the geotechnical behavior of infrastructures made of waste rock under diverse laboratory and field conditions. Its application to investigate the natural mixing behavior of a paste backfill and dumped waste rock will be presented in Part II of this study as a companion paper.

6.2 Preliminary laboratory tests and numerical modeling

The waste rock samples used in the tests was taken from a mine located at the northwest of Québec, Canada. Waste rock samples having different values of $d_{\max}$ were prepared by applying the scalping down technique, which has been partly validated by experimental work (Deiminiat and Li 2022). Figure 6.1 presents a picture (Figure 6.1a) of the scalped waste rock samples with $d_{\max}$ values of

8.0, 5.0, 3.35, and 2.0 mm, having masses M_{wr} of 900, 700, 300, and 200 g, respectively. The corresponding particle size distribution (PSD) curves of four scalped waste rock samples are presented in Figure 6.1b.

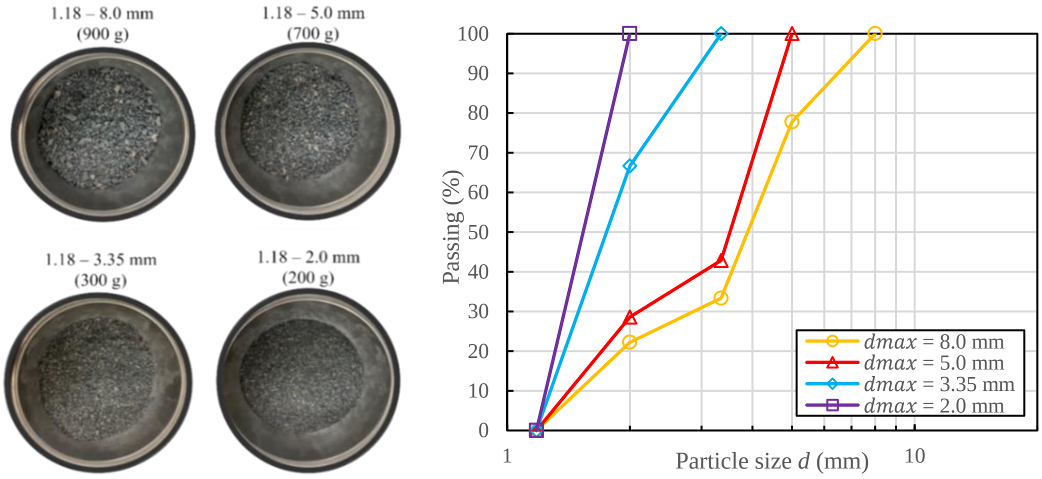

(a) (b)

Figure 6.1: Scalped waste rock samples having d_{max} values of 8.0, 5.0, 3.35, and 2.0 mm, respectively: (a) a picture of the samples; (b) PSD curves

Figure 6.2 presents a schematic presentation (Figure 6.2a) and a picture (Figure 6.2b) of the repose angle tests with the scalped waste rock sample having a d_{max} value of 8.0 mm and a mass of 900 g. The utilized funnel has an open diameter of 19 cm on top, an open diameter of 4.0 cm at the base, and an overall height of 12 cm. The test was conducted by gently lifting the funnel at a rate of approximately 0.01m/s in the vertical direction until the empty of the funnel.

Figure 6.3 presents a side view (Figure 6.3a) and top view (Figure 6.3b) of the resulted waste rock pile on the table at the end of the repose angle test. The repose angle θ of the waste rock pile was then calculated by measuring the height H and diameter D of the pile. The same test procedure was repeated on the waste rock samples with d_{max} values of 5.0, 3.35 and 2.0 mm, having masses of 700, 300, and 200 g, respectively. The obtained repose angles θ for different values of d_{max}, are presented in Table 6.1. One sees that the repose angle increases as d_{max} increases from 2.0 to 8.0 mm, as what has been shown in Deiminiat and Li (2022). These experimental results will be used in the numerical modeling with EDEM to obtain the rolling resistance coefficient as a function of d_{max} through the process of calibration.

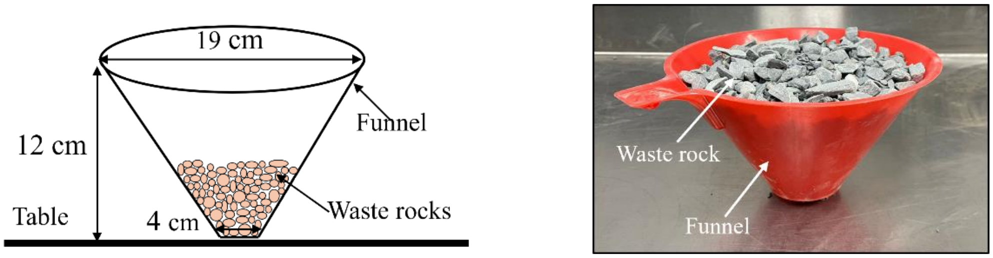

(a) (b)

Figure 6.2: Waste rock repose angle test: (a) a schematic presentation; (b) photo of the funnel with waste rock $d_{\max}$ of 8.0 mm

(a) (b)

Figure 6.3: Photos of a waste rock pile with $d_{\max}$ of 8.0 mm and a mass of 900 g

Table 6.1: Measured repose angle θ with the four scalped waste rock samples

Scalped waste rock sample	$d_{\max}$ (mm)	M_{wr} (g)	θ (°)
1	2.0	200	33.47
2	3.35	300	34.65
3	5.0	700	36.54
4	8.0	900	37.17

Table 6.2 presents the material parameters for the tested waste rock. The particle density of the tested waste rock was measured in our laboratory. The Poisson's ratio and static friction coefficient were measured by Major and Knupp (2008) for the same waste rock used in this study. The restitution coefficient of tested waste rock was determined by the drop tests results conducted by

Sandeep et al. (2021). The rolling resistance coefficient of the studied waste rock is the only unknown parameter and needs to be obtained by calibration against experimental results.

Table 6.2: Material parameters for the tested waste rock

	Material parameter	Values	Determination
Waste rock particle parameter	Particle density, ρ (kg/m^3)	2760	Measured
	Young's modulus, (GPa)	46.8	Measured†
	Poisson's ratio, ν	0.19	Measured†
Particle – particle interaction	Restitution coefficient, μ_e	0.79	Measured‡
	Static friction coefficient, μ_s	0.466	Measured†
	Rolling resistance coefficient, μ_r	--	Unknown

Note: †by Major and Knupp (2008); ‡ by Sandeep et al. (2021).

Figure 6.4 illustrates the numerical model built with EDEM for simulating the repose angle test of waste rock with d_{max} of 2.0 mm and a mass of 200 g. The physical model shown in Figure 6.2a was reproduced. The waste rock particles were generated in the funnel using EDEM's dynamic factory feature. After that, the funnel was lifted at a speed of 0.01 m/s in the vertical direction until the empty of the funnel. The repose angle θ of the waste rock pile was measured using the protractor tool in EDEM by clipping the waste rock pile at its center.

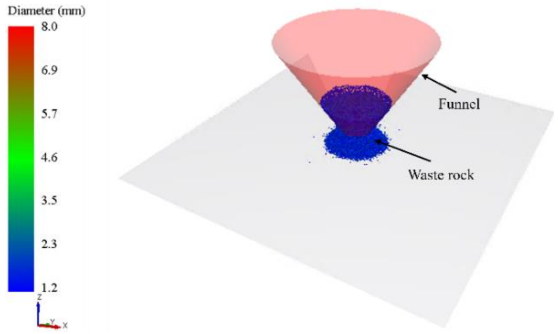

Figure 6.4: Numerical model built with EDEM for simulating the repose angle test of waste rock with d_{max} of 2.0 mm and a mass of 200 g

Before making any comparisons with experimental results, one needs first to ensure that the numerical results are stable and reliable. Sensitivity analyses of time step is necessary to reach the optimal numerical model that ensures stable and reliable numerical results with minimum time of calculation (Zhang and Li 2024). The repose angle of the waste rock pile with a rolling resistance coefficient of 0.05, obtained with the numerical modeling is 22.49°, which is much smaller than the measured value of 33.47°. The rolling resistance coefficient needs to be changed to obtain a good agreement between the measured repose angle and that obtained by numerical modeling. The above presented numerical modeling procedure has to be repeated with different values of rolling resistance coefficient.

Figure 6.5 presents the variation of repose angle as a function of rolling resistance coefficient, obtained by numerical modeling. The measured repose angle of the waste rock pile is also plotted in the figure. One sees that the numerical modeling with a rolling resistance coefficient of 0.15 produces the best agreement with the measured repose angle of the waste rock pile. The calibrated rolling resistance coefficient for the scalped waste rock sample having a $d_{\max}$ of 2.0 mm is 0.15.

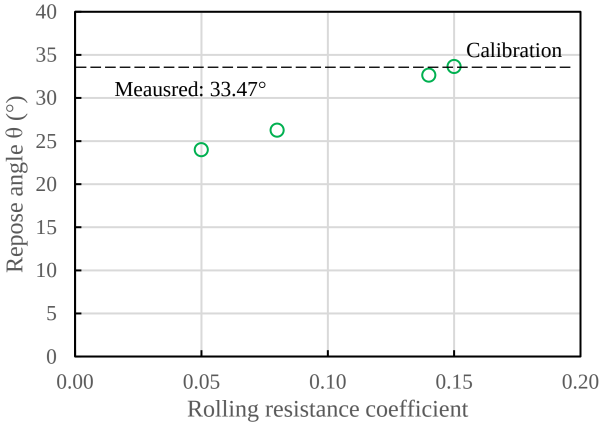

Figure 6.5: Variation of repose angle as function of rolling resistance coefficient, obtained by numerical simulations with optimal numerical models for the scalped waste rock sample having a $d_{\max}$ of 2.0 mm and a mass of 200 g

The above presented calibration process was repeated for the scalped waste rock samples with $d_{\max}$ values of 3.35 and 5.0 mm. Figure 6.6 presents the variation of rolling resistance coefficient as a function of $d_{\max}$. Surprisingly, one notes that the rolling resistance coefficient of the tested waste rock does not significantly change as the value of $d_{\max}$ increases from 2.0 to 5.0 mm. This trend leads to a predicted value of 0.15 for the rolling resistance coefficient of the scalped waste rock sample having a $d_{\max}$ of 8 mm. The numerical modeling with this predicted rolling resistance coefficient of 0.15 results a repose angle of 38.25°, a value very close to the measured repose angle of 37.17°.

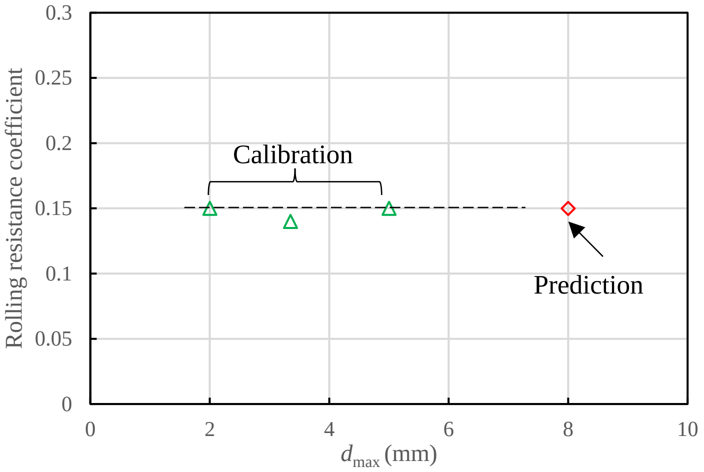

Figure 6.6: Variation of calibrated rolling resistance coefficient as a function of d_{max}

Table 6.3 presents a summary of the repose angle measurements and numerical modeling of the preliminary tests. The good agreements between the measured repose angles and those obtained by numerical modeling indicate that the calibrated EDEM model can be used to analyze the geotechnical behavior of various sizes of infrastructures made of different sizes of waste rock under diverse conditions. Nevertheless, the contradiction between the constant value of rolling resistance coefficient and the increase of measured repose angle as d_{max} increases from 2 to 8 mm needs to be explained.

Table 6.3: Measured and numerical reproduced repose angle θ with the four scalped waste rock samples

Scalped waste rock	d_{max} (mm)	M_{wr} (g)	Numerical modeling			Measured
			How	Rolling resistance	θ (°)	θ (°)
1	2.0	200	Calibration	0.15	33.64	33.47
2	3.35	300	Calibration	0.14	34.37	34.65
3	5.0	700	Calibration	0.15	36.87	36.54
4	8.0	900	Prediction	0.15	38.25	37.17

6.3 Additional laboratory tests and numerical modeling

Repose angle is one of the intrinsic properties of granular materials. It is expected to be constant and independent on the variation of d_{max} because the calibrated rolling resistance coefficients of the scalped waste rock samples are constant and independent on the variation of d_{max}. This expectation is contradictory to the variation of measured repose angle of scalped waste rock samples shown in Table 6.1.

To further understand the contradiction between the laboratory test results and numerical modeling, the stability, reliability and representativeness of the measured repose angles of the waste rock piles are questioned and revaluated. One may note that larger repose angle of waste rock pile was obtained with larger mass of waste rock, as shown in Table 6.1. If one places little waste rock at the bottom of the funnel, a repose angle close to zero can be expected. This indicates that the repose angle of waste rock pile can be dependent on the mass of waste rock. The repose angle tests of four scalped waste rock samples were thus conducted again by using different masses.

Figure 6.7 presents the variation of repose angle θ as function of waste rock mass M_{wr} for the four scalped waste rock samples having different values of d_{max}, obtained by using the funnel having an open diameter of 4.0 cm at the base. It can be seen that the repose angles of the four scalped waste rock samples increase as the mass of waste rock increases from 50 to 900 g. When the used waste rock mass reaches or exceeds 900 g, the repose angle becomes stable and does not change any more with further change in the mass. These results explain well the observed increase in the repose angle as d_{max} increases from 2 to 5 mm because the masses used in repose angle tests for the scalped waste rock samples having d_{max} equaling to 2, 3.35, and 5 mm are smaller than the minimum required mass of 900 g, as what can be seen in Table 1. They also reveal that the measured repose angles of these scalped waste rock samples are neither stable and nor representative.

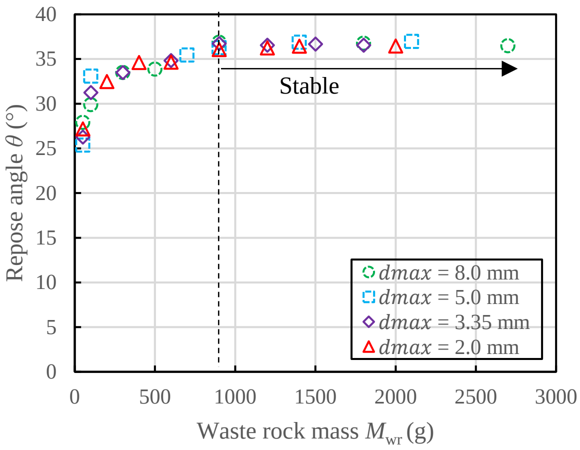

Figure 6.7: Variation of repose angle θ as function of waste rock mass M_{wr} for scalped waste rock with different values of d_{max}, obtained by using the funnel having an open diameter of 4.0 cm at the base

Another factor that can affect the measured repose angle is the open diameter at the base of the funnel, W. Figure 6.8 presents four funnels having open diameters W of 60, 40, 30 and 10 mm, respectively at the base.

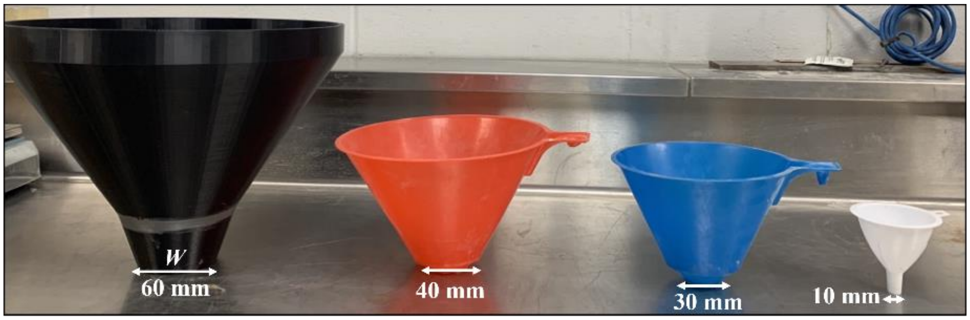

Figure 6.8: Funnels with four different base diameters W for the repose angle tests

Figue 6.9 shows the variation of measred repose angle θ as function of W/d_{max} ratio, obtained by using the four funnels on waste rock sample having a d_{max} of 8.0 mm. When the tests were conducted by using the smallest funnel having an open diameter of 10 mm at the base ($W/d_{max} =$ 1.25), the measured repose angle is zero because all the waste rock particles were stuck in the base of the funnel during the tests. Once the W/d_{max} ratio exceeds 3.75, the response angle remains stable. These results indicate that the open diameter at the base of the used funnel can affect the stability and reliability of the measured repose angle. However, as the funnel used in all previously presented tests has an open diameter of 40 mm at the base, the $W/d_{\max}$ ratio is equal to or larger than 3.75. The effect of open diameter at the base of funnel was avoided.

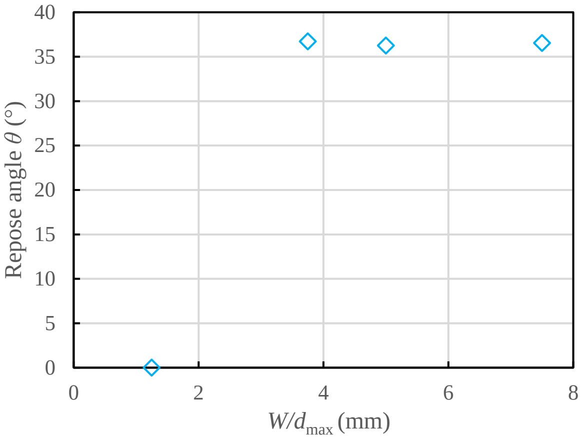

Figure 6.9: Variation of measured repose angle of waste rock sample having a $d_{\max}$ of 8 mm as a function of $W/d_{\max}$ ratio, obtained by using four funnels with different base diameters

Knowing that the repose angle tests must be performed by using funnel having large enough open diameter at the base with sufficient materials, all the repose angle tests were repeated on the four scalped waste rock samples by using the funnel with base diameter of 40 mm. The masses of waste rock with $d_{\max}$ of 2.0, 3.35, 5.0, and 8.0 mm are 1000, 1500, 3500, and 4500 g, respectively. The minimum required mass of 900 g and the minimum required $W/d_{\max}$ ratio of 3.75 were respected. Figure 6.10 shows the variation of measured repose angle θ as a function of $d_{\max}$, obtained on the four scalped waste rock samples by respecting the minimum required mass and $W/d_{\max}$ ratio. One sees that the repose angles θ do not change significantly as $d_{\max}$ increases from 2 to 8 mm. These new experimental results correspond well to the trend exhibited by the numerical modeling with the calibrated and predicted rolling resistance coefficient.

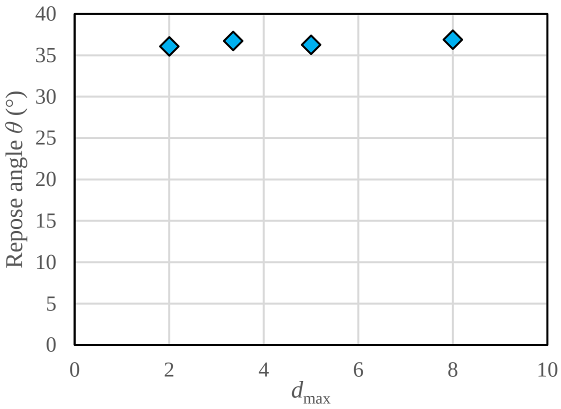

Figure 6.10: Variation of repose angle θ as a function of d_{max}, obtained by repose angle tests by respecting the minimum required mass of 900 g and the minimum required W/d_{max} ratio of 3.75

Figure 6.11 presents the numerical models for predicting the experimental results. The numerical results and the new experimental results obtained by respecting the minimum required mass and $W/d_{\text{\_max}}$ ratio are plotted in Figure 6.12. The good agreements between the numerical modeling prediction and the measured results indicate once again the validation of the calibrated numerical model (i.e. the EDEM code with the calibrated rolling resistance coefficient of 0.15). The calibrated EDEM model can be used to analyze the geotechnical behavior of any infrastructures made of any sizes of waste rock under different conditions, including the mixing behavior of dumped waste rock and paste backfill.

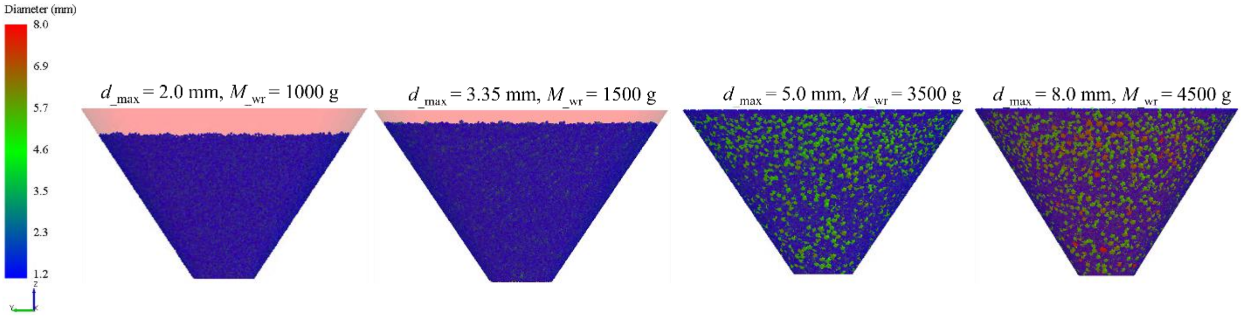

Figure 6.11: Numerical models for predicting the experimental results presented in Figure 6.10 (repose angle of waste rock with d_{max} of 2.0, 3.35, 5.0 mm and 8.0 mm, respectively)

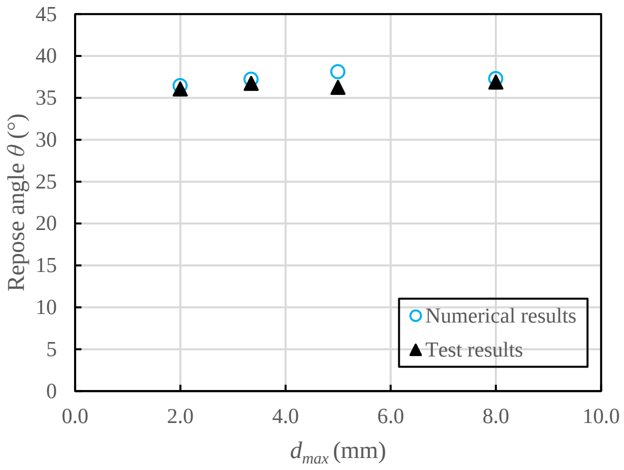

Figure 6.12: Variation of repose angle as a function of $d_{\max}$, obtained by laboratory tests and predicted by the calibrated numerical model (rolling resistance coefficient of 0.15)

This calibrated numerical model is further applied to predict the repose angle test results of waste rock having $d_{\max}$ of 2.0 mm with different masses. Figure 6.13 presents the numerical models for predicting the repose angle of waste rock with $d_{\max}$ of 2.0 mm and different masses of 200, 400, 600, 900, and 1200 g, respectively.

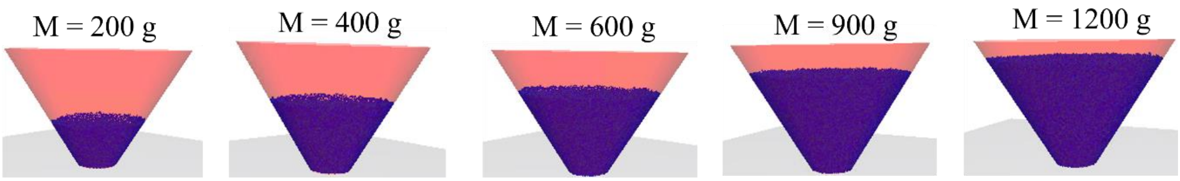

Figure 6.13: Calibrated numerical models (rolling resistance coefficient of 0.15) for predicting the repose angle test results of waste rock with $d_{\max}$ of 2.0 mm and mass of 200, 400, 600, 900 and 1200 g, respectively

Figure 6.14 presents the variation of repose angle as a function of mass, obtained by the laboratory tests and predicted by numerical modeling with the calibrated numerical model. Notably, the numerical results also match well with the experimental results for waste rock with different masses. These results along with the results presented in Figure 6.12 indicate that the calibrated numerical model possesses the necessary accuracy to predict the repose angle of waste rock with different values of $d_{\max}$ and masses.

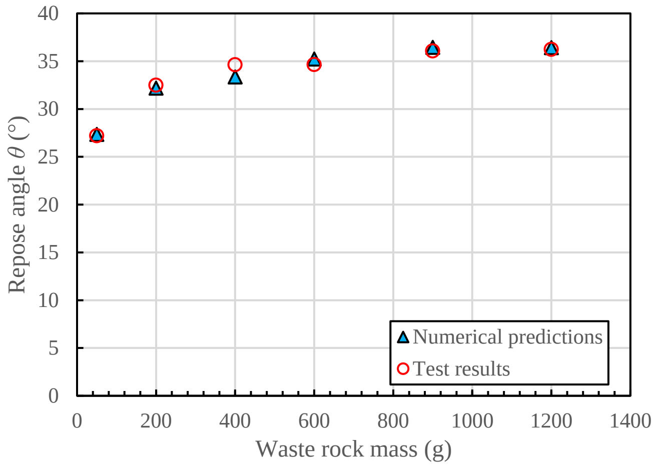

Figure 6.14: The variation of repose angle of waste rock with $d_{\max}$ of 2.0 mm as a function of mass, obtained by the laboratory tests and predicted by numerical modeling with the calibrated numerical model (rolling resistance coefficient of 0.15)

6.4 Discussion

In this study, repose angle tests with waste rock samples having different $d_{\max}$ and masses are conducted to calibrate and validate a numerical model that can be used to study the geotechnical behavior of any infrastructures made of any sizes of waste rock under laboratory or field conditions, including the mixing behavior of dumped waste rock and paste backfill in mine stopes. The results show that the calibrated numerical model can predict the repose angle of waste rock under various conditions. The numerical model can thus be applied to predict the natural mixing behavior of dumped waste rock and paste backfill.

A surprise associated with the constant and independence of rolling resistance coefficient on $d_{\max}$ reveals that the repose angle tests must be formed by using funnels having large enough open diameter at the base with sufficient mass of tested waste rock. In addition, both the numerical modeling and experimental results obtained by using funnels having large enough open diameter at the base with sufficient mass of tested waste rock indicate that the repose angle of the tested waste rock is independent on $d_{\max}$. This tends to indicate that the repose angle of the tested waste rock remains constant at a value of around 36 to 37° whatever the value of $d_{\max}$. If it is true, the repose angle of in situ waste rock piles can be obtained by laboratory repose angle tests with scalped waste rock samples. To verify this assumption, repose angle test with a scalped waste rock sample having a $d_{\max}$ of 70 mm was performed. Figure 6.15a shows a picture of the waste rock sample with a $d_{\max}$ of 70 mm. The corresponding PSD curve, along with those having $d_{\max}$ of 8.0, 5.0, 3.35, and 2.0 mm, are presented in Figure 6.15b.

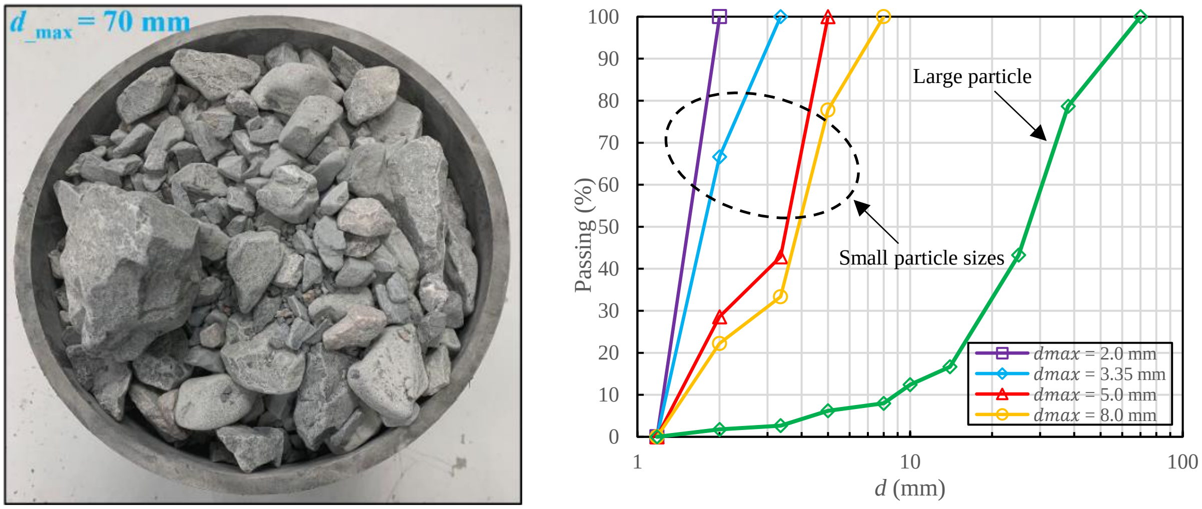

(a)

(b)

Figure 6.15: Waste rock used in the large-scale repose angle tests: (a) a photo of waste rock with $d_{\max}$ of 70 mm; (b) PSD curves of waste rock samples with different $d_{\max}$

To perform the large-scale tests, the waste rock was placed in a cylindrical column with a diameter of 300 mm and a height of 500 mm (Figure 6.16a). The repose angle test was then conducted by gently lifting the cylindrical column until the empty of the column. To ensure the test results are stable and reliabe, large-scale tests were repeated multiple times using the waste rock with different masses.

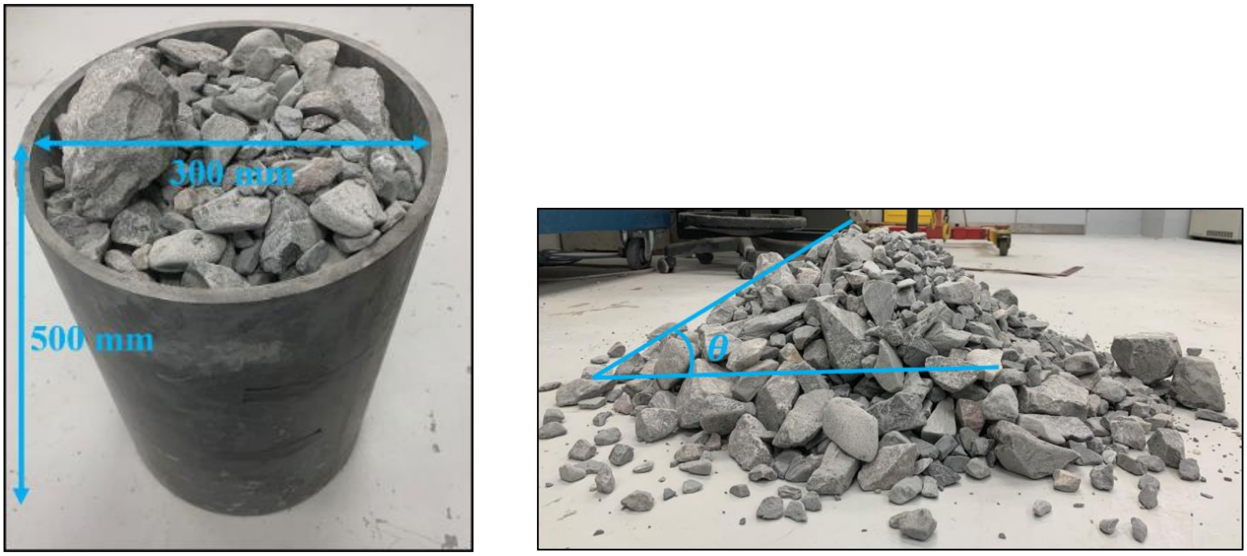

(a) (b)

Figure 6.16: Large-scale waste rock repose angle tests: (a) a photo of cylindrical column filled with waste rock with $d_{\_max}$ of 70 mm; (b) a photo of large-scale waste rock pile

Figure 6.17 presents the variation of repose angle as a function of the waste rock mass, obtained with the waste rock having a d_{max} of 70 mm. It is noted that the repose angle increases as the mass increases and becomes constant and stabilizes at a value of around 36.5°, a value corresponding well to the predicted value based on the repose angle tests with scalped waste rock samples having small values of d_{max}. More interestingly, the observed repose angle of an on-site waste rock pile with a d_{max} of 2 m is well in the range of 36 to 37°, predicted by the laboratory test and numerical modeling. The scalping down technique is validated once again, at least for the repose angle tests of waste rock.

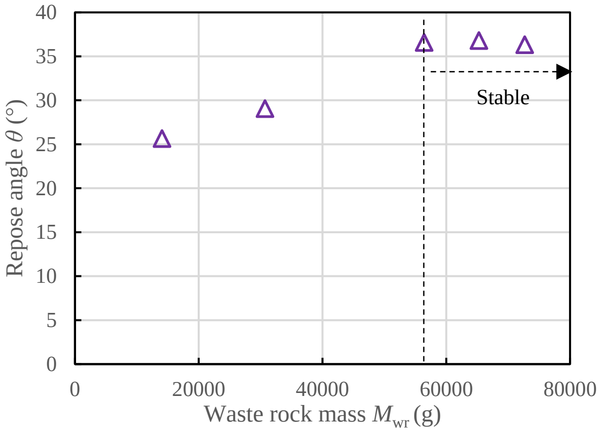

Figure 6.17: Variation of the repose angle of waste rock as a function of mass, obtained by large-scale repose angle tests with waste rock d_{max} of 70 mm

As the repose angle of large-scale waste rock piles both in lab and in field conditions has been successfully predicted by using the relationship established with the repose angles of scalped waste rock, the necessity of numerical modeling can be questioned. Numerical modeling is always necessary as long as an analysis more complicated than the repose angle is necessary. This can include, for instance, the analyse of segregation or internal structure of waste rock piles and mixing behaviour between waste rock and paste backfill.

In this study, the repose angle of waste rock obtained by numerical modeling is obtained from a single time simulation. In DEM simulations, the numerical results can be varied because the particle information (e.g., particle generation positions and particle numbers) are not the same in each run. This variation can lead to differences in the repose angle of waste rock obtained in each simulation. To ensure accurate predictions, it is recommended to conduct multiple simulations for each case to determine the error margin. Additionally, the measurement of the repose angle in EDEM code can also lead to slight differences. Multiple measurements are recommended to minimize the measurement errors in the software.

The calibrated numerical model has been successfully validated against the experiment results. The validated numerical model can thus be further applied to predict many behaviors of large-scale or even on-site scale waste rock pile. These additional simulations will help to confirm the predictability of the validated numerical model. However, for simulating the large-scale or field conditions with numerous particles will result in extremely long simulation times. To conduct these simulations, more powerful computers equipped with more advanced computing techniques, such as powerful GPU (Graphic Processing Units), maybe needed.

In the simulations, the spherical particles are used to represent the non-spherical waste rock particles, which necessitates the calibration of rolling resistance coefficient to account for shape effects. In future work, using the actual shapes of waste rock particles could provide more realistic conditions and potentially reduce the number of parameters that require calibration. However, such simulations will require more advanced and expensive simulation techniques, as calculating contacts for irregular shapes significantly increases simulation time.

6.5 Conclusions

The major purpose of the study is to analyze the natural mixing behaviour of dumped waste rock and paste backfill under various conditions. To better present the results, the study is divided into two parts. This paper presents Part I of the study, which focuses on calibrating and validating a numerical model. In this part, a series of repose angle tests are conducted on waste rock samples prepared using the scalping down technique. The test results are used to calibrate the rolling resistance coefficient of waste rock samples with different $d_{\max}$. A relationship curve between the calibrated rolling resistance coefficient and $d_{\max}$ is established to predict the rolling resistance coefficient of samples with larger $d_{\max}$ using extrapolation technique. The calibrated numerical model is applied to predict the repose angle of waste rock with larger $d_{\max}$ and different masses. The validated numerical model can be applied to predict the geotechnical behavior of infrastructures made of waste rock under diverse conditions, as well as the natural mixing behavior of dumped waste rock and paste backfill in underground mine stopes. The detailed investigation of the natural mixing behavior by using the validated numerical model will be presented in Part II of the study. The major conclusions of this study (Part I) can be drawn as follows:

- The mass of waste rock and specimen size W to $d_{\max}$ ratio can influence the stability and reliability of the repose angle test results. To obtain stable and reliable repose angle test results, the minimum required mass and specimen size ratio must be respected.
- The scalping down technique is validated for preparing the waste rock samples for the repose angle tests. The established relationship curve between the repose angle θ and $d_{\max}$, based on additional laboratory tests, can accurately predict the repose angle of the large-scale waste rock pile in the laboratory and the on-site waste rock pile having larger value of $d_{\max}$.

- The rolling resistance coefficient of the tested waste rock does not significantly change as the value of $d_{\max}$ increases from smaller value to larger value. The curve can be used to predict the rolling resistance coefficient of waste rock with larger $d_{\max}$.
- The good agreements between the measured repose angles and those predicted by numerical modeling indicate that the calibrated numerical model can be used to analyze the geotechnical behavior of various sizes of infrastructures made of different sizes of waste rock under diverse conditions, including field conditions as long as the necessary computing resources are available.

Acknowledgements

The authors acknowledge the financial support from the Natural Sciences and Engineering Research Council of Canada (NSERC RGPIN-2018-06902), Natural Sciences and Engineering Research Council of Canada (NSERC ALLRP 580767 - 22), and industrial partners of the Research Institute on Mines and the Environment (RIME UQAT – Polytechnique; http://rime-irme.ca).

References

Baldwin, G. and A. Grice (2000). Engineering the new Olympic Dam backfill system. *Proceedings Massmin*, 705-711.

Abbas, S. M. (2011). Behaviour of rockfill materials: based on nature of particles, *LAP Lambert Academic Publishing*.

Cerato, A. B. and A. J. Lutenegger (2006). Specimen size and scale effects of direct shear box tests of sands. *Geotechnical Testing Journal*, 29(6), 507-516.

Deiminiat, A. and L. Li (2022). Experimental study on the reliability of scaling down techniques used in direct shear tests to determine the shear strength of rockfill and waste rocks. *CivilEng*, 3(1), 35-50.

Deiminiat, A., L. Li and F. Zeng (2022). Experimental study on the minimum required specimen width to maximum particle size ratio in direct shear tests. *CivilEng*, 3(1), 66-84.

Deiminiat, A., L. Li, F. Zeng, T. Pabst, P. Chiasson, R. Chapuis and P. P. Rossi (2020). Determination of the shear strength of rockfill from small-scale laboratory shear tests: A critical review. *Advances in Civil Engineering*, 2020, 1-18.

EDEM (2022). *Altair EDEM 2022.2 Release Notes*. Altair Engineering Inc.

Emad, M. Z., H. S. Mitri and J. G. Henning (2012). Effect of blast vibrations on the stability of cemented rockfill. *International Journal of Mining, Reclamation and Environment*, 26(3), 233-243.

Frossard, E., W. Hu, C. Dano and P.-Y. Hicher (2012). Rockfill shear strength evaluation: a rational method based on size effects. *Géotechnique*, 62(5), 415-427.

Gupta, A. (2009). Triaxial behaviour of rockfill materials. *Electronic Journal of Geotechnical Engineering*, *2009*, 14, 1-18.

Hamidi, A., E. Azini and B. Masoudi (2012). Impact of gradation on the shear strength-dilation behavior of well graded sand-gravel mixtures. *Scientia Iranica*, 19(3), 393-402.

Honkanadavar, N., S. Dhanote and S. Bajaj (2016). 161 Prediction of shear strength parameter for prototype alluvial rockfill material. *Indian Geotechnical Conference*.

James, M., M. Aubertin and B. Bussière (2013). On the use of waste rock inclusions to improve the performance of tailings impoundments. *18th International Conference on Soil Mechanics and Geotechnical Engineering*. Paris, France: 735-738.

Li, L. (2022). Special issue on numerical modeling in civil and mining geotechnical Engineering. *Processes*, 10(8).

Lingga, B. A. (2018). *Investigation of cemented rockfill properties used at a Canadian diamond mine*. Master thesis, University of Alberta.

Lommen, S., D. Schott and G. Lodewijks (2014). DEM speedup: Stiffness effects on behavior of bulk material. *Particuology*, 12, 107-112.

Major, G. and R. Knupp (2008). *Report on feasibility-level pit slope design criteria Osisko Canadian Malartic project*. Golder Associates Inc.

Maknoon, M. (2016). *Slope stability analyses of waste rock piles under unsaturated conditions following large precipitations*. Ph.D. thesis, École Polytechnique de Montréal.

Marachi, N. (1969). *Strength and deformation characteristics of rockfill materials*. Ph.D. thesis, University of California, Berkeley.

Marschi, N. D., K. Chan Clarence and H. B. Seed (1972). Evaluation of properties of rockfill materials. *Journal of the Soil Mechanics and Foundations Division*, 98(1), 95-114.

Martin, V., M. Aubertin and G. Lessard (2019). An assessment of hydrogeological properties of waste rock using infiltration tests and numerical simulations. *GeoStJohn's 2019*, 72.

Mirzaeifar, H., A. Abouzar and M. R. Abdi (2013). Effects of direct shear box dimensions on shear strength parameters of geogrid-reinforced Sand. *66th Canadian geotechnical conference and the 11th joint CGS/IAH-CNC groundwater conference*, Montreal, 1-6.

Omar, T. and A. Sadrekarimi (2015). Effect of triaxial specimen size on engineering design and analysis. *International Journal of Geo-Engineering*, 6(1), 5.

Ovalle, C., S. Linero, C. Dano, E. Bard, P.-Y. Hicher and R. Osses (2020). Data compilation from large drained compression triaxial tests on coarse crushable rockfill materials. *Journal of Geotechnical and Geoenvironmental Engineering*, 146, 06020013.

Palmeira, E. and G. W. E. Milligan (1990). Scale effects in direct shear tests on sand. *Proc. 12th international conference on soil mechanics and foundation engineering*, Rio de Janeiro, 739-742.

Qiu, P. and T. Pabst (2023). Characterization of particle size segregation and heterogeneity along the slopes of a waste rock pile using image analysis. *Environ Earth Sci*, 82(23), 573.

Rana, N. M., N. Ghahramani, S. G. Evans, S. McDougall, A. Small and W. A. Take (2021). Catastrophic mass flows resulting from tailings impoundment failures. *Engineering Geology*, 292.

Sainsbury, D. and B. Sainsbury (2014). Design and implementation of cemented rockfill at the Ballarat Gold Project. *Mine Fill 2014: Proceedings of the Eleventh International Symposium on Mining with Backfill*, Australian Centre for Geomechanics.

Sandeep, C. S., K. Senetakis, D. Cheung, C. E. Choi, Y. Wang, M. R. Coop and C. W. W. Ng (2021). Experimental study on the coefficient of restitution of grain against block interfaces for natural and engineered materials. *Canadian Geotechnical Journal*, 58(1), 35-48.

Seymour, J. B., L. A. Martin, M. J. Raffaldi, S. N. Warren and L. A. Sandbak (2019). Long-term stability of a 13.7 x 30.5-m (45 x 100-ft) undercut span beneath cemented rockfill at the Turquoise Ridge Mine, Nevada. *Rock Mech Rock Eng*, 2019, 1-17.

Varadarajan, A., K. G. Sharma, S. M. Abbas and A. K. Dhawan (2006). The role of nature of particles on the behavior of rockfill materials. *Soils and Foundations*, 46(5), 569-584.

Xu, Y. (2018). Shear strength of granular materials based on fractal fragmentation of particles. *Powder Technology*, 333, 1-8.

Zahran, K. and H. Naggar (2020). Effect of sample size on TDA shear strength parameters in direct shear tests. *Transportation Research Record: Journal of the Transportation Research Board*, 2674, 036119812093448.

Zhang, Z., Q. Sheng, X. Fu, Y. Zhou, J. Huang and Y. Du (2019). An approach to predicting the shear strength of soil-rock mixture based on rock block proportion. *Bulletin of Engineering Geology and the Environment*, 79.

Ziaie moayed, R., M. Alibolandi and A. Alizadeh (2016). Specimen size effects on direct shear test of silty sands. *International Journal of Geotechnical Engineering*, 1-8.

Zhang, Y. and L. Li (2023). Experimental study on the natural mixing behavior of waste rocks poured in a paste backfill. *International Journal of Mining, Reclamation and Environment*, 37(10), 953-977.

Zhang, Y. and L. Li (2024). Optimization of discrete element method model to obtain stable and reliable numerical results of mechanical response of granular materials. *Minerals*, 14(8), 758.

CHAPTER 7 NUMERICAL AND EXPERIMENTAL STUDIES OF NATURAL MIXING BEHAVIOR BETWEEN A PASTE BACKFILL AND DUMPED WASTE ROCK IN STOPES FROM LABORATORY TO FIELD CONDITIONS. PART II: APPLICATION AND PREDICTION OF THE CALIBRATED AND VALIDATED NUMERICAL MODEL

Abstract:

Transporting large amounts of waste rock from underground to ground surface requires substantial energy consumption and operation costs. Alternatively, waste rock can be directly dumped into mine stope being filled with cemented paste backfill. This practice reduces the amount of waste rock that needs to be transported, thus reducing the energy consumption and operational costs. The natural mixture of waste rock and paste backfill is expected to have better mechanical properties compared to individual paste backfill and waste rock. Despite these advantages, the practice presents some challenges. If the cohesionless waste rock is not fully mixed with the cemented paste backfill, the poor mixture can fail and collapse upon exposure, potentially leading to ore dilution or even ore loss. Therefore, it is critical to understand the natural mixing behavior of dumped waste rock and paste backfill in a stope. However, achieving this understanding is challenging because conducting laboratory tests with oversized field samples under conditions similar to those in the field is impractical. To address this, the scaling down technique is applied to remove large particles, thus allowing small scale tests to be conducted in the laboratory. Despite this, these test results are insufficient to predict the natural mixing behavior of dumped waste rock and a paste backfill in a stope. Thus, numerical modeling must be applied. In this study, the natural mixing behavior of a paste backfill and dumped waste rock is analyzed by conducting both laboratory tests and numerical simulations. Laboratory tests were performed at different scales, starting with small-scale tests where waste rock with a smaller maximum particle size $d_{\max}$ was used. Subsequently, larger large-scale tests were performed using waste rock with a larger $d_{\max}$. A calibrated and validated numerical model obtained in Part I of the study, was then applied to predict the test results. The results indicate that the numerical model can correctly predict the test results of both small-scale and large-scale tests with different $d_{\max}$ of waste rock and mold sizes. The applicability and predictability of the numerical model are validated by these test results. The numerical model can thus be further applied to predict the natural mixing behavior of a paste backfill and dumped waste rock at different scales under various laboratory or even field conditions.

Keywords: Waste rock; Paste backfill; Underground mines; Maximum particle size; Natural mixing behavior; Numerical modeling

7.1 Introduction

Underground mines generate large quantity of waste rock during the development work to access ore bodies. Traditionally, most of the waste rock should be transported and hoisted to ground surface to dispose as waste rock piles due to the limited storage spaces in underground. The transportation process requires substantial energy consumption and additional operational costs. An alternative commonly practice in many underground mines in Canada (and probably also elsewhere in other countries) is to directly dump the waste rock into mine stopes being filled with cemented paste backfill. This practice significantly reduces the quantity of waste rock to be transported at long distance and height, avoiding or reducing the need of energy consumption and operational costs. In addition, fully mixed waste rock and cemented paste backfill can exhibit mechanical strength much better than the individual component (i.e. waste rock or cemented paste alone) of the mixture (Hane et al. 2017; Qiu et al. 2020; Qiu et al. 2022). However, collapses of fill mass generated by dumping waste rock in stopes being filled with cemented backfill took place in some mines, resulting in severe ore dilution or loss. The reason for these reported collapses remains unknown. When an excessive quantity of cohesionless waste rock is dumped into a stope being filled with cemented backfill, poor mixture or even absence of mixing between dumped waste rock and cemented backfill can happen. The generated fill mass can thus contain some weak portions or structures that fail and collapse upon a side- or base- exposure associated with a neighboring excavation. Understanding the natural mixing behavior between dumped waste rock and paste backfill in stopes is thus crucial.

To date, most studies on mining backfills have been concentrated on one single material, which can be hydraulic fill, paste backfill, or rockfill (e.g., Hassani & Archibald 1998; Potvin et al. 2005; El Mkadmi et al. 2014; Liu et al. 2017; Yang et al. 2017; Liu et al. 2018; Béket Dalcé et al. 2019; Pagé et al. 2019; Keita et al. 2021; Qin et al. 2021; Zhai et al. 2021). Only a few studies were reported on mechanical mixtures of graded waste rock and tailings slurry for backfilling (Baldwin and Grice 2000; Kugan and Ian 2001; Potvin et al. 2005; Lee and Gillot 2014; Sun et al. 2018). For these mechanical mixtures, special equipment, energy consumption, and additional operational costs are necessary. The concept is thus entirely different from the natural mixture of dumped waste rock and paste backfill. Until now, studies on the natural mixing behavior of dumped waste rock and paste backfill are still absent.

Recently, Zhang and Li (2023) have reported a laboratory study on the natural mixing behavior of a paste backfill and dumped waste rock. This preliminary study revealed that the mixing behavior of the two materials can be influenced by the solids content of paste backfill, the size of waste rock, and falling height of waste rock. Good mixture can be expected with low solid percentage backfill, large size of waste rock, and high falling height of waste rock. Poor mixture happens when the paste backfill is too thick or when too much waste rock is poured on top of the paste backfill. This study thus provided a direct insight on the mixing behavior between dumped waste rock and paste backfill in small-scale laboratory conditions. More laboratory tests can be conducted with larger box and larger sizes of waste rock. However, it remains impossible to conduct full-scale tests to evaluate the mixing behavior of dumped waste rock and paste backfill under field conditions. Numerical modeling is necessary, even though the public does not have high confidence in numerical modeling in geotechnical engineering (Li 2022). Efforts are needed to earn public's confidence by increasing the stability, reliability, and representativeness of numerical modeling and experimental work as what have been shown in Li (2022) and Zhang and Li (2024a; 2024b). A new example is provided in Part I as a companion paper to show how to obtain reliable numerical results with an optimal and calibrated numerical model. The particle size effects of waste rock on the geotechnical behavior have been taken into account both in experimental work though sample preparation by applying the scalping down technique (Deiminiat and Li 2022) and numerical model through the rolling resistance coefficient as a function of the largest particle size, $d_{\max}$, of waste rock.

In this part, a series of laboratory tests are performed to evaluate the natural mixing behavior of dumped waste rock and paste backfill using waste rock having different values of $d_{\max}$ and different mold sizes. The calibrated and validated numerical model presented in the companion paper (Part I) is then applied to reproduce, by prediction, the experimental results under various test conditions. Upon success, the validated numerical model can then be used to predict the natural mixing behavior of the two materials at any scale under various laboratory and field conditions.

7.2 Laboratory tests of pouring waste rock on paste backfill

7.2.1 Tested materials

The waste rock samples used in this study are the same as those for repose angle tests presented in the companion paper (Part I). Scalping down technique was applied to obtain waste rock samples having $d_{\max}$ values of 2.0, 5.0, and 50.0 mm, respectively. The mass of each scalped sample is 400, 1400 and 4441 g, respectively. Figure 7.1 shows their texture (Figure 7.1a) and particle size distribution (PSD) curves (Figure 7.1b). Particles smaller than 1.18 mm were excluded in order to facilitate the numerical modeling.

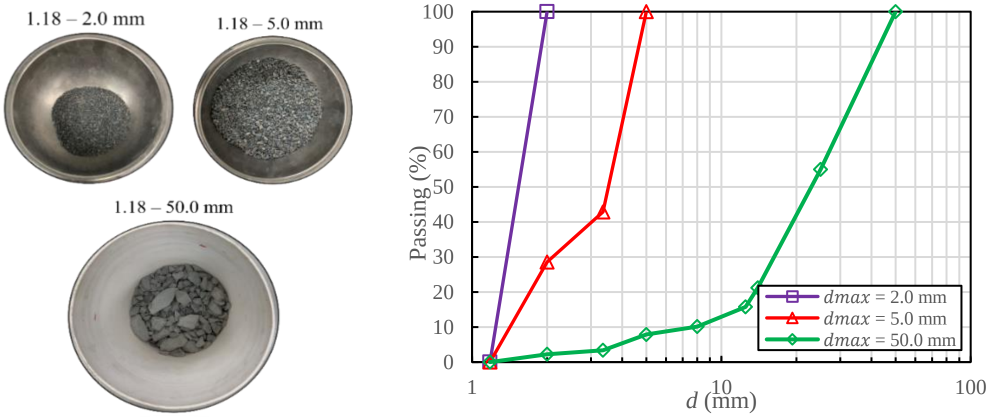

(a)

(b)

Figure 7.1: Scalped waste rock samples with $d_{\max}$ of 50.0, 5.0, and 2.0 mm, respectively: (a) a picture of the samples; (b) PSD curves

The tested tailings were collected from the same mine as the waste rock. The PSD curve is presented in Figure 7.2. The tailings have a $d_{\max}$ of 0.63 mm, with approximately 77% of particles smaller than 80 µm and 36% smaller than 20 µm.

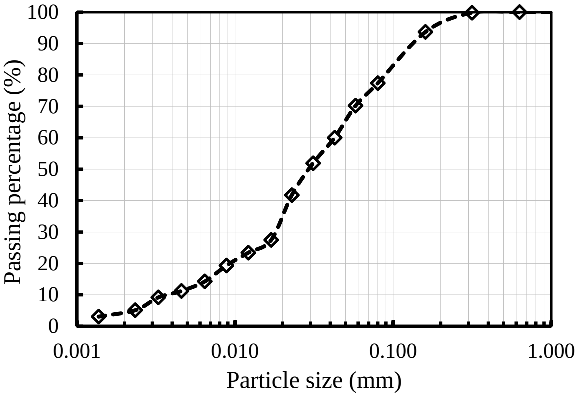

Figure 7.2: PSD curve of the tested tailings

The backfill made of these tailings meets the criterion of paste backfill in terms of PSD, which requires at least 15% of particle smaller than 20 µm (Potvin et al. 2005; Zheng and Li 2020; Zhang and Li 2023). The paste backfills were prepared at a solids content by mass of 75%. Figure 7.3 presents a photo of paste backfill with a solids content by mass of 75%. One sees that the paste backfill is thick and viscous.

Figure 7.3: A photo of tested paste backfill at a solids content by mass of 75%

7.2.2 Test procedure

In this study, two sets of mixing tests were performed. The first set was realized by using scalped waste samples having $d_{\max}$ values of 2.0 and 5.0 mm, with masses of 400 and 1400, respectively. Figure 7.4 presents a schematic presentation (Figure 7.4a) and a photograph (Figure 7.4b) of the testing model. A box in wood of 16.5 cm (length) × 20 cm (width) × 25 cm (height) was used to simulate an underground mine stope (Figure 7.4b). The paste backfill was first poured into the mini stope to a height of 10 cm (Figure 7.4b). After that, a given quantity of waste rock was poured into the paste backfill using a funnel positioned at the middle of the long side of the mold with a falling height H_F (measured from the bottom of the funnel to the top surface of the paste backfill) of 40 cm. After a period of two weeks in order for the mixture to become hard enough, the mold was disassembled. The mixture was cut to evaluate the mixing behavior between the waste rock and the paste backfill.

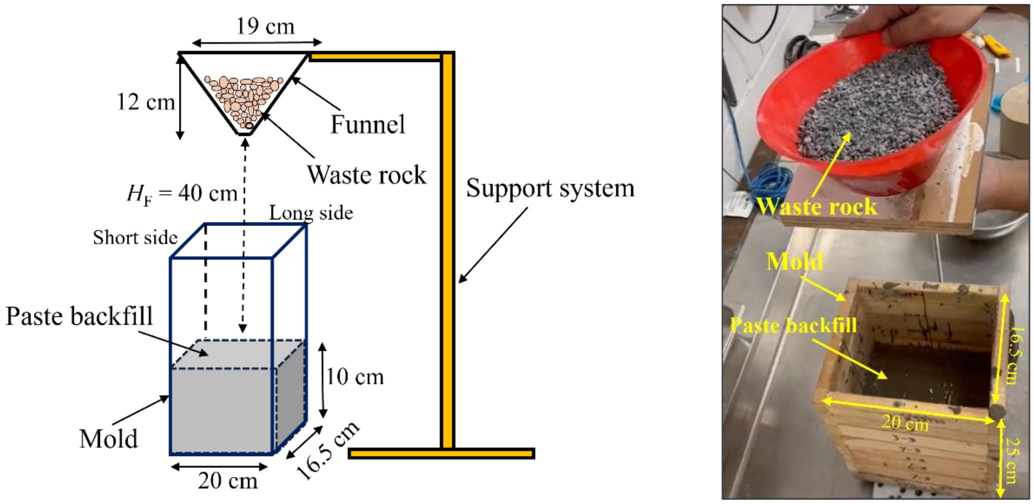

(a) (b)

Figure 7.4: Small-scale test of pouring waste rock samples on the paste backfill at a falling height of 40 cm: (a) schematic presentation; (b) a photo

The second set of tests was conducted by using the waste rock sample having a d_{max} of 50 mm. A photo of the large-scale test model is presented in Figure 7.5. A box in wood of 36 cm (length) × 36 cm (width) × 20 cm (height) was used to simulate a larger underground mine stope. The paste backfill was first poured into the large-scale mold to a height of 15 cm. A total mass of 4441 g of the waste rock was dumped on the paste backfill through a wood incline at the center point of the mold with a falling height of 75 cm. To note that the dumping of the waste rock was performed by quickly turning the wood incline in vertical position. Dropping of waste rock particles during the operation was minimized by hand-holding the waste rock particles at the bottom of the wood incline. After a period of three weeks in order for the mixture to become harden enough, the mixture was cut to evaluate the mixing behavior of the waste rock and paste backfill.

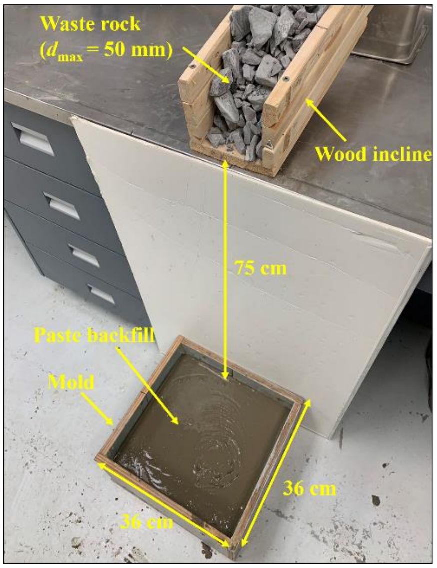

Figure 7.5: A photo of the large-scale test by pouring waste rock with d_{max} of 50.0 mm and a total mass of 4441 g on the paste backfill at a falling height of 75 cm

7.2.3 Test results

Figure 7.6 presents a top view (Figure 7.6a) and a side front view without any cut (Figure 7.6b) of the mixture between the dumped waste rock having a d_{max} of 2.0 mm and a total mass of 400 g, and paste backfill with a falling height of H_F = 40 cm. It can be seen that a large amount of waste rock remains on the top surface of the paste backfill. This is due to the combined effects of the high solids content of the paste backfill and small sizes of waste rock particles. The impact energy of the waste rock particles is small, and the drag force of the paste backfill against the penetration of waste rock particles is high (Zhang and Li 2023). These combined effects result in an unmixed waste rock of 364.7 g and an amount of 35.3 g of waste rock mixed with the paste backfill, measured after the cut of the mixture.

(a)

(b)

Figure 7.6: A top view (a) and a side front view without any cut (b) of the mixing state of the dumped waste rock having a d_{max} of 2.0 mm and a total mass of 400 g with the paste backfill at a falling height of 40 cm

Figure 7.7 presents a top view (Figure 7.7a) and a side front view without any cut (Figure 7.7b) of the mixture between the dumped waste rock having a d_{max} of 5.0 mm and a total mass of 1400 g, and paste backfill with a falling height of H_F = 40 cm. From the top view (Figure 7.7a), one sees a substantial amount of waste rock remaining on the top surface of the paste backfill. The front view (Figure 7.7b) of the mixture before any cut also indicates that there is no mixture between the dumped waste rock and paste backfill. The mass of waste rock unmixed with paste backfill was measured to be 1207 g, indicating an amount of 193 g of waste rock mixed with the paste backfill. These results indicate that the paste backfill having a solids content of 75% is probably too thick for the tested waste rock sizes.

(a) (b)

Figure 7.7: A top view (a) and a side front view without any cut (b) of the mixing state of the dumped waste rock having a d_{max} of 5.0 mm and a total mass of 1400 g with the paste backfill at a falling height of 40 cm

Figure 7.8 presents a top view (Figure 7.8 a) and a cut view (Figure 7.8b) of the mixture between the dumped waste rock having a d_{max} of 50.0 mm and a total mass of 4441 g, and paste backfill with a falling height of H_F = 75 cm. Both views show a small portion of waste rock remaining on the top surface of the paste backfill. A large portion of the dumped waste rock penetrated into the paste backfill. These results are very different from those obtained with the waste rock samples having d_{max} of 2.0 and 5.0 mm, probably due to the combined effects of large waste rock size and high falling height. Waste rock with larger particle sizes and dumped from a higher falling height generates more impact energy, allowing the waste rock to penetrate deeper into the paste backfill. The mass of waste rock unmixed with paste backfill was measured to be 444.5 g, indicating an amount of 3996.5 g of waste rock mixed with the paste backfill.

(a) (b)

Figure 7.8: A top view (a) and a cut view (b) of the mixing state of the dumped waste rock having a d_{max} of 50 mm and a total mass of 441 g with the paste backfill at a falling height of 75 cm

7.3 Reproduction of the experimental results by numerical prediction

To numerically predict the experimental results of dumping waste rock into paste backfill, the numerical model based on EDEM code was used (EDEM 2022). The validation of this numerical model against the analytical solutions to ensure stable and reliable numerical results has been presented in Zhang and Li (2024a; 2024b). Numerical model calibration and validation against the experimental results are presented in the companion paper (Part I). The obtained numerical model can be directly applied to predict the natural mixing behavior of the dumped waste rock and paste backfill. Table 7.1 presents the material parameters of the tested waste rock and paste backfill. The material parameters of the waste rock are the same as those presented in the Part I. For the paste backfill, the yield stress was measured by slump tests, while the viscosity was obtained by numerical calibration against steel ball drop test in the tested paste backfill; details can be found in Zhang and Li (2024a).

Table 7.1: Material parameters for the tested waste rock and paste backfill

Waste rock particle	Particle density (kg/m^3)	2760	Measured
	Young's modulus (GPa)	46.8	Measured[1]
	Poisson's ratio	0.19	Measured[1]
Particle - particle interaction of waste rock	Restitution coefficient	0.79	Measured[2]
	Static friction coefficient	0.466	Measured[2]
	Rolling resistance coefficient	0.15	Calibrated
Paste backfill	Yield stress (Pa)	136	Measured[3]
	Viscosity (Pa.s)	0.7	Calibrated[3]

Note: [1] measured by Major and Knupp (2008) for the same waste rock; [2] measured by Sandeep et al. (2021); [3] measured and calibrated by Zhang and Li (2024a).

Figure 7.9 illustrates the numerical model constructed with EDEM to predict the test results obtained by pouring 400 g waste rock having a $d_{\max}$ of 2.0 mm on the paste backfill at a falling height of 40 cm. The waste rock particles were generated inside the funnel using EDEM dynamic factory (Figure 7.9a). After then, the waste rock was released from the funnel at a falling height of 40 cm to fall on the paste backfill (Figure 7.9b).

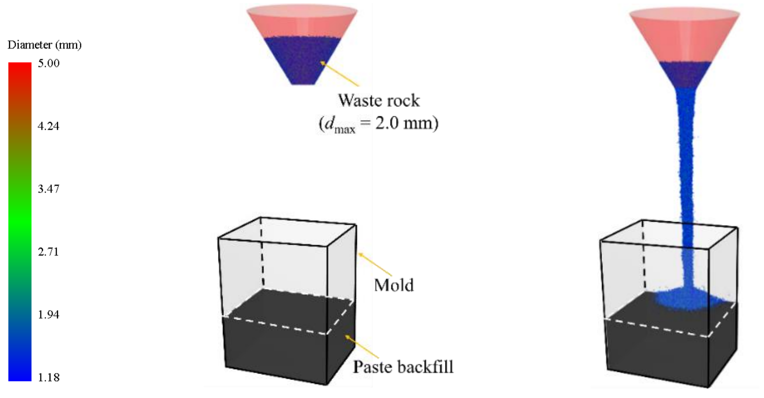

(a) (b)

Figure 7.9: Numerical model built with EDEM for predicting the test results of pouring waste rock having a $d_{\max}$ of 2.0 mm and a mass of 400 g on the paste backfill at a falling height of 40 cm: (a) generation of waste rock particles; (b) pouring waste rock on the paste backfill

Figure 7.10 presents the mixing state between the dumped waste rock and paste backfill obtained by the numerical modeling. The test results are also plotted in the figure for comparison. One sees that the numerical results show a very similar outcome to those obtained by the laboratory test. The measured mass of unmixed waste rock is 364.7 g, indicating that only 35.3 g of waste rock penetrated and mixed with the paste backfill. The masses of waste rock mixed and unmixed with the paste backfill obtained by the numerical prediction are 59.46 and 340.54 g, respectively. The latter is quite close to the measured mass of 364.7 g, while the former is different from the measured mass of 35.3 g.

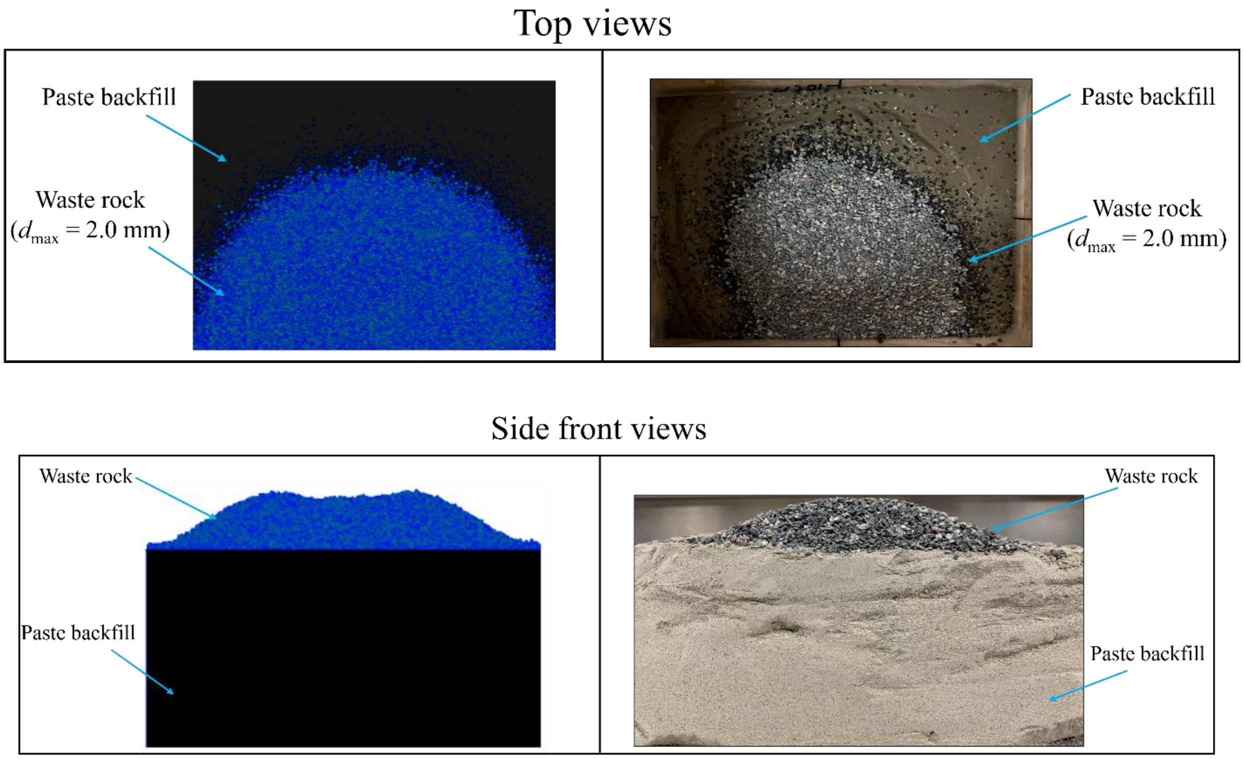

Left: mumerical modeling; Right: test results

Figure 7.10: Mixing state between the paste backfill and the dumped waste rock having a d_{max} of 2.0 mm and a mass of 400 g at a falling height of 40 cm, obtained by numerical predictions and laboratory tests

Figure 7.11 illustrates the numerical model constructed with EDEM to predict the test results obtained by pouring 1400 g waste rock having a d_{max} of 5.0 mm on the paste backfill at a falling height of 40 cm. Once again, the waste rock particles were generated inside the funnel using EDEM dynamic factory (Figure 7.11a). After then, the waste rock was released from the funnel at a falling height of 40 cm to fall on the paste backfill (Figure 7.11b).

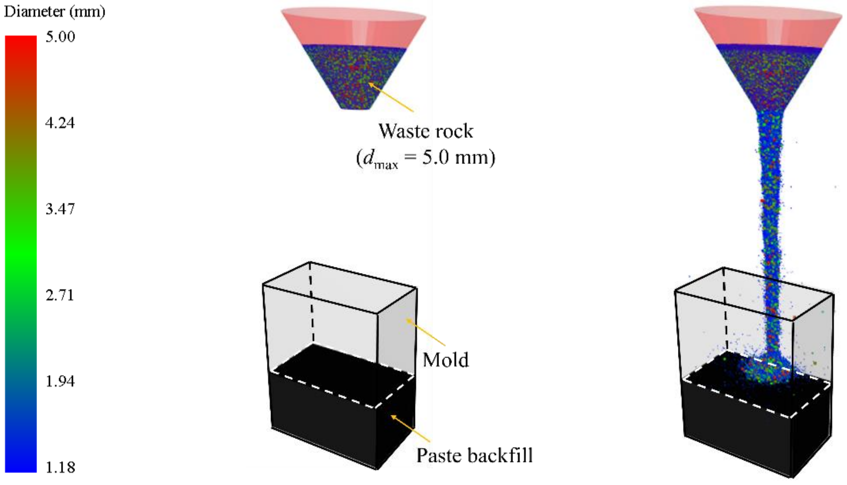

(a) (b)

Figure 7.11: Numerical model built with EDEM for predicting the test results of pouring waste rock having a d_{max} of 5.0 mm and a mass of 1400 g on the paste backfill at a falling height of 40 cm: (a) generation of waste rock particles; (b) pouring waste rock on the paste backfill

Figure 7.12 presents the mixing state between the dumped waste rock and paste backfill obtained by the numerical modeling. The test results are also plotted in the figure for comparison. Once again, a similar outcome is obtained between the numerical modeling and laboratory test results. The masses of waste rock mixed and unmixed with the paste backfill obtained by the numerical prediction are 131.08 and 1268.9 g, respectively. They are quite close to the measured masses of 193 and 1207 g, respectively.

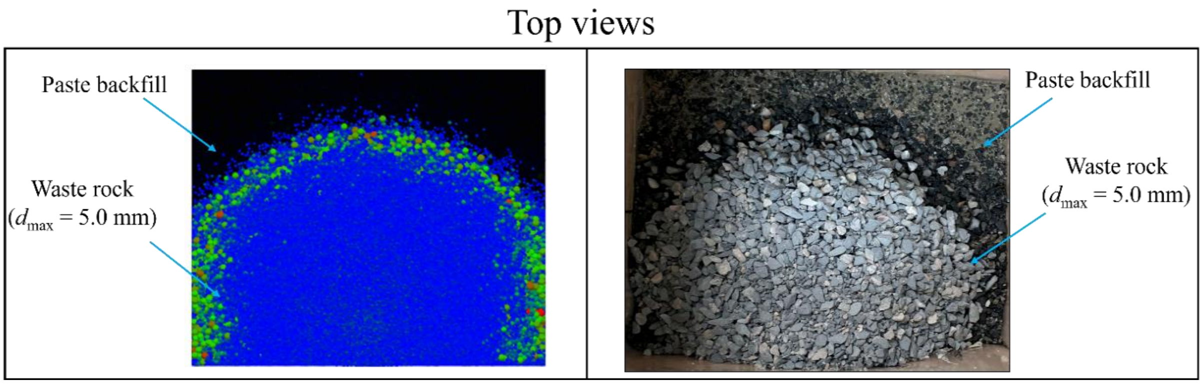

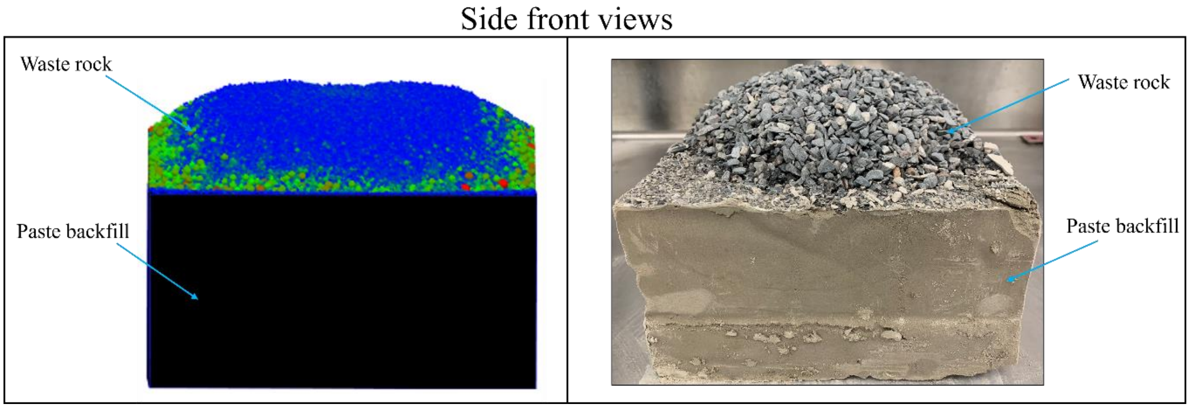

Figure 7.12: Mixing state between the paste backfill and the dumped waste rock having a d_{max} of 5.0 mm and a mass of 1400 g at a falling height of 40 cm, obtained by numerical predictions and laboratory tests

Figure 7.13 presents the numerical model built with EDEM for predicting the large-scale test results obtained by pouring 4441 g waste rock having a d_{max} of 50.0 mm on the paste backfill at a falling height of 75 cm. The waste rock particles were generated inside the funnel using EDEM dynamic factory and released at a falling height of 75 cm to fall on the paste backfill.

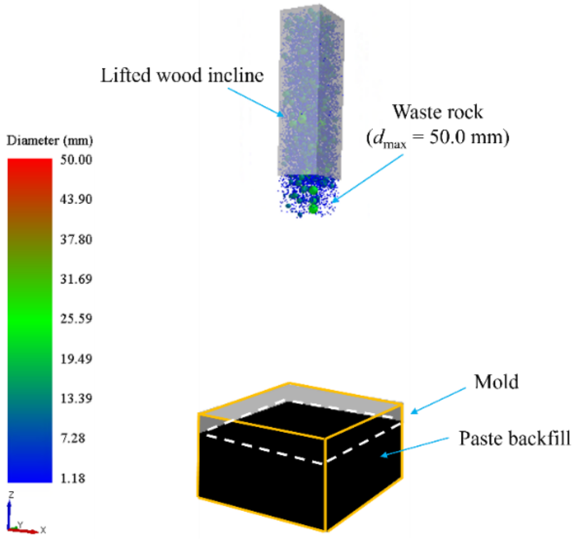

Figure 7.13: Numerical model built with EDEM for predicting the large-scale test results of pouring waste rock having a d_{max} of 50.0 mm and a mass of 4441 g on the paste backfill at a falling height of 75 cm

Figure 7.14 presents the mixing state between the dumped waste rock and paste backfill obtained by the numerical modeling and experimental results. Again, a similar outcome is obtained between the numerical prediction and laboratory test results. The masses of waste rock mixed and unmixed with the paste backfill obtained by the numerical prediction are 3537.66 and 903.34 g, respectively. The former is quite close to the measured mass of 3996.5 g, while the latter is quite different from the measured mass of 444.5 g.

Top views

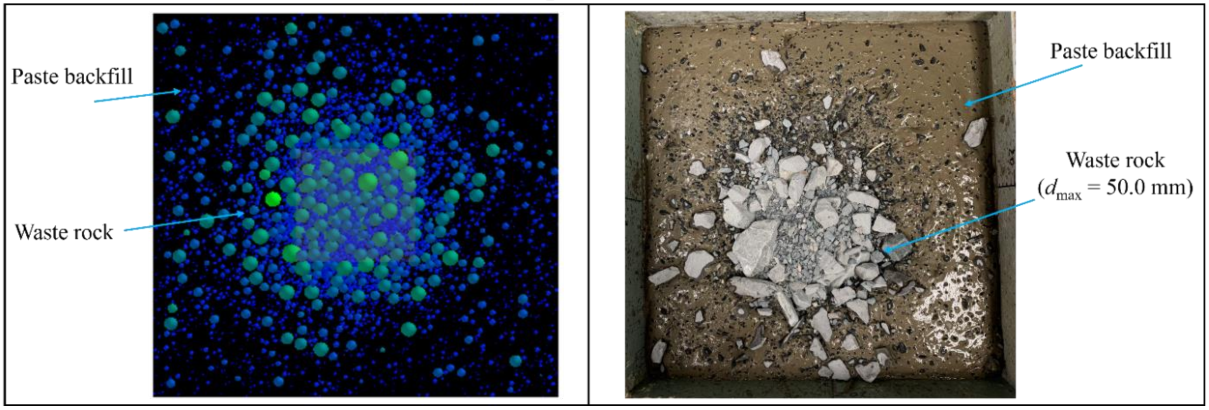

Cut views

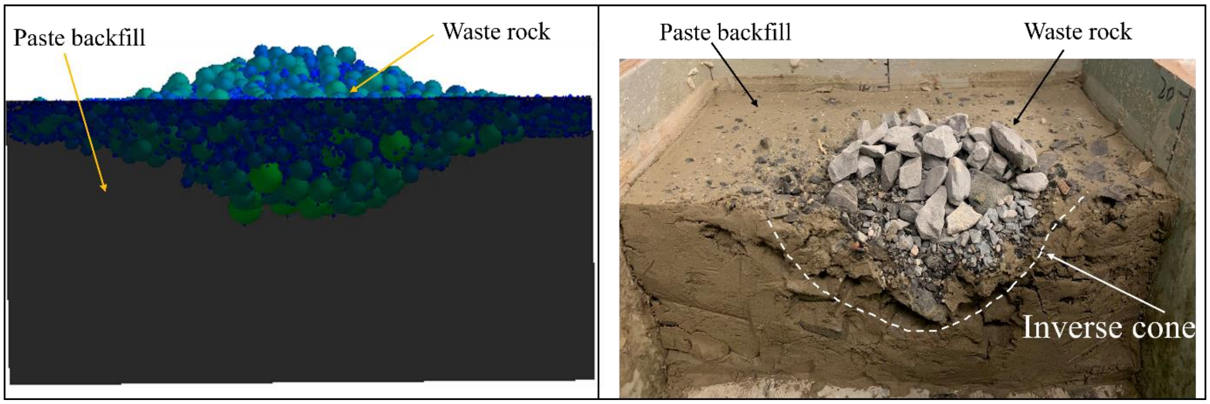

Left: mumerical modeling; Right: test results

Figure 7.14: Mixing state between the paste backfill and the dumped waste rock having a d_{max} of 50.0 mm and a mass of 4441 g at a falling height of 75 cm, obtained by numerical predictions and laboratory tests

The above results indicate that applying the calibrated and validated numerical model can well predict the mixing behavior of dumped waste rock and paste backfill qualitatively in all cases and quantitatively in some cases. The numerical model can thus be applied to evaluate or predict the natural mixing behavior of paste backfill and dumped waste rock under laboratory and field conditions. To further understand why the poor quantitative agreements between the numerical and experimental results for the first and third cases, one can question the numerical prediction, the experimental results, or even both. As the numerical modeling has been done rigorously, one does not question the reliability of the numerical prediction. Subsequently, the discrepancies can only be attributed to the experimental results.

With this question in mind, one comes back to the test procedure. For the case of large-scale test, one can quickly find that the lift of the decline wood and dumping of the waste rock could result in significant differences for the position and failing height compared to the initial design, as what we can see in Figure 7.5. These differences were considered as negligible. They were not taken into account in the numerical modeling/prediction.

For small-scale tests, a funnel was used to pour the waste rock along the sidewall at a predetermined falling height. Such conditions have been considered in numerical modeling or prediction. During the waste rock dumping tests, however, the funnel's position and falling height are probably different from the initial design as what we can see in Figure 7.15. When the funnel base is far from the sidewall and toward the center, more mixed mass of waste rock can be expected. When the funnel is close to the sidewall, some particles of waste rock can fall outside of the box. All these aspects were neglected in the laboratory tests and the numerical model. More laboratory tests with better control and more numerical model, which can take into account the neglected aspects can be necessary. Nevertheless, these results and analyses show once again that numerical modeling is very useful if it is done correctly. It cannot only be used to make analyses and design, but also help to identify possible problems in laboratory tests.

Figure 7.15. A picture taken during the dumping of waste rock on paste backfill for small-scale tests

7.4 Discussion

The natural mixing behavior of waste rock and paste backfill is investigated through multiple scales of laboratory tests and numerical simulations. The predictability of numerical model is validated by predicting the test results. The numerical model can thus be further applied to predict the natural mixing behavior of paste backfill and dumped waste rock with larger $d_{\max}$. However, some assumptions and limitations of this study need to be addressed.

In the simulations, the paste backfill is represented by the buoyance and drag forces. The model thus does not fully correspond to the real situation with the physical presence of the simulated fluid. Additionally, tailing particles cannot be considered in the simulations due to their small sizes and too large in number. Although the numerical model can predict the mass of waste rock penetrated into paste backfill, the mixing quality between the waste rock and paste backfill remains unknown due to the absence of tailings particles. To conduct more realistic conditions, tailings particles may require to be considered in the future studies. However, the simulations of tailings particles may require significant computation time and much more powerful computers.

In the numerical model, the fluid is assumed to be at rest (velocity equals to zero). Consequently, the slip velocity between the particles and fluid is considered equal to the settling velocity of the particles. The model cannot account for the effects of particle movement on the motion of fluids, such as the movement of paste backfill induced by the impact of waste rock, or the flow of paste backfill between the waste rock particles. For these complex simulations, two-way coupling numerical methods (where the fluid flow affects particle movement and the particles, in turn, affect the fluid motion) will be necessary.

For a real paste backfill, tailings particles usually settle very quickly, leading to lower density and viscosity in the upper parts of paste backfill. This reduced viscosity allows waste rock to penetrate deeper inside the paste backfill because lower drag forces exhibited in the top area. As a result, the amount of unmixed waste rock remaining on top surface of the paste backfill is reduced. However, in numerical model, the variation in viscosity along the depth of the paste backfill is not considered.

In this study, the numerical model is applied to simulate the dumping of waste rock into paste backfill with solids content by mass of 75%. To further test the model's applicability under various conditions, additional simulations should be conducted with paste backfill having a wide range of solids contents. In addition, more large-scale tests with different values of $d_{\max}$ are required to further confirm the ability of the numerical model for predicting the natural mixing behavior of dumped waste rock and paste backfill in large scale scenarios.

The numerical results presented in this study are obtained from a single simulation. However, in DEM simulations, the numerical results can vary because the particle information (e.g., particle positions and particle numbers) are not the same in each numerical modeling. This leads to the differences in the results of each simulation. To ensure accurate predictions, it is recommended to conduct multiple simulations for each case to determine the error margin. In addition, the paste backfill properties can change with time (e.g., the variation of water content, particle settlement), these aspects cannot be considered in the numerical model. Future studies are suggested to investigate the effect of time on numerical results.

7.5 Conclusions

In this paper, the natural mixing behavior of dumped waste rock and a paste backfill has been studied through laboratory tests and numerical modeling. Laboratory tests were conducted at different scales, starting with small-scale tests using waste rock with smaller maximum particle size $d_{\max}$, and progressing to large-scale tests with waste rock having larger $d_{\max}$. The calibrated and validated numerical model obtained in part I of the study, was applied to predict the experimental results. The results show that the validated and calibrated numerical model can correctly predict the test outcomes from small-scale tests with small $d_{\max}$ and falling height of waste rock to large-scale tests with large $d_{\max}$ and falling height. The model's applicability and predictability are thus confirmed by successfully predicting the test results under several conditions. Consequently, the validated numerical model can be further applied to predict the natural mixing behavior of a paste backfill and dumped waste rock with larger $d_{\max}$ in a large-scale scenario.

Acknowledgements

The authors acknowledge the financial support from the Natural Sciences and Engineering Research Council of Canada (NSERC RGPIN-2018-06902), Natural Sciences and Engineering Research Council of Canada (NSERC ALLRP 580767 - 22), and industrial partners of the Research Institute on Mines and the Environment (RIME UQAT – Polytechnique; http://rime-irme.ca).

References

Baldwin, G. and A. Grice (2000). Engineering the new Olympic Dam backfill system. *Proceedings Massmin*, 705-711.

Dalcé, J. B., L. Li and P. Yang (2019). Experimental study of uniaxial compressive strength (UCS) distribution of hydraulic backfill associated with segregation. *Minerals*, 9(3).

EDEM (2022). *Altair EDEM 2022.2 Release Notes*. Altair Engineering Inc.

El Mkadmi, N., M. Aubertin and L. Li (2014). Effect of drainage and sequential filling on the behavior of backfill in mine stopes. Canadian Geotechnical Journal, 51(1), 1-15.

Hane, I., T. Belem, M. Benzaazoua and A. Maqsoud (2017). Laboratory characterization of cemented tailings paste containing crushed waste rocks for improved compressive strength development. Geotechnical and Geological Engineering, 35(2), 645-662.

Hassani, F., Archibald, J., Canadian Institute of Mining, M., & Petroleum. (1998). *Mine backfill 1998.* Canadian Institute of Mining, Metallurgy and Petroleum, Montréal, Canada.

Keita, A. M. T., A. Jahanbakhshzadeh and L. Li (2021). Numerical analysis of the failure mechanisms of sill mats made of cemented backfill. *International Journal of Geotechnical Engineering*, 16(7), 802-814.

Kugan, K. and S. Ian (2001). A non-segregating "Rocky Paste Fill (RPF) produced by co- disposal of cemented de-slimed tailings slurry and graded rockfill. *Society for Mining, Metallurgy & Exploration*.

Lee, C. and P. Gillot (2014). Case study – a high strength paste aggregate backfill at Randgold's Loulo mine in Mali. *Mine Fill 2014: Proceedings of the Eleventh International Symposium on Mining with Backfill*. Australian Centre for Geomechanics, 231-242.

Li, L. (2022). Special issue on numerical modeling in civil and mining geotechnical engineering. *Processes*, 10(8).

Liu, G., L. Li, X. Yang and L. Guo (2018). Required strength estimation of a cemented backfill with the front wall exposed and back wall pressured. *International Journal of Mining and Mineral Engineering*, 9(1), 1-20.

Liu, G., L. Li, M. Yao, D. Landry, F. Malek, X. Yang and L. Guo (2017). An investigation of the uniaxial compressive strength of a cemented hydraulic backfill made of alluvial sand. *Minerals*, 7(1).

Major, G. and R. Knupp (2008). *Report on feasibility-level pit slope design criteria Osisko Canadian Malartic project*. Golder Associates Inc.

Pagé, P., L. Li, P. Yang and R. Simon (2019). Numerical investigation of the stability of a base-exposed sill mat made of cemented backfill. *International Journal of Rock Mechanics and Mining Sciences*, 114, 195-207.

Potvin, Y., E. Thomas, A. Fourie and A. C. f. Geomechanics (2005). *Handbook on mine fill*. Australian Centre for Geomechanics.

Qin, J., J. Zheng and L. Li (2021). Experimental study of the shrinkage behavior of cemented paste backfill. *Journal of Rock Mechanics and Geotechnical Engineering*, 13(3), 545-554.

Qiu, H., F. Zhang, L. Liu, D. Hou and B. Tu (2020). Influencing factors on strength of waste rock tailing cemented backfill. *Geofluids*, *2020*, 1-7.

Qiu, H., F. Zhang, W. Sun, L. Liu, Y. Zhao and C. Huan (2022). Experimental study on strength and permeability characteristics of cemented rock-tailings backfill. *Frontiers in Earth Science*, 10.

Sandeep, C. S., K. Senetakis, D. Cheung, C. E. Choi, Y. Wang, M. R. Coop and C. W. W. Ng (2021). Experimental study on the coefficient of restitution of grain against block interfaces for natural and engineered materials. *Canadian Geotechnical Journal*, 58(1), 35-48.

Sun, W., H. Wang and K. Hou (2018). Control of waste rock-tailings paste backfill for active mining subsidence areas. *Journal of Cleaner Production*, 171, 567-579.

Yang, P., L. Li, M. Aubertin, M. Brochu-Baekelmans and S. Ouellet (2017). Stability analyses of waste rock barricades designed to retain paste backfill. *International Journal of Geomechanics*, 17(3).

Zhai, Y., P. Yang and L. Li (2021). Analytical solutions for the design of shotcrete waste rock barricades to retain slurried paste backfill. *Construction and Building Materials*, 307.

Zhang, Y. and L. Li (2023). Experimental study on the natural mixing behaviour of waste rocks poured in a paste backfill. *International Journal of Mining, Reclamation and Environment*, 1-25.

Zhang, Y. and L. Li (2024a). Introduction and implementation of fluid forces in a DEM code for simulating particle settlement in fluids. *Powder Technology*, 433.

Zhang, Y. and L. Li (2024b). Optimization of discrete element method model to obtain stable and reliable numerical results of mechanical response of granular materials. Minerals, 14(8), 758.

Zheng, J. and L. Li (2020). Experimental study of the “short-term” pressures of uncemented paste backfill with different solid contents for barricade design. *Journal of Cleaner Production*, 275.

CHAPTER 8 GENERAL DISCUSSION

The primary objective of this project is to understand the natural mixing behavior of dumped waste rock and paste backfill under various conditions. The objective was achieved through a series of experimental tests, numerical modelling, and analyses. The numerical model has been validated and calibrated against laboratory tests, taking into account the scale effects related to stope geometry and particle sizes of waste rock. The numerical model can thus be used to evaluate and quantify the natural mixing behavior of dumped waste rock and paste backfill in underground mine stopes. Nevertheless, these studies still involve several limitations.

- All the experimental works from the beginning to the end of this thesis were conducted by using non-cemented paste backfill. The test conditions do not fully correspond to field conditions. The effect of cement on the natural mixing behavior of waste rock and paste backfill is thus unknown and needs to be investigated.
- The well-mixed mixture between the waste rock and paste backfill has a texture that looks like concrete and can be expected to have a better mechanical behavior than single material of waste rock and paste backfill. However, no laboratory tests were done to measure the mechanical properties of the natural mixture. As a result, no comparisons were made between the mechanical properties of the natural mixture and those of individual waste rock and paste backfill.
- The bulk density of waste rock is not expected to remain constant after being dumped into paste backfill. However, due to the challenges in accurately determining the actual bulk density of waste rock within the paste backfill, we have assumed it to be equivalent to the bulk density of waste rock in its natural state for the calculation of mixing degree. This assumption may not fully capture the actual conditions, and further investigation is necessary to accurately assess the bulk density of waste rock in paste backfill.
- The laboratory test results presented in Chapter 3 provide a fundamental understanding of the natural mixing behavior of the dumped waste rock and paste backfill. To quantitatively evaluate the effects of influencing factors such as solids content of paste backfill, particle size, and falling height of waste rock on the natural mixture, it would be valuable to establish a relationship between the influence factors and the resulted mixture.

- In order to evaluate the natural mixing behavior of dumped waste rock and paste backfill in stopes, a new component was developed and implemented in an existing numerical code (EDEM). The buoyance and drag forces were taken into account. The effects of particle movement on fluid motion, such as splash of fluid after the drop of multiple particles in the fluid, were not taken into account. In addition, the drag force model was developed for particles with spherical shapes. More work is needed to evaluate if this approach is suitable for any shapes of particles.
- One can also question the suitability of the drag force model used in the numerical model because the drag force model was established based on test results of spheres settling in clay suspensions. More experiment works are necessary to obtain more results of spheres settling in paste backfill with different solids contents. All these mentioned and unmentioned limitations can partly explain the differences observed between numerical predictions and experimental results presented in Chapter 7.
- In the numerical models used in this study, spherical particles were employed to represent the non-spherical waste rock particles. The effects of particle shape and sizes were accounted for by calibrating the rolling resistance coefficient. In future studies, it would be valuable to conduct numerical simulations using the actual non-spherical shapes of waste rock to explore the differences between these two approaches.
- We highlight that the PSD curve cannot be arbitrarily cut for numerical models, and sensitivity analysis is necessary. However, it is found that the standard sieve sizes commonly used in geotechnical engineering are not dense enough. Assumptions and approximations have to be made in the numerical model to generate particles between two neighboring sieves. The actual particle size distributions (e.g., particle sizes and corresponding mass proportions) between two consecutive standard sieves are unknown due to the lack of intermediate sieves. If the PSD generated in EDEM corresponds well to the actual PSD of the tested waste rock between two consecutive sieves can be questionable.
- In this study, we showed how to achieve an optimal PSD cut by excluding fine particles. This methodology can only be considered valid for mechanical behaviors (e.g., repose angle) because very fine particles can remain free within the pores or void spaces between large particles when their sizes and quantities are negligible (but huge in number of particles). This explains well why PSD cuts can be made by excluding some fine particles

through sensitivity analysis in numerical modeling. For hydraulic and thermal behaviors of granular materials, it is well known that the properties can be significantly influenced by the sizes and quantities of fine particles. The method PSD cut by excluding fine particle become invalid. In addition, the method also becomes invalid for fine bonded particles.

- In Chapter 6, the calibrated numerical model has been successfully validated against the repose angle tests under different conditions (e.g., different maximum particle sizes and masses of waste rock). The validated numerical model can thus be considered to be able to predict the behavior of waste rock in field conditions. It remains however as an assumption as long as the validated and calibrated numerical model is not validated by field tests with full size of waste rock.
- The validated and calibrated numerical model can be further applied to predict many behaviors of large-scale or even on-site scale waste rock piles, such as segregation and stability analyses. However, simulating large-scale or field tests needs the generation of huge number of particles and requires powerful computers equipped with more advanced computing techniques.
- During the experimental work, it was observed that the tailings particles typically settle down very quickly. This rapid settlement results in changes in the density and viscosity at different depths. Additionally, variations in the water content of paste backfill over time can also alter the properties of paste backfill. As a result, the mixing behavior of dumped waste rock and paste backfill is likely to be different from the case with a uniform paste backfill. In numerical modeling, these aspects were not considered.
- In Chapter 7, the unmixed and mixed mass of waste rock obtained from the numerical model shows some differences compared to the test results. The differences can be attributed to several factors. In the tests, we used a funnel to pour the waste rock from a predetermined position and height. However, the funnel’s position and height could shift in the test because it was not entirely stable when filled with waste rock. Additionally, some waste rock was lost due to the collisions with the walls of the mold, but these losses were neglected in the tests. In contrast, in the numerical model, the funnel’s position is fully fixed. This fixed position may not accurately reflect the real pouring conditions in the tests. To further investigate these effects, additional simulations were necessary to evaluate the impact of funnel’s pouring conditions on the numerical results.

- In DEM simulations, the numerical results can vary between simulations because the particle information (e.g., particle positions and particle numbers) can differ across each time. These variations can lead to some differences in the simulation outcomes. To improve the reliability of the numerical predictions, it is recommended to perform multiple simulations for each case and determine the associated error margin.

CHAPTER 9 CONCLUSIONS AND RECOMMENDATIONS

9.1 Conclusions

In this thesis, the natural mixing behavior of dumped waste rock and paste backfill is investigated for the first time. The investigation began with small-scale laboratory tests, which provided preliminary understanding of the mixing behavior between the two materials. However, the small-scale test results are insufficient to fully understand the natural mixing behavior of dumped waste rock and paste backfill in a stope. Therefore, the numerical model must be applied due to the limitations of conducting full-scale laboratory tests and lacking scale factors. A numerical model was then developed to simulate the settlement of particles in viscous fluids. Before applying the numerical model to simulate the mixture, it was essential to ensure its stability and reliability. To achieve this, a methodology for constructing an optimal numerical model to ensure stable and reliable numerical results was proposed. The numerical model, with stable and reliable numerical results, was then calibrated and validated based on a series of laboratory tests by considering the particle size effects and scale effects. This calibrated and validated numerical model can be used to investigate the natural mixing behavior of dumped waste rock and paste backfill under various conditions, from laboratory to field applications. The main conclusions are recalled and summarized as follows:

- The natural mixing behavior of dumped waste rock and paste backfill is influenced by factors such as particle size, falling height of waste rock, and the solids content of paste backfill. The quantity of unmixed waste rock can be expected to increase with the increase of solids content of paste backfill. The mixing degree of the dumped waste rock and paste backfill can be improved by using the paste backfill with a lower solids content, and the waste rock with a larger particle size and a higher falling height.
- In the f-EDEM model, fluid forces are formulated and directly implemented within the EDEM code. This allows for the simulation of particle settlement in fluids using a single DEM code, without the need for coupling with a CFD or SPH solver. The perfect agreement between the analytical results and the numerical results for the settling velocity of a particle in water confirms the successful validation of the f-EDEM model. Further comparisons between the numerical and experimental results of spheres settling in clays and steel balls falling into paste

backfill demonstrate the f-EDEM model is capable of simulating particle settlement in different fluids.

- The validation of a numerical model is crucial, particularly for new users, as it helps us learn how to use the code correctly, to identify potential errors or limitations in the numerical model. Additionally, validation can help the users to achieve an optimal numerical model, which ensures stable and reliable numerical results with the shortest computation time. Validation can be accomplished by performing sensitivity analyses on various parameters (e.g., time step, mesh size, domain size, tolerance, etc.) and comparing the numerical results with analytical results.
- The sensitivity analysis of time step indicates that the time step recommended by DEM code manuals is sometime conservative. While this recommended time step may be acceptable for small models with a limited number of particles due to shorter overall calculation times, it can significantly increase the computation time for large models with large amount of particles. Therefore, it is always worthwhile to perform a time step sensitivity analysis on a case-by-case basis to determine the optimal the optimal time step, ensuring stable and reliable numerical results while minimizing computation time.
- In numerical modeling, calibration is only recommended for model parameters that cannot be measured or for which measurements are unreliable. Physical and mechanical parameters should be measured whenever possible. The measured values need be directly used to minimize the number of model parameters obtained through calibration. They should not be simply neglected, changed or calibrated unless their measurements are unreliable with valid justifications.
- In the simulation of mechanical behavior of granular materials, a portion of fine particles can indeed be excluded to reduce the simulation time. However, the PSD cut for excluding fine particles can not be done arbitrarily. Sensitivity analyses should be conducted to determine the optimal PSD cut, ensuring stable and reliable numerical results. Young’s modulus of granular materials can be reduced to decrease the calculation time without altering the numerical results. However, the optimal Young’s modulus should be determined through sensitivity analyses.
- The mass of waste rock and specimen size W to $d_{\max}$ ratio can influence the stability and reliability of the repose angle test results. To obtain stable and reliable repose angle test results, the minimum required mass and specimen size ratio should be respected. The scalping down

technique is validated for preparing the waste rock samples for the repose angle tests. The established relationship curve between the repose angle θ and $d_{\max}$ can accurately predict the repose angle of the large-scale waste rock pile in the laboratory and the on-site waste rock pile having larger value of $d_{\max}$. The rolling resistance coefficient of the tested waste rock does not significantly change as the value of $d_{\max}$ increases from smaller value to larger value. The established curve can be used to predict the rolling resistance coefficient of waste rock with larger $d_{\max}$. The good agreements between the measured repose angles and those predicted by numerical modeling indicate that the calibrated numerical model can be used to analyze the geotechnical behavior of various sizes of infrastructures made of different sizes of waste rock under diverse conditions, including field conditions as long as the necessary computing resources are available.

- The validated and calibrated numerical model can correctly predict the test results from small-scale tests with small $d_{\max}$ and falling height of waste rock to large-scale tests with large $d_{\max}$ and falling height. The model's applicability and predictability are thus confirmed by successfully predicting the test results of dumping waste rock into paste backfill under several conditions. Consequently, the validated numerical model can be further applied to predict the natural mixing behavior of a paste backfill and dumped waste rock with larger $d_{\max}$ in a large-scale scenario.

9.2 Recommendations

In addition to the outcomes presented in the thesis, recommendations are given on several aspects as following for further research to better understand the natural mixing behavior of dumped waste rock and paste backfill:

- More laboratory tests and numerical modeling should be done by using cement paste backfill. The effects of binder type and cement content on the natural mixing behavior of waste rock and paste backfill need to be evaluated in future studies.
- The mechanical properties of natural mixtures are recommended to be measured in future studies.
- The actual bulk density of waste rock within the paste backfill needs to be further investigated.
- The viscosity of paste backfill should be measured by conducting rheology tests (Belem 2024).

- An analytical solution can be developed to estimate the scale effects associated with particle sizes of waste rock and mold dimensions on the mixing behavior of dumped waste rock and paste backfill (Ovalle 2024).
- A relationship can be established between the system's energy (e.g., by considering the effects of particle size, mass and falling height of waste rock) and the mixture degree to quantitatively describe the effects of various influencing factors on the natural mixture (Ovalle 2024).
- The effects of particle movement on the fluid motion should be considered in the numerical model by incorporating two-way simulations, where the fluid flows affect particle movement and the particles, in turn, affect fluid motion.
- Additional experiment works are suggested to obtain more results of spheres settling in paste backfill with different solids contents to further test the applicability of the proposed drag force model.
- The drag force model is developed for particles with spherical shapes settling in viscous fluids. A drag force model for non-spherical particles settling in viscous fluids should be developed to better reflect the physical reality.
- The effects of tailings particle settlement on the movement of waste rock are suggested to be taken into account in numerical model. Additionally, variations in the water content of the paste backfill associated with the dumping of waste rock should also be taken into account (Cui 2024).
- The non-spherical waste rock particles are represented by the spherical particles in the EDEM model. The shape effects were addressed by calibrating the rolling resistance coefficient. It would be interesting to evaluate whether this approach can also capture the shape effects for particles immersed in fluids (Ovalle 2024).
- Numerical simulations using the actual non-spherical shapes of waste rock are recommended for future studies.
- More numerical simulations using waste rock having the same $d_{\max}$ as that of field material should be conducted to confirm the predictability of the numerical model. Of course, more powerful computers with advanced computing techniques can be necessary for the numerical simulations of such full-scale problems (Cacciari 2024).
- Future studies should consider conducting numerical simulations of the natural mixing behavior of waste rock and paste backfill under field conditions (Ouellet 2024).

- In DEM simulations, the numerical results can vary because the particle information (e.g., particle positions and particle numbers) are not the same in each time of simulation. This leads to slight differences in the results of each simulation. Multiple simulations can be necessary for each case to determine the error margin.

BIBLIOGRAPHY

Abzalov, M. (2016). Mining methods. *Applied Mining Geology*, 5-18.

Ahmed, H. M., Bharathan, B., Kermani, M., Hassani, F., Hefni, M. A., Ahmed, H. A. M., Hassan, G. S. A., Moustafa, E. B., Saleem, H. A., & Sasmito, A. P. (2022). Evaluation of rheology measurements techniques for pressure loss in mine paste backfill transportation. *Minerals*, 12(6).

Ancey, C., Balmforth, N. J., & Frigaard, I. (2008). Visco-plastic fluids: from theory to application. *Applied Rheology*, 18(1), 48-50.

Annor, A. (1999). *A study of the characteristics and behaviour of composite backfill material*. Ph.D. thesis, McGill University.

Ansley, R. W., & Smith, T. N. (1967). Motion of spherical particles in a Bingham plastic. *AIChE Journal*, 13, 1193-1196.

Arabi, A. S., & Sanders, R. S. (2016). Particle terminal settling velocities in non-Newtonian viscoplastic fluids. *The Canadian Journal of Chemical Engineering*, 94(6), 1092-1101.

Askew, J., McCarthy, P., & Fitzgerald, D. (1978). Backfill research for pillar extraction at ZC/NBHC. *Mining with backfill*, 12, 100-110.

Aubertin, M. (2013). Waste rock disposal to improve the geotechnical and geochemical stability of piles. *23rd World Mining Congress (WMC 2013)*, Montréal, Québec.

Aubertin, M., Bussière, B., & Bernier, L. (2002). *Environnement et gestion des rejets miniers*. Presses Internationales Polytechnique.

Aubertin, M., & Li, L. (2004). A porosity-dependent inelastic criterion for engineering materials. *International Journal of Plasticity*, 20(12), 2179-2208.

Aubertin, M., Li, L., & Simon, R. (2000). A multiaxial stress criterion for short-and long-term strength of isotropic rock media. *International Journal of Rock Mechanics and Mining Sciences*, 37(8), 1169-1193.

Aubertin, M., Li, L., Simon, R., & Buissière, B. (2003). *A general plasticity and failure criterion for materials of variable porosity*. Technical Report EPM-RT-2003-11. École Polytechnique de Montréal, Montréal, Québec.

Aubertin, M., Li, L., Simon, R., & Khalfi, S. (1999). Formulation and application of a short-term strength criterion for isotropic rocks. *Canadian Geotechnical Journal*, 36(5), 947-960.

Awwad, H. A., Rami, O. A., & Hani, M. A. (2021). Open pit mining. *Mining techniques.* Rijeka: IntechOpen, 1-22.

Azam, S., & Li, Q. (2010). Tailings dam failures: a review of the last one hundred years. *Geotechnical news*, 28(4), 50-54.

B., B., Benzaazoua, M., Aubertin, M., & Mbonimpa, M. (2004). A laboratory study of covers made of low-sulphide tailings to prevent acid mine drainage. *Environmental Geology*, 45(5), 609-622.

Baldwin, G., & Grice, A. (2000). Engineering the new Olympic Dam backfill system. *Proceedings Massmin*, 705-711.

Behera, S., Ghosh, C., Mishra, K., Mishra, D. P., Singh, P., Mandal, P., Buragohain, J., & Sethi, M. (2020). Utilisation of lead–zinc mill tailings and slag as paste backfill materials. *Environmental Earth Sciences*, 79, 1-18.

Béket Dalcé, J., Li, L., & Yang, P. (2019). Experimental study of uniaxial compressive strength (UCS) distribution of hydraulic backfill associated with segregation. *Minerals*, 9(3).

Belem, T. (2024). *Recommendation during the Q/A of the Ph.D. defense of Yuyu Zhang*. Polytechnique Montréal, Montréal.

Belem, T., & Benzaazoua, M. (2007). Design and application of underground mine paste backfill technology. *Geotechnical and Geological Engineering*, 26(2), 147-174.

Belem, T., Benzaazoua, M., & Bussière, B. (2000). Mechanical behaviour of cemented paste backfill. *Proc. of 53rd Canadian Geotechnical Conference,* Montreal, 373-380.

Belem, T., Benzaazoua, M., Bussière, B., & Dagenais, A. (2022). Effects of settlement and drainage on strength development within mine paste backfill. *Tailings and Mine Waste 2002,* 139-148.

Belem, T., El Aatar, O., Bussière, B., & Benzaazoua, M. (2016). Gravity-driven 1-D consolidation of cemented paste backfill in 3-m-high columns. *Innovative Infrastructure Solutions*, 1(1), 1-12.

Benzaazoua, M., Bussière, B., Demers, I., Aubertin, M., Fried, É., & Blier, A. (2008). Integrated mine tailings management by combining environmental desulphurization and cemented paste backfill: application to mine Doyon, Quebec, Canada. *Minerals Engineering*, 21(4), 330-340.

Berger, K. J., & Hrenya, C. M. (2014). Challenges of DEM: II. wide particle size distributions. *Powder Technology*, 264, 627-633.

Beya, F., Mbonimpa, M., Belem, T., Li, L., Marceau, U., Kalonji, P., Benzaazoua, M., & Ouellet, S. (2019). Mine backfilling in the permafrost, Part I: numerical prediction of thermal Curing conditions within the cemented paste backfill matrix. *Minerals*, 9(3).

Blackery, J., & Mitsoulis, E. (1997). Creeping motion of a sphere in tubes filled with a Bingham plastic material. *Journal of Non-Newtonian Fluid Mechanics*, 70(1), 59-77.

Blight, G. E. (2009). *Geotechnical engineering for mine waste storage facilities*. CRC Press.

Blowes, D. W. (1990). *The Geochemistry, hydrogeology and mineralogy of decommissioned sulfide tailings: a comparative study*. Ph.D. thesis, University of Waterloo.

Bokharaeian, M., Naderi, R., & Csámer, Á. (2021). Numerical experimental comparison of mudflow by smoothed particle hydrodynamics (SPH). *International Review of Applied Sciences and Engineering*, 13(1), 22-28.

Brady, B. H. G., & Brown, E. T. (2007). *Rock mechanics: for underground mining*. Springer science & business media.

Brosh, T., Kalman, H., & Levy, A. (2014). Accelerating CFD–DEM simulation of processes with wide particle size distributions. *Particuology*, 12, 113-121.

Brown, P. P., & Lawler, D. F. (2003). Sphere drag and settling velocity revisited. *Journal of Environmental Engineering*, 129(3), 222-231.

Bullock, R. L. (2011). Comparison of underground mining methods. *SME mining engineering handbook*, 385-403.

Burns, S. J., & Hanley, K. J. (2016). Establishing stable time-steps for DEM simulations of non-collinear planar collisions with linear contact laws. *International Journal for Numerical Methods in Engineering*, 110(2), 186-200.

Burns, S. J., Piiroinen, P. T., & Hanley, K. J. (2019). Critical time step for DEM simulations of dynamic systems using a Hertzian contact model. *International Journal for Numerical Methods in Engineering*, 119(5), 432-451.

Bussière, B. (2007). Colloquium 2004: Hydrogeotechnical properties of hard rock tailings from metal mines and emerging geoenvironmental disposal approaches. *Canadian Geotechnical Journal*, 44(9), 1019-1052.

Bussière, B., Aubertin, M., & Chapuis, R. P. (2003). The behavior of inclined covers used as oxygen barriers. *Canadian Geotechnical Journal*, 40(3), 512-535.

Bussière, B., Aubertin, M., Mbonimpa, M., Molson, J. W., & Chapuis, R. P. (2007). Field experimental cells to evaluate the hydrogeological behaviour of oxygen barriers made of silty materials. *Canadian Geotechnical Journal*, 44(3), 245-265.

Cacciari, P. (2024). *Recommendation during the Q/A of the Ph.D. defense of Yuyu Zhang*. Polytechnique Montréal, Montréal.

Cacciuttolo, C., & Cano, D. (2023). Spatial and temporal study of supernatant process water pond in tailings storage facilities: use of remote sensing techniques for preventing mine tailings dam failures. *Sustainability*, 15(6), 4984.

Cacciuttolo, C., & Marinovic, A. (2023). Experiences of underground mine backfilling using mine tailings developed in the Andean region of Peru: A green mining solution to reduce socio-environmental impacts. *Sustainability*, 15(17), 12912.

Capozzi, L. C., Barresi, A. A., & Pisano, R. (2019). Supporting data and methods for the multi-scale modelling of freeze-drying of microparticles in packed-beds. *Data Brief*, 22, 722-755.

Casarin, J., Franco, A., Germer, E., & Pivovarski, R. (2022). Numerical simulation of the particle settling in a Bingham fluid using the two-way coupling CFD-DEM scheme. *Journal of Theoretical and Applied Mechanics*, 409-422.

Cheng, N.-S. (2009). Comparison of formulas for drag coefficient and settling velocity of spherical particles. *Powder Technology*, 189(3), 395-398.

Chhabra, R. (2006). *Bubbles, drops, and particles in non-Newtonian fluids*. CRC Press.

Chung, Y. C., & Ooi, J. Y. (2011). Benchmark tests for verifying discrete element modelling codes at particle impact level. *Granular Matter*, 13(5), 643-656.

Church, J. A., Peele, R., Wiley, J., Sons, Chapman, & ., H. (1956). *Mining engineers' handbook: in two volumes.* Wiley Engineering Handbook Series.

Clayton, S., Grice, T. G., & Boger, D. V. (2003). Analysis of the slump test for on-site yield stress measurement of mineral suspensions. *International Journal of Mineral Processing*, 70(1-4), 3-21.

Cleary, P. W. (2015). Prediction of coupled particle and fluid flows using DEM and SPH. *Minerals Engineering*, 73, 85-99.

Cleary, P. W., Hilton, J. E., & Sinnott, M. D. (2017). Modelling of industrial particle and multiphase flows. *Powder Technology*, 314, 232-252.

Cleary, P. W., & Prakash, M. (2004). Discrete-element modelling and smoothed particle hydrodynamics: potential in the environmental sciences. *Philosophical Transactions of the Royal Society of London. Series A: Mathematical, Physical and Engineering Sciences*, 362(1822), 2003-2030.

Cleary, P. W., Sinnott, M., & Morrison, R. (2006). Prediction of slurry transport in SAG mills using SPH fluid flow in a dynamic DEM based porous media. *Minerals Engineering*, 19(15), 1517-1527.

Concha Arcil, F. (2009). Settling velocities of particulate systems. *KONA Powder and Particle Journal*, 27, 18-37.

Cooke, R. (2006). Thickened and paste tailings pipeline systems: design procedure–part 1. *Paste 2006: Proceedings of the Ninth International Seminar on Paste and Thickened Tailings*, Australian Centre for Geomechanics, 371-381.

Cross, R. (2016). Coulomb's law for rolling friction. *American Journal of Physics*, 84(3), 221-230.

Cui, L. (2024). *Recommendation during the Q/A of the Ph.D. defense of Yuyu Zhang*. Polytechnique Montréal, Montréal.

Cui, L., & Fall, M. (2015). A coupled thermo–hydro-mechanical–chemical model for underground cemented tailings backfill. *Tunnelling and Underground Space Technology*, 50, 396-414.

Cui, L., & Fall, M. (2016). Mechanical and thermal properties of cemented tailings materials at early ages: Influence of initial temperature, curing stress and drainage conditions. *Construction and Building Materials*, 125, 553-563.

Cui, L., & Fall, M. (2017). Multiphysics modeling of arching effects in fill mass. *Computers and Geotechnics*, 83, 114-131.

Cui, L., & Fall, M. (2018). Multiphysics modeling and simulation of strength development and distribution in cemented tailings backfill structures. *International Journal of Concrete Structures and Materials*, 12(1), 25.

Cundall, P. A., & Strack, O. D. L. (1979). A discrete numerical model for granular assemblies. *Géotechnique*, 29(1), 47-65.

Dalcé, J. B., Li, L., & Yang, P. (2019). Effect of segregation on the geotechnical properties of a hydraulic backfill. *Eighth international conference on case histories in geotechnical engineering*, Reston, VA: American Society of Civil Engineers, 269-276.

Dams, I. C. o. L. (2001). *Tailings dams: risk of dangerous occurrences: lessons learnt from practical experiences*. United Nations Publications.

Darling, P. (2011). *SME mining engineering handbook (Vol. 1)*. Society for Mining, Metallurgy & Exploration (SME).

Davies, M. P. (2002). Tailings impoundment failures are geotechnical engineers listening? *GEOTECHNICAL NEWS-VANCOUVER-*, 20(3), 31-36.

Deb, D., T, S., Dey, G. K., & Panchal, S. (2016). Paste backfill technology: essential characteristics and assessment of its application for mill rejects of Uranium ores. *Transactions of the Indian Institute of Metals*, 70(2), 487-495.

Dedegil, M. Y. (1987). Drag coefficient and settling velocity of particles in non-Newtonian suspensions. *Journal of Fluids Engineering*, 109(3), 319-323.

Deiminiat, A., & Li, L. (2022). Experimental study on the reliability of scaling down techniques used in direct shear tests to determine the shear strength of rockfill and waste rocks. *CivilEng*, 3(1), 35-50.

Deiminiat, A., Li, L., & Pabst, T. (2023). Experimental study on specimen size effect and the minimum required specimen diameter to maximum particle size ratio for constant head permeability tests. *Environmental Earth Sciences*, 82(14), 355.

Deiminiat, A., Li, L., & Zeng, F. (2022). Experimental study on the minimum required specimen width to maximum particle size ratio in direct shear tests. *CivilEng*, 3(1), 66-84.

Deiminiat, A., Li, L., Zeng, F., Pabst, T., Chapuis, R., & Chiasson, P. (2020). An overview on the determination of the shear strength of coarse grain materials (rockfills) from small scale laboratory tests. *Geo Virtual 2020*, 14-16.

Deiminiat, A., Li, L., Zeng, F., Pabst, T., Chiasson, P., Chapuis, R., & Rossi, P. P. (2020). Determination of the shear strength of rockfill from small-scale laboratory shear tests: a critical review. *Advances in Civil Engineering*, 2020, 1-18.

Di Felice, R. (1994). The voidage function for fluid-particle interaction systems. *International Journal of Multiphase Flow*, 20(1), 153-159.

Dight, P., & Cowling, R. (1979). Determination of material parameters in cemented fill. *ISRM Congress*, ISRM-4CONGRESS.

Domínguez, J., Fourtakas, G., Altomare, C., Canelas, R., Tafuni, A., García Feal, O., Martínez-Estévez, I., Mokos, A., Vacondio, R., Crespo, A., Rogers, B., Stansby, P., & Gesteira, M. (2021). State-of-the-art SPH solver DualSPHysics: from fluid dynamics to multiphysics problems. *Computational Particle Mechanics*, 9(5), 867-895.

Dwumfour, D., Dixon, J., & Mylvaganam, J. (2020). Waste rock characterisation and stability assessments for feasibility level studies. *Proceedings of the 2020 International Symposium on Slope Stability in Open Pit Mining and Civil Engineering*, 677-690.

EDEM (2011). *EDEM 2.4 Programming guide*. 2011 DEM Solutions.

EDEM (2014). *EDEM 2.6 Reference guide*. 2014 DEM Solutions.

EDEM (2022). *Altair EDEM 2022.2 release notes*. Altair Engineering.

Edraki, M., Baumgartl, T., Manlapig, E., Bradshaw, D., Franks, D. M., & Moran, C. J. (2014). Designing mine tailings for better environmental, social and economic outcomes: a review of alternative approaches. *Journal of Cleaner Production*, 84, 411-420.

El Mkadmi, N., Aubertin, M., & Li, L. (2014). Effect of drainage and sequential filling on the behavior of backfill in mine stopes. *Canadian Geotechnical Journal*, 51(1), 1-15.

Elimelech, M., Gregory, J., Jia, X., & Williams, R. A. (1995). Colloidal hydrodynamics and transport. *Particle Deposition & Aggregation*, 68-109.

Emad, M. Z. (2014). Dynamic performance of cemented rockfill under blast-induced vibrations. Ph.D. thesis, McGill University.

Emad, M. Z., Mitri, H., & Kelly, C. (2014a). Effect of blast-induced vibrations on fill failure in vertical block mining with delayed backfill. *Canadian Geotechnical Journal*, 51(9), 975-983.

Emad, M. Z., Mitri, H., & Kelly, C. (2014b). State-of-the-art review of backfill practices for sublevel stoping system. *International Journal of Mining, Reclamation and Environment*, 29(6), 544-556.

Emad, M. Z., Mitri, H. S., & Henning, J. G. (2012). Effect of blast vibrations on the stability of cemented rockfill. *International Journal of Mining, Reclamation and Environment*, 26(3), 233-243.

Emad, M. Z., Vennes, I., Mitri, H., & Kelly, C. (2014). Backfill practices for sublevel stoping system. *Mine Planning and Equipment Selection: Proceedings of the 22nd MPES Conference*, Dresden, Germany, 391-402.

Fabio, M. (2011). Three major mining challenges and their technological solutions. *Mining Engineering*, 63(9).

Falaknaz, N., Aubertin, M., & Li, L. (2015a). Evaluation of the stress state in two adjacent backfilled stopes within an elasto-plastic rock mass. *Geotechnical and Geological Engineering*, 1-24.

Falaknaz, N., Aubertin, M., & Li, L. (2015b). Numerical analyses of the stress state in two neighboring stopes excavated and backfilled in sequence. *International Journal of Geomechanics*, 15(6), 04015005.

Falaknaz, N., Aubertin, M., & Li, L. (2015c). Numerical investigation of the geomechanical response of adjacent backfilled stopes. *Canadian Geotechnical Journal*, 52(10), 1507-1525.

Fall, M. L., Benzaazoua, M., & Ouellet, S. (2004). Effect of tailings properties on paste backfill performance. *Proceedings of the 8th International Symposia on Mining with Backfill*, Beijing, China, 193-202.

Farsangi, P. N. (1996). *Improving cemented rockfill design in open stoping*. Ph.D. thesis, McGill University.

Fehrsen, M., & Cooke, R. (2006). Paste fill pipeline distribution systems-current status. *Rise of the Machines–The State of the Art in Mining, Mechanisation, Automation, Hydraulic Transport and Communications*, 1-13.

Feng, Y. T., & Owen, D. R. J. (2014). Discrete element modelling of large scale particle systems—I: exact scaling laws. *Computational Particle Mechanics*, 1(2), 159-168.

Ferdosi, B., James, M., & Aubertin, M. (2015). Investigation of the effect of waste rock inclusions configuration on the seismic performance of a tailings impoundment. *Geotechnical and Geological Engineering*, 33(6), 1519-1537.

Ferreira, V. O., Geitani, T. E., Silva, D., Blais, B., & Lopes, G. C. (2023). In-depth validation of unresolved CFD-DEM simulations of liquid fluidized beds. *Powder Technology*, 426, 118652.

Fonceca Junior, J., Maza, D., & Hidalgo, R. (2021). Modeling particle-fluid interaction in a coupled CFD-DEM framework. *EPJ Web of Conferences*, 249, 09004.

Gamache-Rochette, A. (2004). *Une étude de caractérisation en laboratoire et sur le terrain des écoulements de l'eau dans les roches stériles.* Master's thesis, École Polytechnique de Montréal.

Gawu, S. K., & Fourie, A. B. (2004). Assessment of the modified slump test as a measure of the yield stress of high-density thickened tailings. *Canadian Geotechnical Journal*, 41(1), 39-47.

Gingold, R. A., & Monaghan, J. J. (1977). Smoothed particle hydrodynamics: theory and application to non-spherical stars. *Monthly Notices of the Royal Astronomical Society*, 181(3), 375-389.

Greberg, J., & Salama, A. (2015). Innovative mining methods and processes for deep steeply dipping deposits : -I2Mine Subtask 2.1.1, *För godkännande*, 60.

Grice, A. G. (2001). Recent mine fill developments in Australia. *Proceedings of the 7th international symposium on mining with Backfill: Minefill*, 351-357.

Hamrin, H. (1980). *Guide to underground mining methods and applications*. Atlas Copco, 1980.

Hamrin, H., Hustrulid, W., & Bullock, R. (2001). Underground mining methods and applications. *Underground mining methods: Engineering fundamentals and international case studies*, 3-14.

Hane, I., Belem, T., Benzaazoua, M., & Maqsoud, A. (2017). Laboratory characterization of cemented tailings paste containing crushed waste rocks for improved compressive strength development. *Geotechnical and Geological Engineering*, 35(2), 645-662.

Härtl, J., & Ooi, J. Y. (2008). Experiments and simulations of direct shear tests: porosity, contact friction and bulk friction. *Granular Matter*, 10(4), 263-271.

Hassani, F., Archibald, J., Canadian Institute of Mining, M., & Petroleum. (1998). *Mine backfill 1998.* Canadian Institute of Mining, Metallurgy and Petroleum, Montréal, Canada.

He, Y., Bayly, A. E., Hassanpour, A., Muller, F., Wu, K., & Yang, D. (2018). A GPU-based coupled SPH-DEM method for particle-fluid flow with free surfaces. *Powder Technology*, 338, 548-562.

He, Y. B. (1994). *The effects of rheology and stability of magnetite dense media on the performance of dense medium cyclones.* Ph.D. thesis, University of British Columbia.

He, Y. B., Laskowski, J. S., & Klein, B. (2001). Particle movement in non-Newtonian slurries: the effect of yield stress on dense medium separation. *Chemical Engineering Science*, 56(9), 2991-2998.

Hedley, D. (1995). Final report on the stiff backfill project for MRD. *Mining Research Directorate, Canadian Rock burst Research Program, Sudbury, Ontario*.

Herget, G., & De Korompay, V. (1978). In-situ drainage properties of hydraulic backfills. *Proceedings of Mining with Backfill, Research and Innovations*, 117-123.

Hertz. On the Contact of Elastic Solids. *Crelle's Journal*, 92, 156-171.

Hertz, H. (1882). Ueber die Berührung fester elastischer Körper. *Journal für die reine und angewandte Mathematik*, 1882(92), 156-171.

Houhamdi, S., Gallego Vazquez, E., & Djeghaba, K. (2022). Particle size effect on DEM simulation of pressures applied on a cylindrical silo with hopper. *Periodica Polytechnica Civil Engineering*, 66(2), 653-669.

Hu, L., Wu, H., Zhang, L., Zhang, P., & Wen, Q. (2017). Geotechnical properties of mine tailings. *Journal of Materials in Civil Engineering*, 29(2), 04016220.

Hustrulid, W. A., & Bullock, R. L. (2001). *Underground mining methods: engineering fundamentals and international case studies*. Society for Mining, Metallurgy & Exploration (SME).

Hustrulid, W. A., McCarter, M. K., & Van Zyl, D. J. (2000). *Slope stability in surface mining*. United States.

Ibrahim Dickey, R. D., Jackson, R. L., & Flowers, G. T. (2011). Measurements of the static friction coefficient between tin surfaces and comparison to a theoretical model. *Journal of Tribology*, 133(3).

Jahanbakhshzadeh, A., Aubertin, M., & Li, L. (2017a). Analysis of the stress distribution in inclined backfilled stopes using closed-form solutions and numerical simulations. *Geotechnical and Geological Engineering*, 36, 1011-1036.

Jahanbakhshzadeh, A., Aubertin, M., & Li, L. (2017b). A new analytical solution for the stress state in inclined backfilled mine stopes. *Geotechnical and Geological Engineering*, 35(3), 1151-1167.

Jajcevic, D., Siegmann, E., Radeke, C., & Khinast, J. G. (2013). Large-scale CFD–DEM simulations of fluidized granular systems. *Chemical Engineering Science*, 98, 298-310.

James, M., Aubertin, M., & Bussière, B. (2013). On the use of waste rock inclusions to improve the performance of tailings impoundments. *18th International Conference on Soil Mechanics and Geotechnical Engineering*, Paris, France, 2-6.

Jaouhar, E. M. (2019). *Études analytiques, numériques et expérimentales pour évaluer les contraintes et les pressions dans les chantiers remblayés et sur les barricades*. Ph.D. thesis, Polytechnique Montréal.

Jaouhar, E. M., & Li, L. (2019). Effect of drainage and consolidation on the pore water pressures and total stresses within backfilled stopes and on barricades. *Advances in Civil Engineering*, 2019, 1-19.

Jehring, M. M., & Bareither, C. A. (2016). Tailings composition effects on shear strength behavior of co-mixed mine waste rock and tailings. *Acta Geotechnica*, 11(5), 1147-1166.

Ji, S., Zeng, W., Li, L., Ma, Q., & Feng, J. (2019). Geometrical characterization of stream potholes in sandstone from the Sunxi River (Chongqing, China) and implications for the development of bedrock channels. *Journal of Asian Earth Sciences*, 173, 374-385.

Jiang, H., Fall, M., & Cui, L. (2016). Yield stress of cemented paste backfill in sub-zero environments: Experimental results. *Minerals Engineering*, 92, 141-150.

Jiang, H., Fall, M., Li, Y., & Han, J. (2019). An experimental study on compressive behaviour of cemented rockfill. *Construction and Building Materials*, 213, 10-19.

Jing, L. (2003). A review of techniques, advances and outstanding issues in numerical modelling for rock mechanics and rock engineering. *International Journal of Rock Mechanics and Mining Sciences*, 40(3), 283-353.

Johnson, J., Seymour, J., Martin, L., Stepan, M., Arkoosh, A., & Emery, T. (2015). Strength and elastic properties of paste backfill at the Lucky Friday Mine, Mullan, Idaho. *ARMA US Rock Mechanics/Geomechanics Symposium*, ARMA-2015.

Jung, S., & Biswas, K. (2002). Review of current high density paste fill and its technology. *Mineral Resources Engineering*, 11(02), 165-182.

Kalonji Kabambi, A., Bussière, B., & Demers, I. (2017). Hydrogeological behaviour of covers with capillary barrier effects made of mining materials. *Geotechnical and Geological Engineering*, 35(3), 1199-1220.

Kesimal, A., Yilmaz, E., & Ercikdi, B. (2004). Evaluation of paste backfill mixtures consisting of sulphide-rich mill tailings and varying cement contents. *Cement and Concrete Research*, 34(10), 1817-1822.

Kloss, C., Goniva, C., König, A., Amberger, S., & Pirker, S. (2012). Models, algorithms and validation for opensource DEM and CFD-DEM. *Progress in Computational Fluid Dynamics*, 12, 140-152.

Kobayashi, T., Tanaka, T., Shimada, N., & Kawaguchi, T. (2013). DEM–CFD analysis of fluidization behavior of Geldart Group A particles using a dynamic adhesion force model. *Powder Technology*, 248, 143-152.

Kugan, K., & Ian, S. (2001). A non-segregating "Rocky Paste Fill" (RPF) produced by co- disposal of cemented de-Slimed tailings slurry and graded rockfill. *Minefill 2001: 7 th International Symposium on Mining with Backfill*, 27-41.

Kuo, H. P., Knight, P. C., Parker, D. J., Tsuji, Y., Adams, M. J., & Seville, J. P. K. (2002). The influence of DEM simulation parameters on the particle behaviour in a V-mixer. *Chemical Engineering Science*, 57(17), 3621-3638.

L.Bolduc, F., & Aubertin, M. (2014). Numerical investigation of the influence of waste rock inclusions on tailings consolidation. *Canadian Geotechnical Journal*, 51(9), 1021-1032.

Lack, D.-C. D., Lechner, I. A., & Petersenschacht, A (2000). *General assessment of the options and conditions for the backfilling operations in Tellus's Chandler project*. K-UTEC AG Salt Technologies.

Landriault, D. (1995). Paste backfill mix design for Canadian underground hard rock mining. *97th Annual General Meeting of CIM. Rock Mechanics and Strata Control Session,* Halifax, Nova Scotia, 238-239.

Lane, W. L., Yanske, T. R., & Roberts, D. P. (1999). Pillar extraction and rock mechanics at the Doe Run Company in Missouri 1991 to 1999. *ARMA US Rock Mechanics/Geomechanics Symposium*, ARMA-99.

Lang, L., Song, K.-I., Lao, D., & Kwon, T.-H. (2015). Rheological properties of cemented tailing backfill and the construction of a prediction model. *Materials*, 8(5), 2076-2092.

Larochelle, C. G., Bussière, B., & Pabst, T. (2019). Acid-generating waste rocks as capillary break layers in covers with capillary barrier effects for mine site reclamation. *Water, Air, & Soil Pollution*, 230(3), 1-16.

Lee, C., & Gillot, P. (2014). Case study – a high strength paste aggregate backfill at Randgold's Loulo mine in Mali. *Mine Fill 2014: Proceedings of the Eleventh International Symposium on Mining with Backfill*, Perth, 231-242.

Lee, C., & Gu, F. (2017). An examination of improvements in co-disposal of waste rock with backfill. *Paste 2017: 20th International Seminar on Paste and Thickened Tailings*, Beijing, 338-345.

Lee, J. K., Ko, J., & Kim, Y. S. (2017). Rheology of fly ash mixed tailings slurries and applicability of prediction models. *Minerals*, 7(9), 165.

Lessard, G. (2011). *Essais d'infiltration sur la halde à stériles Petit-Pas de la mine Tio, Havre-St-Pierre*. Rapport de maîtrise, École Polytechnique de Montréal.

Li, L. (2014a). Analytical solution for determining the required strength of a side-exposed mine backfill containing a plug. *Canadian Geotechnical Journal*, 51(5), 508-519.

Li, L. (2014b). Generalized solution for mining nackfill design. *International Journal of Geomechanics*, 14(3), 04014006.

Li, L. (2022). Special issue on numerical modeling in civil and mining geotechnical engineering. *Processes*, 10(8), 1571.

Li, L., Alvarez, I. C., & Aubertin, J. D. (2013). Self-weight consolidation of slurried deposition: tests and interpretation. *International Journal of Geotechnical Engineering*, 7(2), 205-213.

Li, L., Aubertin, J. D., & Dubé, J.-S. (2014). Stress distribution in a cohesionless backfill poured in a silo. *The Open Civil Engineering Journal*, 8(1).

Li, L., & Aubertin, M. (2002). A crack-induced stress approach to describe the tensile strength of transversely isotropic rocks. *Canadian Geotechnical Journal*, 39(1), 1-13.

Li, L., & Aubertin, M. (2003). A general relationship between porosity and uniaxial strength of engineering materials. *Canadian Journal of Civil Engineering*, 30(4), 644-658.

Li, L., & Aubertin, M. (2008a). An elastoplastic evaluation of the stress state around cylindrical openings based on a closed multiaxial yield surface. *International Journal for Numerical and Analytical Methods in Geomechanics*, 33(2), 193-213.

Li, L., & Aubertin, M. (2008b). An improved analytical solution to estimate the stress state in subvertical backfilled stopes. *Canadian Geotechnical Journal*, 45(10), 1487-1496.

Li, L., & Aubertin, M. (2008c). Influence of water pressure on the stress state in stopes with cohesionless backfill. *Geotechnical and Geological Engineering*, 27(1), 1-11.

Li, L., & Aubertin, M. (2008d). *An investigation of the stress state in inclined backfilled stopes using flac-2D*. Technical Report, EPM-RT-2008-01.

Li, L., & Aubertin, M. (2009a). Horizontal pressure on barricades for backfilled stopes. Part I: Fully drained conditions. *Canadian Geotechnical Journal*, 46(1), 37-46.

Li, L., & Aubertin, M. (2009b). Horizontal pressure on barricades for backfilled stopes. Part II: Submerged conditions. *Canadian Geotechnical Journal*, 46(1), 47-56.

Li, L., & Aubertin, M. (2009c). Numerical investigation of the stress state in inclined backfilled stopes. *International Journal of Geomechanics*, 9(2), 52-62.

Li, L., & Aubertin, M. (2009d). A three-dimensional analysis of the total andeffective stresses in submerged backfilled stopes. *Geotechnical and Geological Engineering*, 27(4), 559-569.

Li, L., & Aubertin, M. (2011a). Limit equilibrium analysis for the design of backfilled stope barricades made of waste rock. *Canadian Geotechnical Journal*, 48(11), 1713-1728.

Li, L., & Aubertin, M. (2011b). *Numerical and analytical solutions for the pore water pressures within barricades made of waste rocks*. Technical Report, EPM-RT-2011-02.

Li, L., & Aubertin, M. (2012). A modified solution to assess the required strength of exposed backfill in mine stopes. *Canadian Geotechnical Journal*, 49(8), 994-1002.

Li, L., & Aubertin, M. (2014a). An improved method to assess the required strength of cemented backfill in underground stopes with an open face. *International Journal of Mining Science and Technology*, 24(4), 549-558.

Li, L., & Aubertin, M. (2014b). Numerical analysis of the stress distribution in symmetrical backfilled trenches with inclined walls. *Indian Geotechnical Journal*, 45(3), 278-290.

Li, L., & Aubertin, M. (2017). Estimation des contraintes dans les roches à partir de l'écaillage autour de trous de forage. *Revue Française de Géotechnique*, 89, 3-11.

Li, L., Aubertin, M., & Belem, T. (2005a). *Development of a 3D analytical solution to evaluate stresses in backfilled vertical openings*. Technical Report, EPM-RT-2005-04.

Li, L., Aubertin, M., & Belem, T. (2005b). Formulation of a three dimensional analytical solution to evaluate stresses in backfilled vertical narrow openings. *Canadian Geotechnical Journal*, 42(6), 1705-1717.

Li, L., Aubertin, M., & Belem, T. (2006). Erratum: formulation of a three dimensional analytical solution to evaluate stresses in backfilled vertical narrow openings. *Canadian Geotechnical Journal*, *43*(3), 338-339.

Li, L., Aubertin, M., & Shirazi, A. (2010). Implementation and application of a new elastoplastic model based on a multiaxial criterion to assess the stress state near underground openings. *International Journal of Geomechanics*, 10(1), 13-21.

Li, L., Aubertin, M., Simon, R., & Bussière, B. (2005). Formulation and application of a general inelastic locus for geomaterials with variable porosity. *Canadian Geotechnical Journal*, 42(2), 601-623.

Li, L., Dubé, J.-S., & Aubertin, M. (2013). An extension of Marston's solution for the stresses in backfilled trenches with inclined walls. *Geotechnical and Geological Engineering*, 31(4), 1027-1039.

Li, L., Dubé, J.-S., & Zangeneh-Madar, Z. (2013). Estimation of total and effective stresses in trenches with inclined walls. *International Journal of Geotechnical Engineering*, 6(4), 525-538.

Li, L., Gamache, M., & Aubertin, M. (2000). Parameter determination for nonlinear stress criteria using a simple regression tool. *Canadian Geotechnical Journal*, 37(6), 1332-1347.

Li, Y., Xu, Y., & Thornton, C. (2005). A comparison of discrete element simulations and experiments for 'sandpiles' composed of spherical particles. *Powder Technology*, 160(3), 219-228.

Lingga, B. A. (2018). *Investigation of cemented rockfill properties used at a Canadian diamond mine*. Master thesis, University of Alberta.

Liston, D. (2014). Utilisation of cemented rockfill, cemented hydraulic fill and paste to successfully achieve ore production expansion to 2 Mtpa at Chelopech Mine. *Mine Fill 2014: Proceedings of the Eleventh International Symposium on Mining with Backfill*, 407-420.

Liu, G., Li, L., Yang, X., & Guo, L. (2016). A numerical analysis of the stress distribution in backfilled stopes considering nonplanar interfaces between the backfill and rock walls. *International Journal of Geotechnical Engineering*, 10(3), 271-282.

Liu, G., Li, L., Yang, X., & Guo, L. (2017). Numerical analysis of stress distribution in backfilled stopes considering interfaces between the backfill and rock walls. *International Journal of Geomechanics*, 17(2), 06016014.

Liu, G., Li, L., Yao, M., Landry, D., Malek, F., Yang, X., & Guo, L. (2017). An investigation of the uniaxial compressive strength of a cemented hydraulic backfill made of alluvial sand. *Minerals*, *7*(1), 4.

Liu, G., Yang, X., Pan, A., Guo, L. J., & Li, L. (2019). Required strength evaluation model and its application for vertically exposed backfill: inspired by Mitchell's physical model tests. *Proceedings of the 22nd International Conference on Paste, Thickened and Filtered Tailings*, Australian Centre for Geomechanics, 451-463.

Lommen, S., Schott, D., & Lodewijks, G. (2014). DEM speedup: stiffness effects on behavior of bulk material. *Particuology*, 12, 107-112.

Lu, G., Third, J. R., & Müller, C. R. (2015). Discrete element models for non-spherical particle systems: From theoretical developments to applications. *Chemical Engineering Science*, 127, 425-465.

Machač, I., Ulbrichová, I., Elson, T. P., & Cheesman, D. J. (1995). Fall of spherical particles through non-Newtonian suspensions. *Chemical Engineering Science*, 50(20), 3323-3327.

Majdanishabestari, K., Girumugisha, G., Ovalle, C., Aubertin, M., & Saez, E. (2022). Slope stability and safety distance for mine waste rock piles built by end/push dumping. *75th Canadian Geotechnical Conference (GeoCalgary 2022)*, Calgary, Alberta, Canada.

Major, G., & Knupp, R. (2008). *Report on feasibility-level pit slope design criteria Osisko Canadain Malartic project*. Golder Associates Inc.

Maknoon, M. (2016). *Slope stability analyses of waste rock piles under unsaturated conditions following large precipitations.* Ph.D. thesis, École Polytechnique de Montréal.

Maknoon, M., & Aubertin, M. (2020). On the use of bench construction to improve the stability of unsaturated waste rock piles. *Geotechnical and Geological Engineering*, 39(2), 1425-1449.

Malik, T. I., & Puigjaner, L. (2002). User needs in batch and specialties chemical processes. In B. Braunschweig & R. Gani (Eds.), *Computer Aided Chemical Engineering*, 11, 49-63.

Malone, K. F., & Xu, B. H. (2008). Determination of contact parameters for discrete element method simulations of granular systems. *Particuology*, 6(6), 521-528.

Marinack, M. C., Musgrave, R. E., & Higgs, C. F. (2013). Experimental investigations on the coefficient of restitution of single particles. *Tribology Transactions*, 56(4), 572-580.

Martin, V., Aubertin, M., & Lessard, G. (2019). An assessment of hydrogeological properties of waste rock using infiltration tests and numerical simulations. *GeoStJohn's*, *2019*, 72.

Matyas, E. L., Welch, D. E., & Reades, D. W. (1984). Geotechnical parameters and behaviour of uranium tailings. *Canadian Geotechnical Journal*, 21(3), 489-504.

Meggyes, T., & Debreczeni, Á. (2006). Paste technology for tailings management. *Land Contamination & Reclamation*, 14(4), 815-827.

Meggyes, T., & Jefferis, S. A. (2012). Mine paste backfill–the behaviour of thickened tailings and pipeline design. In *GeoCongress 2012: State of the Art and Practice in Geotechnical Engineering*, 4116-4125.

Melati, S., Wattimena, R. K., Sahara, D. P., Syafrizal, Simangunsong, G. M., Hidayat, W., Riyanto, E., & Felisia, R. R. S. (2023). Block caving mining method: transformation and its potency in Indonesia. *Energies*, 16(1), 9.

Mindlin, R. D. (1949). Compliance of elastic bodies in contact. *Journal of Applied Mechanics*, 16, 259-268.

Mindlin, R. D., & Deresiewicz, H. (1953). Elastic spheres in contact under varying oblique forces. *Journal of Applied Mechanics*, 20, 327-344.

Minkin, L., & Sikes, D. (2018). Coefficient of rolling friction - lab experiment. *American Journal of Physics*, 86(1), 77-78.

Mizani, S. (2010). *Rheology of thickened gold tailings for surface deposition.* Ph.D. thesis, Carleton University.

Mizani, S., & Simms, P. (2016). Method-dependent variation of yield stress in a thickened gold tailings explained using a structure based viscosity model. *Minerals Engineering*, 98, 40-48.

Montgomery, C. W., & Szablewski, G. S. (2006). *Environmental geology*. New York: McGraw-Hill, 540.

Moreira, A. B., Leroy, A., Violeau, D., & Taveira-Pinto, F. d. A. (2020). Overview of large-scale smoothed particle hydrodynamics modeling of dam hydraulics. *Journal of Hydraulic Engineering*, 146(2), 03119001.

Murata, K., & Kanazawa, T. (2007). Determination of Young's modulus and shear modulus by means of deflection curves for wood beams obtained in static bending tests. *Holzforschung*, 61(5), 589-594.

Nguyen, G. T., Chan, E. L., Tsuji, T., Tanaka, T., & Washino, K. (2021). Resolved CFD–DEM coupling simulation using Volume Penalisation method. *Advanced Powder Technology*, 32(1), 225-236.

Nicholson, R. V., Gillham, R. W., Cherry, J. A., & Reardon, E. J. (1989). Reduction of acid generation in mine tailings through the use of moisture-retaining cover layers as oxygen barriers. *Canadian Geotechnical Journal*, 26(1), 1-8.

Niroshan, N., Sivakugan, N., & Veenstra, R. L. (2018). Flow characteristics of cemented paste backfill. *Geotechnical and Geological Engineering*, 36(4), 2261-2272.

Nordstrom, D. K., Blowes, D. W., & Ptacek, C. J. (2015). Hydrogeochemistry and microbiology of mine drainage: An update. *Applied Geochemistry*, 57, 3-16.

O'Sullivan, C. (2011). Particle-based discrete element modeling: geomechanics perspective. *International Journal of Geomechanics*, 11(6), 449-464.

Ohno, K., Nitta, T., & Nakai, H. (2017). SPH-based fluid simulation on GPU using verlet list and subdivided cell-linked list. *2017 Fifth International Symposium on Computing and Networking (CANDAR)*, 132-138.

Okesanya, T., Kuru, E., & Sun, Y. (2020). A new generalized model for predicting the drag coefficient and the settling velocity of rigid spheres in viscoplastic fluids. *SPE Journal*, 25(06), 3217-3235.

Ouellet, S. (2024). *Recommendation during the Q/A of the Ph.D. defense of Yuyu Zhang*. Polytechnique Montréal, Montréal.

Ovalle, C. (2024). *Recommendation during the Q/A of the Ph.D. defense of Yuyu Zhang*. Polytechnique Montréal, Montréal.

Ovalle, C., & Dano, C. (2020). Effects of particle size–strength and size–shape correlations on parallel grading scaling. *Géotechnique Letters*, 10(2), 191-197.

Ovalle, C., Linero, S., Dano, C., Bard, E., Hicher, P.-Y., & Osses, R. (2020). Data compilation from large drained compression triaxial tests on coarse crushable rockfill materials. *Journal of Geotechnical and Geoenvironmental Engineering*, 146(9), 06020013.

Pagé, P., Li, L., Yang, P., & Simon, R. (2019). Numerical investigation of the stability of a base-exposed sill mat made of cemented backfill. *International Journal of Rock Mechanics and Mining Sciences*, 114, 195-207.

Palma, S., Ihle, C. F., Tamburrino, A., & Dalziel, S. B. (2016). Particle organization after viscous sedimentation in tilted containers. *Physics of Fluids*, 28(7).

Park, S.-H., Jo, Y. B., Ahn, Y., Choi, H. Y., Choi, T. S., Park, S.-S., Yoo, H. S., Kim, J. W., & Kim, E. S. (2020). Development of multi-GPU–based smoothed particle hydrodynamics code for nuclear thermal hydraulics and safety: potential and challenges. *Frontiers in Energy Research*, 8, 86.

Pashias, N., Boger, D. V., Summers, J. M., & Glenister, D. J. (1996). A fifty cent rheometer for yield stress measurement. *Journal of Rheology*, 40, 1179-1189.

Paterson, A. (2006). Rheology control of thickened tailings and paste pumping systems. *Paste 2006: Proceedings of the Ninth International Seminar on Paste and Thickened Tailings*, Australian Centre for Geomechanics, 47-56.

Peng, C., Zhan, L., Wu, W., & Zhang, B. (2021). A fully resolved SPH-DEM method for heterogeneous suspensions with arbitrary particle shape. *Powder Technology*, 387, 509-526.

Peng, Z., Doroodchi, E., Luo, C., & Moghtaderi, B. (2014). Influence of void fraction calculation on fidelity of CFD-DEM simulation of gas-solid bubbling fluidized beds. *AIChE Journal*, 60(6), 2000-2018.

Pépin, N., Aubertin, M., & James, M. (2012). Seismic table investigation of the effect of inclusions on the cyclic behaviour of tailings. *Canadian Geotechnical Journal*, 49(4), 416-426.

Peregoedova, A. (2012). *Étude expérimentale des propriétés hydrogéologiques des roches stériles à une échelle intermédiaire de laboratoire.* Master's thesis, École Polytechnique de Montréal.

Pettibone, H. C., & Kealy, C. D. (1971). Engineering properties of mine tailings. *Journal of the Soil Mechanics and Foundations Division*, 97(9), 1207-1225.

Picabea, J., Maestri, M., Cassanello, M., Salierno, G., De Blasio, C., Cardona, M. A., Hojman, D., & Somacal, H. (2022). Validation of CFD-DEM simulation of a liquid–solid fluidized bed by dynamic analysis of time series. *Particuology*, 68, 75-87.

Piciacchia, L. (1984). *The behaviour of cemented backfill employed in cut and fill stoping*. Master thesis, McGill University.

Pierce, M., Bawden, W., & Paynter, J. (1998). Laboratory testing and stability analysis of paste backfill at the Golden Giant Mine. *In Minefill 98, Proceedings of the 6* International Symp. on Min. with Backfill,* Australasian JMM, 210.

Pirouz, B., Lu, Z., & Javadi Rudd, S. (2023). Estimating rheological properties of liquefied tailings for dam break simulation using site-specific parameters and laboratory testing. *Paste 2023: 25th International Conference on Paste, Thickened and Filtered Tailings*, Austrilian Centre for Geomechanics, Banff, Canada.

Platzer, F., & Fimbinger, E. (2021). Modelling pasty material behaviour using the discrete element method. *Multiscale Science and Engineering*, 3(2), 119-128.

Potvin, Y., Thomas, E., & Fourie, A. (2005). *Handbook on Mine FIll.* Australian Centre for Geomechanics.

Pouliot, S., Bussière, B., Dagenais, A.-M., Wilson, W., & Létourneau, Y. (2018). Evaluation of the use of sulphide paste rock as cover material in mine reclamation. *Wolkersdorfer, Ch.; Sartz, L.; Weber, A*, 559-564.

Prashant, & Derksen, J. J. (2011). Direct simulations of spherical particle motion in Bingham liquids. *Computers & Chemical Engineering*, 35(7), 1200-1214.

Puderbach, V., Schmidt, K., & Antonyuk, S. (2021). A coupled CFD-DEM model for resolved simulation of filter cake formation during solid-liquid separation. *Processes*, 9(5), 826.

Qi, C., & Fourie, A. (2019). Cemented paste backfill for mineral tailings management: Review and future perspectives. *Minerals Engineering*, 144, 106025.

Qin, J., Zheng, J., & Li, L. (2021). An analytical solution to estimate the settlement of tailings or backfill slurry by considering the sedimentation and consolidation. *International Journal of Mining Science and Technology*, 31(3), 463-471.

Qiu, H., Zhang, F., Liu, L., Hou, D., & Tu, B. (2020). Influencing factors on strength of waste rock tailing cemented backfill. *Geofluids*, 2020(1), 8847623.

Qiu, H., Zhang, F., Sun, W., Liu, L., Zhao, Y., & Huan, C. (2022). Experimental study on strength and permeability characteristics of cemented rock-tailings backfill. *Frontiers in Earth Science*, 10, 802818.

Qiu, P., & Pabst, T. (2024). Effect of construction method and bench height on particle size segregation during waste rock disposal. *International Journal of Mining, Reclamation and Environment*, 1-24.

Qiu, P., & Pabst, T. (2022). Waste rock segregation during disposal: calibration and upscaling of discrete element simulations. *Powder Technology*, 412, 117981.

Qiu, P., & Pabst, T. (2023). Characterization of particle size segregation and heterogeneity along the slopes of a waste rock pile using image analysis. *Environ Earth Sci*, 82(23), 573.

Qiu, Y., & Sego, D. (2001). Laboratory properties of mine tailings. *Canadian Geotechnical Journal*, 38(1), 183-190.

Rackl, M., & Hanley, K. J. (2017). A methodical calibration procedure for discrete element models. *Powder Technology*, 307, 73-83.

Radeke, C. A., Glasser, B. J., & Khinast, J. G. (2010). Large-scale powder mixer simulations using massively parallel GPUarchitectures. *Chemical Engineering Science*, 65(24), 6435-6442.

Raffaldi, M. J., Seymour, J. B., Richardson, J., Zahl, E., & Board, M. (2019). Cemented paste backfill geomechanics at a narrow-vein underhand cut-and-fill mine. *Rock Mech Rock Eng*, 52(12), 4925-4940.

Rana, N. M., Ghahramani, N., Evans, S. G., McDougall, S., Small, A., & Take, W. A. (2021). Catastrophic mass flows resulting from tailings impoundment failures. *Engineering Geology*, *292*, 106262.

Rankine, J. (2005). *An investigation into the drainage characteristics and behaviour of hydraulically placed mine backfill and permeable minefill barricades*. Ph.D. thesis, James Cook University.

Rankine, K. J., Sivakugan, N., & Cowling, R. (2006). Emplaced geotechnical characteristics of hydraulic fills in a number of Australian mines. *Geotechnical & Geological Engineering*, 24(1), 1-14.

Rankine, R. M., & Sivakugan, N. (2007). Geotechnical properties of cemented paste backfill from Cannington mine, Australia. *Geotechnical and Geological Engineering*, 25(4), 383-393.

Reynolds, P., & Jones, T. (1989). An experimental study of the settling velocities of single particles in non-Newtonian fluids. *International Journal of Mineral Processing*, 25(1-2), 47-77.

Rico, M., Benito, G., Salgueiro, A. R., Diez-Herrero, A., & Pereira, H. G. (2008). Reported tailings dam failures: a review of the European incidents in the worldwide context. *J Hazard Mater*, 152(2), 846-852.

Rimstidt, J. D., & Vaughan, D. J. (2003). Pyrite oxidation: a state-of-the-art assessment of the reaction mechanism. *Geochimica et Cosmochimica Acta*, 67(5), 873-880.

Robb, D. M., Gaskin, S. J., & Marongiu, J.-C. (2016). SPH-DEM model for free-surface flows containing solids applied to river ice jams. *Journal of Hydraulic Research*, 54(1), 27-40.

Robinsky, E. (1975). Thickened discharge. a new approach to tailings disposal. *Canadian Institute of Mining, Metallurgy and Petroleum*, 47-53.

Robinson, M., Luding, S., & Marco Ramaioli, M. (2013). Grain sedimentation with SPH-DEM and its validation. *AIP Conference Proceedings*, American Institute of Physics,1079-1082.

Roessler, T., & Katterfeld, A. (2018). Scaling of the angle of repose test and its influence on the calibration of DEM parameters using upscaled particles. *Powder Technology*, 330, 58-66.

Saebimoghaddam, A. (2005). *Rheological yield stress measurements of mine paste fill material*. Master thesis, McGill University.

Sainsbury, B.-A., Gharehdash, S., & Sainsbury, D. (2021). Large-scale characterisation of cemented rock fill performance for exposure stability analysis. *Construction and Building Materials*, 308, 124995.

Sainsbury, D., & Sainsbury, B. (2014). Design and implementation of cemented rockfill at the Ballarat Gold project. *Mine Fill 2014: Proceedings of the Eleventh International Symposium on Mining with Backfill*, Australian Centre for Geomechanics, 205-216.

Salama, A. (2014). *Haulage system optimization for underground mines : A discrete event simulation and mixed integer programming approach*. Ph.D. thesis, Luleå tekniska universitet.

Salamat, J., & Genç, B. (2023). Numerical simulation of granular flow in concrete batching plant via discrete element method. *The European Journal of Research and Development*, 3(2), 11-28.

Saleh-Mbemba, F., Aubertin, M., Mbonimpa, M., & Li, L. (2015). Experimental characterization of the shrinkage and water retention behaviour of tailings from hard rock mines. *Geotechnical and Geological Engineering*, 34(1), 251-266.

Salvoldi, B., Van Der Spuy, B., & Wilson, S. (2019). Optimisation of cemented aggregate backfill at New Luika Gold Mine. *Paste 2019: Proceedings of the 22nd International Conference on Paste, Thickened and Filtered Tailings*, Australian Centre for Geomechanics, 437-450.

Sandeep, C. S., Senetakis, K., Cheung, D., Choi, C. E., Wang, Y., Coop, M. R., & Ng, C. W. W. (2021). Experimental study on the coefficient of restitution of grain against block interfaces for natural and engineered materials. *Canadian Geotechnical Journal*, 58(1), 35-48.

Sarabian, M., Rosti, M. E., Brandt, L., & Hormozi, S. (2020). Numerical simulations of a sphere settling in simple shear flows of yield stress fluids. *Journal of Fluid Mechanics*, 896, A17.

Saw, H., Prentice, S., & Villaescusa, E. (2011). Characterisation of cemented rock fill materials for the Cosmos nickel mine, Western Australia. *Proceedings International Conference on Advances in Construction Materials through Science and Engineering*, 907-914.

Saw, H. A., & Villaescusa, E. (2013). Geotechnical properties of mine fill. *Proceedings of the 18th Southeast Asian Geotechnical Conference: Advances in Geotechnical Infrastructure, Geotechnical Society of Singapore*, Singapore, 787-792.

Schiller, L. (1933). A drag coefficient correlation. *Zeit. Ver. Deutsch. Ing.*, 77, 318-320.

Seymour, J. B., Martin, L. A., Raffaldi, M. J., Warren, S. N., & Sandbak, L. A. (2019). Long-term stability of a 13.7 x 30.5-m (45 x 100-ft) undercut span beneath cemented rockfill at the Turquoise Ridge mine, Nevada. *Rock Mech Rock Eng*, 2019, 1-17.

Shamsai, A., Pak, A., Bateni, S. M., & Ayatollahi, S. A. H. (2007). Geotechnical characteristics of copper mine tailings: a case study. *Geotechnical and Geological Engineering*, 25(5), 591-602.

Shekhar, G. (2020). *Draw control strategy for sublevel caving mines: A holistic approach.* Ph.D. thesis, Luleå University of Technology.

Shen, Z., Wang, G., Huang, D., & Jin, F. (2022). A resolved CFD-DEM coupling model for modeling two-phase fluids interaction with irregularly shaped particles. *Journal of Computational Physics*, 448, 110695.

Shenavar, M., Ataee-pour, M., & Rahmanpour, M. (2019). Production scheduling in sublevel caving method with the objective of NPV maximization. *Proceedings of the 27th International Symposium on Mine Planning and Equipment Selection - MPES 2018*, Springer International Publishing, 153-163.

Sheshpari, M. (2015). A review of underground mine backfilling methods with emphasis on cemented paste backfill. *Electronic Journal of Geotechnical Engineering*, 20(13), 5183-5208.

Shirazi, A., Li, L., & Aubertin, M. (2006). *Numerical implementation of an elasto-plastic model based on the MSDPu multiaxial criterion*. Technical Report, EPM-RT-2006-08.

Shirgaonkar, A. A., MacIver, M. A., & Patankar, N. A. (2009). A new mathematical formulation and fast algorithm for fully resolved simulation of self-propulsion. *Journal of Computational Physics*, 228(7), 2366-2390.

Shokrollahzadeh, A. (2015). *Terminal settling velocity of a sphere in a non-Newtonian fluid*. Master thesis, University of Alberta.

Shrestha, B. K., Tannant, D. D., Proskin, S., Reinson, J., & Greer, S. (2008). Properties of cemented rockfill used in an open pit mine. *GeoEdmonton*, 8, 609-616.

Shuai, X., Liang, R., Suorineni, F., & Li, Y. (2021). Evaluation of the use of sublevel open stoping in the mining of moderately dipping medium-thick orebodies. *International Journal of Mining Science and Technology*, 31(2), 333-346.

Siegmann, E., Enzinger, S., Toson, P., Doshi, P., Khinast, J., & Jajcevic, D. (2021). Massively speeding up DEM simulations of continuous processes using a DEM extrapolation. *Powder Technology*, 390, 442-455.

Silva, M., Hansson, M., & Silva, M. C. e. (2021). Rheological yield stress measurement of paste fill: New technical approaches. *Minefill 2020-2021,* CRC Press, 169-182.

Sivakugan, N. (2015). Drainage issues and stress developments within hydraulic fill mine stopes. *Australian Journal of Civil Engineering*, 5(1), 61-70.

Sivakugan, N., Rankine, K., & Rankine, R. (2005). *Geotechnical aspects of hydraulic filling of underground mine stopes in Australia*. In Elsevier Geo-Engineering Book Series, 3, 513-538.

Sivakugan, N., Rankine, R. M., Rankine, K. J., & Rankine, K. S. (2006). Geotechnical considerations in mine backfilling in Australia. *Journal of Cleaner Production*, 14(12-13), 1168-1175.

Sivakugan, N., Veenstra, R., & Naguleswaran, N. (2015). Underground mine backfilling in Australia using paste fills and hydraulic fills. *International Journal of Geosynthetics and Ground Engineering*, 1(2), 1-7.

Skawina, B. (2017). *Rock Mass Transportation Systems in Underground Mines: Consequences and Solutions when Mining at Greater Depths.* Ph.D. thesis, Luleå University of Technology.

Smith, L. (2021). Hydrogeology and mineral resource development. *The Groundwater Project: Guelph, ON, Canada*.

Smith, L. J. D., Blowes, D. W., Jambor, J. L., Smith, L., Sego, D. C., & Neuner, M. (2013). The Diavik Waste Rock Project: Particle size distribution and sulfur characteristics of low-sulfide waste rock. *Applied Geochemistry*, 36, 200-209.

Sobhi, M. A., & Li, L. (2017). Numerical investigation of the stresses in backfilled stopes overlying a sill mat. *Journal of Rock Mechanics and Geotechnical Engineering*, 9(3), 490-501.

Sofra, F. (2017). Rheological properties of fresh cemented paste tailings. *Paste Tailings Management*, 33-57.

Sofrá, F., & Boger, D. V. (2002). Environmental rheology for waste minimisation in the minerals industry. *Chemical Engineering Journal*, 86(3), 319-330.

Sofrà, F., & Boger, D. V. (2011). Rheology for thickened tailings and paste — history, state-of-the-art and future directions. *Paste 2011: Proceedings of the 14th International Seminar on Paste and Thickened Tailings*, Australian Centre for Geomechanics, 131-133.

Stevens, J. (1982). Unified soil classification system. *Civil Engineering—ASCE*, 52(12), 61-62.

Stokes, G. G. (1851). *On the effect of the internal friction of fluids on the motion of pendulums.* Transactions of the Cambridge Philosophical Society, Part II, 9, 8-106.

Stone, D. (2014). The evolution of paste for backfill. *Mine Fill 2014: Proceedings of the Eleventh International Symposium on Mining with Backfill*, Australian Centre for Geomechanics, 31-38.

Sun, W., Wang, H., & Hou, K. (2018). Control of waste rock-tailings paste backfill for active mining subsidence areas. *Journal of Cleaner Production*, 171, 567-579.

Sun, X., Sakai, M., & Yamada, Y. (2013). Three-dimensional simulation of a solid–liquid flow by the DEM–SPH method. *Journal of Computational Physics*, 248, 147-176.

Svanberg, A., Larsson, S., Mäki, R., & Jonsén, P. (2020). Full-scale simulation and validation of bucket filling for a mining rope shovel by using a combined rigid FE-DEM granular material model. *Computational Particle Mechanics*, 8(4), 825-843.

Tabuteau, H., Coussot, P., & de Bruyn, J. R. (2007). Drag force on a sphere in steady motion through a yield-stress fluid. *Journal of Rheology*, 51(1), 125-137.

Taha, H., Nguyen, N.-S., Marot, D., Hijazi, A., & Abou-Saleh, K. (2022). A DEM study of the effect of the loss of fine particles on the mechanical behavior of gap-graded soils. *Geomechanics for Energy and the Environment*, 31, 100305.

Talbot, A. N., Brown, H. A., Station, U. o. I. E. E., Knipp, C. T., & Richart, F. E. (1923). *The strength of concrete: its relation to the cement aggregates and water*. University of Illinois, 137-138.

Tatiya, R. R. (2005). *Surface and underground excavations methods, techniques and equipment* (1st ed.). CRC press.

Tesarik, D. R., Seymour, J. B., & Yanske, T. R. (2009). Long-term stability of a backfilled room-and-pillar test section at the Buick Mine, Missouri, USA. *International Journal of Rock Mechanics and Mining Sciences*, 46(7), 1182-1196.

Thoeni, K., Servin, M., Sloan, S. W., & Giacomini, A. (2019). Designing waste rock barriers by advanced numerical modelling. *Journal of Rock Mechanics and Geotechnical Engineering*, 11(3), 659-675.

Thompson, B. D., Bawden, W. F., & Grabinsky, M. W. (2012). In situ measurements of cemented paste backfill at the Cayeli Mine. *Canadian Geotechnical Journal*, 49(7), 755-772.

Tian, Y., Zhang, S., Lin, P., Yang, Q., Yang, G., & Yang, L. (2017). Implementing discrete element method for large-scale simulation of particles on multiple GPUs. *Computers & Chemical Engineering*, 104, 231-240.

Timoshenko, S., Timoshenko, S., & Goodier, J. N. (1951). *Theory of Elasticity*. McGraw-Hill Book Company, New York.

Trujillo-Vela, M. G., Galindo-Torres, S. A., Zhang, X., Ramos-Cañón, A. M., & Escobar-Vargas, J. A. (2020). Smooth particle hydrodynamics and discrete element method coupling scheme for the simulation of debris flows. *Computers and Geotechnics*, 125, 103669.

Tsuji, Y., Kawaguchi, T., & Tanaka, T. (1993). Discrete particle simulation of two-dimensional fluidized bed. *Powder Technology*, 77(1), 79-87.

Turton, R., & Levenspiel, O. (1986). A short note on the drag correlation for spheres. *Powder Technology*, 47(1), 83-86.

Uhlherr, P. H., Guo, J., Fang, T.-N., & Tiu, C. (2002). Static measurement of yield stress using a cylindrical penetrometer. *Korea-Australia Rheology Journal*, 14(1), 17-23.

Utili, S., Zhao, T., & Houlsby, G. T. (2015). 3D DEM investigation of granular column collapse: Evaluation of debris motion and its destructive power. *Engineering Geology*, 186, 3-16.

Valdez-Balderas, D., Domínguez, J. M., Rogers, B. D., & Crespo, A. J. C. (2013). Towards accelerating smoothed particle hydrodynamics simulations for free-surface flows on multi-GPU clusters. *Journal of Parallel and Distributed Computing*, 73(11), 1483-1493.

Valentik, L., & Whitmore, R. L. (1965). The terminal velocity of spheres in Bingham plastics. *British Journal of Applied Physics*, 16(8), 1197.

Van Buijtenen, M. S., Van Dijk, W.-J., Deen, N. G., Kuipers, J., Leadbeater, T., & Parker, D. (2011). Numerical and experimental study on multiple-spout fluidized beds. *Chemical Engineering Science*, 66(11), 2368-2376.

Veenstra, R. L. (2013). *A design procedure for determining the in situ stresses of early age cemented paste backfill*. Ph.D. thesis, University of Toronto.

Veenstra, R. L., & Grobler, J. J. (2021). Paste-waste design and implementation at Newmont Goldcorp's Tanami Operation. *Minefill 2020-2021*, CRC Press, 382-397.

Vennes, I. (2014). *Determination of cemented rockfill strength with large scale UCS tests under in-situ conditions*. Master thesis, McGill University.

Vick, S. G. (1990). *Planning, design, and analysis of tailings dams*. BiTech Publishers Ltd.

Wang, B., Xiong, T., Gao, L., Chai, Y., Cui, X., & Ding, W. (2019). Effects of tailings gradation on rheological properties of filling slurry. *Advances in Civil Engineering*, 2019, 1-11.

Wang, C., Harbottle, D., Liu, Q., & Xu, Z. (2014). Current state of fine mineral tailings treatment: A critical review on theory and practice. *Minerals Engineering*, 58, 113-131.

Wang, L., Meguid, M., & Mitri, H. S. (2021). Impact of ballast fouling on the mechanical properties of railway ballast: insights from discrete element analysis. *Processes*, 9(8), 1331.

Wang, R. (2021). *Numerical Analyses of the Stability and Geomechanical Behavior of Side-exposed Backfill Associated with Closure of Rock Walls*. Ph.D. thesis, Polytechnique Montréal.

Wang, R., & Li, L. (2019). A non-stationary power law model to predict the secondary creep rate of rocks. *Eighth International Conference on Case Histories in Geotechnical Engineering*, Reston, VA: American Society of Civil Engineers, 476-483.

Wang, R., Li, L., & Simon, R. (2019). A model for describing and predicting the creep strain of rocks from the primary to the tertiary stage. *International Journal of Rock Mechanics and Mining Sciences*, 123, 104087.

Wang, R., Zeng, F., & Li, L. (2021a). Applicability of constitutive models to describing the compressibility of mining backfill: a comparative study. *Processes*, 9(12), 2139.

Wang, R., Zeng, F., & Li, L. (2021b). Stability analyses of side-exposed backfill considering mine depth and extraction of adjacent stope. *International Journal of Rock Mechanics and Mining Sciences*, 142, 104735.

Washino, K., Chan, E. L., Miyazaki, K., Tsuji, T., & Tanaka, T. (2016). Time step criteria in DEM simulation of wet particles in viscosity dominant systems. *Powder Technology*, 302, 100-107.

Washino, K., Chan, E. L., & Tanaka, T. (2018). DEM with attraction forces using reduced particle stiffness. *Powder Technology*, 325, 202-208.

Watson, A., Corser, P., Garces Pardo, E., Lopez Christian, T., & Vandekeybus, J. (2010). A comparison of alternative tailings disposal methods—the promises and realities. *Mine Waste 2010: Proceedings of the First International Seminar on the Reduction of Risk in the Management of Tailings and Mine Waste*, Australian Centre for Geomechanics, 499-514.

Wickland, B. E., & Wilson, G. W. (2005). Self-weight consolidation of mixtures of mine waste rock and tailings. *Canadian Geotechnical Journal*, 42(2), 327-339.

Wickland, B. E., Wilson, G. W., & Wijewickreme, D. (2010). Hydraulic conductivity and consolidation response of mixtures of mine waste rock and tailings. *Canadian Geotechnical Journal*, 47(4), 472-485.

Wickland, B. E., Wilson, G. W., Wijewickreme, D., & Klein, B. (2006). Design and evaluation of mixtures of mine waste rock and tailings. *Canadian Geotechnical Journal*, 43(9), 928-945.

Williams, D., & Kuganathan, V. (1992). Co-disposal of coal mine tailings and coarse reject. *Third Large Open Pit Mining Conference*, 429-432.

Williams, D. J., & Walker, L. (1985). Laboratory and field strength of mine waste rock. *Civil Eng Tran*, 27(3), 299-304.

Williams, T. J., Brady, T. M., Bayer, D. C., Bren, M. J., Pakalnis, R. C., Marjerison, J. A., & Langston, R. B. (2007). Underhand cut and fill mining as practiced in three deep hard rock mines in the United States. *Proceedings of the CIM Conference and Exhibition*, Canadian Institute of Mining, Metallurgy and Petroleum, 1-11.

Wilson, G., Wickland, B., & Miskolczi, J. (2008). Design and performance of paste rock systems for improved mine waste management. *Rock Dumps 2008: Proceedings of the First International Seminar on the Management of Rock Dumps, Stockpiles and Heap Leach Pads*, Australian Centre for Geomechanics, 107-116.

Wu, A., Cheng, H., Yang, Y., & Zhang, L.-f. (2017). Development and challenge of paste technology in China. *Paste 2017: Proceedings of the 20th International Seminar on Paste and Thickened Tailings*, University of Science and Technology Beijing, 2-11.

Wu, D., Chen, W., Glowinski, D., & Wheeler, C. (2020). Modelling mineral slurries using coupled discrete element method and smoothed particle hydrodynamics. *Powder Technology*, 364, 553-561.

Wu, J., Feng, M., Mao, X., Xu, J., Zhang, W., Ni, X., & Han, G. (2018). Particle size distribution of aggregate effects on mechanical and structural properties of cemented rockfill: Experiments and modeling. *Construction and Building Materials*, 193, 295-311.

Xu, W.-J., Dong, X.-Y., & Ding, W.-T. (2019). Analysis of fluid-particle interaction in granular materials using coupled SPH-DEM method. *Powder Technology*, 353, 459-472.

Yan, Z., Wilkinson, S. K., Stitt, E. H., & Marigo, M. (2015). Discrete element modelling (DEM) input parameters: understanding their impact on model predictions using statistical analysis. *Computational Particle Mechanics*, 2(3), 283-299.

Yang, H., Fan, M., Liu, A., & Dong, L. (2015). General formulas for drag coefficient and settling velocity of sphere based on theoretical law. *International Journal of Mining Science and Technology*, 25(2), 219-223.

Yang, P. (2016). *Investigation of the Geomechanical Behavior of Mine Backfill and its Interaction with Rock Walls and Barricades.* Ph.D. thesis, École Polytechnique de Montréal.

Yang, P., & Li, L. (2017). Evolution of water table and pore-water pressure in stopes with submerged hydraulic fill. *International Journal of Geomechanics*, 17(9), 04017052.

Yang, P., Li, L., & Aubertin, M. (2017a). A new solution to assess the required strength of mine backfill with a vertical exposure. *International Journal of Geomechanics*, 17(10), 04017084.

Yang, P., Li, L., & Aubertin, M. (2017b). Stress ratios in entire mine stopes with cohesionless backfill: a numerical study. *Minerals*, 7(10), 201.

Yang, P., Li, L., Aubertin, M., Brochu-Baekelmans, M., & Ouellet, S. (2017). Stability analyses of waste rock barricades designed to retain paste backfill. *International Journal of Geomechanics*, 17(3), 04016079.

Yang, P., Li, L., & Yang, G. (2019). A numerical study of the effect of wick drains applied in mine stopes with paste fill. *Proceedings of the 8th International Congress on Environmental Geotechnics*, 3, 227-233.

Yilmaz, E., & Fall, M. (2017). *Introduction to paste tailings management*. Springer International Publishing.

Yowa, G. G., Sivakugan, N., Tuladhar, R., & Arpa, G. (2022). Strength and rheology of cemented pastefill using waste pitchstone fines and common pozzolans compared to using Portland cement. *International Journal of Geosynthetics and Ground Engineering*, 8(5), 56.

Yu, T., & Counter, D. (1983). Backfill practice and technology at Kidd Creek Mines. *CIM bulletin*, 76(856), 56-65.

Zeng, F., Li, L., Aubertin, M., & Simon, R. (2022). Implementation of the non-associated elastoplastic MSDPu model in FLAC3D and application for stress analysis of backfilled stopes. *Processes*, 10(6), 1130.

Zhai, Y. (2021). *Design of Barricades Made of Waste Rocks for Backfilled Stopes*. Ph.D. thesis, Polytechnique Montréal.

Zhang, Y., & Li, L. (2023). Experimental study on the natural mixing behaviour of waste rocks poured in a paste backfill. *International Journal of Mining, Reclamation and Environment*, 37(10), 953-977.

Zhang, Y., & Li, L. (2024). Introduction and implementation of fluid forces in a DEM code for simulating particle settlement in fluids. *Powder Technology*, 433, 119238.

Zhang, Z., Qiu, Y., Xiong, H., & Tang, R. (2023). Resolved CFD-DEM simulation of free settling of polyhedral particles with various orientations: insights provided by oscillation behavior in quiescent liquid. *Journal of Marine Science and Engineering*, 11(9), 1685.

Zhang, Z., & Yin, T. (2018). A coupled CFD–DEM simulation of slurry infiltration and filter cake formation during slurry shield tunneling. *Infrastructures*, 3(2), 15.

Zhao, J., & Shan, T. (2013). Coupled CFD–DEM simulation of fluid–particle interaction in geomechanics. *Powder Technology*, 239, 248-258.

Zhao, T., Houlsby, G. T., & Utili, S. (2014). Investigation of granular batch sedimentation via DEM–CFD coupling. *Granular Matter*, 16(6), 921-932.

Zheng, J., & Li, L. (2019). A solution to estimate stresses in backfilled stopes by considering self-weight consolidation and arching. *Proceedings of the 8th International Congress on Environmental Geotechnics*, 3, 181-189.

Zheng, J., & Li, L. (2020). Experimental study of the "short-term" pressures of uncemented paste backfill with different solid contents for barricade design. *Journal of Cleaner Production*, *275*, 123068.

Zheng, J., Li, L., & Li, Y.-C. (2020a). Solutions to estimate the excess PWP, settlement and volume of draining water after slurry deposition. Part I: impervious base. *Environmental Earth Sciences*, 79(6), 124.

Zheng, J., Li, L., & Li, Y. (2019). Total and effective stresses in backfilled stopes during the fill placement on a pervious base for barricade design. *Minerals*, 9(1), 38.

Zheng, J., Li, L., & Li, Y. C. (2020b). A solution to estimate the total and effective stresses in backfilled stopes with an impervious base during the filling operation of cohesionless backfill. *International Journal for Numerical and Analytical Methods in Geomechanics*, 44(11), 1570-1586.

Zhou, S., & Li, L. (2022). Numerical investigation on the impact of tailings slurry on catch dams built at the downstream of a breached tailings pond. *Processes*, 10(5), 898.

Zhu, H. P., Zhou, Z. Y., Yang, R. Y., & Yu, A. B. (2008). Discrete particle simulation of particulate systems: a review of major applications and findings. *Chemical Engineering Science*, 63(23), 5728-5770.

Zhu, S., Wu, C., & Yin, H. (2021). Virtual experiments of particle mixing process with the SPH-DEM model. *Materials (Basel)*, 14(9), 2199.

APPENDIX A SETTLING VELOCITY OF SPHERES IN CLAY SUSPENSIONS OBTAINED BY TESTS AND NUMERICAL MODEL

In Chapter 4, the numerical model is applied to predict the test results of spheres settling in clay suspensions conducted by Valentik and Whitmore (1965). The detailed settling velocity of each sphere in six different suspensions obtained by obtained by Valentik and Whitmore (1965) and numerical model is provided here:

Table A.1: The settling velocity of each sphere in different clay suspensions obtained by laboratory tests (Valentik and Whitmore 1965) and numerical model

	Sphere diameter (m)	Sphere radius (m)	Particle density (kg/m^3)	Settling velocity obtained by tests (m/s)	Clay density (kg/m^3)	Clay viscosity (Pa.s)	Clay yield stress (Pa)	Setting velocity obtained by numerical model (m/s)
Suspension 1	0.019	0.0095	5832	0.21	1280	0.0131	30.5	0.41
	0.019	0.0095	6032	0.36	1280	0.0131	30.5	0.59
	0.019	0.0095	6513	0.65	1280	0.0131	30.5	0.90
	0.019	0.0095	7290	0.98	1280	0.0131	30.5	1.24
	0.0254	0.0127	4804	0.41	1280	0.0131	30.5	0.57
	0.0254	0.0127	5237	0.78	1280	0.0131	30.5	0.94
	0.0254	0.0127	5544	0.98	1280	0.0131	30.5	1.13
	0.0254	0.0127	6142	1.3	1280	0.0131	30.5	1.43
	0.0254	0.0127	7034	1.63	1280	0.0131	30.5	1.79
	0.0381	0.01905	3431	0.48	1280	0.0131	30.5	0.15
	0.0381	0.01905	3603	0.57	1280	0.0131	30.5	0.53
	0.0381	0.01905	3742	0.72	1280	0.0131	30.5	0.74
	0.0381	0.01905	3990	0.88	1280	0.0131	30.5	1.02
	0.0381	0.01905	4025	0.95	1280	0.0131	30.5	1.05
	0.0381	0.01905	4479	1.16	1280	0.0131	30.5	1.41

Table A.1: The settling velocity of each sphere in different clay suspensions obtained by laboratory tests (Valentik and Whitmore 1965) and numerical model (continued)

	Sphere diameter (m)	Sphere radius (m)	Particle density (kg/m^3)	Settling velocity obtained by tests (m/s)	Clay density (kg/m^3)	Clay viscosity (Pa.s)	Clay yield stress (Pa)	Setting velocity obtained by numerical model (m/s)
Suspension 1	0.0381	0.01905	7160	2.25	1280	0.0131	30.5	2.31
	0.0508	0.0254	2673	0.30	1280	0.0131	30.5	0.15
	0.0508	0.0254	2909	0.58	1280	0.0131	30.5	0.15
	0.0508	0.0254	3416	1.21	1280	0.0131	30.5	1.15
	0.0571	0.02855	2728	0.51	1280	0.0131	30.5	0.15
	0.0571	0.02855	2981	0.81	1280	0.0131	30.5	0.86
	0.0571	0.02855	3124	0.94	1280	0.0131	30.5	1.07
	0.0571	0.02855	3621	1.25	1280	0.0131	30.5	1.61
	0.0571	0.02855	3958	1.47	1280	0.0131	30.5	1.90
Suspension 2	0.0381	0.01905	2937	0.48	1254	0.0095	22.5	0.40
	0.0381	0.01905	3214	0.83	1254	0.0095	22.5	0.84
	0.0381	0.01905	3815	1.4	1254	0.0095	22.5	1.38
	0.0381	0.01905	4179	1.66	1254	0.0095	22.5	1.62
	0.0381	0.01905	7160	2.5	1254	0.0095	22.5	2.36
	0.0571	0.02855	2352	0.54	1254	0.0095	22.5	0.30
	0.0571	0.02855	2765	1.14	1254	0.0095	22.5	1.15
	0.0571	0.02855	4003	2.04	1254	0.0095	22.5	1.95
	0.0508	0.0254	2437	0.41	1254	0.0095	22.5	0.13
	0.0508	0.0254	2673	0.85	1254	0.0095	22.5	0.76
	0.0508	0.0254	4083	1.83	1254	0.0095	22.5	1.86
	0.0254	0.0127	2795	0.22	1226	0.0081	17.5	
	0.0254	0.0127	3179	0.54	1226	0.0081	17.5	0.331

Table A.1: The settling velocity of each sphere in different clay suspensions obtained by laboratory tests (Valentik and Whitmore 1965) and numerical model (continued)

	Sphere diameter (m)	Sphere radius (m)	Particle density (kg/m^3)	Settling velocity obtained by tests (m/s)	Clay density (kg/m^3)	Clay viscosity (Pa.s)	Clay yield stress (Pa)	Setting velocity obtained by numerical model (m/s)
Suspension 3	0.0254	0.0127	3704	1.01	1226	0.0081	17.5	0.90
	0.0254	0.0127	6123	1.88	1226	0.0081	17.5	1.75
	0.0317	0.01585	3005	0.7	1226	0.0081	17.5	0.68
	0.0317	0.01585	8195	2.4	1226	0.0081	17.5	2.38
	0.0444	0.0222	2295	0.53	1226	0.0081	17.5	0.11
	0.0444	0.0222	2987	1.28	1226	0.0081	17.5	1.28
	0.0508	0.0254	2183	0.6	1226	0.0081	17.5	0.25
	0.0508	0.0254	2493	1.07	1226	0.0081	17.5	0.95
	0.0508	0.0254	3002	1.49	1226	0.0081	17.5	1.47
	0.0508	0.0254	4000	1.95	1226	0.0081	17.5	1.87
	0.0571	0.02855	2229	0.75	1226	0.0081	17.5	0.72
	0.0571	0.02855	2706	1.33	1226	0.0081	17.5	1.41
Suspension 4	0.019	0.0095	3200		1207	0.0067	13	
	0.019	0.0095	3560	0.65	1207	0.0067	13	0.70
	0.019	0.0095	4035	0.97	1207	0.0067	13	0.99
	0.019	0.0095	7290	1.75	1207	0.0067	13	1.72
	0.0254	0.0127	2711	0.15	1207	0.0067	13	0.39
	0.0254	0.0127	2779	0.54	1207	0.0067	13	0.49
	0.0254	0.0127	3210	0.88	1207	0.0067	13	0.91
	0.0254	0.0127	3649	1.15	1207	0.0067	13	1.20
	0.0381	0.01905	2702	0.97	1207	0.0067	13	1.08
	0.0571	0.02855	1910	0.58	1207	0.0067	13	0.51

Table A.1: The settling velocity of each sphere in different clay suspensions obtained by laboratory tests (Valentik and Whitmore 1965) and numerical model (continued)

	Sphere diameter (m)	Sphere radius (m)	Particle density (kg/m^3)	Settling velocity obtained by tests (m/s)	Clay density (kg/m^3)	Clay viscosity (Pa.s)	Clay yield stress (Pa)	Setting velocity obtained by numerical model (m/s)
	0.0571	0.02855	2098	0.9	1207	0.0067	13	0.92
	0.0571	0.02855	2595	1.45	1207	0.0067	13	1.40
	0.0571	0.02855	3707	1.88	1207	0.0067	13	1.92
Suspension 5	0.019	0.0095	2887	0.67	1184	0.0054	8.5	0.71
	0.019	0.0095	3891	1.1	1184	0.0054	8.5	1.14
	0.019	0.0095	7290	1.89	1184	0.0054	8.5	1.75
	0.254	0.127	2018	0.295	1184	0.0054	8.5	0.08
	0.254	0.127	2394	0.61	1184	0.0054	8.5	0.64
	0.254	0.127	2544	0.78	1184	0.0054	8.5	0.79
	0.254	0.127	3041	1.08	1184	0.0054	8.5	1.09
	0.254	0.127	4604	1.52	1184	0.0054	8.5	1.51
	0.254	0.127	6123	1.79	1184	0.0054	8.5	1.83
	57.1	28.55	1711	0.69	1184	0.0054	8.5	0.62
	57.1	28.55	2204	1.22	1184	0.0054	8.5	1.22
	57.1	28.55	2801	1.57	1184	0.0054	8.5	1.56
Suspension 6	0.019	0.0095	2000		1149	0.004	4	
	0.019	0.0095	2516	0.82	1149	0.004	4	0.82
	0.019	0.0095	3838	1.26	1149	0.004	4	1.18
	0.019	0.0095	6032	1.64	1149	0.004	4	1.60
	0.019	0.0095	7290	1.9	1149	0.004	4	1.80
	0.0254	0.0127	1708	0.42	1149	0.004	4	0.43
	0.0254	0.0127	2009	0.71	1149	0.004	4	0.75

Table A.1: The settling velocity of each sphere in different clay suspensions obtained by laboratory tests (Valentik and Whitmore 1965) and numerical model (continued)

	Sphere diameter (m)	Sphere radius (m)	Particle density (kg/m^3)	Settling velocity obtained by tests (m/s)	Clay density (kg/m^3)	Clay viscosity (Pa.s)	Clay yield stress (Pa)	Setting velocity obtained by numerical model (m/s)
Suspension 6	0.0254	0.0127	3006	1.18	1149	0.004	4	1.13
	0.0254	0.0127	4102	1.49	1149	0.004	4	1.44
	0.0254	0.0127	6023	1.92	1149	0.004	4	1.86
	0.0381	0.01905	2000	0.77	1149	0.004	4	0.93
	0.0381	0.01905	2310	1.02	1149	0.004	4	1.09
	0.0381	0.01905	5932	2.31	1149	0.004	4	2.26
	0.0571	0.02855	1314	0.17	1149	0.004	4	0.05
	0.0571	0.02855	1481	0.63	1149	0.004	4	0.68
	0.0571	0.02855	2007	0.98	1149	0.004	4	1.15
	0.0571	0.02855	2832	1.51	1149	0.004	4	1.63
	0.0571	0.02855	3879	1.89	1149	0.004	4	2.09
	0.0571	0.02855	6002	2.8	1149	0.004	4	2.79

APPENDIX B PYTHON PROGRAM SCRIPTS FOR CHAPTER 4

The python scripts used for displaying the spatial distribution of steel balls in the paste backfill (Chapter 4) is presented as follows:

```
import numpy as np
import pandas as pd
import plotly.graph_objs as go
# Load the sphere data from CSV
sphere_data = pd.read_csv( "C:\\Users\\ Coordinates.csv")
# Define the vertices and edges of the cube
vertices = [[0, 0, 0], [20, 0, 0], [20, 16.5, 0], [0, 16.5, 0], [0, 0, 15], [20, 0, 15], [20, 16.5, 15], [0, 16.5, 15]]
edges = [(0, 1), (1, 2), (2, 3), (3, 0), (4, 5), (5, 6), (6, 7), (7, 4), (0, 4), (1, 5), (2, 6), (3, 7)]
# Define the x, y, and z coordinates of the edges
x_edges = []
y_edges = []
z_edges = []
for e in edges:
    x_edges += [vertices[e[0]][0], vertices[e[1]][0], None]
    y_edges += [vertices[e[0]][1], vertices[e[1]][1], None]
    z_edges += [vertices[e[0]][2], vertices[e[1]][2], None]
# Create a trace for the edges of the cube
cube_trace = go.Scatter3d(x=x_edges, y=y_edges, z=z_edges, mode='lines', line=dict(color='black', width=5))
# Create a list to store the sphere traces
sphere_traces = []
```

```
# Define the color scale based on the z axis values
color_scale = [[0, 'red'], [0.5, 'green'], [1, 'blue']]
# Iterate over the sphere data and create a trace for each sphere
for i, row in sphere_data.iterrows():
    center = [row['x'], row['y'], row['z']]
    radius = row['radius']
    # Define the sphere's surface
    theta = np.linspace(0, 2 * np.pi, 10)
    phi = np.linspace(0, np.pi, 10)
    x = radius * np.outer(np.cos(theta), np.sin(phi)) + center[0]
    y = radius * np.outer(np.sin(theta), np.sin(phi)) + center[1]
    z = radius * np.outer(np.ones(np.size(theta)), np.cos(phi)) + center[2]
    # Create a surface trace for the sphere
    sphere_trace = go.Surface(x=x, y=y, z=z, opacity=1, colorscale=color_scale, cmin=0, cmax=15, showscale=True, colorbar=dict(title='Z-Axis Height'))
    # Add the trace to the list
    sphere_traces.append(sphere_trace)
# Create the plot
fig = go.Figure(data=[cube_trace] + sphere_traces)
# Set the layout
fig.update_layout(scene=dict(
    xaxis=dict(range=[0, 20], zeroline=True, zerolinewidth=3, zerolinecolor='grey', title = 'X (cm)'),
    yaxis=dict(range=[0, 20], zeroline=False,title = 'Y (cm)'),
    zaxis=dict(range=[0, 20], zeroline=True,title = 'Z (cm)'),
    aspectmode="manual",
```

```
    xaxis_autorange="reversed",
    aspectratio=dict(x=1, y=1, z=1)
), margin=dict(l=0, r=0, b=0, t=0))
# Set color of axises and grid
fig.update_layout(scene=dict(
                          xaxis=dict(backgroundcolor= 'white', showgrid = False),
                          yaxis=dict(backgroundcolor='white', showgrid = False),
                          zaxis=dict(backgroundcolor='white', showgrid = False)
                          ))
# Show the plot
fig.show()
```